SOLUTION GROWTH OF TUNGSTEN OXIDE ON TWO DIMENSIONAL TITANATE AND HEXANIOBATE NANOSHEETS FOR PHOTOCATALYTIC DYE DEGRADATION

A THESIS SUBMITTED TO

D. Y. PATIL EDUCATION SOCIETY (DEEMED TO BE UNIVERSITY), KOLHAPUR

FOR THE DEGREE OF

DOCTOR OF PHILOSOPHY

IN

PHYSICS

UNDER THE FACULTY OF

INTERDISCIPLINARY STUDIES

BY

Mr. YOGESH MURLIDHAR CHITARE

M. Sc.

UNDER THE SUPERVISION OF

Dr. JAYAVANT LAXMAN GUNJAKAR

M. Sc., Ph. D.

CENTRE FOR INTERDISCIPLINARY RESEARCH,

D. Y. PATIL EDUCATION SOCIETY (DEEMED TO BE UNIVERSITY),

KOLHAPUR- 416 006, MAHARASHTRA, (INDIA)

2024

DECLARATION

I am *Yogesh Murlidhar Chitare*, hereby declare that the thesis entitled *"SOLUTION GROWTH OF TUNGSTEN OXIDE ON TWO DIMENSIONAL TITANATE AND HEXANIOBATE NANOSHEETS FOR PHOTOCATALYTIC DYE DEGRADATION"* submitted for the degree of *Doctor of Philosophy (Ph.D.)* in the *Physics*, Faculty of Interdisciplinary Studies, under the guidance of *Dr. Jayavant Laxman Gunjakar, Centre for Interdisciplinary Research (CIR), D. Y. Patil Education Society (Deemed to be University), Kolhapur* is completed and written by me, has not before made the basis for the award of any other higher education institute in India or any other country. To the best of my knowledge and belief the thesis contains no material previously published or written by another person except where due reference is made. Further, I declare that I have not violated any of the provisions under the copyright and piracy/cyber/IPR Act amended from time to time.

Research Student

Place: Kolhapur

Date: /   / 2024   **Mr. Yogesh Murlidhar Chitare**

CERTIFICATE OF GUIDE

This is to certify that the thesis entitled *"SOLUTION GROWTH OF TUNGSTEN OXIDE ON TWO DIMENSIONAL TITANATE AND HEXANIOBATE NANOSHEETS FOR PHOTOCATALYTIC DYE DEGRADATION"* which is being submitted herewith for the award of the Degree of *Doctor of Philosophy (Ph.D.)* in *Physics*, Faculty of Interdisciplinary Studies, under the guidance of *Dr. Jayavant Laxman Gunjakar*, **Centre for Interdisciplinary Research (CIR)**, **D. Y. Patil Education Society (Deemed to be University), Kolhapur**, is the result of the original research work completed by *Mr. Yogesh Murlidhar Chitare* under my supervision and guidance and to the best of my knowledge and belief the work embodied in this thesis has not formed earlier the basis for the award of any degree or similar title of this or any other university or examining body.

Research Guide

Place: Kolhapur

Date: / / 2024

Dr. Jayavant Laxman Gunjakar
Associate Professor,
Centre for Interdisciplinary Research,
D. Y. Patil Education Society,
(Deemed to be University),
Kolhapur- 416 006

Forwarded through,

Prof. C. D. Lokhande

Dean and Research Director,
Centre for Interdisciplinary Research,
D. Y. Patil Education Society (Deemed to be University),
Kolhapur- 416 006

ACKNOWLEDGEMENT

I would like to give special thanks to my colleagues, **Mr. Vikas Magdum and Ms. Shirin Kulkarni**, for their assistance and support in my research endeavors. I would like to express sincere thanks to my seniors, **Dr. Rohini Shinde, Dr. Navnnath Padalkar, Dr. Shrikant Sadavar, Dr. Satish Jadhav**, **Dr. Sachin Pujari**, **Dr. Suraj Khalate**, **Dr. Prity Bagwade**, **Dr. Shital Kale, Dr. Supriya Marje**, **Dr. Pranv Katkar**, and **Dr. Shivaji Ubale** for their insightful guidance, scientific discussions, and valuable suggestions on the present work.

To my dear friends **Vinod Patil**, **Umesh Jagdale**, **Rushiraj Bhosale**, and **Ganesh Mane**, I extend my heartfelt gratitude for always being there for me in every situation and for your unwavering support and assistance. I would like to acknowledge my colleagues and juniors at the Centre for Interdisciplinary Research, **Shweta Talekar, Shraddha Pawar, Prashant Sawant, Sayali Kulkarni, Mayura Medhekar, Rakesh Mohite, Ajinkya Bagde, Ranjit Nikam, Sambhaji Kumbhar, Shraddha Bhosale, Sohel Shaikh, Ganesh Jadhav, Sambhaji Khot, Dilip Patil, Manohar Lad, Satish Phalke, Ketaki Kadam, Sumita Patil, Kuldip Belekar, Sujata Patil, Dhanashri Phadatare, Suhasini Yadav, Vinay Nimat, Shivprasad Jadhav, Anil Sutar**, and **Sagar Patil** for their wonderful collaboration. I want to thank them for their support and valuable suggestions during research work.

I am also thankful to all teaching and non-teaching staff of the Centre for Interdisciplinary Research for their cooperation.

I hereby express my deepest appreciation and regards to my wife **Priya**, my son **Samvidh**, my father (**Bhau**), my late mother (**Jiji**), my brother (**Pramod**), my sister-in-law (**Snehal Vahini**), nephew (**Krinjal**), beloved in-laws family, and all of the family members who despite their hard times and sufferings, continuously supported and encouraged me to complete my research.

~Yogesh Chitare

Place: Kolhapur

SUMMARY OF RESEARCH WORK

A) *Granted / Published (Indian) Patents*: (04)

1) **Title of Invention:** Liquid column based optical infrared filter
   (Patent No: 501334)
   Inventors: Jayavant L. Gunjakar, Akash S. Patil, Vikas V. Magdum, ***Yogesh M. Chitare***, Abhaya S. Patil

2) **Title of Invention:** Infrared cut-off water filter assembly
   (Design No: 407337-001)
   Inventors: Jayavant L. Gunjakar, ***Yogesh M. Chitare***, Vikas V. Magdum, Shirin P. Kulkarni, Akash S. Patil, Abhaya S. Patil

3) **Title of Invention:** A method for depositing uniform coating of 2D titanate nanosheets
   (Application No: 202421035776)
   Inventors: Jayavant L. Gunjakar, Vikas V. Magdum, ***Yogesh M. Chitare***, Shirin P. Kulkarni, Chandrakant D. Lokhande

4) **Title of Invention:** A method for deposition of two-dimensional titanate nanosheets thin films using cylindrical graphite electrophoretic cell
   (Application No: 202421051560)
   Inventors: Jayavant L. Gunjakar, ***Yogesh M. Chitare***, Vikas V. Magdum, Chandrakant D. Lokhande

B) *Registered Copyrights:* (02)

1) **Title of the Work:** Thin film photocatalytic setup for dye degradation
   (Registration No: L-144382/2024)
   Authors: Jayavant L. Gunjakar, ***Yogesh M. Chitare***, Vikas V. Magdum

2) **Title of the Work:** Figure representing schematic of microprocessor-controlled dip-coating instrument
   (Registration No: L-147009/2024)
   Authors: Jayavant L. Gunjakar, Vikas V. Magdum, ***Yogesh M. Chitare***

C) *Papers Published/Submitted at International Journals:* (24)

1) ***Yogesh M. Chitare***, Vikas V. Magdum, Shirin P. Kulkarni, Shweta V. Talekar, Shraddha A. Pawar, Prashant D. Sawant, Dhanaji B. Malavekar, Umakant M. Patil, Chandrakant D. Lokhande, Jayavant L. Gunjakar, Preferentially oriented m-tuned WO_3 thin-films photocatalysts for the multitargeted degradation of organic molecules, *Appl. Surf. Sci. Adv., 2024, 19, 100573,*
   https://doi.org/10.1016/j.apsadv.2024.100573 **(I. F. - 6.2)**.

2) ***Yogesh M. Chitare***, Vikas V. Magdum, Shirin P. Kulkarni, Shweta V. Talekar, Shraddha A. Pawar, Prashant D. Sawant, Dhanaji B. Malavekar, Umakant M. Patil, Jin H. Kim, Sabah Ansar, Jayavant L. Gunjakar, Vertically aligned interlocked tungsten oxide nanosheet thin film for photocatalytic application: Effect of deposition cycles, *J. Mater. Sci.: Mater. Electron., 2024, 35, 1-15,* https://doi.org/10.1007/s10854-024-13184-1 **(I. F. - 2.8)**.

3) ***Yogesh M. Chitare***, Vikas V. Magdum, Shirin P. Kulkarni, Ravindra N. Bulakhe, Dhanaji B. Malavekar, Umakant M. Patil, Jin H. Kim, Sultan Alshehri, Jayavant L. Gunjakar, Lattice engineered two dimensional titanate and tungsten oxide hybrid heterostructure thin films for visible light driven photooxidation of organic compounds, *J. Mater. Chem. C* (Under review) **(I. F. - 5.7)**.

4) ***Yogesh M. Chitare***, Vikas V. Magdum, Shirin P. Kulkarni, Dhanaji B. Malavekar, Jin H. Kim, Deu S. Bhange, Sultan Alshehri, Jayavant L. Gunjakar, Efficient visible-light-induced photocatalytic antibiotic degradation by stratified 2D-titanate and tungsten oxide heterolayered thin films, *J. Alloys Compd* (Under review) **(I. F. - 5.8)**.

5) Vikas V. Magdum, ***Yogesh M. Chitare***, Shirin P. Kulkarni, Dhanaji B. Malavekar, Amol U. Pawar, Ravindra N. Bulakhe, Chandrakant D. Lokhande, Umakant M. Patil, Sharad B. Patil, Jayavant L. Gunjakar, Tailoring the physicochemical properties of chemically deposited MoS_2 thin films for photocatalytic dye and TC degradation: Effect of different cationic precursors, *J. Mater. Sci. Mater. Electron., 2024, 35, 1433,* https://doi.org/10.1007/s10854-024-13186-z (**I. F. - 2.8**).

6) Shirin P. Kulkarni, ***Yogesh M. Chitare***, Vikas V. Magdum, Prashant D. Sawant, Shweta V. Talekar, Shraddha A. Pawar, Dhanaji B. Malavekar, Sabah Ansar, Jin H. Kim, Jayavant L. Gunjakar, Nanohybrids of layered titanate and bismuth vanadate as visible light driven photocatalysts for the degradation of dyes and antibiotic, *ACS Appl. Nano Mater., 2024,* 7, 11411-11422, https://doi.org/10.1021/acsanm.4c01039 **(I. F. - 6.14)**.

7) Shirin P. Kulkarni, ***Yogesh M. Chitare***, Vikas V. Magdum, Prashant D. Sawant, Shweta V. Talekar, Shraddha A. Pawar, Umakant M. Patil, Kishor V. Gurav, Dhanaji B. Malavekar, Amol U. Pawar, Jayavant L. Gunjakar, Chemically synthesized facet-controlled visible light active $BiVO_4$ thin films for photoelectrochemical water splitting, *Appl. Phys. A, 2023, 129, 876,* https://doi.org/10.1007/s00339-023-07164-1 **(I. F. - 2.98)**.

8) Shirin P. Kulkarni, Vikas V. Magdum, **Yogesh M. Chitare**, Prashant D. Sawant, Shweta V. Talekar, Shraddha A. Pawar, Amol U. Pawar, Dhanaji B. Malavekar, Shrikrishna D. Sartale, Ayman A. Ghfar, Jayavant L. Gunjakar, Modified successive ionic layer adsorption and reaction for interconnected bismuth vanadate nanograins: Highly active visible light harvesting

photoanodes, *J. Photochem. Photobiol. A: Chem., 2024, 454, 115737*, https://doi.org/10.1016/j.jphotochem.2024.115737 **(I. F. - 4.3)**.

9) Shirin P. Kulkarni, Vikas V. Magdum, *Yogesh M. Chitare*, Dhanaji B. Malavekar, Jin H. Kim, Sultan Alshehri, Shashikant Patole, Jayavant L. Gunjakar, 2D Porous hexaniobate-bismuth vanadate hybrid photocatalysts for photodegradation of aquatic refractory pollutants, *Haliyon, 2024, 10, 39235*, https://doi.org/10.1016/j.heliyon.2024.e39235 **(I. F. - 3.4)**.

10) Rohini B. Shinde, Navnath S. Padalkar, Shrikant V. Sadavar, Akash S. Patil, Shital B. Kale, Vikas V. Magdum, *Yogesh M. Chitare*, Shirin P. Kulkarni, Umakant M. Patil, Vinayak G. Parale, Jayavant L. Gunjakar, Lattice engineering route for self-assembled nanohybrids of 2D layered double hydroxide with 0D isopolyoxovanadate: Chemiresistive SO_2 sensor, *Mater. Today Chem., 2022, 24, 100801*, https://doi.org/10.1016/j.mtchem.2022.100801 **(I. F. - 7.3)**.

11) Rohini B. Shinde, Navnath S. Padalkar, Shrikant V. Sadavar, Shital B. Kale, Vikas V. Magdum, *Yogesh M. Chitare*, Shirin P. Kulkarni, Umakant M. Patil, Vinayak G. Parale, Hyung-Ho Park, Jayavant L. Gunjakar, 2D-2D Lattice engineering route for intimately coupled nanohybrids of layered double hydroxide and potassium hexaniobate: Chemiresistive SO_2 sensor, *J. Hazard. Mater., 2022 432, 128734*, https://doi.org/10.1016/j.jhazmat.2022.128734 **(I. F. - 13.6)**.

12) Rohini B. Shinde, Akash S. Patil, Shrikant V. Sadavar, *Yogesh M. Chitare*, Vikas V. Magdum, Navnath S. Padalkar, Umakant M. Patil, Saji T. Kochuveedu, Vinayak G. Parale, Hyung-Ho Park, Chandrakant D. Lokhande, Jayavant L. Gunjakar, Polyoxotungstate intercalated self-assembled nanohybrids of Zn-Cr-LDH for room temperature Cl2 sensing, *Sens. Actuators B Chem, 2022, 352, 131046*, https://doi.org/10.1016/j.snb.2021.131046 **(I. F. - 8.4)**.

13) Shrikant V. Sadavar, Navnath S. Padalkar, Rohini B. Shinde, Akash S. Patil, Umakant M. Patil, Vikas V. Magdum, *Yogesh M. Chitare*, Shirin P. Kulkarni, Ravindra N. Bulakhe, Saji T. Kochuveedu, Jayavant L. Gunjakar, Lattice engineering exfoliation-restacking route for 2D layered double hydroxide hybridized with 0D polyoxotungstate anions: Cathode for hybrid asymmetric supercapacitors, *Energy Storage Mater., 2022, 48, 101-113*, https://doi.org/10.1016/j.ensm.2022.03.005 **(I. F. - 20.4)**.

14) Shrikant V. Sadavar, Navnath S. Padalkar, Rohini B. Shinde, Akash S. Patil, Umakant M. Patil, Vikas V. Magdum, *Yogesh M. Chitare*, Shirin P. Kulkarni, Ravindra N. Bulakhe, Vinayak G. Parale, and Jayavant L. Gunjakar, Graphene oxide an efficient hybridization matrix for exploring electrochemical activity of 2D cobalt-chromium-layered double hydroxide based nanohybrids, *ACS Appl.*

Energy Mater., 2022, 5, 2083-2092, https://doi.org/10.1021/acsaem.1c03619 **(I. F. - 6.4)**.

15) Navnath S. Padalkar, Chae H. Cho, Vikas V. Magdum, *Yogesh M. Chitare*, Shirin P. Kulkarni, Umakant M. Patil, Jong P. Park, Jayavant L. Gunjakar, Self-assembled architecture of 2D layered double hydroxide pillared with 0D polyoxomolybdate anions: High performance redox-type cathode for solid-state asymmetric supercapacitor, *J. Energy Storage, 2023, 74, 109538,* https://doi.org/10.1016/j.est.2023.109538 **(I. F. - 9.4)**.

16) Navnath S. Padalkar, Shrikant V. Sadavar, Rohini B. Shinde, Akash S. Patil, Umakant M. Patil, Vikas V. Magdum, *Yogesh M. Chitare*, Shirin P. Kulkarni, Ravindra N. Bulakhe, Vinayak G. Parale, Jayavant L. Gunjakar, 2D-2D nanohybrids of Ni-Cr-layered double hydroxide wrapped with graphene oxide nanosheets: Electrode for hybrid asymmetric supercapacitors, *Electrochim. Acta*, *2022, 424, 140615,* https://doi.org/10.1016/j.electacta.2022.140615 **(I. F. - 6.6)**.

17) Prity P. Bagwade, Vikas V. Magdum, D hanaji B. Malavekar, *Yogesh M. Chitare*, Jayavant L. Gunjakar, Umakant M. Patil, Chandrakant D. Lokhande, Synthesis, characterization and visible light driven dye degradation performance of one-pot synthesized amorphous $CoWO_4$ powder, *J. Mater. Sci. Mater. Electron., 2022, 33, 24646-24662*, https://doi.org/10.1007/s10854-022-09174-w **(I. F. - 2.8)**.

18) Vikas V. Magdum, *Yogesh M. Chitare*, Shirin P. Kulkarni, Dhanaji B. Malavekar, Jin H. Kim, Jayavant L. Gunjakar, MoS_2 nanospheres anchored 2D titanate nanosheet hybrid photocatalyst thin films for efficient photocatalytic degradation of organic pollutants. *Mater. Sci. Eng. B* (Revision submitted) **(I. F. - 3.9)**.

19) Shraddha A. Pawar, Shweta V. Talekar, Prashant D. Sawant, Vikas V. Magdum, Shirin P. Kulkarni, *Yogesh M. Chitare*, Chandrakant D. Lokhande, Hemraj M. Yadav, Jayavant L. Gunjakar, Aqueous exfoliated 2D cobalt-iron-layered double hydroxide nanosheets: effect of Co:Fe ratio on electrocatalytic oxygen evolution reaction, *Colloid Surf. A Physicochem. Eng Aspects* (Revision submitted) **(I. F. - 4.9)**.

20) Ketaki kadam, Dhanaji B. Malavekar, Satish B. Jadhav, Vikas V. Magdum, *Yogesh M. Chitare*, Jayavant L. Gunjakar, Jin H. Kim, Vishwajeet M. Khot, Recyclable manganese substituted zinc ferrite nanoparticles for efficient photocatalytic degradation of organic dyes, *J. Mater. Sci.* (Revision submitted) **(I. F. - 3.5)**

21) Vikas V. Magdum, *Yogesh M. Chitare*, Shirin P. Kulkarni, Sharad B. Patil, Jayavant L. Gunjakar, Chemically grown MoS_2 nanosphere thin films for efficient photocatalytic decomposition of tetracycline hydrochloride. *Physica B Condens. Mater* (Submitted) **(I. F. - 2.8)**.

22) Maruti B. Kumbhar, Vinod V. Patil, Vaishali S. Chandak, Sohel B. Shaikh, *Yogesh M. Chitare*, Jayavant L. Gunjakar, Prakash M. Kulal, Preparation of binder-free nickel oxide thin film electrodes via a simple synthetic method for use as highly stable cathodes in flexible solid state hybrid supercapacitor devices, *J. Power Sources*, (Under review) **(I. F. - 8.1)**.

23) Maruti B. Kumbhar, Vinod V. Patil, Vaishali S. Chandak, *Yogesh M. Chitare*, Jayavant L. Gunjakar, Prakash M. Kulal, Exploring copper-doped nickel oxide as a superior cathode electrode material for flexible hybrid solid-state supercapacitor device, *J. Energy Storage*, (submitted) **(I. F. - 10)**.

24) Maruti B. Kumbhar, Vinod V. Patil, Vaishali S. Chandak, *Yogesh M. Chitare*, Jayavant L. Gunjakar, Prakash M. Kulal, Investigating cobalt-doped nickel oxide as an excellent cathode electrode ingredient for flexible hybrid solid-state supercapacitor devices, *Energy Fuels*, (submitted) **(I. F. - 5.2)**.

D) *Review Published at International Journals:* (02)

1) *Yogesh M. Chitare*, Satish B. Jadhav, Padmja N. Pawaskar, Vikas V. Magdum, Jayavant L. Gunjakar, Chandrakant D. Lokhande, Metal oxide-based composites in nonenzymatic electrochemical glucose sensors, Ind. Eng. Chem. Res., 60, 2021, 18195-18217, https://doi.org/10.1021/acs.iecr.1c03662 (**I. F. - 4.2**).

2) Vikas V. Magdum, *Yogesh M. Chitare*, Shirin P. Kulkarni, Prashant D. Sawant, Shraddha A. Pawar, Shweta V. Talekar, Chandrakant D. Lokhande, Umakant M. Patil, Sharad B. Patil, Jayavant L. Gunjakar, Versatility of group VI layered metal chalcogenide thin films synthesized by solution-based deposition methods, *J. Mater. Chem. C*, 2023, 11, 9768-9786, https://doi.org/10.1039/D3TC01470C (**I. F. - 6.4**).

E) *Book Chapter Published:* (01)

1) *Y. M. Chitare*, V. V. Magdum, S. B. Jadhav, S. P. Kulkarni, C. D. Lokhande, J. L. Gunjakar, "Rare earth element-based nonenzymatic glucose sensor" in 'Chemically Deposited Metal Chalcogenide-based Carbon Composites for Versatile Applications' Springer Nature (2023), 393-410.

F) *Papers/Poster Presented at National/International Conferences:* (06)

1) Poster presentation at the National Conference on "Recent Trends in Functional Materials and Their Applications (RTFMA-2024)" held at Shardabai Pawar Mahila Arts, Commerce & Science College Shardanagar, Malegoan, Baramati, from 13th to 14th March 2024. (**First prize**)

2) Poster presentation at the International Conference on "Nanotechnology Addressing the Convergence of Materials Science, Biotechnology, and Medical Science (IC-NACMBM-2024)" held at D. Y. Patil Education Society (Deemed to be University), Kolhapur, from 12th -14th February 2024. (**Third prize**)

3) Poster presentation at the "Annual Convention of Chemists (ACC 2023)" held at IIT Indian Institute of Technology (IIT), Delhi, from 20th -21st December 2023.

4) Oral presentation at "2nd Asian e-Conference on Engineered Science" held online, from 5th to 6th December 2021.

5) Attended National e-Conference on "Advanced Materials and Applications (AMA-2021)", held online, on 23rd October 2021.

6) Participated in the workshop and hands-on training on XRD organized by Shivaji University, Kolhapur held during 11-12th Nov. 2021.

CONTENTS

List of Abbreviations

- **1D**   One-dimensional
- **2D**   Two-dimensional
- **3D**   Three-dimensional
- **CB**   Conduction band
- **CBD**   Chemical bath deposition
- **CV**   Crystal violet
- **CVD**   Chemical vapor deposition
- **DDW**   Double distilled water
- **EBT**   Eriochrome black T
- **EDS**   Energy dispersive spectroscopy
- **EPD**   Electrophoretic deposition
- **FESEM**   Field emission scanning electron microscopy
- **FT-IR**   Fourier transform infrared spectroscopy
- **Hexaniobate-NS** Hexaniobate nanosheets
- **HQ**   Hydroquinone
- **IC**   Indigo carmine
- **INs**   Inorganic nanosheets
- **IP**   Ionic product
- **ITO**   Indium doped tin oxide
- **LDH**   Layered double hydroxide
- **LMC**   Layered metal chalcogenides
- **LMO**   Lamellar metal oxide
- **MB**   Methylene blue
- **MO**   Methyl orange
- **MONs**   Metal oxide nanosheets
- **MV**   Malachite green
- **Nb_2O_5**   Niobium oxide
- **NbW-C**   Hexaniobate nanosheets-WO_3 deposited by CBD method
- **NbW-S**   Hexaniobate nanosheets-WO_3 deposited by SILAR method
- **NHE**   Normal hydrogen electrode
- **Rh B**   Rhodamine B
- **SILAR**   Successive ionic layer adsorption and reaction
- **SP**   Solubility product
- **TiO_2**   Titanium oxide
- **Titanate-NS**   Titanate nanosheets
- **TiW-C**   Titanatae nanosheets-WO_3 deposited by CBD method
- **TiW-S**   Titanatae nanosheets-WO_3 deposited by SILAR method
- **TMOs**   Transition metal oxides
- **UV**   Ultraviolet
- **UV-vis DRS**   Ultraviolet-visible diffuse reflectance spectroscopy
- **VB**   Valence band
- **WO_3**   Tungsten oxide
- **XPS**   X-ray photoelectron spectroscopy
- **XRD**   X-ray diffraction

LIST OF FIGURES

Chapter I: General Introduction and Literature Survey

Chapter II: Theoretical Background of Synthesis Process and Thin Film Characterization Techniques

Chapter III: Exfoliative Synthesis and Characterization of Pristine Titanate-NS and Hexaniobate-NS

Chapter IV: Synthesis and characterization of WO₃-titanate-NS heterostructure thin films by CBD: application in photocatalytic dye degradation

Chapter V: Synthesis and characterization of WO$_3$ titanate-NS heterostructure thin films by SILAR: application in photocatalytic dye degradation

Chapter VI: Synthesis and characterization of WO₃-hexaniobate-NS heterostructure thin films by CBD: application in photocatalytic dye degradation

Chapter VII: Synthesis and characterization of WO$_3$-hexaniobate-NS heterostructure thin films by SILAR: application in photocatalytic dye degradation

LIST OF TABLES/CHARTS

CHAPTER-I

General Introduction and Literature Survey

CHAPTER I

General Introduction and Literature Survey

1.1 Water pollution: General introduction

Rapid industrial development at the global level raised the human living standard at the expense of damaging the environment and generate many problems for humans and living organisms. The main reason behind the damaging environment is pollution. Unfavorable environmental changes occur because of the addition of different contaminants called pollution. Contaminants may be physical, chemical, biological, and many others. There are several types of pollution, such as air, soil, water, noise, and light pollution [1]. All countries are facing the issue of environmental pollution irrespective of their economic status due to the burning of conventional energy sources, including coal, petroleum, natural gases, and nuclear energy.

Among the pollutions, water pollution has emerged as a severe threat to the global environment and living organisms. Water covers about 71% of the Earth's surface. Of these, 96.5% is saline water, 1.7% is groundwater, and 1.7% is fixed in glaciers and ice caps in the Arctic and Antarctic circles. Only 2.5% of Earth's water is freshwater, with 98.8% of it in ice and groundwater. Therefore, protecting safe drinking water is essential for living organisms [2]. However, industrialization and urbanization are rapidly growing to fulfil the needs of the increased population, which is leading to more water pollution. There are many reasons behind the pollution of water, including waste produced by animals, underground storage leakage of pipes, leakage of sewer lines, fertilizers and pesticides used by the farmer, plastics, fossil fuel burning, household garbage, sewage, radioactive waste, industrial waste, etc. [3]. The various sources of water pollution are shown in **Fig. 1.1**.

Fig. 1.1. Sources of water pollution [4-6].

1.2 Water pollution due to industrial dyes:

Ground and running water pollution severely threatens humans and aquatic life. Many dyestuffs are used in advanced industries like plastic, leather, textile, cosmetics,

rubber, printing, food processing, etc. More than 100,000 commercially available dyes have various applications in different industries for different purposes. Worldwide, more than 700,000 tons of dyestuff are produced annually. Approximately 12% of dyes are wasted during manufacturing and operation, and about 20% of this enters industrial wastewater, causing water pollution [7, 8]. These dyes can affect aquatic life by decreasing light penetration and lowering photosynthetic activity. These dyes may also be toxic to some of the marine life due to the presence of metals and aromatics. Some of the dyes are also carcinogenic and mutagenic. The presence of dyes in water for a long time causes food chain contamination. In addition, it can cause severe damage to human beings as well as animals through infection of the kidney, reproductive system, liver, brain, and central nervous system. Therefore, removing dyes from polluted water has attracted considerable attention in recent years [9]. **Fig. 1.2** shows the dyes used in different industries.

Fig 1.2. Dyes used in industries [10-12].

1.3 Dyes and their classification:

Dye is a natural or synthetic substance used to color something. Pigments differ from dyes because they do not chemically bind to the material where they color, and they are insoluble in water, whereas dyes are soluble in water. Based on their synthesis, they are classified into two groups: natural and synthetic. The classification of dyes is shown in **chart 1.1** [13-17].

1.3.1 Natural dyes:

Natural dye refers to any dye that is derived from natural sources such as plants, animals, and minerals. In earlier eras large number of natural dyes were used, but now they are replaced by synthetic dyes because of:

- Natural dyes are not pure.

- ▪ Unsuitable for large-scale applications.
- ▪ Lack of uniformity in quality.
- ▪ Do not possess fastness property.
- ▪ Time consuming process.
- ▪ They are expensive.
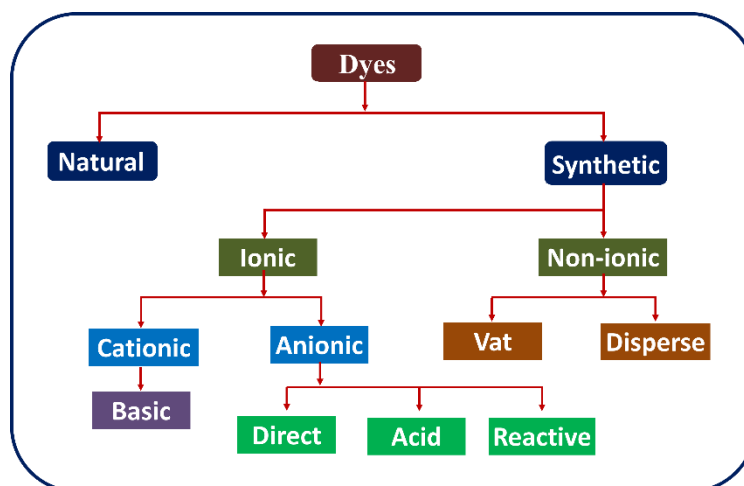
Chart 1.1. Classification of dyes [13-17].

1.3.2 Synthetic dyes:

Dyes derived from organic and inorganic compounds are known as synthetic dyes. Synthetic dyes are used everywhere because they are cheaper, readily available, brighter, and easily applied to fabric.

Synthetic dyes are classified into ionic and non-ionic dyes:

I) Ionic dyes: Ionic dyes are classified into cationic and anionic dyes.

a) Cationic dyes: The materials having components that make them dissociate into positively charged ions in an aqueous medium are known as cationic dyes.

Basic dyes: Basic dyes are synthetic dyes with a cationic nature (positive charge), mostly based on amino groups, and are soluble in water. These are powerful coloring agents useful to color any fabric, like silk, cotton, wool, and acrylic fibre.

b) Anionic dyes: The materials having components that make them dissociate into negatively charged ionic species in an aqueous medium are known as anionic dyes.

i) Direct dyes: These are anionic dyes soluble in water that do not require chemicals during the dyeing procedure. Direct dyes attached to cellulosic fiber with hydrogen bonding. These dyes generally contain sulphonic acid groups.

ii) Acid dyes: Acid dyes are water-soluble dyes with the acidic group. They were applied to fiber from an acidic bath and held due to ionic forces. Most acid dyes are sulfonic

acid salts containing azo, anthraquinone, triphenylmethane, nitro, nitroso, and chromophoric groups.

iii) Reactive dyes: Reactive dyes are the most common dyes used worldwide. In the dying process, a reaction occurs between dyes and fiber. These dyes are anionic, which is soluble in water. Reactive dyes are very cheap and have better fastness properties. With reactive dyes, the dying process is carried out at room and high temperatures, depending on the type of reactive dyes. The dying process can be done only in an alkaline medium with a high pH value. It is bright and forms a covalent bond with the substrate.

II) Non-ionic dyes: Non-ionic dyes are classified into vat and disperse dyes.

i) Vat dyes: Vat dyes are different from other dyes because they are insoluble in water. Indigo was the first vat dye obtained from plants. Vat dyes become soluble in strong reducing agents (sodium hydrosulfite dissolved in sodium hydroxide). The process in which insoluble vat dyes convert into soluble form is known as vatting. The vatting process is done using an alkaline solution.

ii) Disperse dyes: Disperse dyes are non-ionic dyes that are insoluble in water. A dispersive agent is needed for the dying process. These insoluble dyes are finely ground and dispersed in water using a suitable dispersing agent. Dispersive dyes are widely used to dye synthetic and polyester fibers.

1.4 Dye removal techniques:

Many techniques, including physical, chemical, and biological have been developed in the last few decades to remove harmful dyes from wastewater [18]. The various dye removal techniques are represented in **Fig. 1.3**.
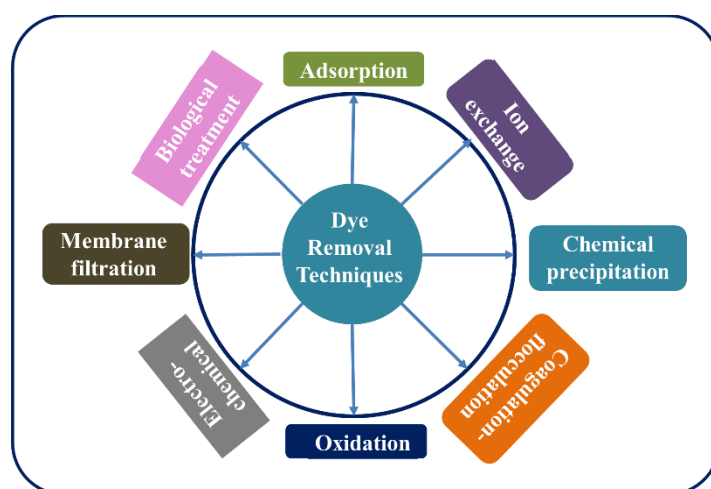
Fig. 1.3. Various dye removal techniques.

I) Adsorption: Adsorption is a process in which ions or molecules from the dissolved solid, liquid, and gas accumulate on the surface of a solid, which is known as adsorption.

This process can be differentiated into physisorption and chemisorptions. In physisorption, adsorbed molecules and solid surfaces are attracted physically due to weak Vander wall forces. However, if the adsorption occurs by chemical bonding between adsorbent molecules and solid surfaces, such adsorption is known as chemisorption. In chemical adsorption, removing adsorbed molecules from solid surfaces is very difficult because of the high strength of chemical bonds [19]. High surface area porous materials such as activated carbon, nanoparticles, and low-cost silica nanomaterials display high dye adsorption, thus useful for eliminating toxic dyes from wastewater and water reservoirs [20-22]. The performance of the adsorption process is studied with the help of different factors such as temperature, contact time, rate of agitation, pH of a solution, initial dye concentration, and reuse in a sequential cycle of adsorption-desorption [23].

II) Ion exchange: Ion exchange is a process in which other ions exchange unwanted dissolved ions with the same charge. There are two types of ions: cation and anion. In the cation exchange process, positively charged ions are exchanged with positively charged ions on the resin surface. In contrast, negatively charged ions are exchanged with negatively charged ions on the resin surface in the anion exchange process. This process is based on the strong interaction between functional groups of resins and charges on dye molecules. Usually, polymeric resins and zeolites are used in this process [24].

III) Chemical precipitation: Chemical precipitation is a very simple wastewater treatment technique to remove unwanted contaminants from wastewater. This technique is used to remove metallic cations and anions such as fluoride, cyanide, and phosphate. The general procedure involves adding chemicals to change the characteristics of ions in wastewater and waiting for the occurrence of an insoluble precipitate that can be easily removed by sedimentation. Chemical precipitation is always followed by a solids separation procedure to remove the precipitates, which may involve coagulation, sedimentation or filtration [25].

IV) Coagulation-Flocculation: Flocculation or coagulation is one of the most often used techniques for removing dyes from wastewater. This process is used on a large scale because it is efficient and straightforward. Neutralization of charge is considered a prerequisite to the coagulation process, whereas flocculation is a physical process that does not involve neutralizing charge. The process of coagulation and flocculation is significantly influenced by pH. pH changes can alter the charge on hydrolysis products

and the precipitation of metal hydroxides. Commonly used traditional coagulants are aluminium and ferric-based salts such as aluminium sulfate, aluminium chloride, ferric chloride, ferric sulfate, etc. [26, 27].

V) Oxidation: Oxidation is a crucial technique for treating wastewater using oxidizing agents.

a) Ozonation: It is one of the appealing dye removal methods due to the strong oxidative effect of ozone. Ozone is a strong oxidant generated by the electric discharge method by introducing oxygen or air into the space between two electrodes. Ozone can immediately decompose into free radicals like OH*, O_2^-, etc., and these free radicals react with dyes present in wastewater [18, 28].

b) Catalytic degradation: Photocatalytic degradation is an effective method that is different from conventional degradation methods. A catalyst is a substance that increases the rate of a chemical reaction without itself undergoing chemical changes. Photocatalysts can generate OH radicals, which are powerful oxidant species; therefore, they can be considered an advanced oxidation process. Upon exposure to light on the photocatalyst, electron-hole pairs are generated and are responsible for reducing and oxidizing a compound adsorbed on the surface of the photocatalyst. Photocatalytic activity of metal oxide occurs in two ways. In the first, OH radicals are generated by the oxidation of OH^-, and O_2^- radicals are generated by the reduction of O_2 [28, 29]. The photocatalytic dye degradation mechanism is discussed further in **section 1.6.3**.

c) Miscellaneous oxidizing systems: In order to enhance the dye degradation performance, the oxidation system can incorporate some processes such as non-thermal plasma treatment, ultrasound, catalytic wet air oxidation, etc. [30-32].

VI) Electrochemical (EC) treatment: EC technologies have emerged as the best treatment technologies for removing contaminants from wastewater. EC wastewater treatments include electrocoagulation (EG), EC oxidation, and reduction. EC oxidation techniques are recognized as the most powerful technique for degrading pollutants in wastewater. In this process, dye molecules adsorbed on the electrode surface are degraded by an electron transfer mechanism [18, 33].

VII) Membrane filtration: A membrane is a barrier that allows a certain thing to pass, and another can block it. Membrane filtration is an advanced technology used for wastewater treatment to remove undesired contents added to the wastewater. In this process, any solutes in the wastewater larger than the membrane pore size can be trapped. Depending upon the pore size, membrane filtration is classified as

microfiltration (MF), ultrafiltration (UF), nanofiltration (NF), and reverse osmosis (RO) membranes [18, 34].

VIII) Biological treatment: This technique is useful because of its eco-friendly nature, energy saving, and minimum chemical uses. In this process, a microorganism can convert biodegradable waste into nonpoisonous species. Usually, aerobic and anaerobic processes are used for the treatment of wastewater. An aerobic process requires free or dissolved oxygen for microbial decomposition, while an anaerobic process does not require oxygen. Various biological candidates such as algae, bacteria, yeast, and enzymes are used for dye degradation. The different functional groups of microbial cell wall components are responsible for creating attractive forces between dye molecules and microbial cell walls [35, 36].

IX) Combined techniques: Each discussed dye removal technique has advantages and disadvantages. Therefore, combined techniques are being developed to improve dye removal efficiency. Many studies reveal that combining different techniques is an effective way to develop a new methodology for removing dyes from wastewater [37-39].

1.5 Catalyst:

A catalyst is a substance that can enhance the rate of a chemical reaction but does not participate in the reaction. There are two types of catalysts: homogeneous and heterogeneous catalysts.

1.5.1 Homogeneous catalysts:

Homogeneous catalysts exist in a single phase as reactants to treat contaminated water. In these catalysts, both reactants and catalysts are in the same phase. It has several advantages, such as being well-defined at a molecular level, readily soluble in the reaction medium, showing good catalytic activity, and better selectivity at mild conditions. However, separating the catalyst and treated reactant becomes complicated due to its homogeneous nature. Moreover, removing contamination of the product is an expensive and monotonous step [40, 41].

1.5.2 Heterogeneous catalyst:

In heterogeneous catalysts, the phase of the catalyst is different from the reactant and product. In this, the catalyst and product can be easily separated and recovered. A heterogeneous catalyst can work over a larger number of different reaction conditions, and the end product of this catalytic reaction is not toxic to the environment [42].

1.6 Photocatalyst: Principle, characteristics, and mechanism of dye degradation

1.6.1 Principle of photocatalyst:

Photocatalysis is the acceleration of photoreaction in the presence of a catalyst. When a photon with appropriate energy (equal to or greater than the band gap energy) strikes the surface of the catalyst electron, electrons make a transition from the valance band (VB) to the conduction band (CB) of the catalyst. At the same time, holes are created in the VB. As a consequence, an electron-hole pairs are generated. The typical photocatalytic process occurs in five steps, as represented in **Fig. 1.4** [43].
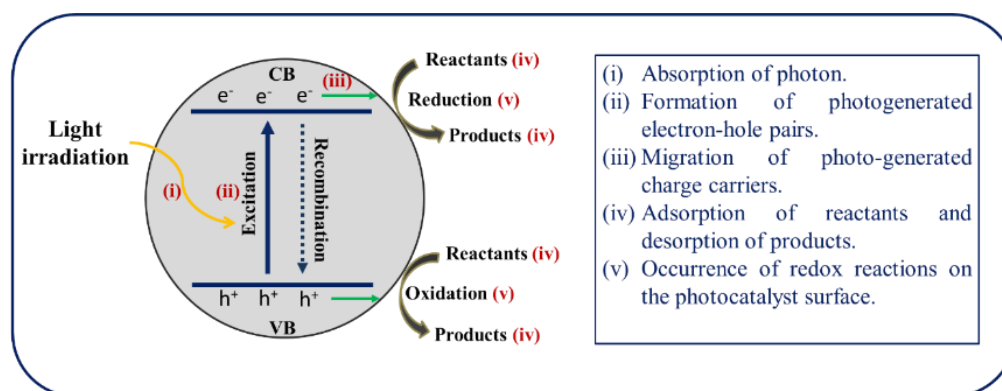
Fig. 1.4. Schematic representation of typical photocatalytic processes [43].

1.6.2 Characteristics of photocatalyst:

➢ It should have a minimum electron-hole pair recombination rate.

➢ It should have a large specific surface area.

➢ It should possess a high density of active sites.

➢ It should have a suitable bandgap energy.

1.6.3 Mechanism of photocatalytic dye degradation:

The degradation of pollutants in wastewater by photocatalysts is a part of the advanced oxidation process, a rising technology to degrade organic pollutants. Two types of reaction mechanisms are involved in the photocatalytic degradation of toxic dyes [44, 45].

I) Indirect dye degradation mechanism: The indirect heterogeneous photocatalytic oxidation mechanism using semiconducting materials can be summarized as follows:

a) Photoexcitation: When a photon with energy (E= hv) equal to or higher than the semiconductor bandgap energy is incident on the photocatalyst, then this energy gets absorbed by the semiconductor material. As a result, the electron gets excited from the filled VB of semiconductor material to the empty CB. The process in which the excitation of electrons by absorption of photon energy is called photoexcitation. In this

process, vacancy is created in the VB because of the excitation of the electron called a hole. Consequently, electron-hole pairs are generated (equation 1.1).

Semiconductor material + hυ → Semiconductor material (e^-(CB) + h^+(VB))   (1.1)

b) Ionization of water: In this process, the photogenerated holes at the VB (h^+(VB)) react with H_2O to generate hydroxyl radicals (OH^*) radicals (equation 1.2).

H_2O (ads) + h^+(VB) → OH^*(ads) + H^+(ads)   (1.2)
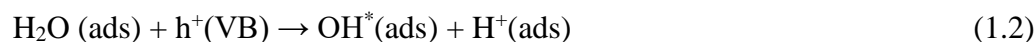
Strong oxidizing agents are the OH* radicals that form on the surface of semiconductor material.

c) Oxygen ionosorption: In this step, while photogenerated holes react with surface-bound water to generate OH^*, an electron in CB (e^-(CB)) of the semiconductor is trapped by O_2 to produce superoxide (O_2^-) (equation 1.3).

O_2 + e^-(CB) → O_2^{-*}(ads)   (1.3)

d) Protonation of superoxide: As superoxide (O_2^{-*}) is created, it protonates to create hydroperoxyl radicals (HO_2^*) and then H_2O_2, which further dissociates into OH^*, which are highly reactive.

O_2^{-*} + H^+ → HOO^* → H_2O_2 → $2OH^*$ (1.4)

Dye + OH^* → Dye intermediates (CO_2 + H_2O)   (1.5)
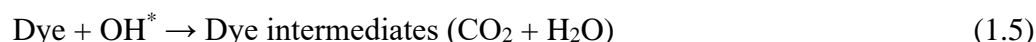
The complete process of the indirect dye degradation mechanism is shown in **Fig. 1.5**.
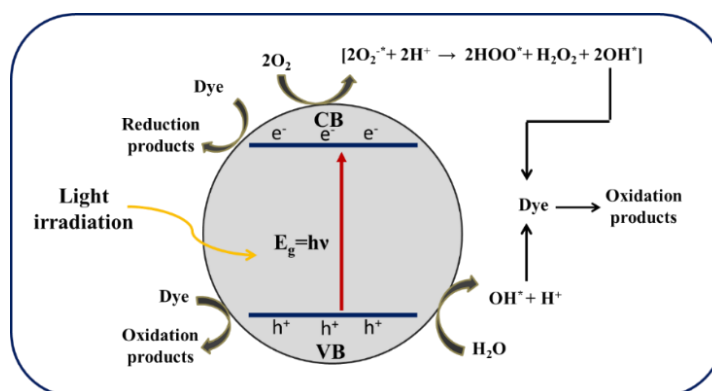
Fig. 1.5. Illustration of indirect dye degradation mechanism [44].

II) Direct dye degradation mechanism:

In this mechanism, photocatalytic degradation of dye is also possible under exposure to visible light. This mechanism consists of initial dye molecule excitation from the ground state (Dye) to the excited state (Dye*) rather than semiconducting metal oxide. This excited state dye species is transformed into a semi-oxidized radical cation (Dye$^+$) by injecting an electron into the CB of a semiconducting metal oxide. Further, O_2^{-*} followed by OH^* are formed due to the reaction between the electron trapped by

semiconducting metal oxide and dissolved oxygen in the system. These OH^* are responsible for the oxidation of organic compounds, as given in equations 1.6 and 1.7 [46, 47]. A pictorial representation of the direct dye degradation mechanism is shown in **Fig. 1.6**.

$$Dye + h\nu \rightarrow Dye^* \tag{1.6}$$

$$Dye^* + Semiconducting\ metal\ oxide \rightarrow Dye^+ + (Semiconducting\ metal\ oxide)^- \tag{1.7}$$
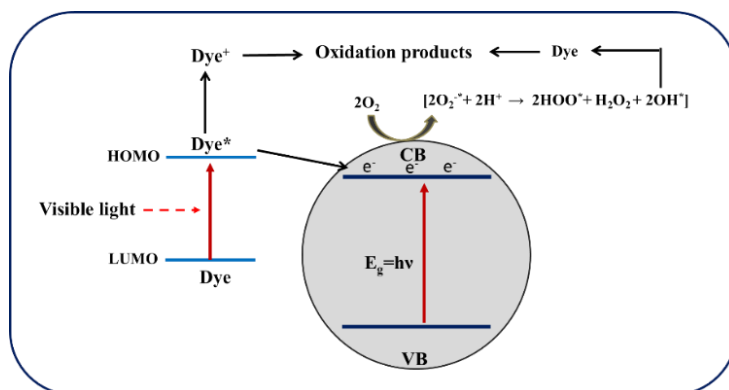
Fig. 1.6. Pictorial representation of direct dye degradation mechanism [44].

1.7 Metal oxide nanomaterials:

Nanomaterials are materials with external dimensions in the range of 1-200 nm. The development of new nanomaterials is rapidly blooming in science and technology. However, from the scientific and technological perspective, metal oxides have become attractive materials because of their different structures and unique properties. Metal oxides are chemical compounds that contain at least one metal and one or more oxygen atoms [48]. The nanoscale metal oxides show different physical, chemical, structural, electrical, and magnetic properties than the bulk form of metal oxide. Transition metal oxides (TMOs) belong to an interesting class of materials and exhibit various structures and properties. Due to the distinct nature of outer shell d-electrons, the TMOs have different properties [49]. They are technologically important materials due to their applicability in industries [50]. The use of TMOs as photocatalysts is the most important from the technical and economic point of view. The present section puts special emphasis on the discussion on TMOs. In particular, titanium oxide (TiO_2), niobium oxide (Nb_2O_5), and tungsten oxide (WO_3), because of their surface chemistry, structural, electronic, and catalytic properties.

1.7.1 Titanium oxide (TiO_2):

Titanium (IV) is one of the benchmarked transition metals in the fourth periodic table group, and it is widely distributed in the Earth's crust [51, 52]. It attracts great

attention because of its interesting properties, including nontoxicity, corrosion resistance, low cost, long-term durability, environmentally friendly, electronic structure, high thermal and photochemical stability, good photostability, etc. [53-55]. Nanosized TiO_2 has been studied for photocatalysts [56], photovoltaic cells [57], gas sensors [58], and dye-sensitized solar cells [59] as it is a low-cost material and possesses remarkable optical and electrical properties [60]. It is an n-type semiconducting material with a band gap of 3.2 eV, sensitive to ultraviolet (UV) light, which only counts for 4% of the total solar spectrum [61, 62].

A) Crystal structure:

TiO$_2$ belongs to a family of TMOs having three crystallographic phases. Anatase and rutile phases of nanostructured TiO_2 have been studied extensively, whereas brookite TiO_2 has been studied rarely [63, 64]. In addition to these phases, TiO_2 (B) is one of the phases of TiO_2.

i) Anatase TiO$_2$: The name anatase was given because it has a longer vertical axis than rutile. It has a tetragonal structure. It possesses higher photocatalytic and mobility properties than rutile and is stable at low temperatures [58, 65, 66]. The anatase phase is the most stable phase in the nanostructured TiO_2, generally converting into irreversible rutile when heated above 600 °C. The phase transition can be extended to 1000-1200°C, depending on morphology, size, structure, etc. [67].

ii) Rutile TiO$_2$: The name rutile comes from the Latin word rutilus. The rutile phase of TiO_2 adopts a tetragonal structure containing six atoms per unit cell. It is thermodynamically the most stable phase at all temperatures and pressures. It is formed by corner-sharing octahedra, with each octahedron surrounded by ten octahedra, of which eight are corner-shared and the remaining two are edge-shared. In the case of anatase, each octahedron is surrounded by eight octahedral edges, of which four are corners and the remaining four are edge-shared [65, 66]. Therefore, the amount of edge-sharing octahedral edges is greater for forming anatase than for rutile. The rutile phase has some advantages over anatase, including low-cost production, higher refractive index, and higher chemical stability [68].

iii) Brookite TiO$_2$: Brookite type TiO_2 is rarely studied compared to anatase and rutile. A. Levy found the mineral known as Brookite in 1825; the name was derived in honor of the mineralogist H. J. Brooke. The crystal structure of Brookite is orthorhombic [65, 66]. The lattice structure of Brookite is like anatase; however, its structural characteristics are between anatase and rutile.

iv) TiO$_2$ (B): This phase has a monoclinic crystalline structure and is often formed through solution synthesis. It is a metastable phase that turns into rutile upon heating [69].

In addition to naturally occurring phases of TiO$_2$, other phases of TiO$_2$, including TiO$_2$-R (ramsdellite-structured), TiO$_2$-H (hollandite-structured), TiO$_2$-II (columbite-type), and TiO$_2$-III (baddeleyite-type) exist under high-pressure condition. All these phases are unstable under ambient conditions [70].

Moreover, the layered titanate structures comprise 2D layers made of octahedral blocks of TiO$_6$ that are combined with cations and neutral molecules. According to crystal symmetry, it can be classified into two subclasses: monoclinic and orthorhombic. All monoclinic and orthorhombic structures belong to space groups C2/m (12) and Immm (71), respectively. The lepidocrocite titanate is an orthorhombic crystal with the space group Immm (71) and can be composed of many TiO$_6$ octahedra. As a consequence, the titanate layer is straight and continuous in one direction. Due to the lack of corner-sharing, the chemical formula H$_x$Ti$_{2-x/4}$□$_{x/4}$O$_4$.nH$_2$O (where □ represents vacancy) results from the charge balance that must be maintained from partial occupancy of Ti sites.

B) Literature survey of TiO$_2$-based photocatalyst for photocatalytic dye degradation:

Different TiO$_2$ and TiO$_2$-based photocatalysts were synthesized using hydrothermal, sol-gel, electrochemical, solution combustion, spin coating, etc. The synthesis method, photocatalyst material, target dye, and corresponding photocatalytic dye degradation performance are summarized in **Table 1.1**.

The effect of the shape and size of 1D and 0D TiO$_2$ nanorods was studied for photocatalytic degradation of red amaranth dye [71]. The various acids (HCl and HNO$_3$) and concentrations were varied to achieve sodium titanate nanorods. As the acid concentration increased, it was observed that the length of TiO$_2$ nanorods decreased with increased diameter. The TiO$_2$ nanorods synthesized with 2M HCl concentration showed almost the entire degradation of red amaranth dye in 60 min under UV light. The maximum dye degradation performance was observed for the HCl-treated TiO$_2$ nanorods because of the elimination of Na from the lattice and enhancement of the crystallinity of TiO$_2$ nanorods. Gautam et al. [72] synthesized various phases of TiO$_2$ nanoparticles using the sol-gel process to study its effect on photocatalytic performance. The degradation efficiencies of anatase and rutile TiO$_2$ for methylene blue (MB) were

88 and 77%, respectively, in 120 min. On the other hand, for methyl orange (MO), rhodamine B (Rh B), indigo carmine (IC), and eriochrome black T (EBT) dyes, anatase TiO$_2$ showed dye degradation of 80.89, 70. 88, 57.76, and 65.64%, respectively. Moreover, rutile TiO$_2$ showed 61.60, 57.61, 55.90, and 55.65 % degradation in 150 min of MO, Rh B, IC, and EBT dyes under UV irradiation, respectively. It indicated that maximum efficiency occurred for anatase TiO$_2$ towards MB dye.

Mehr et al. [73] synthesized ZnO/TiO$_2$ core-shell structure by sol-gel method in which ZnO nanoparticles were coated with TiO$_2$ at different synthesis time intervals of 5 to 45 min. The ZnO/TiO$_2$ core-shell synthesized for 15 min synthesis time showed a maximum MB degradation performance of 98% only in 20 min. The excellent performance was due to heterojunction formation, which lowered the electron-hole recombination rate. The hydrothermal method was employed to synthesize Ag-modified TiO$_2$ nanotubes to degrade malachite green (MG) and crystal violet (CV) dyes [74]. The non-modified TiO$_2$ nanotube showed 66% and 42% MG and CV degradation under UV light exposure. The Ag-modified TiO$_2$ nanotube with 10 wt% Ag displayed a maximum performance of 74.83% for MG and 47.97% for CV. Zhao et al. [75] synthesized Au/TiO$_2$/RGO nanocomposite by hydrothermal method and applied for wastewater treatment under visible and UV light. The photocatalytic activity of Au/TiO$_2$/RGO was tested for the decomposition of MB and hydroquinone (HQ). It was found that, after 120 min illumination of visible light, the degradation rate reached 74.8%, while it was 85.6% after 40 min under UV light. On the other hand, after 60 min of visible light irradiation, the degradation rate for HQ reaches 77.3%, whereas it was 90% under UV light. The degradation of MB and HQ indicated the effective visible light photocatalytic activity of Au/TiO$_2$/RGO nanocomposites.

Luo et al. [76] synthesized TiO$_2$/RGO nanocomposites using a hydrothermal method useful for MB degradation in visible light. The TiO$_2$/RGO composite showed MB degradation of 45% after 120 min, which was higher than that of commercial RGO. The AgInSe$_2$-TiO$_2$ hybrid nanostructured photocatalysts were prepared using thermal and microwave methods and tested for photodegradation of MB [77]. The maximum degradation efficiency of 86.74% was archived for MB with AgInSe$_2$-TiO$_2$ hybrid photocatalyst synthesized by microwave method. The GeO$_2$-TiO$_2$ nanocomposite photocatalysts were synthesized via the solution combustion method to study its effect on photocatalytic Rh B dye degradation [78]. The optimized GeO$_2$-TiO$_2$ nanocomposite shows complete degradation of Rh B dye in 3 h under sunlight illumination. The

recyclability of the optimized catalyst was also studied up to five cycles, which resulted in only a 3-5% reduction in the Rh B degradation rate.

Ga_2O_3-TiO_2 photocatalysts prepared via mechanomixing followed by sonication methods were used for the photodegradation of Rh B dye [79]. Ga_2O_3-TiO_2 photocatalyst shows a maximum Rh B degradation performance of 95% in visible-light illumination. The Cuo/TiO_2 nanocomposites were synthesized using the sol-gel method, and their photoactivity for Rh B dye degradation was tested [80]. The Cuo/TiO_2 nanocomposite showed maximum degradation performance of Rh B more in the presence of UV light than sunlight. The maximum performance (100% in 90 min) is due to the high intensity of UV light, which can easily penetrate, resulting in the formation of more radicals for the surface-redox reaction. The anatase TiO_2 was co-alloying with Nb, and N was prepared using the sol-gel method and tested for photocatalytic activity for MB dye degradation [81]. In visible light, the optimized TiO_2: Nb, N photocatalyst exhibited 93% degradation in 2 h. The photocatalytic activity of RGO-Ag-TiO_2 nanocomposites was synthesized using a vacuum filtration method and employed for the degradation of organic dyes [82]. The optimized RGO-Ag-TiO_2 nanocomposite exhibited complete MB and Rh B degradation in 160 and 200 min, respectively. The higher performance was due to the higher surface area and effective contact between them, which hinders the recombination of electron-hole pairs. A vapor phase polymerization method was used to coat ultra-thin polyaniline (PANI) on TiO_2 nanoparticles and tested for photodegradation of Rh B dye [83]. The PANI-TiO_2 composite showed a maximum Rh B dye degradation efficiency of 91.8% in 120 min. The synergetic effect of PANI and TiO_2 was the main reason for the enhanced degradation efficiency of the composite PANI-TiO_2 photocatalyst. Mastropietro et al. [84] prepared TiO_2/α-Al_2O_3 porous membranes for MB degradation. The optimized TiO_2/α-Al_2O_3 photocatalyst showed 90% degradation of MB in 70 min under simulated solar irradiation.

The hydrothermal method was used to synthesize GO/TiO_2 composites and applied for Rh B dye degradation [85]. The GO/TiO_2 composite photocatalyst displays complete degradation of Rh B in 60 min of visible light exposure. The $TiO_2/RGO/PMMA$ composites were developed using electrochemical technique and their photoactivity for degradation of Rh B dye was tested [86]. The optimized $TiO_2/RGO/PMMA$ composite showed enhanced efficiency of 94% in 140 min of light

exposure. Organic-inorganic hybrid nanocomposites of GO/PANI/TiO$_2$ were synthesized by chemical oxidative method and tested for degradation of MB dye [87]. The GO/PANI/TiO$_2$ nanocomposite exhibited enhanced MB dye degradation performance of 98% in 40 min.

Table 1.1. A literature survey of TiO$_2$-based photocatalysts for dye degradation.

S. N.	Photo-catalyst	Method	Catalyst (mg)	Target Dye	Dye conc. (Quantity in ml)	Degradation performance	Ref.
1	TiO$_2$	Hydrothermal	5	Red amaranth	20 ppm (250)	~ 100% in 60 min	[71]
2	TiO$_2$-anatase	Sol-gel	100	MB	100 ppm (50)	88% in 120 min	[72]
				Rh B		70% in 150 min	
	TiO$_2$- rutile			MB		77% in 120 min	
				Rh B		57% in 150 min	
3	ZnO/TiO$_2$	Sol-gel	100	MB	50 ppm (100)	98% in 20 min	[73]
4	Ag-TiO$_2$	Hydrothermal	10	MG	15 ppm (100)	75% in 180 min	[74]
				CV		48% in 180 min	
5	Au-TiO$_2$-RGO	Hydrothermal	10	MB	10 ppm (50)	75% in 120 min	[75]
				HQ		77% in 60 min	
6	TiO$_2$/RGO	Hydrothermal	40	MB	50 ppm (80)	45% in 120 min	[76]
7	AgInSe$_2$-TiO$_2$	Microwave Thermal	100	MB	100 ppm (50)	87% in 150 min	[77]
				Rh B		59% in 150 min	
8	GeO$_2$-TiO$_2$	Solution combustion	50	Rh B	2 x 10^{-5} M (100)	100% in 180 min	[78]
9	Ga$_2$O$_3$-TiO$_2$	Mechano-mixing and sonication	100	Rh B	10 ppm (100)	95% in 60 min	[79]
10	CuO/TiO$_2$	Sol-gel	1000	Rh B	5 ppm (100)	100% in 90 min	[80]
11	TiO$_2$: Nb, N	Sol-gel	50	MB	40 ppm (50)	93% in 120 min	[81]
12	RGO-Ag-TiO$_2$	Vacuum filtration	5	MB	20 ppm (100)	~100% in 160 min	[82]
				Rh B	30 ppm (100)	~100% in 200 min	
13	PANI-TiO$_2$	Vapor phase polyme-rization	25	Rh B	30 ppm (25)	92% in 120 min	[83]
14	TiO$_2$/α-Al$_2$O$_3$	Sol-gel with spin coating	-	MB	1 x 10^{-5} M (120)	90% in 70 min	[84]
15	GO/TiO$_2$	Hydrothermal	50	Rh B	10 ppm (50)	~100% in 60 min	[85]
16	TiO$_2$/RGO/PMMA	Electro-chemical	100	Rh B	3 ppm (100)	94% in 140 min	[86]
17	GO/PANI/TiO$_2$	Chemical oxidative method	-	MB	50 ppm (-)	98% in 40 min	[87]

1.7.2 Niobium oxide (Nb_2O_5):

Niobium was originally named Columbian for its place of discovery in the basin of the Columbia River in 1801. More than 80% of produced niobium is used as an alloying element in steel and iron [88]. It mainly exists in the form of stoichiometric NbO (+2), Nb_2O_3 (+3), NbO_2 (+4), and Nb_2O_5 (+5). Among all the different stoichiometric forms of niobium oxide, Nb_2O_5 is relatively abundant in nature, has high resistance to corrosion, and is thermodynamically stable. It is an n-type TMO with an energy band gap of about 3.4 eV. It is also a water-insoluble solid material exhibiting different polymorphic forms [89, 90]. Due to its remarkable properties, it is widely used in the field of catalysts [91], sensors [92], photoelectrodes [93], electrochromism [94], etc.

A) Crystal structure:

The crystal structure of Nb_2O_5 is ReO_3, an orthogonal package of oxygen octahedra. Most Nb_2O_5 phases comprise octahedra with six oxygen atoms surrounding a niobium atom in the center. Nb_2O_5 can exist in almost 15 different polymorphic forms. However, the most common phases are commonly orthorhombic (T-Nb_2O_5), monoclinic (H-Nb_2O_5), and pseudohexagonal (TT-Nb_2O_5). Amorphous Nb_2O_5 is usually obtained at relatively low-temperature synthesis, mainly crystallized in T-Nb_2O_5 or H-Nb_2O_5 phases after heat treatment. In addition, various intermediate phases can also exist between the two phases. TT-Nb_2O_5 and T-Nb_2O_5 phases are crystallized between temperatures 500-800 °C. At a temperature of nearly 800 °C, it transforms into a tetragonal (M-Nb_2O_5) phase, and above a temperature of 1000 °C, it forms the H-Nb_2O_5 phase. The M-Nb_2O_5 and H-Nb_2O_5 phases have close structures and transition temperatures to these forms are between 900-1000 °C. The monoclinic B phase is also reported between 600-800 °C. The effect of temperature on crystal structures, method of synthesis, presence of impurities, nature of starting material, initial chemical composition, and interaction with other components plays a significant role in forming Nb_2O_5 crystal [90, 95].

B) Literature survey of Nb_2O_5-based photocatalyst for photocatalytic dye degradation:

Various Nb_2O_5 and Nb_2O_5-based photocatalysts were synthesized using different methods such as ion exchange, ball milling, sol-gel, hydrothermal, co-precipitation, etc. The synthesis method, photocatalysts, target dye, and corresponding photocatalytic dye degradation performance are summarized in **Table 1.2**.

The microwave-assisted hydrothermal method was employed to synthesize Nb_2O_5 photocatalyst using different precursors and applied for Rh B photodegradation [96]. The Nb_2O_5 photocatalyst synthesized with ammoniacal oxalate shows 92.87% degradation, whereas the Nb_2O_5 photocatalyst synthesized with niobium chloride shows 98.99% photodegradation under the same experimental condition. The co-precipitation method was employed to synthesize hydrated Nb_2O_5 and then converted into anhydrate form by heating at a temperature of 550 ˚C. The hydrate and anhydrate Nb_2O_5 photocatalysts were tested for the photocatalytic decomposition of MB dye [97]. The hydrated Nb_2O_5 showed higher photocatalytic degradation (100% in 125 min) than anhydrous Nb_2O_5. The enhanced performance was ascribed to the specific surface area, number of active sites, and OH-surface groups on the catalytic surface.

Shao et al. [98] synthesized biomorphic hexagonal Nb_2O_5 (H-Nb_2O_5) and orthorhombic Nb_2O_5 (O-Nb_2O_5) photocatalysts for MB decomposition. The O-Nb_2O_5 photocatalyst showed low degradation activity (38%), whereas the H-Nb_2O_5 photocatalyst exhibited higher degradation activity (96%) in 50 min. However, the mixture of 25% of O-Nb_2O_5 and 75% H-Nb_2O_5 enhanced its activity and showed maximum degradation of 83% only in 20 min. The impregnation method was used to synthesize the Nb_2O_5 and Ag-supported Nb_2O_5 (Ag/Nb_2O_5) for photocatalytic degradation of textile dyes [99]. The Ag/Nb_2O_5 photocatalysts display enhanced photocatalytic degradation of 99.45% in 24 h. This study emphasizes the significance of Ag in the catalysts. Silva et al. [100] studied the effect of Nb addition on the transformation of phase and photocatalytic properties of TiO_2 nanoparticles. The TiO_2 and $Ti_{1-x}Nb_xO_2$ powder photocatalysts were synthesized and annelaed from 400 to 900 ˚C. The Nb-doped TiO_2 sample annealed at 900 ˚C showed maximum degradation performance of 35% and 45% for MB and Rh B, respectively. This finding highlights the addition of Nb and annealed temperature can enhance photocatalytic degradation activity.

The $TiNb_2O_7$ nanoparticle was synthesized by combining sol-gel and hydrothermal methods and tested for photoactivity of reactive red (RR) dye [101]. The $TiNb_2O_7$ photocatalyst calcined at 700 ˚C showed a maximum dye degradation performance of 80% in 150 min of UV light exposure. The superior photocatalytic activity was due to the good crystallinity of $TiNb_2O_7$ nanoparticles. The $NaNbO_3$/Ag_2S core-shell heterostructure was synthesized using the ion-exchange method and tested for photocatalytic degradation of MB dye [102]. The $NaNbO_3$/Ag_2S core-shell

heterostructure showed the highest degradation performance of 95.5% for MB dye after 40 min. The reusability tests show approximately 89% dye degradation after the fourth cycle, highlighting the stability of $NaNbO_3/Ag_2S$ heterostructure during photocatalytic experiments. The ball milling method was employed to synthesize the Z-scheme $NaNbO_3/WO_3$ photocatalyst and tested for degradation of MB and Rh B dyes [103]. The optimized $NaNbO_3/WO_3$ photocatalyst displays rate constants of 3.4 and 4.9 times higher than pure WO_3 for MB and Rh B dyes, respectively. Anchored Ag nanoclusters with TiO_2/Nb_2O_5 hybrids were synthesized and tested for the photocatalytic degradation of MG dye [104]. The optimized $Ag/TiO_2/Nb_2O_5$ hybrid photocatalyst showed 100% MG dye degradation in 20 min of light exposure. Wu et al. [105] synthesized fluorine-doped $H_2(H_2O) Nb_2O_6$ photocatalyst using the hydrothermal method for organic dye degradation. After adsorption-desorption, Nb_2O_5 nanoparticles and Nb_2O_5 nanorods showed 85.6 and 57.2% dye degradation performance after 10 min, respectively, whereas the F-doped $H_2(H_2O) Nb_2O_6$ photocatalyst exhibited 99.8% in the same period. Hydrothermally synthesized C, N modified Nb_2O_5 nanoneedles were used as photocatalysts to decompose Rh B under visible light [106]. The synthesized photocatalyst showed almost complete Rh B degradation after 40 min. The enhancement in degradation performance was attributed to the visible-light harvesting characteristics, good crystallinity, high surface area, and specific morphology on which carbonate and nitrate species co-exist.

Highly active TiO_2 modified by Nb_2O_5, PANI, and RGO composites were synthesized by Zarrin et al. [107]. The $TiO_2/Nb_2O_5/RGO$ composite showed the highest dye degradation performance of 97% in 240 min, whereas 93% for $TiO_2/Nb_2O_5/PANI$, 82% for TiO_2/RGO, and 69% for TiO_2/Nb_2O_5 degradation were achieved within the same time. The maximum performance for $TiO_2/Nb_2O_5/RGO$ was due to the good separation efficiency for the electron-hole pair of Nb_2O_5 and the high adsorption ability of RGO. Oliveria et al. [108] synthesized Zn-doped Nb_2O_5 by hydrothermal method and tested for photodegradation of Rh B dye. The Zn-doped Nb_2O_5 photocatalyst showed 90% degradation under visible light in 180 min. The degradation performance of Zn-doped Nb_2O_5 photocatalyst under visible light was higher due to the doping of low metal content, resulting in a decreasing band gap and the availability of more active sites for degradation.

The co-precipitation method synthesized metal (Co, Ag, Fe, and Pd) doped hybrid Nb_2O_5/carbon xerogel photocatalysts were used for MB dye degradation [109]. Among the metal-doped hybrid photocatalysts, the Pd-doped Nb_2O_5/carbon xerogel photocatalyst showed superior photocatalytic activity (30% in 300 min) under visible light. The enhanced performance was due to its crystalline structure, lower band gap, and higher absorption of visible light. The $BiNb_5O_{14}$ and $BiNb_5O_{14}/Nb_2O_5$ heterojunction were synthesized by the co-precipitation method and used for the photodegradation of Rh B [110]. The $BiNb_5O_{14}/Nb_2O_5$ heterojunction displays superior photocatalytic activity of 90% in 150 min.

Table 1.2. A literature survey of Nb_2O_5-based photocatalysts for dye degradation.

S. N.	Photo-catalyst	Method	Catalyst (mg)	Target Dye	Dye conc. (Quantity in ml)	Degradation performance	Ref.
1	Nb_2O_5	Hydrothermal	50	Rh B	1×10^{-5} M (50)	99% in 60 min	[96]
2	Nb_2O_5	Co-precipitation	1000	MB	10 ppm (500)	100% in 125 min	[97]
3	Nb_2O_5	-	200	MB	15 ppm (200)	83% in 20 min	[98]
4	Ag/Nb_2O_5	Wet Impregnation	1000	Dark blue neutracyl	10 ppm (200)	9% 24 h	[99]
5	Nb/TiO_2	Polymeric precursor	-	MB	20 ppm (20)	35% in 150 min	[100]
				Rh B		45% in 150 min	
6	$TiNb_2O_7$	Sol-gel and hydrothermal	100	RR 141	50 ppm (500)	80% in 150 min	[101]
7	$NaNbO_3/Ag_2S$	Ion exchange	25	MB	1×10^{-5} M (100)	96% in 40 min	[102]
8	$NaNbO_3/WO_3$	Ball milling	2	MB	5×10^{-5} M (300)	-	[103]
				Rh B	1×10^{-5} M (300)	-	
9	$Ag/TiO_2/Nb_2O_5$	-	30	MG	-	100% in 20 min	[104]
10	$F-H_2(H_2O)-Nb_2O_6$	Hydrothermal	100	MB	20 ppm (60)	99.8% in 10 min	[105]
11	C, N-Nb_2O_5	Hydrothermal	100	Rh B	10 ppm (100)	~ 100% in 40 min	[106]
12	$TiO_2/Nb_2O_5/RGO$	Hydrothermal	-	MB	20 ppm (-)	97% in 240 min	[107]
13	$ZnNb_2O_5$	Hydrothermal	10	Rh B	10 ppm (10)	90% in 180 min	[108]
14	$Pd/Nb_2O_5/$ carbon xerogel	Co-precipitation	50	MB	10 ppm (-)	30% in 300 min	[109]
15	$BiNb_5O_{14}/Nb_2O_5$	Co-precipitation	50	Rh B	10 ppm (300)	90% in 150 min	[110]

1.7.3 Tungsten oxide (WO₃):

Tungsten oxide (WO_3) belongs to the TMO group. It is also known as tungsten trioxide or tungstic anhydride. In the last 50 years, great attention has been given to the field of research related to tungsten and its oxide [111]. WO_3 is a chemical compound with several oxidation states, such as +2, +3, +4, +5, and +6. Out of these, +6 is the most common state. It is a typical intrinsic n-type semiconductor with a narrow energy band gap (2.4-2.8 eV) widely investigated due to its diverse structures, tunable energy band gap, and other physiochemical properties [112, 113]. It has been widely used for photocatalytic water splitting [114], O_2 generation [115], gas sensors [116], and degradation of organic dyes [117].

A) Crystal structure:

The WO_3 crystals have five phases at different temperatures, as shown in **Table 1.3**. [118].

Temperature	Crystal Structure (Phase)
Below -43 ˚C	Monoclinic-II (ε-WO_3)
From -43 to 17 ˚C	Triclinic (δ-WO_3)
From 17 to 330 ˚C	Monoclinic-I (γ-WO_3)
From 330 to 740 ˚C	Orthorhombic (β-WO_3)
Above 740 ˚C	Tetragonal structure (α-WO_3)

Table 1.3: Different phases of WO_3 crystal at different temperatures.

At room temperature, monoclinic-I (γ-WO_3) is the most common crystal structure observed. Below room temperature, monoclinic-II (ε-WO_3) and triclinic (δ-WO_3) exist. When monoclinic (γ-WO_3) is annealed at higher temperatures, its crystal structure changes into orthorhombic (stable up to 740˚C) and tetragonal (T > 740 ˚C). These two phases are stable at higher temperatures and converted back to the original phase upon cooling. Another metastable phase observed is hexagonal WO_3 (h-WO_3), which is an intermediate metastable state of WO_3. The hexagonal phase is obtained from the dehydration of tungsten oxide hydrate. Upon heating T > 400˚C and colling, it converts into γ-WO_3 and cannot retain its original phase [111, 119].

The non-stoichiometry tungsten with oxygen deficiency WO_x (2.625-2.91) can exist in various suboxides such as $W_{32}O_{84}$ ($WO_{2.625}$), W_3O_8, ($WO_{2.667}$), $W_{18}O_{49}$ ($WO_{2.72}$), $W_{17}O_{47}$ ($WO_{2.765}$), W_5O_{14} ($WO_{2.8}$), $W_{20}O_{58}$ ($WO_{2.9}$), $WO_{2.92}$, W_2O_5, WO_2, and $W_{25}O_{73}$ and they are known as magneli phases. The orthorhombic crystal structure is observed

for $WO_{2.625}$ and $WO_{2.667}$, monoclinic for $WO_{2.72}$, $WO_{2.765}$, $WO_{2.9}$, and $WO_{2.92,}$ and tetragonal for $WO_{2.8}$. All these sub-oxides with enough oxygen vacancy can lower the energy band gap, showing strong adsorption affinity towards electrolytes and offering free surface electrons, which show high electrical conductivity [120].

B) Literature survey of WO_3-based photocatalyst for photocatalytic dye degradation:

Various WO_3 and their based photocatalyst were synthesized using different methods such as hydrothermal, reflux, solvothermal, hydrothermal, co-precipitation, etc. The synthesis method, photocatalysys, target dye, and corresponding photocatalytic dye degradation performance are summarized in **Table 1.4**.

The WO_3 nanorods were synthesized via a hydrothermal method with a structure-directing agent such as Na_2SO_4 and employed for the degradation of Rh B dye [121]. The WO_3 nanorods shows photocatalytic dye degradation performance of 86% in 120 min. Also, it shows good photostability after the use of four connective cycles. Hierarchical architecture self-assembled 3D WO_3 and WO_3 with Ag were synthesized by hydrothermal route and tested for photocatalytic degradation of Rh B dye [122]. The WO_3 with Ag showed more than 98% degradation of Rh B dye in 30 min. The maximum performance was attributed to the heterojunction between Ag and WO_3 semiconductors, which could enhance photogenerated charge carriers and lower the rate of electron-hole pairs recombination. The effect of Ce-doped WO_3 nanoparticles was studied by Salim et al. [123] for the photodegradation of MB dye in the presence of sunlight. The Ce-doped WO_3 photocatalyst showed a maximum degradation performance of 89% in 180 min. The degradation performance was increased upon doping of Ce because of an increase in crystalline defects, and Ce ions can act as mediators of interfacial charge transfer.

The sol-gel process was employed to synthesize TiO_2/WO_3 photocatalysts and used for photodegradation of Rh B [124]. The TiO_2/WO_3 photocatalysts showed complete degradation for Rh B dye in 120 min of light exposure. The increased performance was due to the coupling of WO_3 and TiO_2, larger specific surface area (60.31 m^2 g^{-1}), and reduced electron-hole recombination. The WO_3 nanorods were grown on graphene nanosheets using the hydrothermal method and tested for degradation of MB [125]. The WO_3-graphene nanostructure showed 80% degradation for MB in 300 min of light exposure. The increased photocatalytic activity was due to efficient charge separation and the decoration of WO_3 nanorods on graphene nanosheets.

The WO$_3$ nanofiber was decorated with palladium oxide (PdO) by the electro-spinning method and examined for photodegradation of MB dye [126]. The PdO/WO$_3$ nanofiber displays 86.4% degradation efficiency in 24 h of visible light exposure.

The WO$_3$@g-C$_3$N$_4$ nanocomposites were synthesized by the reflux method and tested for photodegradation of Rh B dye under sunlight illumination [127]. The WO$_3$@g-C$_3$N$_4$ nanocomposite showed enhanced degradation of 99.5% in 90 min. The enhanced performance was attributed to minimal electron-hole recombination, increased light absorption, and the large surface area of the photocatalyst. The WO$_3$-ZnO photocatalyst was synthesized by physical mixing and tested photodegradation of MB dye [128]. The nanocuboid-like morphology of WO$_3$ and nanobelt-like morphology of ZnO showed an enhancement in degradation performance upon physical mixing. The WO$_3$-ZnO photocatalyst shows an enhanced degradation performance of 93% in 120 min. Bilal Tahir et al. [129] synthesized fullerene-WO$_3$ composite by the hydrothermal route and was used to evaluate the photocatalytic activity of MB and Rh B. The fullerene-WO$_3$ composite showed maximum photocatalytic activity of 94 and 92% for MB and Rh B, respectively.

The Ag$_2$MoO$_4$ particles were deposited on the surface of WO$_3$ nanoplates to synthesize Ag$_2$MoO$_4$-WO$_3$ heterojunction and tested for photodegradation of Rh B dye [130]. The optimized Ag$_2$MoO$_4$-WO$_3$ heterojunction exhibited a maximum dye degradation efficiency of 97% in 160 min, which was nearly 2 and 1.9 times higher than pristine Ag$_2$MoO$_4$ and WO$_3$, respectively. A simple impregnation method was employed to synthesize WO$_3$ nanorod/TiO$_2$ nanotube composites and tested for MB dye degradation [131]. The WO$_3$/TiO$_2$ composites with optimal loading of WO$_3$ exhibited the highest degradation of 92% in 30 min in presence of visible light. The WO$_3$ nanorods were synthesized by ion exchange and hydrothermal methods followed by decoration of Au nanoparticles for photocatalytic degradation of Rh B dye [132]. The Au-WO$_3$ composite exhibited an enhanced Rh B dye degradation performance of 95% in 120 min. The hydrothermal method was employed to synthesize 2D black phosphorus and WO$_3$ heterojunction and tested for degradation of Rh B dye [133]. The black phosphorus/WO$_3$ heterojunction exhibited maximum Rh B removal efficiencies of 92% within 120 min. The black phosphorus/WO$_3$ heterojunction significantly improved the separation of photogenerated electron-hole pairs.

Yang et al. [134] synthesized a TiO$_2$-Cs$_x$WO$_3$ composite using a solvothermal method followed by calcination and used for photodegradation of Rh B dye. The TiO$_2$-

Cs_xWO_3 composite exhibited enhanced performance of almost 100% in 160 min. Ultrasonically synthesized WO_3-GO nanocomposite was used to study the photocatalytic degradation of MB dye [135]. The pure WO_3 showed a maximum degradation efficiency of 78.96%, whereas the WO_3-GO nanocomposite showed a photodegradation efficiency of 97% in 150 min. The enhancement in photocatalytic performance was attributed to the high surface area and minimal electron-hole pairs recombination.

Table 1.4. A literature survey of WO_3-based photocatalysts for dye degradation.

S. N.	Photo-catalyst	Method	Catalyst (mg)	Target Dye	Dye conc. (Quantity in ml)	Degradation performance	Ref.
1	WO_3	Hydrothermal	5	Rh B	20 ppm (50)	86% in 120 min	[121]
2	WO_3-Ag	Hydrothermal	20	Rh B	10 ppm (20)	98% in 30 min	[122]
3	Ce-WO_3	Co-precipitation	20	MB	4 ppm (50)	89% in 180 min	[123]
4	TiO_2/WO_3	Colloidal crystal-template	40	Rh B	10 ppm (50)	97% in 100 min	[124]
5	WO_3-graphene	Hydrothermal	2	MB	10 ppm (20)	80% in 300 min	[125]
6	PdO-WO_3	Electro-spinning	-	MB	3 ppm (-)	86% in 24 h	[126]
7	WO_3@g-C_3N_4	Reflux	20	Rh B	100 ppm (100)	99.5% in 90 min	[127]
8	WO_3 and ZnO	Physical mixing	50	MB	10 ppm (50)	93% in 120 min	[128]
9	Fullerene-WO_3	Co-precipitation	-	MB	-	94% in 90 min	[129]
				Rh B		92% in 90 min	
10	Ag_2MoO_4-WO_3	In situ deposition	100	Rh B	10 ppm (100)	97% in 160 min	[130]
11	WO_3/TiO_2	Simple impregnation	25	MB	10 ppm (50)	92% in 30 min	[131]
12	Au-WO_3	Hydrothermal	-	Rh B	5 ppm (-)	95% in 120 min	[132]
13	Black phophrous/WO_3	Hydrothermal	50	Rh B	10 ppm (50)	92% in 120 min	[133]
14	TiO_2-Cs_xWO_3	Solvothermal	200	Rh B	2×10^{-5} M (300)	~100% in 160 min	[134]
15	WO_3-GO	Ultrasonic	15	MB	20 ppm (75)	97% in 150 min	[135]

The above literature survey clearly indicated that TMOs attract great attention in photocatalytic dye degradation due to their surface morphology, tunable band structure, large surface area, well-defined crystal structure, and high photostability. In particular, the effect of synthesis strategy, calcination temperature, core-shell structure, doping,

and/or decoration of one metal oxide over another metal oxide as well as the decoration of noble metals, illumination of light, heterostructure, etc., affected the photocatalytic dye degradation performance have been studied by the number of researchers across the globe.

In addition, the above literature clearly pointed out the crucial role of hybridization in the enhancement of the photocatalytic activity of individual semiconductors. Various narrow bandgap semiconductors are applied for photocatalytic dye degradation. The TiO_2 and Nb_2O_5 nanostructures demonstrated significant enhancement of photocatalytic activity when coupled with other semiconductor photocatalysts. Though WO_3-based hybrid materials were tested for photocatalytic application, the optimum performance has yet to be realized in practical applications.

1.8 Orientation of problem:

Photocatalytic oxidation using semiconductors has been regarded as essential significance due to environmentally friendly reactions. Therefore, nanocrystalline metal oxides like TiO_2, ZnO, WO_3, $BiVO_4$, and Nb_2O_5 have been considered potential materials. However, most of them suffered from low quantum yield caused by inherent surface defects, high recombination rate of excitons, poor photostability, and unsuitable band positions for the reduction of protons and the oxidation of hydroxide ions. Also, in many cases, wide band gap energy restricts its photocatalytic activity due to a limited light absorption profile over a narrow UV region of the solar spectrum (4%). To address these issues, a strategy to hybridize wide-bandgap semiconductors with narrow-band gap semiconductors is tested. This hybridization approach is essential to increase the photocatalytic activity of individual photocatalysts by spatial electronic coupling with the increased lifetime of excitons. Recent studies, exfoliated titanate-NS and hexaniobate-NS can be the best platform for the hybridization with various narrow band gap semiconductors due to their unique 2D morphology, high surface electrostatic charge, excellent photocatalytic activity, outstanding photostability, oxidative power, nontoxicity and low production cost for degradation of hazardous pollutants. Therefore, exfoliated titanate-NS and hexaniobate-NS are selected as wide-bandgap semiconducting materials for hybridization. Due to a narrow band gap to cover visible light of the solar spectrum and very interesting photocatalytic properties, WO_3 is selected as guest hybridizing species with titanate-NS and hexaniobate-NS.

WO_3 hybridized with titanate-NS and WO_3 hybridized with hexaniobate-NS are chosen for the photocatalytic dye degradation application. These hybrid assemblies can

lead to the formation of high surface area morphology and strong electronic coupling between the hybridizing species. The strong electronic coupling between the WO_3 hybridized with titanate-NS and WO_3 hybridized with hexaniobate-NS can be highly beneficial for the increased lifetime of excitons and enhances the photocatalytic activity with high stability and efficiency. The objectives of the thesis are as follows,

1. The exfoliated 2D titanate-NS and hexaniobate-NS will be synthesized by exfoliation of highly crystalline host crystals of $Cs_{0.7}Ti_{1.825}\square_{0.175}O_4$ and $K_4Nb_6O_{17}$.

2. WO_3 hybridization over exfoliated 2D titanate-NS and hexaniobate-NS will be carried out using CBD and SILAR methods.

3. Characterizations of WO_3 hybridized with titanate-NS (WO_3-titanate-NS) and WO_3 hybridized with hexaniobate-NS (WO_3-hexaniobate-NS).

4. The photocatalytic performance of WO_3-titanate-NS and WO_3-hexaniobate-NS nanohybrids will be evaluated using methylene blue (MB) and rhodamine B (Rh B) degradation.

For the WO_3 hybridization with nanosheets, CBD and SILAR methods are selected due to their obvious advantages. Both the CBD and SILAR methods are very simple, convenient, and inexpensive for large-area deposition, even at room temperature, and do not require any vacuum arrangement. The rate of deposition and thickness can be controlled by controlling parameters like concentration of solution, pH, time, temperature, etc. The WO_3 hybridized with titanate-NS and WO_3 hybridized with hexaniobate-NS are characterized by different techniques. Structural characterization is done by using X-ray diffraction (XRD). Morphological studies are carried out by field emission scanning electron microscope (FE-SEM). Chemical bonding of the synthesized nanohybrids is evaluated by micro-Raman and Fourier transform infrared (FT-IR) spectroscopy studies. For the identification of chemical composition and oxidation states, the X-ray photoelectron spectroscopy (XPS) technique is employed. Optical properties are probed using ultra-violet-visible diffuse reflectance spectroscopy (UV-vis DRS). Photocatalytic activity of the WO_3 hybridized with titanate-NS and WO_3 hybridized with hexaniobate-NS are tested for dye degradation efficiency and stability. Finally, the best performance of WO_3 hybridized with titanate-NS and WO_3 hybridized with hexaniobate-NS are used for photocatalytic water purification.

1.9 References:

[1]   F. R. Spellman, The science of environmental pollution, third edition, CRC Press, Taylor and Francis Group, 2017. ISBN: 978-1-315-22614-9.

[2]   N. Khatri, S. Tyagi, Front. Life Sci., 8 (2015) 23.

[3]   N. Akhtar, M. I. S. Ishak, S. A. Bhawani, K. Umar, Water, 13 (2021) 2660.

[4]   https://www.solitudelakemanagement.com/the-impact-of-phosphorus-pollution-on-waterbodies.

[5]   https://images.app.goo.gl/xQR4jzgSLF6xV1Br8.

[6]   R. Rao, RECENT APPROACHES in Sustainable Agriculture Development and Food Security, Crop Management, Forestry, Food Technology and Environmentally Balanced Production Enhancement, Mahima Research Foundation and social welfare, 2021. ISBN: 978-81-943375-4-6.

[7]   M. Rajabi, K. Mahanpoor, O. Moradi, RSC Adv., 7 (2017) 47083.

[8]   N. Peng, D. Hu, J. Zeng, Y. Li, L. Liang, C. Chang, ACS Sustain. Chem. Eng., 4 (2016) 7217.

[9]   H. Sun, L. Cao, L. Lu, Nano Res., 4 (2011) 550.

[10]   https://www.textiledyes.net/paper-dyes-for-paper-industry.html.

[11]   https://www.omnipotent.co.in/polymers-pvc.

[12]   https://indiantextilejournal.com/bihar-has-potential-of-multiple-textile-hubs-minister-3.

[13]   G. Ahmet, A. Metin, G. Kubra, G. M. Sadi, Dyes and pigments, first edition, Springer, 2016. ISBN: 978-3-319-33890-3.

[14]   S. K. Panda, I. Aggarwal, H. Kumar, L. Prasad, A. Kumar, A. Sharma, D. V. Vo, D. V. Thuan, V. Mishra, Environ. Chem. Lett., 19 (2021) 2487.

[15]   G. R. Chatwal, Synthetic dyes, Himalaya publishing house, 2009. ISBN: 978-81-84882-20-9.

[16]   R. Tim, M. Geo, M. Roger, N. Poonam, Bioresour. Tech., 77 (2001) 247.

[17]   K. Hunger, Industrial dyes: chemistry, properties, application, first edition, WILEY-VCH, 2003, ISBN: 3-527-30426-6.

[18]   A. Ahmad, S. H. Mohd-Setapar, C. S. Chuong, A. Khatoon, W. A. Wani, R. Kumar, M. Rafatullah, RSC Adv., 5 (2015) 30801.

[19]   V. K. Gupta and Suhas, J. Environ. Manage., 90 (2009) 2313.

[20]   E. N. El Qada, S. J. Allen, G. M. Walker, Chem. Eng. J., 135 (2008) 174.

[21]   B. Chi, W. Bian, R. Li, C. Lin, Y. Wang, Y. Wang, J. Nanosci. Nanotech., 17 (2017) 5796.

[22]   S. Larous, A. H. Meniai, M. B. Lehocine, Desalination, 185 (2005) 483.

[23]   G. Z. Kyzas, N. K. Lazaridis, A. C. Mitropoulos, Chem. Eng. J., 189 (2012) 148.

[24]   A. A. Ali and R. El-Bishtawi, J. Chem. Tech. Biotechnol., 69 (1997) 27.

[25]   L. K. Wang, Yung-T. Hung, N. K. Shammas, Physocochemical treatment process: Handbook of environmental engineering, first edition, Humana press, 2005. ISBN: 1-58829-165-0.

[26]   S. S. Moghaddam, M. A. Moghaddam, M. Arami, J. Hazard. Mater., 175 (2010) 651.

[27]   B. Shi, G. Li, D. Wang, C. Feng, H. Tang, J. Hazard. Mater., 143 (2007) 567.

[28]   T. E. Agustina, H. M. Ang, V. K. Vareek, J. Photochem. Photobiol. C: Photochem. Rev., 6 (2005) 264.

[29]   M. M. Khan, S. F. Adil, A. Al-Mayouf, J. Saudi Chem. Soc., 19 (2015) 462.

[30]   L. O. de Brito Benetoli, B. M. Cadorin, V. Z. Baldissarelli, R. Geremias, I. G. de Souza, N. A. Debacher, J. Hazard. Mater., 237 (2012) 55.

[31]   Z. Eren, J. Environ. Manag., 104 (2012) 127.

[32]   L. Hua, H. Ma, L. Zhang, Chemosphere, 90 (2013) 143.

[33]   C. A. Martínez-Huitle and E. Brillas, Appl. Catal. B: Environ., 87 (2009) 105.

[34]   M. Mulder, Basic principles of membrane technology, second edition, Kluwer academic publishers, 1996. ISBN: 978-0-7923-4248-9.

[35]   Y. J. Chan, M. F. Chong, C. L. Law, D. G. Hassell, Chem. Eng. J., 155 (2009) 11.

[36]   L. Seghezzo, G. Zeeman, J. B. van Lier, H. V. Hamelers, G. Lettinga, Bioresour. Tech., 65 (1998) 175.

[37]   I. Oller, S. Malato, J. Sanchez-Perez, Sci. Total Environ., 409 (2011) 4141.

[38]   A. Azizi, M. A. Moghaddam, R. Maknoon, E. Kowsari, Process Saf. Environ. Prot., 95 (2015) 255.

[39]   F. P. Van der Zee and S. Villaverde, Water Res., 39 (2005) 1425.

[40]   S. Shylesh, V. Schünemann, W. R. Thiel, Angew. Chem., Int. Ed., 49 (2010) 3428.

[41]   J. Falbe, H. Bahrmann, J. Chem. Educ., 61 (1984) 961.

[42]   N. M. Julkapli, S. Bagheri, Int. J. Hydro. Energy., 40 (2015) 948.

[43]   J. J. Yu, M. Jaroniec, S. Wageh, A. A. Al-Ghamdi, Adv. Mater., 29 (2017) 1601694.

[44]   A. Ajmal, I. Majeed, R. N. Malik, H. Idriss, M. A. Nadeem, RSC Adv., 70 (2014) 37003.

[45]   M. A. Rauf and S. S. Ashraf, Chem. Eng. J., 151 (2009) 10.

[46]   J. Zhao, C. Chen, W. Ma, Top. Catal., 35 (2005) 269.

[47]   F. Chen, Y. Xie, J. Zhao, G. Lu, Chemosphere, 44 (2001) 1159.

[48]   N. Golbamaki, B. Rasulev, A. Cassano, R. L. Robinson, E. Benfenati, J. Leszczynski, M. T. Cronin, Nanoscale, 7 (2015) 2154.

[49]   C. N. Rao, Annu. Rev. Phys. Chem., 40 (1989) 291.

[50] A. Akbari, M. Amini, A. Tarassoli, B. Eftekhari-Sis, N. Ghasemian, E. Jabbari, Nano-Struct. Nano-Objects., 14 (2018) 19.

[51] S. Mallakpour and M. Madani, Prog. Org. Coat., 86 (2015) 194.

[52] C. Leyens and M. Peters, Titanium and Titanium Alloys: Fundamentals and Applications, WILEY-VCH, 2003. ISBN: 3-527-30534-3.

[53] S. Guo, J. Yi, Y. Sun, H. Zhou, Energy Environ. Sci., 9 (2016) 2978.

[54] M. Wang, J. Ioccozia, L. Sun, C. Lin, Z. Lin, Energy Environ. Sci., 7 (2014) 2182.

[55] A. Sarkar, K. Karmakar, G. G. Khan, J. Phys. Chem. C, 121 (2017) 1.

[56] I. Paramasivam, H. Jha, N. Liu, P. Schmuki, Small, 8 (2012) 3073.

[57] C. D. Lokhande, M. Sun-Ki, K. D. Jung, O. S. Joo, J. Mater. Sci., 39 (2004) 6607.

[58] A. M. More, J. L. Gunjakar, C. D. Lokhande, Sens. Actuators B Chem., 129 (2008) 671.

[59] B. Oregan, M. Gratzel, Nature, 353 (1991) 737.

[60] U. M. Patil, K. V. Gurav, O. S. Joo, C. D. Lokhande, J. Alloys Comp., 478 (2009) 711.

[61] C. H. Huang, I. K. Wang, Y. M., Y. H. Tseng, C. M. Lu, J. Mol. Catal. A Chem., 316 (2010) 163.

[62] V. Etacheri, C. Di Valentin, J. Schneider, D. Bahnemann, S. C. Pillai, J. Photochem. Photobiol. C: Photochem. Rev., 25 (2015) 1.

[63] R. Daghrir, P. Drogui, D. Robert, Ind. Eng. Chem. Res., 52 (2013) 3581.

[64] Y. Zhang, Z. Jiang, J. Huang, L. Y. Lim, W. Li, J. Deng, D. Gong, Y. Tang, Y. Lai, Z. Chen, RSC Adv., 5 (2015) 79479.

[65] O. Carp, C. L. Huisman, A. Reller, Prog. Solid State Chem., 32 (2004) 33.

[66] S. G. Kumar and K. K. Rao, Nanoscale, 6 (2014) 11574.

[67] A. Sarkar and G. G. Khan, Nanoscale, 11 (2019) 3414.

[68] R. S. Mane, O. S. Joo, S. K. Min, C. D. Lokhande, S. H. Han, Appl. Surf. Sci., 253 (2006) 581.

[69] J. Cai, J. Shen, X. Zhang, Y. H. Ng, J. Huang, W. Guo, C. Lin, Y. Lai, Small Methods, 3 (2019) 1800184.

[70] T. Peng and J. A. Lalman, Catalysis by Metal Complexes and Nanomaterials: Fundamentals and Applications, Am. Chem. Soc., 1317 (2019) 135.

[71] J. D. de Leon, J. Rojas, D. Dominguez, Y. Esqueda-Barron, J. M. Romo-Herrera, S. Fuentes-Moyado, Nano-Struct. Nano-Objects, 26 (2021) 100738.

[72] A. Gautam, A. Kshirsagar, R. Biswas, S. Banerjee, P. K. Khanna, RSC Adv., 6 (2016) 2746.

[73] M. E. Mehr, H. Maleki-Ghaleh, M. Yarahmadi, M. Kavanlouei, M. H. Siadati, J. Alloys Comp., 882 (2021) 160777.

[74] C. Y. Tsai, C. W. Liu, H. C. Hsi, K. S. Lin, Y. W. Lin, L. C. Lai, J. Chem. Tech. Biotech., 94 (2019) 3251.

[75] L. Zhao, H. Xu, B. Jiang, Y. Huang, Part. Part. Syst. Charact., 34 (2017) 1600323.

[76] J. Luo, Z. Wang, H. Jiang, S. Liu, F. Q. Xiong, J. Ma, Langmuir, 36 (2020) 4637.

[77] A. S. Kshirsagar and P. K. Khanna, Inorg. Chem. Front., 5 (2018) 2242.

[78] K. Natarajan, H. C. Bajaj, R. J. Tayade, Mater. Chem. Front., 2 (2018) 741.

[79] E. Amdeha, R. A. El-Salamony, A. M. Al-Sabagh, Appl. Organomet. Chem., 34 (2020) 5336.

[80] T. N. Ravishankar, M. D. Vaz, S. R. Teixeira, New J. Chem., 44 (2020) 1888.

[81] T. M. Breault and B. M. Bartlett, J. Phys. Chem. C, 116 (2012) 5986.

[72] Q. Chen, Z. Yu, F. Li, Y. Yang, Y. Pan, Y. Peng, X. Yang, G. Zeng, J. Chem. Tech. Biotech., 93 (2018) 761.

[83] S. Majumdar and D. Mahanta, RSC Adv. 10 (2020) 17387.

[84] T. F. Mastropietro, C. Meringolo, T. Poerio, F. Scarpelli, N. Godbert, G. Di Profio, E. Fontananova, Ind. Eng. Chem. Res., 56 (2017) 11049.

[85] M. S. Adly, S. M. El-Dafrawy, S. A. El-Hakam, J. Mater. Res. Tech., 8 (2019) 5610.

[86] M. T. Momen, F. Piri, R. Karimian, React. Kinet., Mech. Catal., 129 (2020) 1145.

[87] S. Baruah, S. Kumar, B. Nayak, A. Puzari, Poly. Bullet., 78 (2021)1703.

[88] C. E. Gibson, S. Kelebek, M. Aghamirian, Int. J. Miner. Process., 137 (2015) 82.

[89] L. Yan, X. Rui, G. Chen, W. Xu, G. Zou, H. Luo, Nanoscale, 8 (2016) 8443.

[90] R. A. Rani, A. S. Zoolfakar, A. P. O'Mullane, M. W. Austin, K. Kalantar-Zadeh, J. Mater. Chem. A, 2 (2014) 15683.

[91] K. Tanabe and S. Okazaki, Appl. Catal. A: Gen., 133 (1995) 191.

[92] R. A. Rani, A. S. Zoolfakar, J. Z. Ou, M. R. Field, M. Austin, K. Kalantar-zadeh, Sens. Actuators B Chem., 176 (2013) 149.

[93] A. Le Viet, R. Jose, M. V. Reddy, B. V. Chowdari, S. Ramakrishna, J. Phys. Chem. C, 114 (2010) 21795.

[94] M. A. Aegerter, M. Schmitt, Y. Guo, Int. J. Photoenergy, 4 (2002) 1.

[95] D. Rosenfeld, R. Sanjines, F. Levy, P. A. Buffat, V. Demarne, A. Grisel, J. Vac. Sci. Technol. A., 12 (1994) 135.

[96] C. L. Ucker, V. Goetzke, S. R. Almeida, E. C. Moreira, M. M. Ferrer, P. L. Jardim, M. L. Moreira, C. W. Raubach, S. Cava, Ceram. Int., 47 (2021) 20570.

[97] N. P. de Moraes, F. N. Silva, M. L. da Silva, T. M. Campos, G. P. Thim, L. A. Rodrigues, Mater. Chem. Phys., 214 (2018) 95.

[98] R. Shao, Z. Cao, Y. Xiao, H. Dong, W. He, Y. Gao, J. Liu, RSC Adv., 4 (2014) 26447.

[99] M. K. Silva, R. G. Marques, N. R. Machado, O. A. Santos, Brazilian J. Chem. Eng., 19 (2002) 359.

[100] L. F. da Silva, W. Avansi Jr, A. C. Catto, J. E. Rodrigues, M. I. Bernardi, V. R. Mastelaro, Phys. Status Solidi A., 215 (2018) 1800321.

[101] G. S. Falk, J. B. Rodrigues Neto, M. Borlaf, S. Y. Gomez, A. P. Novaes de Oliveira, D. Hotza, Int. J. Ceram. Eng. Sci., 1 (2019) 235.

[102] S. Kumar, A. P. Singh, C. Bera, M. Thirumal, B. R. Mehta, A. K. Ganguli, ChemSusChem., 9 (2016) 1850.

[103] C. Shifu, J. Lei, T. Wenming, F. Xianliang, Dalton Trans., 42 (2013)10759.

[104] T. Goswami, K. M. Reddy, A. Bheemaraju, Chem. Select, 4 (2019) 6790.

[105] J. Wu, J. Wang, H. Li, Y. Du, X. Jia, B. Liu, CrystEngComm., 16 (2014) 9675.

[106] J. Xue, R. Wang, Z. Zhang, S. Qiu, Dalton Trans., 45 (2016) 16519.

[107] S. Zarrin and F. Heshmatpour, J. Hazard. Mater., 351 (2018) 147.

[108] J. A. Oliveira, M. O. Reis, M. S. Pires, L. A. Ruotolo, T. C. Ramalho, C. R. Oliveira, L. C. Lacerda, F. G. Nogueira, Mater. Chem. Phys., 228 (2019) 160.

[109] N. P. de Moraes, M. L. da Silva, L. A. Rodrigues, Mater. Lett., 228 (2018) 486.

[110] Y. Huang, L. Mi, X. Liu, S. Bi, H. J. Seo, J. Lumin., 207 (2019) 149.

[111] C. C. Mardare, A. W. Hassel, Phys. Status Solidi A., 216 (2019) 1900047.

[112] D. P. DePuccio, P. Botella, B. O'Rourke, C. C. Landry, ACS Appl. Mater. Interfaces, 7 (2015) 1987.

[113] X. Fang, M. Yao, L. Guo, Y. Xu, W. Zhou, M. Zhuo, C. Shi, L. Liu, L. Wang, X. Li, W. Chen, ACS Sustain. Chem. Eng., 5 (2017) 10735.

[114] Y. Shabdan, A. Markhabayeva, N. Bakranov, N. Nuraje, Nanomate., 10 (2020) 1871.

[115] Y. H. Chew, J. Y. Tang, L. J. Tan, B. W. Choi, L. L. Tan, S. P. Chai, Chem. Comm., 55 (2019) 6265.

[116] M. S. Patil, V. L. Patil, N. L. Tarwal, D. D. More, V. V. Alman, L. D. Kadam, P. S. Patil, J. H. Kim, J. Electron. Mater., 48 (2019) 526.

[117] R. Ebrahimi, A. Maleki, Y. Zandsalimi, R. Ghanbari, B. Shahmoradi, R. Rezaee, M. Safari, S. W. Joo, H. Daraei, S. H. Puttaiah, O. Giahi, J. Indus. Engg. Chem., 73 (2019) 297.

[118] J. Y. Zheng, Z. Haider, T. K. Van, A. U. Pawar, M. J. Kang, C. W. Kim, Y. S. Kang, CrystEngComm., 17 (2015) 6070.

[119] Z. Hai, Z. Wei, C. Xue, H. Xu, F. Verpoort, J. Mater. Chem. C., 7 (2019) 12968.

[120] P. A. Shinde, S. C. Jun, ChemSusChem., 13 (2020) 11.

[121] T. Govindaraj, C. Mahendran, V. S. Manikandan, R. Suresh, J. Mater. Sci.: Mater Electron., 31 (2020) 17535.

[122] R. A. Capeli, C. J. Dalmaschio, S. R. Teixeira, V. R. Mastelaro, A. J. Chiquito, E. Longo, F. M. Pontes, RSC Adv., 10 (2020) 6625.

[123] M. Saleem, J. Iqbal, A. Nawaz, B. Islam, I. Hussain, Int. J. App. Ceram. Tech., 17 (2020) 1918.

[124] K. Huang, Z. Cai, Z. Anorg. Allg. Chem., 644 (2018) 1072.

[125] M. E. Khan, M. M. Khan, M. H. Cho, RSC Adv., 6 (2016) 20824.

[126] H. Lee, M. Kim, D. Sohn, S. H. Kim, S. G. Oh, S. S. Im, I. S. Kim, RSC Adv., 7 (2017) 6108.

[127] S. Borthakur, P. Basyach, L. Kalita, K. Sonowal, A. Tiwari, P. Chetia, L. Saikia, New J. Chem., 44 (2020) 2947.

[128] S. Adhikari, D. Sarkar, G. Madras., RSC Adv., 5 (2015) 11895.

[129] M. Bilal Tahir, G. Nabi, M. Rafique, N. R. Khalid, Int. J. Energy Res., 42 (2018) 4783.

[130] H. Wang, Y. Wang, A. Xu, Q. Yang, F. Tao, M. Ma, Z. Song, X. Chen, RSC Adv., 9 (2019) 34804.

[131] M. R. Joice, T. M. David, P. Wilson, J. Phys. Chem. C, 123 (2019) 27448.

[132] Q. Xiang, G. F. Meng, H. B. Zhao, Y. Zhang, H. Li, W. J. Ma, J. Q. Xu, J. Phys. Chem. C., 114 (2010) 2049.

[133] Q. Wang, B. Li, P. Zhang, W. Zhang, X. Hu, X. Li, RSC Adv., 10 (2020) 27538.

[134] J. Yang, J. Liu, Y. Qiao, F. Shi, S. Ran, Y. Dong, S. Liu, CrystEngComm., 22 (2020) 573.

[135] G. Jeevitha, R. Abhinayaa, D. Mangalaraj, N. Ponpandian, J. Phys. Chem. Solids, 116 (2018) 137.

CHAPTER-II

Theoretical Background of Synthesis Process and Thin Film Characterization Techniques

CHAPTER II

Theoretical Background of Synthesis Process and Thin Film Characterization Techniques

2.1 Introduction: Thin films

Interest in the study of science and technology of thin films increased due to their applicability, properties, technical values, and curiosity in two-dimensional solids. Thin films have been developed to investigate the co-relationship between thickness, physical properties and structure of solids. Additionally, thin films are employed in a variety of technologies, including magnetic information storage devices, electrical circuits, and optical equipment [1].

In the formation of thin film, the material is deposited on the surface of a clean substrate up to a certain thickness of film. Such a surface is bounded between two parallel planes extending infinitely in two dimensions and restricted in the third dimension. Changes in physicochemical properties are observed in thin film form due to the alteration of the material's structure (bulk to thin film), which is dependent on the order and periodicity. At most, the thin-film system has a 2D order or periodicity, significantly impacting physical and chemical properties. Thin film technology is extremely useful in optics, magnetism, sensors, electronics, and energy storage devices. Thin film materials in the nanocrystalline form possess several benefits, including a large surface area, high electrical resistivity, and excellent mechanical characteristics [2]. Two synthesis approaches, top-down and bottom-up, are employed to synthesize nanomaterials. In a top-down approach, bulk materials are broken down into nanoscale via chemical or mechanical processes, and in a bottom-up approach, material is developed from atomic or molecular species. Consequently, in a bottom-up approach, numerous chemical synthesis methods have been used to prepare nanocrystalline materials.

The desired properties of thin films can be obtained by choosing the appropriate deposition techniques and preparative conditions. Thin film deposition techniques fall into two categories: physical methods and chemical methods [3, 4]. The Chart 2.1 depicts several thin film deposition methods. The physical methods are divided into vaccum evaporation and sputtering. In vaccum evaporation, the pressure of the liquid (to be deposited) reduced below its vapour pressure, due to which the liquid gets evaporate. The vaccum allows vapour particles to travel directly to the target substrate. On the other hand, in sputtering method, a slab of the material that is deposited onto the substrates is electrically energized in a vacuum chamber with an inert atmosphere [5]. The chemical approach has two branches as well. One branch is the gas phase chemical

process, which includes several deposition methods such as metal organo-chemical vapor deposition (MOCVD), plasma accelerated CVD, laser CVD, photo CVD, and conventional chemical vapor deposition (CVD). Another branch is liquid phase chemical processes, which include electroplating, chemical bath deposition (CBD), successive ionic layer adsorption and reaction (SILAR), spray pyrolysis, liquid phase epitaxy, sol-gel, reflux method, spin coating, and dip coating [6]. Physical methods have several limitations, including high working temperatures, limited area deposition, the need for expensive systems/complex instrumentation, material waste and high vacuum. Chemical approaches are easier, more affordable, and suited for large-area deposition over any substrate [3, 5, 6]. Thus, chemical methods are widespread to prepare materials in thin film form.
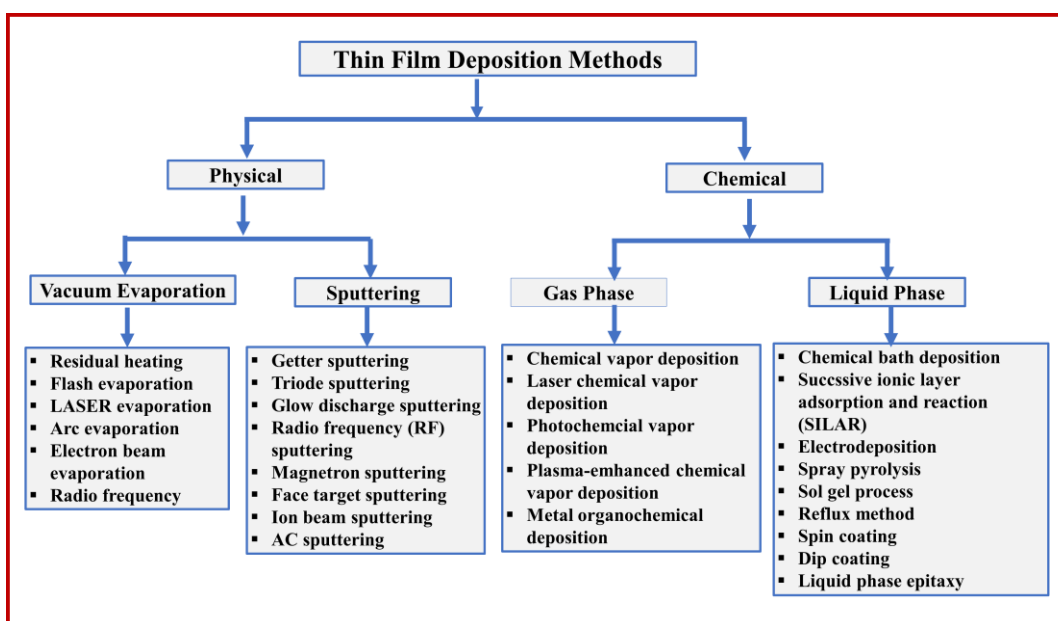
Chart 2.1: Classification of thin film deposition methods [5, 6].

This chapter has five sections: the first four sections deal with the theoretical background of CBD, SILAR, solid-state reaction, and electrophoretic deposition (EPD) methods. The fifth section deals with the various physicochemical characterization techniques used to probe the properties of envisioned materials.

2.2 Chemical bath deposition (CBD) method:

Thin film generation in chemical synthesis relies on thermodynamic equilibrium and kinetic approaches. The CBD process is based on a thermodynamic approach. The synthesis process through this approach consists of three steps: (i) supersaturation, (ii) nucleation, and (iii) subsequent growth. The CBD method is widely employed to synthesize various thin films in nanomaterial form. This method starts by initiating

nanomaterials nucleation on a solid surface, from a liquid-phase medium [7, 8]. The CBD method requires a few pieces of glassware, chemicals and a hotplate with a stirrer, which are essential and readily available instruments for thin film deposition. With the help of such simple instruments, pinhole-free and uniform thin films can be deposited on the desired substrate. The CBD method can also be used to develop nanomaterials with controlled size, shape, and composition. The characteristics of thin film are mainly determined by preparative parameters, which can be controlled in the CBD process. Mane and Lokhande's [9] review paper thoroughly discusses thin film deposition through the CBD approach. Numerous review articles exist on the CBD method for thin film deposition [10, 11].

2.2.1 Basic principle of CBD:

The CBD method for thin film deposition is depends on the controlled precipitation in the solution. Generally, thin film deposition via CBD methods follows the formation of solid phase from a soluton, which involves two steps: (i) nucleation and (ii) particle growth [3, 4]. In the CBD method, precipitate formation occurs when the ionic product (IP) should be higher than the solubility product (SP) [3]. When a sparingly soluble salt XY is added to the solvent, it results in a saturated solution with ions (X^+ and Y^-) and undissolved solid (XY). The expression for the equilibrium among the ions and solid phase in the solution is,

$$XY_{(s)} \rightarrow X^+ + Y^- \qquad (2.1)$$

By the law of mass action to equilibrium condition,

$$K = \frac{C_X^+ C_Y^-}{C_{XY}(S)} \qquad (2.2)$$

Where, C_X^+, C_Y^- and C_{XY} is the concentration of X^+, Y^- ions, and XY compound in solution.

Equation 2.2 can be written as- $C_{XY}(S) = \text{constant} = K'$

$$K = \frac{C_X^+ C_Y^-}{K'} \qquad (2.3)$$

where $C_{XY}(S) = \text{constant} = K'$

$$KK' = C_X^+ C_Y^- \qquad (2.4)$$

Here, K, K' is constant and product of KK' is also constant and denoted by K_s, then the above equation can be written as,

$$K_s = C_X^+ C_Y^- \qquad (2.5)$$

K_s and $C_X^+ C_Y^-$ are called SP and the IP, respectively. At the saturated condition, IP is equal to the SP of ions in the solution. When IP is more than SP, i.e., IP/SP = S > 1, the solution becomes supersaturated, and precipitation takes place, which leads to the formation of nuclei in the solution (homogeneous) as well as on the substrate surface (heterogeneous) [9].

In the CBD method, the substrate is immersed in a chemical bath containing cations and anions. When supersaturation state is reached, a heterogenous reaction occurs and these ions form nuclei on the surface of the substrate. Without supersaturation, thin film deposition via CBD method is impossible.

2.2.2 Theoretical background of nucleation and growth:

Fundamentals of nucleation and growth:

In chemical deposition, the film is deposited on the substrate because the reaction occurs in a solution. Several stages are involved in the preparation of film, such as nucleation and growth of crystals, followed by thin film growth [7].

1) Nucleation: There are two kinds of nucleation based on the deposition mechanism: homogeneous nucleation and heterogeneous nucleation. Homogeneous nucleation occurs when concentration of anions and cations exceeds the SP. However, heterogeneous nucleation take place when individual ions/subcritical clusters adsorb on the substrate surface. The process of ions/subcritical clusters adsorption on the substrate surface is depicted schematically in **Fig. 2.1**. As heterogeneous nucleation proceeds, a deposition of a thin material layer will occur.
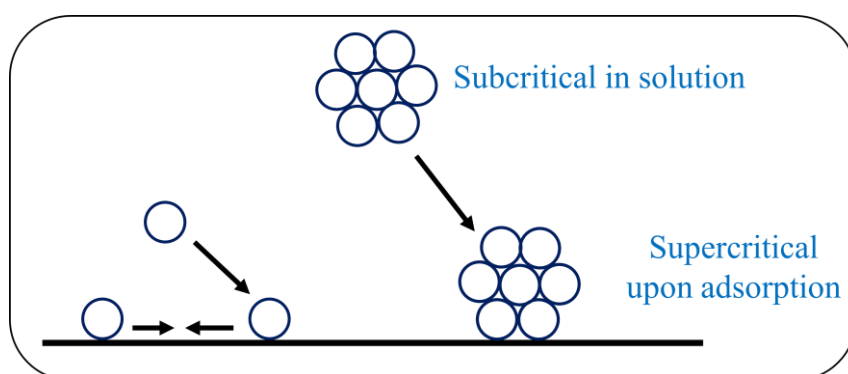
Fig. 2.1: Processes involved in heterogeneous nucleation on the surface of a substrate.

2) Crystal growth: Growth can occur via mainly two ways: one of which is self-assembling and the other is Ostwald ripening. In the first step, self-assembling growth can occur after nuclei formation. On the other hand, growth occurs through particle rearrangement due to aggregation and coalescence, known as Ostwald ripening. As

shown in **Fig. 2.2**, the process of aggregation is the adsorption of individual particles on one another, and the process of coalescence is the smaller or unstable particles near a larger crystal dissolve and grow into the crystal [7].
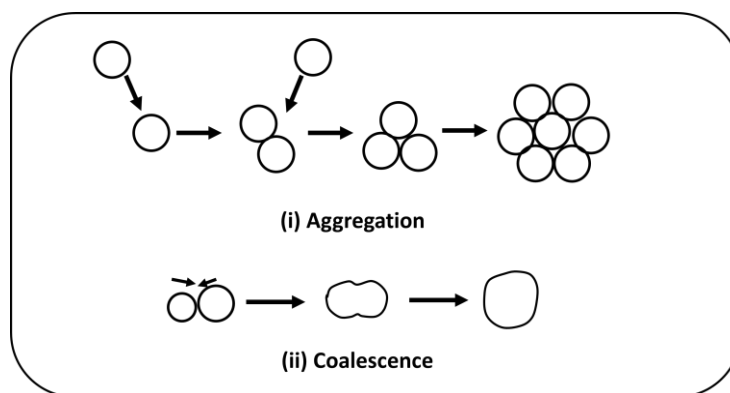
Fig. 2.2: Particle growth by (i) aggregation and (ii) coalescence process [7].

3) Thin film growth: The chemical methods can deposit uniform and adherent thin films. Growth in chemical methods is accomplished by ion-by-ion and cluster (hydroxide) mechanisms.

i) Ion-by-ion growth mechanism: The degree of saturation is needed for homogeneous nucleation. The surface of the substrate acts as a nucleation centre. When nucleation occurs on the substrate surface, it helps to grow the films. The deposition rate is faster at the nucleated center than at the other parts of the substrate. The material growth persisted until it was stopped by certain processes or interrupted by certain substances.

ii) Cluster (hydroxide) mechanism: Generally, in CBD method, the preparative conditions are often carried out where metal hydroxide is formed. This might seem to imply that the metal hydroxide precipitate is formed at the intial of CBD. In fact, the metal hydroxide formed is either as a colloid rather than a precipitate or as an adsorbed species on the substrate but not in the bulk of the solution [10].

2.2.3   Effect of preparative parameters:

The rate of a chemical reaction influences the adherence and uniform growth of thin films. The deposition rate and thickness of the film are highly influenced by the supersaturation of the solution and the abundance of nucleation centers. Various parameters, such as pH, temperature, complexing agent, and deposition time affect the film growth kinetics and alter the properties of deposited materials. The effect of preparative parameters on the growth mechanism is explained below.

❖ **Complexing agent:** The CBD deposition is typically carried out in a supersaturated solution. The complexing agents are used to avoid rapid material

precipitation by lowering free metal ion concentration in the reaction bath through complex formation. An increase in the complexing agent lowers the reaction rate that enables slow deposition rate. Such controlled deposition rate can able to tune the particle size, shape, and orientation.

- ❖ **pH of solution:** The supersaturation state governs the rate of reaction and deposition. A metal ions complex becomes more stable by chaining the pH of the reaction bath and decreasing the abundance of free metal ions. This affects the reaction rate, which can result in a alteration of film thickness and morphology.

- ❖ **Temperature of the solution:** The temperature of the reaction bath is another factor that influences the reaction rate. As the temperature of the solution rises, the complex dissociates more effectively, increasing the kinetic energy of molecules and improving the interaction between the ions. The degree of supersaturation with temperature affects the thin film thickness. Also, high deposition temperature can enable high nucleation sites that can affect the particle size and uniformity.

- ❖ **Nature of substrate:** The substrate's nature significantly impacts film adhesion and reaction kinetics. The presence of nucleation centers on the surface of the substrate is essential for nucleation and subsequent growth. Thus, a highly clean substrate surface is a prime requirement to grow uniform pinhole-free deposits. Therefore, cleaning the substrate is an essential step in thin film deposition.

2.3 Successive ionic layer adsorption and reaction (SILAR) method:

2.3.1 Theoretical background:

The SILAR method is simple and cost-effective for depositing many materials in thin film form. The mechanism of the SILAR method was first reported by Ristov et al. [12] and Nicolau et al. [13]. The SILAR method is also referred to as the modified CBD method. Generally, the SILAR method entails steps of adsorption, reaction, and rinsing between them. The SILAR is based on a series of reactions at the substrate surface, followed by rinsing. Rinsing allows for the uniform growth of the solid phase. This method uses a heterogeneous chemical reaction between adsorbed cations, pK^{a+}, and anions, aA^{p-}, at the solid solution interface to build thin films of water-insoluble ionic or ion covalent compounds of type KpAa. The following relationship can be used to illustrate the reaction.

$(p\mathrm{K_{aq}}^{a+} + q\mathrm{X_{aq}}^{b-}) + (b'\mathrm{Y_{aq}}^{q'+} + a\mathrm{A}^{p-}) \rightarrow \mathrm{K}p\mathrm{A}a_s \downarrow + q\mathrm{X_{aq}}^{b-} + b'\mathrm{Y}_{\,aq}^{\,q'+}$ \hfill (2.6)

with $ap = bq = b'q'$

where K represents cations, p represents the number of cations, a represents the numerical value of charge on cation, X is an ion in cationic precursors having a negative charge, q represents the number of X in cationic precursors, and b is the numerical value of charges on X. Y ion is attached to chalcogen ion, b' is the number of Y in anionic solution, q' is the numerical value of charge on Y. A is the chalcogen ion and a is the number of anions.

The above reaction might be expressed as, in the presence of a complexing agent,

$p[(\mathrm{KC})^{a+}]_{aq} + q\mathrm{X_{aq}}^{b-} + b'\mathrm{Y}^{q'+}{}_{aq} + a\mathrm{A}^{p-} \rightarrow \mathrm{K}p'\mathrm{A}a'_s \downarrow + \mathrm{C} + q\mathrm{X}^{b-}{}_{aq} + b'\mathrm{Y}^{q'+}{}_{aq}$ \hfill (2.7)
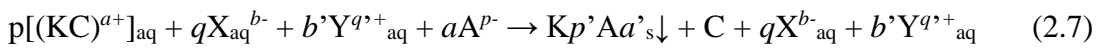
where C is the complexing agent. **Fig. 2.3** depicts the fundamental representation of the four-beaker SILAR method. The various steps involved in the SILAR method are detailed below.
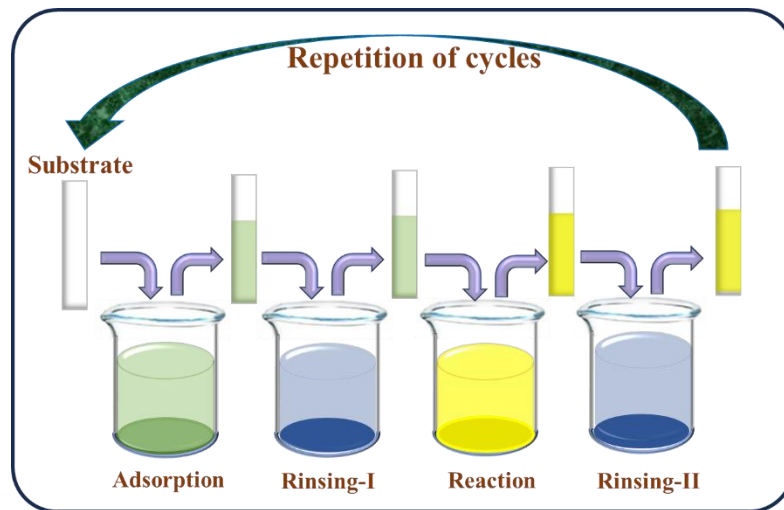
Fig. 2.3: Fundamental representation of the four-beaker SILAR method.

(A) Adsorption: Adsorption is the first step in which positive ions are adsorbed on the substrate surface, forming the Helmholtz electric double layer. Due to Vander Waals forces, two ionic layers are formed on the substrate surface: the inner layer is of positively charged ions (cations), while the exterior layer is negatively charged ions (anions).

(B) First rinsing: The above adsorption step involves the formation of multiple ionic layers on the substrate surface that may be loosely bounded. Such weak adsorption may result in loosely bound deposit particles. The rinsing procedure removes the loosely

adsorbed cations on the substrate surface. Also, the rinsing step avoids the mixing of anionic and cationic solutions and avoids unnecessary precipitation. Rinsing impacts the morphology, particle size, crystallinity, and thin film adherence to the substrate. Double distilled water (DDW) is commonly used as a rinsing solution.

(C) Reaction: Anions from the anionic precursor solution enter the reaction process in this stage. A solid substance with the chemical formula KpAa forms at the interface due to the strong reactivity of cations and anions. The irreversible chemical reaction between preadsorbed cations (pK^{a+}) and anions (aA^{p-}) from the solution occurs in this stage.

(D) Second rinsing: This is the final stage in the SILAR method, and it is used to remove unreacted excess species and secondary reaction products (aA^{p-}, X, Y) from the diffusion layer. DDW is used as a rinsing solution, just as it was in stage two.

Sometimes, the SILAR method is modified to achieve various physicochemical properties of the thin films. Such modification is related to the rinsing step of the SILAR method. Therefore, the authors named this method as simple SILAR method [14]. In this thesis, we used the modified SILAR (m-SILAR) method, where the rinsing step is removed.

2.3.2 Effect of preparative parameters:

Various steps and preparative parameters involved in SILAR deposition can significantly affect film properties. The thin film growth rate is influenced by preparative parameters such as solution temperature, number of repeated cycles, solution pH, cationic and anionic precursors concentration, rinsing time, adsorption and reaction time, complexing agent and concentration. The effects of different parameters on the growth of film are discussed below.

❖ **Concentration of precursors:** In almost all chemical deposition methods, the solution concentration influences the film formation rate. Adsorption and reaction rates are affected by the precursor solution concentration. The higher reaction rate results in nonadherent and nonhomogeneous film thickness. Higher precursor concentrations result in the deposition of maximum film thickness and increase the chance of forming insoluble impurities in the film [15]. The optimal concentration of both precursors should be found experimentally.

❖ **Temperature:** Variations in film thickness can be achieved by changing the temperature of the solution bath. Dissociation of the complex and formation of free ions are both influenced by temperature. At high temperatures, dissociation is more substantial, which results in a faster deposition rate. The rate of film growth slows down at room or lower temperatures. The thickness of the film increases linearly as the temperature rises.

❖ **Complexing agent:** A complexing agent can control free metal ion concentration in the solution. The complexing agents are also known as ligands. They contain one or more donor atoms capable of forming coordination covalent bonds with metal ions in solution. Due to the complexing agent, the reaction rate and precipitate formation slows down.

❖ **pH:** The pH of solutions plays a crucial role. Extreme pH values affect the substrate surface condition and the desired compound solubility. As the pH of the reaction changes, it stabilizes the metal ion complex and reduces the availability of free metal ions. This affects the deposition process, which can result in film thickness and morphology variation. A complexing agent can used to change the pH of the bath.

❖ **Number of cycles:** As each deposition cycle adds a few layers of materials on the substrate, a larger number of cycles results in a thicker film. A large number of cycles results in the creation of a particle cluster. As a result, after a certain number of repetitions, the thin film begins to peel off from the substrate surface.

2.4 Electrophoretic deposition (EPD) method:

2.4.1 Theoretical background:

EPD is a simple deposition technique in which charged particles from the colloidal solution are deposited using an electric field on conducting substrates.

The EPD process involves two steps: In the first electrophoresis step, an electric field is applied between two electrodes (dipped in colloidal solution), moving suspended charged particles toward the oppositely charged electrode. In the second step of deposition, particles condense at one of the electrodes and make a compact deposit on it. Generally, any colloidal suspension containing charged particles can used for the EPD [16, 17].

EPD setup: EPD setup consists of three main parts: high voltage power supply, electrophoretic deposition cell with appropriate electrophoretic bath, and working and

counter electrodes. The EPD setup is schematically depicted in **Fig. 2.4**. The EPD method depends on which electrode the deposition takes place. When colloidal particles are negatively charged, deposition occurs on the anode (positive electrode), known as anodic EPD. In contrast, the deposition of positively charged colloidal particles occurs on the cathode (negative electrode) is termed cathodic EPD [18-20]. The term electrodeposition (ED) is sometimes misused for EPD, but there is a primary difference between EPD and ED. The EPD depends on the use of particle suspension, whereas ED depends on the solution of metal salts i.e., ionic species.
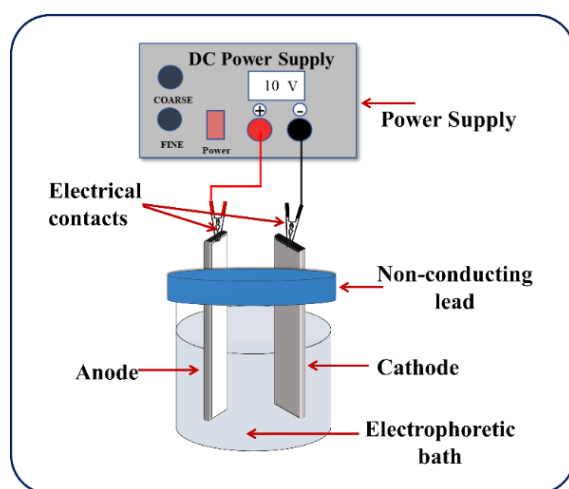
Fig. 2.4: Schematic representation of EPD.

2.4.2 Effect of preparative parameters:

❖ **Particle size:** The formation of the stable suspension significantly depends on the particle size. Stable suspension is a prime requirement of the EPD process. Particles must stay stable and dispersed in suspension for uniform and smooth deposition.

❖ **Dielectric constant:** If the dielectric constant of the solvent is low, deposition fails due to insufficient dissociate power. On the other hand, with a high dielectric constant, a high concentration of ions in liquid reduces the size of the double-layer region. It is found that the dielectric constant of the solvent should be between 12-25.

❖ **Suspension conductivity:** Suspension conductivity is an important component in the EPD process. If the suspension conductivity is too high, the motion of particles is reduced. On the other hand, if suspension conductivity is too low, the particle charges electronically and the stability of the suspension is lost.

❖ **Deposition time:** The deposition time decides the film thickness at a constant applied potential. Initially, the deposition rate linearly increases with deposition time, but as more time allows, the deposition rate decreases and attains a plateau.

❖ **Applied potential:** The deposition rate and quality are determined by applied potential. The higher applied potential may cause turbulence in the suspension which deteriorates the quality of deposited thin film. The lower applied potential is not capable of triggering the electrophoresis. Therefore, the best quality of deposits is obtained at a moderate applied potential.

2.5 Solid state synthesis:

2.5.1 Theoretical background of solid-state synthesis:

The solid-state reaction approach employs chemical decomposition reactions, which include heating a mixture of solid reactants to produce new solid compositions. The solid-state reaction technique is most commonly used to prepare polycrystalline solids. Solids do not react together at room temperature, so it is necessary to heat them at higher temperatures (1000-1500 °C). The conditions of the reaction, structural properties of the reactants, the surface area of the solids, their reactivity, and the thermodynamic free energy change associated with the reaction are some elements that affect the rate of a solid-state reaction [21].

Solid state reaction experimental procedure:

❖ **Reagents:** These are the solid reactants from which it is proposed to prepare a solid crystalline compound. The selection of reactant chemicals depends on the reaction parameters and the anticipated nature of the final product.

❖ **Mixing:** The reactants are mixed after they have been weighed out in the proper amounts. Agate mortar and pestle are generally employed for manual homogeneous mixing of small quantities. A ball milling may be needed for mechanical mixing of large quantities (> 20 g), which may take several hours.

❖ **Container material:** It is essential to select an appropriate container material that is chemically inert to the reactants under high-temperature heating conditions. Containers can be crucibles or boats made of alumina, quartz, ceramic, noble metals (platinum, gold), or molybdenum, which are usually suitable.

❖ **Heat treatment:** The heating program highly impacts the final product. The

solid-state reaction is a controlled reaction that significantly depends on the calcination temperature. Thus, control of heating temperature is crucial. Consequently, a heating furnace with a precision temperature controller can be used for the solid-state reaction. Moreover, pelletizing samples at high pressure can increase the area of contact between the reactant grains before heating [22].

2.5.2 Synthesis and exfoliation of layered metal oxides (LMOs):

The LMO is synthesized using a solid-state process. Highly crystalline LMOs and their protonated derivatives were synthesized using a conventional solid-state reaction followed by acid treatment. The LMOs were exfoliated by intercalating bulky ammonium cations between the layers of the protonated LMOs, followed by sequential sonication/shaking. The schematic representation of exfoliation of LMO is shown in **Fig. 2.5**.
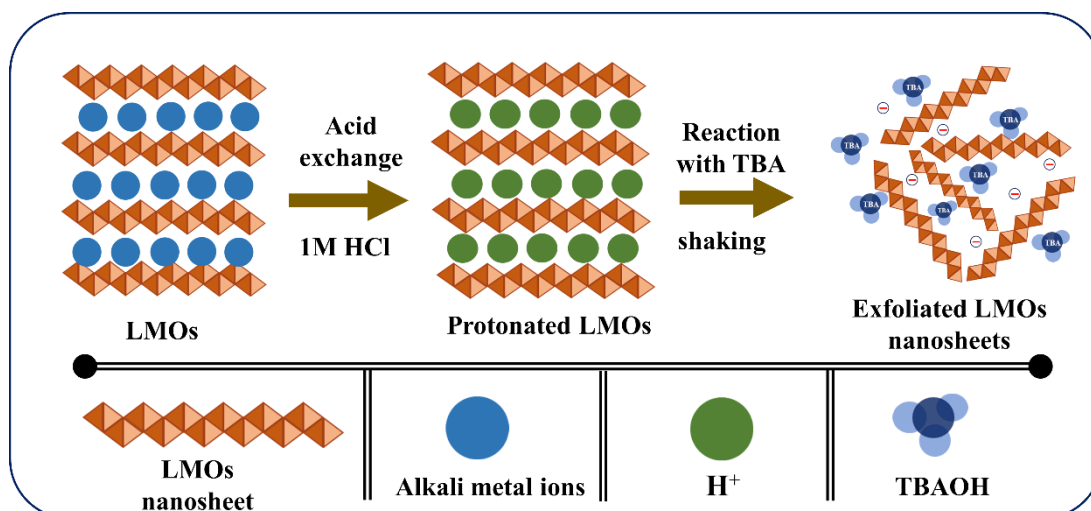
Fig. 2.5: Schematic representation of exfoliation of LMOs.

❖ **Intercalation:** Traditional solid-state reaction synthesizes the LMOs at high temperatures. To carry out solid-state reactions, precursor materials and alkali metal salts are intimately mixed and heated at elevated temperatures. As a result, alkali metal ions intercalated into the inter-gallery space of LMO crystals [23].

❖ **Protonation:** Alkali metal ions have ion-exchange characteristics. The interlayer space of layered material contains alkali metal ions that can be replaced by protons when reacted with the acid solution. Consequently, the protonated derivative of LMOs can be formed without disturbing the original layered structure.

❖ **Ion-exchange:** Electrostatic interaction exists between the host layers and the charge-balancing species of protonated layered materials. Because of the interaction between the host layers and guest species, the guest species are intercalated into the inter-lamellar spacing of the layered crystal resulting in an increase in interlayer distance. The bulky guest species, such as organic molecules, are used to substitute the interlayer protons.

❖ **Successive aqueous sonication or exfoliation:** When ion-exchanged layered crystals are subjected to sonication or vigorous stirring, resulting in the exfoliation of inorganic layered crystals. This process results in the formation of inorganic nanosheets. The intercalated bulky ions increase the inter-gallery space of layered crystal. Due to this expansion, the electrostatic interaction between the host layers and guest ions is reduced. When such swelled layered crystals are exposed to mechanical agitation or sonication, the layered crystals are exfoliated into individual nanosheets [24]. Such an exfoliation process can lead to aqueous colloidal suspension of metal oxide nanosheets [25]. These exfoliated LMO nanosheets are used as basic building blocks for synthesizing new materials.

2.6 Physicochemical characterization techniques:

Materials physical and chemical characteristics are the most important for their use in appropriate applications. The physicochemical properties of materials must be studied using various characterization techniques such as XRD, FT-IR, RAMAN, FESEM, EDS, XPS, UV-vis spectroscopy, and UV-vis DRS.

2.6.1 X-ray diffraction (XRD):

When monochromatic X-rays strike a sample at an angle of incidence 'θ', the X-rays are diffracted from parallel lattice planes separated by the interplanar distance 'd'. The intensity of diffracted X-rays as a function of the scattering angle is measured to produce a diffraction pattern. According to Bragg's condition, when the path difference matches the integral multiple of the wavelength of the incident X-rays, the diffracted X-rays interfere constructively, and then intense peaks are obtained [26]. XRD is a basic technique used to determine the crystal structure and its orientations, phase, crystallite size, and crystal strain.

2.6.2 Fourier transform infrared (FT-IR) spectroscopy:

FT-IR spectroscopy is used to identify chemical bonds in a molecule by detecting the absorption of infrared (IR) radiation at a specific wavelength. Infrared spectroscopy

is a non-destructive technique for investigating atomic arrangement and interatomic forces in chemical compounds and materials. Infrared radiation is absorbed by molecules and converted into molecular vibration energy. The frequencies at which a molecule absorbs radiation reveal details about the molecule groups present in the sample. Absorption in the infrared range is caused primarily by the excitation of molecular vibrations. An organic/inorganic compound can vibrate in six ways: symmetrical and anti-symmetrical stretching, wagging, scissoring, rocking, and twisting [27]. FT-IR spectroscopy is used to identify chemical bonds in a molecule by detecting the absorption of infrared (IR) radiation at a specific wavelength.

2.6.3 Raman spectroscopy:

When a gas, liquid, or solid is subjected to monochromatic light, most of the photons that are scattered have equal energy as that of incident photons. This kind of scattering is called Rayleigh scattering. Only 1% of the light is scattered with different frequencies from the incident frequency. This is referred to as Raman scattering or inelastic scattering. When photons interact with the molecule, the molecule may advance to the virtual state (higher energy level) by exciting the electrons in them. The excited electrons lose energy and make a transition to the ground state by emitting photons because virtual states are unstable. Consequently, the molecule relaxes to a vibrational energy level distinct from its initial state [28].

Three different types of scattering are discussed below [29].

1) **Stokes Raman scattering:** In this type, an excited electron falls to the vibrational level instead of ground level. This indicates that the molecule absorbed some energy, which caused light to be emitted with a greater wavelength than the incident light ($E<E_0$).

2) **Rayleigh scattering:** As there is no energy change when an electron falls to the ground state, light with the same wavelength ($E=E_0$) is reemitted. Such a type of scattering is known as Rayleigh scattering.

3) **Anti-Stokes Raman scattering:** In this type, an electron is excited from a vibrational level and reaches a virtual level with more energy. A photon is emitted when an electron transitions from the virtual to the ground level. The emitted photon has more energy than the incident photon, resulting in a shorter wavelength ($E>E_0$).

Raman spectroscopy provides distinctive details of a molecule's specific vibrations, making it useful for identifying materials. Additionally, it offers more details about lower frequency modes and vibrations, which can provide insight into the crystal and molecular structures.

2.6.4 Field-emission scanning electron microscopy (FE-SEM):

FE-SEM can reveal topographical and elemental details at magnifications between 10-300,000X, with a virtually infinite depth of field. Compared to conventional scanning electron microscopy (SEM), FE-SEM yields clearer and less electrostatically distorted pictures. Very tiny topographic details on the surface of objects can be seen using FE-SEM [30]. In FE-SEM, high-energy electron (primary electrons) beams are generated by heating the cathode (electron gun). The potential difference between cathode and anode allows the generated electrons to accelerate to the material surface. Electromagnetic lenses focus these electron beams into a sharp spot. The precoated sample is placed on a specific holder and put into the microscope high vacuum section via a sample exchange chamber. When the electron beam hits the sample, it releases secondary electrons from the specimen. These secondary electrons carry the topographical details of the sample. A detector processes these electrons, generating an electrical signal that is amplified and converted into an image. The FE-SEM is always carried out in a high vacuum to obtain high resolution and prevent the interaction of high-energy electrons with gas molecules [31].

2.6.5 Energy dispersive X-ray spectroscopy (EDS):

The composition of the elements contained in the material can be determined using EDS. It is also called energy dispersive X-ray analysis (EDAX). When highly energetic electrons are incident on the sample surface, the atom absorbs this energy and ejects the core-shell electrons. These ejected electrons leave holes behind, and when higher energy electrons occupy those holes, energy is released. The energy released in this procedure is used to determine which elements are present and in what proportions. The material's elemental composition is analyzed using a spectrum from the number of counts against the X-ray's energy [32].

2.6.6 X-ray photoelectron spectroscopy (XPS):

The XPS technique, also known as electron spectroscopy for chemical analysis (ESCA), can be used to determine the surface characteristics of a material. This technique is based on the photoelectric effect in which X-rays are used as a source of

photons. It can determine the elemental composition, chemical state, electronic structure, etc. [33].

When an X-ray beam incident on the material surface, electrons are emitted. The kinetic energies of the emitted photoelectrons, associated with the binding energy of each electron, are used for elemental determination. The kinetic energy of emitted photoelectrons can be calculated using the equation (2.8).

$$KE = h\nu - BE - \varphi \qquad (2.8)$$

Where KE, hν, BE, and φ are kinetic energy, photon energy, the binding energy of atomic orbital, and work function, respectively [34]. Each element generates a collection of distinctive peaks. The peaks at specific energies indicated the existence of a particular element.

2.6.7 UV-visible absorption spectroscopy:

The UV-visible absorption spectroscopy is based on the measurement of light absorption due to the transition of electrons from a lower to a higher electronic energy state in the sample. The absorbed energy is equal to the energy difference between these two states. The operating principle is based on Beer-Lambert's law, which states that the absorbance is directly proportional to the path length of light '*b*' and concentration '*c*' of the sample (equation 2.9).

$$A = \varepsilon bc \qquad (2.9)$$

where ε, *b,* and *c* are molar absorptivity, path length, and concentration, respectively. Absorbance can also be calculated by using the formula (equation 2.10).

$$A = \log_{10} (I_0/I_t) \qquad (2.10)$$

I_0 and I_t are the intensity of the incident and transmitted light, respectively [35].

The UV-vis absorption spectroscopy is used to determine the energy bandgap of materials and change in the concentration of the dye solution.

2.6.8 UV-visible diffuse reflectance spectroscopy (UV-vis DRS):

UV-vis DRS depends on the reflection of light from a solid sample. In UV-vis DRS, the ratio of scattered light from the thick layer of solid samples and non-absorbing reference samples is measured as a function of wavelength [36, 37]. The diffused reflected light from a non-absorbing medium includes photons scattered in all directions. The reference materials, such as $BaSO_4$, MgO, etc., have low reflectance at wavelengths below 250 nm, implying that a wavelength below 250 nm is not reliable for recording spectra [38].

2.7 Photocatalytic setup:

The photocatalytic activities of prepared thin films were evaluated for photooxidation of organic molecules (MB and Rh B dyes) upon visible light illumination (λ=420 nm, light intensity= 100 mW cm^{-2}). In a typical experiment, the synthesized thin film (1 cm^2) was placed vertically in the quartz cell filled with 3 ml of dye solution. Before irradiation by light, the dye solution was allowed to be equilibrated with target molecules under the dark for 30 min to ensure adsorption/desorption equilibrium of the dye molecules on the catalyst surface. All the photocatalytic tests were carried out at room temperature. During the photocatalytic tests, the light was calibrated by passing through the IR filter followed by AM 1.5G and cutoff (λ=435 nm) filters. The calibrated light was focused on the photocatalytic reactor. The experimental arrangement of photocatalytic dye degradation is shown in **Fig. 2.6**. The synthesized thin film was withdrawn intermittently during the illumination, and the change in the concentration of the dye solution was analyzed using a UV-vis spectrophotometer. The concentration changes of MB and Rh B dyes were monitored by measuring the absorbance at characteristic wavelengths of 665 and 554 nm, respectively.
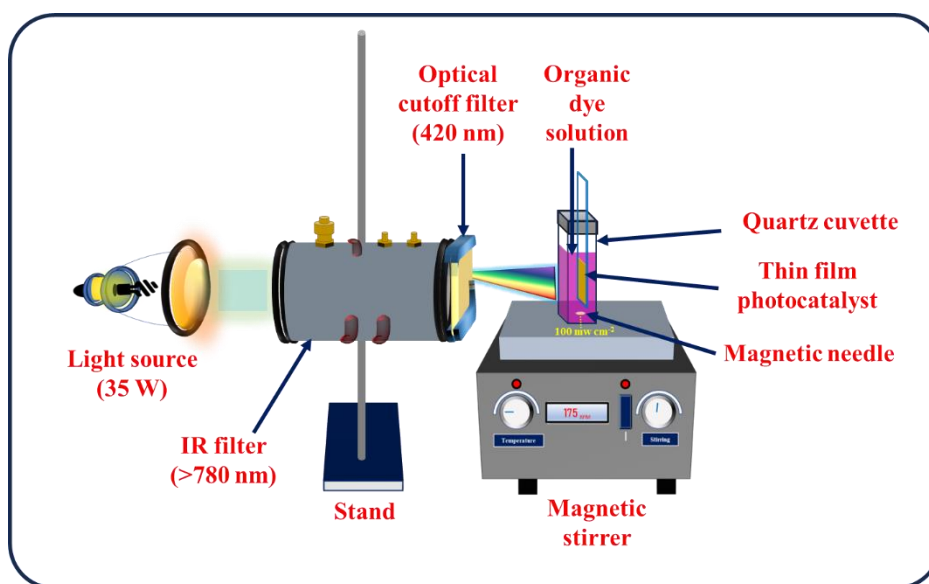
Fig. 2.6: Photocatalytic dye degradation setup.

From the analysis of absorption spectra, photocatalytic degradation efficiency was determined by using the following equation [39]

$$\text{Percentage degradation} = \frac{C_0 - C_t}{C_0} \times 100 \qquad (2.11)$$

where, C_0 and C_t denote absorbance of dye at times t=0 and t=t, respectively.

Also, the first-order kinetic model is used to study degradation kinetics using the following equation [40]

$$\ln\left(\frac{C_0}{C_t}\right) = kt \qquad\qquad (2.12)$$

where k, C_0 and C_t represent the rate constant (min^{-1}), absorbance at times t=0 and t=t, respectively.

2.8 References:

[1]   M. Benelmekki, A. Erbe, Front. Nanosci., 14 (2019) 1.
[2]   I. Gurrappa, L. Binder, Sci. Tech. Adv. Mater., 9 (2008) 43001.
[3]   J. George, Preparation of thin films, Marcel Dekker, 1992, ISBN: 0-8247-8196-1.
[4]   K. L. Chopra, I. Kaur, Thin film device applications, first edition, Plenum press, 1983, ISBN-13: 978-1-4613-3684-6.
[5]   T. P. Niesen, M. R. De Guire, J. Electroceramics, 6 (2001) 169.
[6]   C. D. Lokhande, Mater. Chem. Phys., 28 (1991) 145.
[7]   G. Hodes, Chemical solution deposition of semiconductor films, Marcel Dekker, 2002, ISBN: 0-8247-0851-2.
[8]   D. P. Dubal, R. Holze, P. Gomez-Romero, Sci. Rep., 4 (2014) 7349.
[9]   R. S. Mane, C. D. Lokhande, Mater. Chem. Phys., 65 (2000) 1.
[10]   S. M. Pawar, B. S. Pawar, J. H. Kim, O. S. Joo, C. D. Lokhande, Curr. Appl. Phys., 11 (2011) 117.
[11]   B. A. Ezekoye, P. O. Offor, V. A. Ezekoye, F. I. Ezema, Int. J. Sci. Res., 2 (2013) 452.
[12]   M. Ristov, G. J. Sinadinovski, I. Grozdanov, Thin Solid Films, 123 (1985) 6.
[13]   Y. F. Nicolau, J. C. Menard, J. Crys. Growth, 92 (1988) 128.
[14]   J. L. Gunjakar, A. M. More, V. R. Shinde, C. D. Lokhande, J. Alloys Comp., 465 (2008) 468.
[15]   Y. F. Nicolau, Appl. Sur. Sci., 22 (1985) 1061.
[16]   A. R. Boccaccini, J. A. Roether, B. J. Thomas, M. S. Shaffer, E. Chavez, E. Stoll, E. J. Minay, J. Ceram. Soc. Japan, 114 (2006) 1.
[17]   M. Diba, D. W. Fam, A. R. Boccaccini, M. S. Shaffer, Prog. Mater. Sci., 82 (2016) 83.
[18]   S. Obregon, G. Amor, A. Vazquez, Adv. Colloid Interface Sci., 269 (2019) 236.
[19]   L. Besra, M. Liu, Prog. Mater. Sci., 52 (2007) 1.
[20]   E. Y. Pikalova, E. G. Kalinina, Renewable Sustainable Energy Rev., 116 (2019) 109440.
[21]   A. R. West, Solid state chemistry and its application, second edition, Wiley, 2014, ISBN: 978-1-119-94294-8.
[22]   https://en.wikipedia.org/wiki/Solid-state_reaction_route.
[23]   Z. J. Chen, B. Z. Lin, Y. L. Chen, K. Z. Zhang, B. Li, H. Zhu, J. Phys. Chem. Solids., 71 (2010) 841.
[24]   J. N. Coleman, M. Lotya, A. O'Neill, S. D. Bergin, P. J. King, U. Khan, K. Young, A. Gaucher, S. De, R. J. Smith, I. V. Shvets, S. K. Arora, G. Stanton, H. Y. Kim, K. Lee, G. T. Kim, G. S. Duesberg, T. Hallam, J. J. Boland, J. J. Wang, J. F. Donegan, J. C. Grunlan, G. Moriarty, A. Shmeliov, R. J. Nicholls, J. M. Perkins, E. M. Grieveson, K. Theuwissen, D. W. McComb, P. D. Nellist, V. Nicolosi, Science, 331 (2011) 568.
[25]   J. L. Gunjakar, I. Y. Kim, J. M. Lee, Y. K. Jo, S. J. Hwang, J. Phys. Chem. C, 118 (2014) 3847.
[26]   B. D. Cullity, Elements of X-rays Diffraction, second edition, Addison-wesley publishing company, inc. 1956, ISBN: 0-201-01174-3.
[27]   D. Titus, E. J. J. Samuel, S. M. Roopan, Micro and Nano Technologies, 2 (2019) 303.
[28]   https://en.wikipedia.org/wiki/Raman_spectroscopy.
[29]   D. W. Shipp, F. Sinjab, I. Notingher, Adv. Opt. Photonics, 9 (2017) 315.
[30]   G. McMahon, Analytical instrumentation: a guide to laboratory, portable and miniaturized instruments, first edition, Wiley, 2008, ISBN: 978-0470-027950.
[31]   S. K. Sharma, D. S. Verma, L. U. Khan, S. Kumar, S. B. Khan, Handbook of material characterization, Springer, 2018, ISBN: 978-3-319-92954-5.
[32]   https://en.wikipedia.org/wiki/Energy-dispersive_X-ray_spectroscopy.
[33]   C. Battistoni, G. Mattogno, E. Paparazzo, Surf. Interface Anal., 7, (1985) 117.
[34]   S. J. Kerber, T. L. Barr, G. P. Mann, W. A. Brantley, E. Papazoglou, J. C. Mitchell, J. Mater. Eng. Perf., 7 (1998) 329.

[35]   M. Picollo, M. Aceto, T. Vitorino, Phys. Sci. Rev., 4 (2018) 20180008.
[36]   J. D. Han, S. I. Woo, Korean J. Chem. Eng., 8 (1991) 235.
[37]   B. Preetha, C. Janardanan, Res. J. Recent Sci. 2277 (2012) 2502.
[38]   R. Ahmad, J. Melsheimer, F. C. Jentoft, R. Schlogl, J. Catal., 218 (2003) 365.
[39]   J. Singh, H. Kaur, M. Rawat, J. Mater. Sci.: Mater. Electron., 29 (2018) 13715.
[40]   Y. Wang, K. Ding, R. Xu, D. Yu, W. Wang, P. Gao, B. Liu, J. Clean. Prod., 247 (2020) 119108.

CHAPTER-III

Exfoliative Synthesis and Characterization of Pristine Titanate-NS and Hexaniobate-NS

CHAPTER III

Exfoliative Synthesis and Characterization of Pristine Titanate-NS and Hexaniobate-NS

3.1 Introduction:

The first two chapters describe the use of semiconductor photocatalysis for an efficient and eco-friendly decomposition of toxic pollutants. Recently, various nanostructured semiconductors, such as transition metal -oxides, -sulfides, -hydroxides, -carbides, and -phosphates, have been explored as photocatalysts for decomposing toxic pollutants [1-4]. Various aspects of materials, such as chemical composition, particle size, crystal structure, doping, particle shape, particle dimensions, and morphology, can play a crucial role in tuning the photocatalytic activity of the semiconductors. Dimensionality is one of the crucial factors at the nanoscale range that can effectively control the physical and chemical characteristics of semiconductors. Thus, many low-dimensional nanostructured semiconducting materials are designed and explored as photocatalysts. Most dimensionality-controlled studies have focused on synthesizing 0D and 1D nanostructured semiconductor photocatalysts [5].

2D nanosheets synthesized by the exfoliation process have greater diversity in their crystal structure, chemical composition and surface properties [6-8]. 2D inorganic nanosheets synthesized from the exfoliation of layered inorganic crystals are superior 2D platforms for hybridization with various guest species. Hybridizing 2D inorganic nanosheets with suitable guest species can tune the physicochemical properties, energy band level, surface characteristics, and chemical bonding nature of hybridized species. These advantages make hybrid materials with tunable physicochemical properties useful for several applications [9]. Various inorganic layered materials, such as LMO, layered double hydroxide (LDH), layered metal chalcogenides (LMC), aluminosilicate clay mineral, etc., can fulfil the requirements of exfoliation. These materials can be exfoliated chemically into separate nanosheets using various techniques [10-13]. Nowadays, LMOs have gained more attention due to their ion exchange/intercalation characteristics, and they can serve as host materials for an exfoliation reaction.

In particular, the highly crystalline LMO such as layered cesium titanate ($Cs_xTi_{2-x/4}\square_{x/4}O_4$; $\square$=vacancy) and layered potassium hexaniobate ($K_4Nb_6O_{17}$) are the potential host materials for the synthesis of titanate and hexaniobate nanosheets. The exfoliated titanate nanosheets (titanate-NS) and potassium hexaniobate nanosheets (hexaniobate-NS) are wide bandgap semiconducting nanostructures highly useful for the hybridization with other narrow bandgap semiconductors for the enhancement of photocatalytic activity. These NSs can be easily derived from aqueous sonication of the

tetrabutylammonium hydroxide (TBAOH) intercalated protonated derivatives ($H_xTi_{2-x/4}\square_{x/4}O_4 \cdot H_2O$ ($\square$=vacancy) or $H_xK_{4-x}Nb_6O_{17}$) of respective host layered crystals [14, 15]. These NSs are reported as a highly stable platform for hybridization with various narrow band gap semiconductors and are used for photofunctional applications. However, most research focuses on bulk powder preparation of reassembled NS or their hybrids [16]. The use of exfoliated NSs for thin film preparation is rarely reported and necessary for the practical application of nanosheets (NSs) for photocatalysis.

In many instances, titanate-NS and hexaniobate-NS have been deposited on the various substrates using exfoliated colloidal suspension. The Langmuir-Blodgett (LB) and layer-by-layer (LBL) deposition methods are commonly used to deposit NSs on various substrates [17-20]. However, these methods have disadvantages such as high cost, high time consumption, the requirement for oppositely charged polymers (binder molecules), and additional steps to remove the binder [21]. On the other hand, the EPD method is a very easy, inexpensive, rapid thin film deposition technique that can give highly adherent and uniform NS films with desired thickness at room temperatures. In addition, the deposition of charged NSs from its colloidal suspension does not require any oppositely charged polymer.

The present chapter deals with the synthesis of titanate-NS and hexaniobate-NS thin films from the exfoliated solution. The various parameters are optimized to deposit exfoliated nanosheets onto the substrate surface to achieve a uniform thin film. Different techniques such as XRD, FT-IR, Raman, FE-SEM, XPS, and UV-vis DRS are used to probe the physicochemical properties of deposited thin films.

3.2 Synthesis and characterizations of pristine titanate-NS:

3.2.1 Experimental details:

3.2.1.1 Chemicals:

Titanium oxide (TiO_2), cesium carbonate (Cs_2CO_3), hydrochloric acid (HCl), TBAOH, and ethanol (C_2H_5OH) were purchased from Sigma-Aldrich (Chemical Co. UK.) and used without purification.

3.2.1.2 Synthesis of exfoliated titanate-NS:

Layered caesium titanate ($Cs_{0.7}Ti_{1.825}\square_{0.175}O_4$, $\square$=vacancy) was synthesized by previously reported conventional solid-state reaction [22]. The intimate mixture of Cs_2CO_3 and TiO_2 (1:5.3 molar ratio) was grind in a crucible and heated at 800 °C for 20 hours. The resultant solid was again crushed and heated at the same conditions to form

highly crystalline $Cs_{0.7}Ti_{1.825}\square_{0.175}O_4$ host crystals. The synthesized $Cs_{0.7}Ti_{1.825}\square_{0.175}O_4$ host crystals were protonated with 1 M HCl at room temperature for three days. After every 24 hours, the acid solution was replaced with a fresh one. Afterwards, the solution was centrifuged and the obtained protonated titanate was thoroughly washed with DDW and dried at room temperature. In order to achieve exfoliated titanate-NS, the protonated titanate ($H_{0.7}Ti_{1.825}\square_{0.175}O_4$) was vigorously shaken with an aqueous solution of TBAOH for two weeks at ambient temperature, as reported previously [23]. The schematic representation of the synthesis of exfoliated titanate-NS is shown in **Fig. 3.1**.
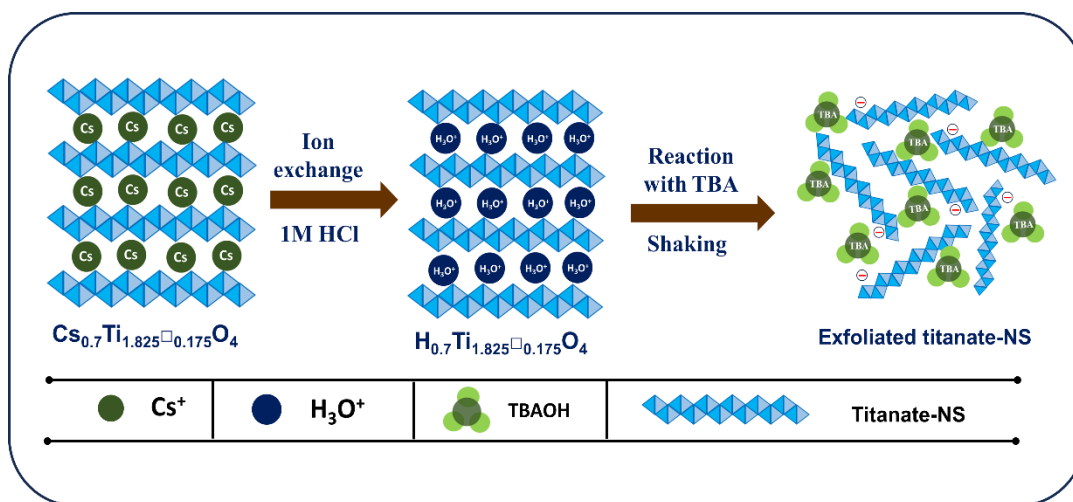
Fig. 3.1. The schematic representation of $Cs_{0.7}Ti_{1.825}\square_{0.175}O_4$ host crystals exfoliation.

3.2.1.3 Synthesis of titanate-NS thin films by EPD:

Titanate-NS thin films were deposited on the well-cleaned indium-doped tin oxide (ITO) coated glass substrates. The ITO-coated glass substrates were cleaned by ultrasonication in ethanol, DDW, acetone, and DDW again. Well-cleaned ITO-coated glass substrates were preserved in deionized water and used for every deposition.

Titanate-NS thin films by EPD were obtained from the colloidal titanate-NS suspension. The titanate-NS colloidal suspension (with pH of 12-12.5) was dialyzed for 10 hours using a dialysis membrane (Dialysis Membrane-135, Av. flat width-33.12 mm, Av. diameter-23.8 mm, Capacity approx.-4.45 ml cm^{-1}) in DDW to attain a pH of 8. The titanate-NS dialysis solution and absolute ethanol were mixed in the 1:3 volume proportion and used for EPD. The titanate-NS thin films were deposited from the specially designed cylindrical graphite cell that acts as a cathode, as shown in **Fig 3.2**. For EPD, the distance between the counter electrode (specially designed graphite cell) and the working electrode (ITO-coated glass substrate) was fixed at 1 cm.

The uniform titanate-NS thin films were deposited on the ITO-coated glass substrate by applying the constant potential of 10 V DC across the ITO and graphite cell. The deposition time of EPD was adjusted between 5 to 15 min. After the deposition, the titanate-NS films were air-dried and annealed at 200 °C for 1 hour in air to remove TBA and improve adherence. The annealed titanate-NS thin films deposited at 5, 10 and 15-minute deposition times are denoted as titanate-NS-5, titanate-NS-10, and titanate-NS-15, respectively.
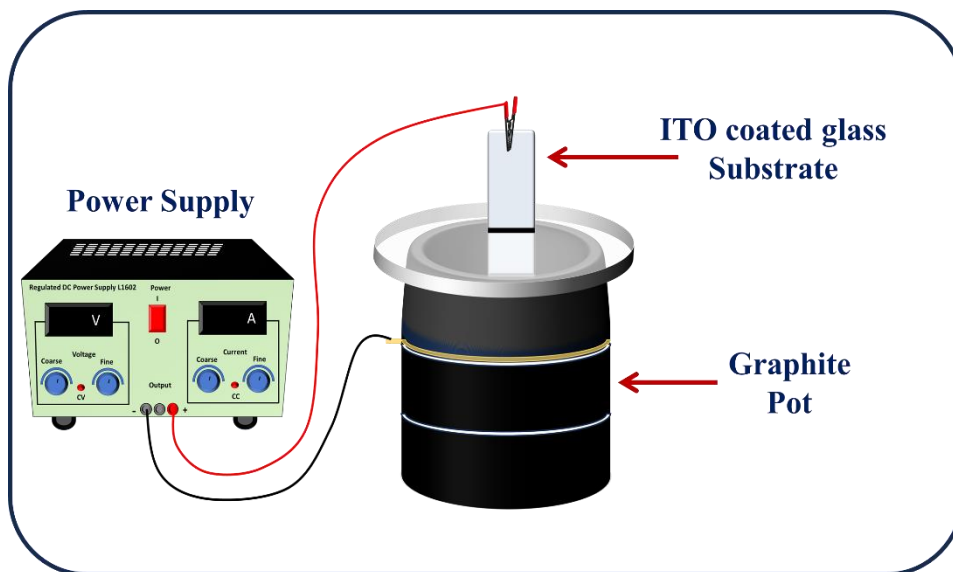
Fig. 3.2. Schematic representation of the EPD method.

3.2.1.4 Material characterizations:

The crystal structures of the deposited thin films were studied by powder XRD technique using Rigaku miniflex-600 with Cu Kα (λ= 0.15406 nm) radiation. The surface morphologies and chemical compositions were probed with a FE-SEM (JEOL JSM–6700F) coupled with EDS. The FT-IR spectra were recorded in the frequency range between 400 to 4000 cm^{-1} using a Jasco FT-IR 4600 spectrophotometer to study the nature of chemical bonding in the prepared sample. The nature of chemical bonding and functional groups of deposited thin films were studied using micro-Raman spectroscopy (Renishaw INVIA Raman microscope with 532 nm laser excitation wavelength). The XPS (Thermo, UK, Al Kα) was used to study the chemical and valence states of the constituent element. The UV-vis-DRS of deposited thin films were recorded on a Jasco V-770 spectrophotometer to check the optical properties of synthesized thin films.

3.2.2 Results and Discussions:

3.2.2.1 XRD study:
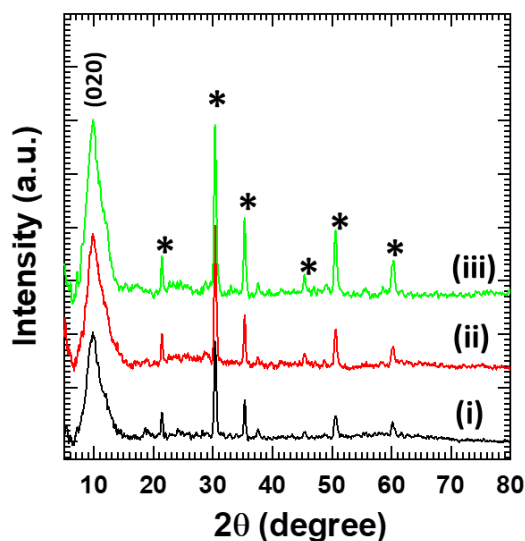
Fig. 3.3. XRD patterns of (i) titanate-NS-5, (ii) titanate-NS-10, and (iii) titanate-NS-15 thin films.

The crystal structure of the titanate-NS thin films was studied using XRD analysis. The XRD patterns of titanate-NS thin film are displayed in **Fig. 3.3**. All the titanate-NS thin films show a high-intensity broad diffraction peak centred at 10° suggesting the titanate nanosheets are layer-by-layer deposited on the substrate and form the oriented titanate-NS thin film. This peak is assigned to the (020) plane of lepidocrocite-type titanate-NS with orthorhombic symmetry having a basal spacing of 0.88 nm [24]. In addition, the peaks marked by '*' correspond to the ITO substrate. No other peaks are matched with other titanium oxide phases, demonstrating the high chemical stability of titanate-NS thin films.

3.2.2.2 FT-IR study:

The chemical bonding nature of titanate-NS thin films was studied using FT-IR spectroscopy. The FTIR spectra of titanate-NS thin films in the range of 400-4000 cm^{-1} are displayed in **Fig. 3.4**. The titanate-NS thin films show absorption peaks $v1$ (475 cm^{-1}) and $v2$ (622 cm^{-1}) are assigned to the bending and stretching modes of Ti-O, respectively [25, 26]. The minute absorption peak $v3$ (1392 cm^{-1}) corresponds to the bending vibrations of the $-CH_2-$ group in the alkyl chain of TBA [27]. The other sharp peak $v4$ (1630 cm^{-1}) and broad absorption peak $v5$ (3415 cm^{-1}) correspond to the bending vibrational modes of water molecules and stretching vibrations of the O-H groups, respectively [28, 29]. These IR features related to Ti-O bonding are characteristic of

deposited titanate-NS. The IR signature related to water indicates the presence of structural water in the titanate-NS thin films.
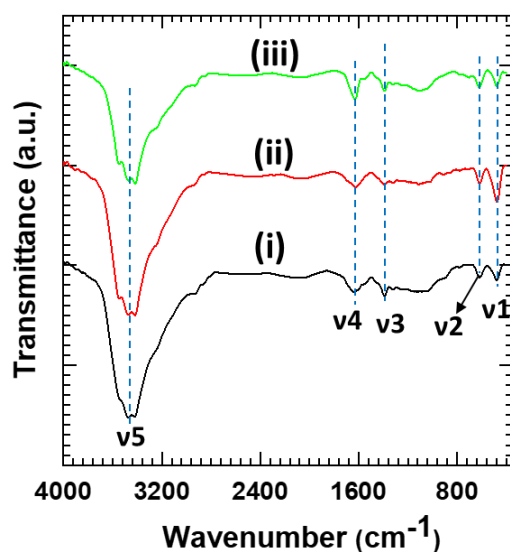
Fig. 3.4. FT-IR spectra of (i) titanate-NS-5, (ii) titanate-NS-10, and (iii) titanate-NS-15 thin films.

3.2.2.3 Micro-Raman study:

The microscopic structural bonding characteristic of titanate-NS thin films was probed with Raman spectroscopy, as shown in **Fig. 3.5**. The titanate-NS thin films commonly discern distinct Raman peaks R1 to R5 corresponding to the titanate-NS. The peaks R1 (282 cm^{-1}) and R2 (448 cm^{-1}) are assigned to *Ag* symmetric vibrations originating from the splitting of the degenerate mode of the TiO_6 octahedron [30].
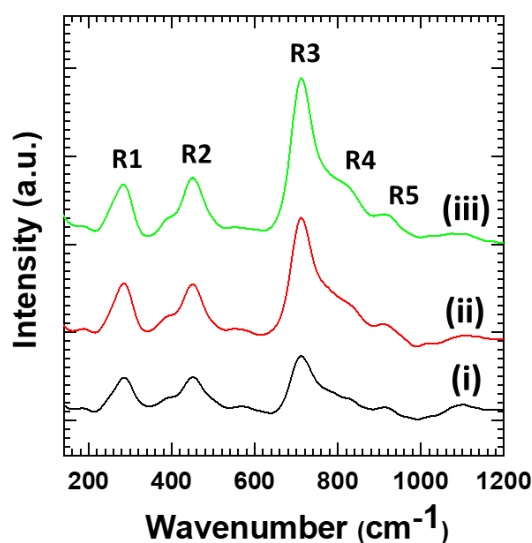
Fig. 3.5. Micro-Raman spectra of (i) titanate-NS-5, (ii) titanate-NS-10, and (iii) titanate-NS-15 thin films.

The peak R3 (708 cm^{-1}) corresponding to symmetric Ti-O vibration belongs to *Ag* symmetric mode [31]. Moreover, the mild Raman peaks R4 (828 cm^{-1}) and R5 (917 cm^{-1}) correspond to the stretching vibrations of Ti-O bonds [31]. These Raman peaks are characteristic of well-developed 2D lepidocrocite-type layered titanate-NS deposition. The presence of these microscopic structural features provides the stabilization of lepidocrocite-type titanate-NS thin films.

3.2.2.4 FE-SEM study:
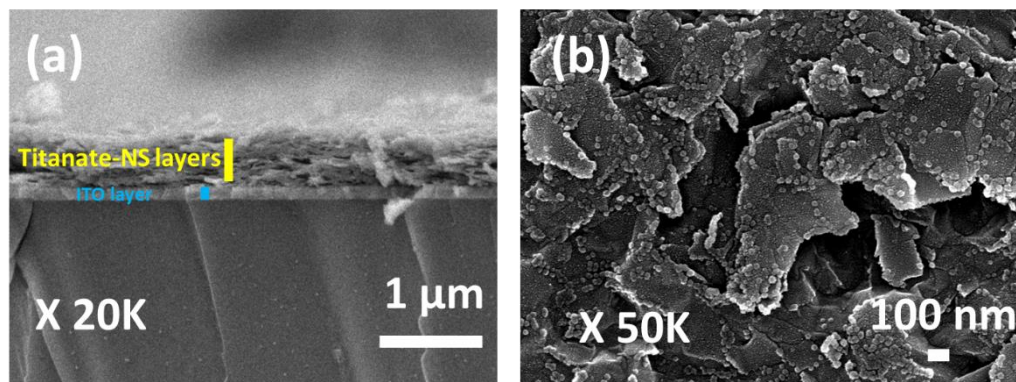
Fig. 3.6. FE-SEM images of (a) cross-section and (b) top-view of titanate-NS-10 thin film.

The cross-sectional and top-view microstructure of the titanate-NS-10 thin film were studied using FE-SEM. The cross-sectional and top views of FE-SEM micrographs of titanate-NS-10 thin film are displayed in **Fig. 3.6(a)** and **Fig. 3.6(b)**, respectively. As displayed in **Fig. 3.6(a)**, the titanate-NS-10 thin film displays nanosheets of titanate lying parallel to the ITO substrate surface, confirming the deposition of titanate nanosheets. The EPD-deposited titanate-NS thin film **(Fig. 3.6(b))** shows parallelly aligned titanate nanosheets on the ITO substrate surface. The lateral sheet size of titanate nanosheets is in the range of 500 to 600 nm. The deposited nanosheets are randomly aggregated on the surface of the ITO substrate, displaying a compact structure of titanate-NS thin film.

3.2.2.5 XPS study:

The chemical environment and valance state of the elements present in the titanate-NS thin film were studied using XPS analysis. The XPS survey spectrum of the titanate-NS-10 thin film demonstrates the spectral features at the binding energies of the elements Ti and O in the titanate-NS thin film, as displayed in **Fig. 3.7**. The present XPS features indicate the presence of Ti and O elements in the EPD-deposited titanate-NS-10 thin film.
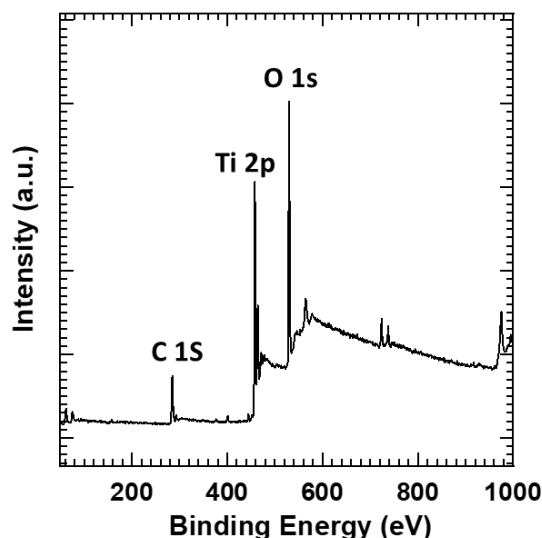
Fig. 3.7. XPS survey spectrum of titanate-NS-10 thin film.
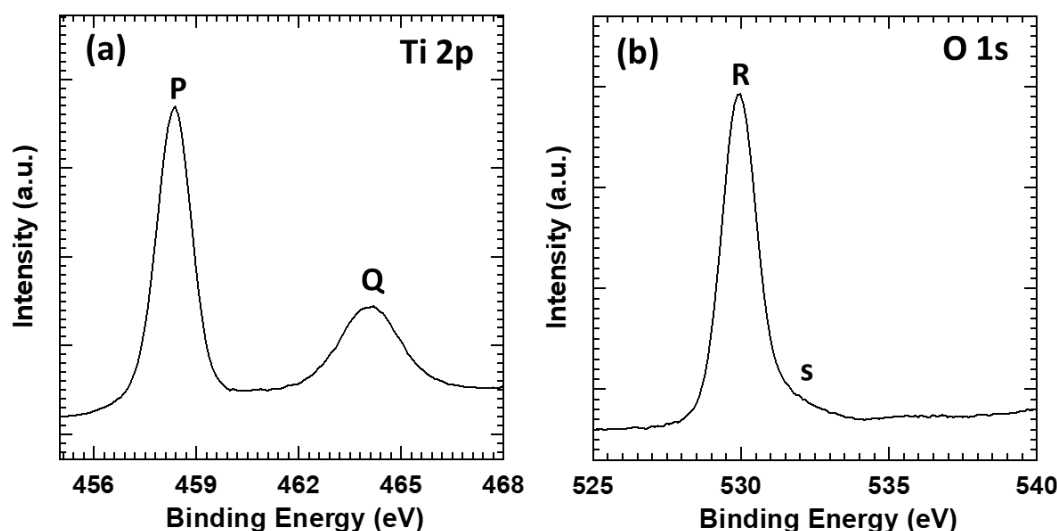
Fig. 3.8. (a) Ti 2p and (b) O 1s core-level XPS spectra of titanate-NS-10 thin films.

As shown in **Fig. 3.8(a)**, the high-resolution Ti 2p spectrum of titanate-NS-10 thin film exhibited two spectral features, P (458.3 eV) and Q (464.1 eV), which are attributed to spin-orbit splitting into Ti $2p_{3/2}$ and Ti $2p_{1/2}$, respectively. These peaks are characteristics signature of Ti^{4+} in titanate-NS thin film. The core-level O 1s XPS spectrum of titanate-NS-10 thin film plotted in **Fig. 3.8(b)** displays broad peak R (529.9 eV) with a shoulder at S (531.7 eV), indicating the presence of oxygen in titanium oxide and a surface hydroxyl group [32-34]. The present XPS features indicated that the Ti^{4+} oxidation state of Ti is present in titanate-NS thin film. These features demonstrate the thermal stability of lepidocrocite titanate-NS thin films.

3.2.2.6 UV-vis DRS and energy band structure study:
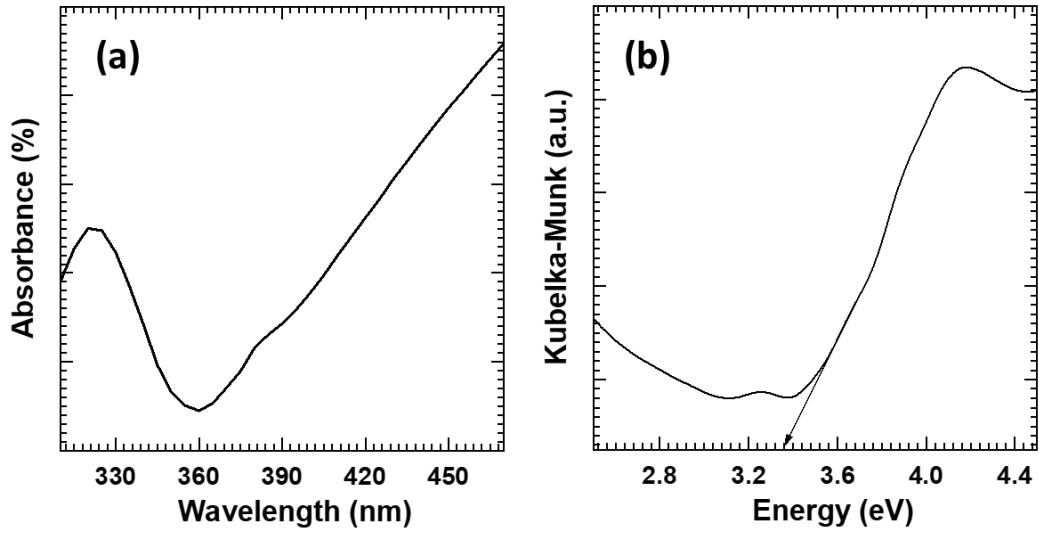
Fig. 3.9. (a) UV-vis absorbance spectrum obtained from UV-vis DRS and (b) UV-vis DRS (plotted as Kubelka-Munk function of reflectance, R) of titanate-NS-10 thin film.

The optical property of titanate-NS thin film was probed with UV-vis DRS. As shown in **Fig. 3.9(a)**, the titanate-NS-10 thin film displays an absorption edge in the UV region of the solar spectrum, demonstrating the capability of titanate-NS thin film to capture UV light. The titanate-NS thin film has an indirect bandgap material with a valance band (VB) and conduction band (CB) mainly composed of O 2p and Ti 3d orbitals, respectively [35, 36]. The titanate-NS thin film absorbs UV light with a wavelength less than 370 nm. The energy band gap of the deposited thin film can be determined using the Kubleka-Munk function given below

$$\alpha = F(R) = (1-R)^2 / 2R \qquad\qquad (3.1)$$

Where α is the absorption coefficient, F(R) is the Kubelka-Munk function, and R is reflectance obtained from UV-vis DRS [37, 38]. The plot of UV-vis DRS (plotted as Kubelka-Munk function of reflectance, R) of titanate-NS-10 thin film is shown in **Fig. 3.9(b)**. The energy bandgap determined from the Kubelka-Munk function is 3.34 eV for titanate-NS-10 thin film. The present study highlights the significant absorption of titanate-NS thin film in the UV region of the electromagnetic spectrum [39, 40].

Based on the energy bandgap, the CB and VB potentials of the titanate-NS thin film can be found by using the formula

$$E_{VB} = \chi - Ee + 0.5E_g \qquad\qquad (3.2)$$
$$E_{CB} = E_{VB} - E_g \qquad\qquad (3.3)$$

where E_{CB}, E_{VB}, Eg, χ, and Ee are the CB potential, VB potential, energy bandgap, electronegativity, and free electron energy vs. hydrogen, respectively. The free electron energy on the hydrogen scale is 4.5 eV [41]. Therefore, the positions of CB and VB of pristine titanate-NS with respect to the normal hydrogen electrode (NHE) scale are -1.11 eV and 2.23 eV. The schematic representation of the energy band structure of titanate-NS thin film is represented in **Fig. 3.10**.
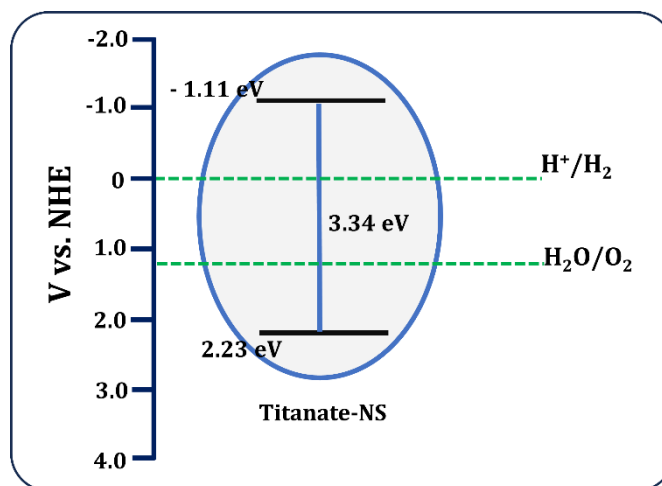
Fig. 3.10. Energy band structure of titanate-NS thin film.

3.3 Synthesis and characterizations of hexaniobate-NS:

3.3.1 Experimental details:

3.3.1.1 Chemicals:

Niobium pentoxide (Nb_2O_5), potassium carbonate (K_2CO_3), HCl, TBAOH, and C_2H_5OH were purchased from Sigma-Aldrich (Chemical Co. UK) and used without any further purification.

3.3.1.2 Synthesis of exfoliated hexaniobate-NS:

Layered potassium hexaniobate ($K_4Nb_6O_{17}$) was synthesized by a previously reported solid-state process [42-44]. Nb_2O_5 and K_2CO_3 in a molar proportion of 2:3 were ground together in a mortal pestle. The mixture was then pressed into pellets, kept in an alumina crucible, and calcinated at 1100 °C for 24 hours. The synthesized $K_4Nb_6O_{17}$ host crystals were protonated with 1 M HCl at room temperature for three days to produce $H_xK_{4-x}Nb_6O_{17}$ (x ≈ 3). After every 24 hours, the acid solution was replaced with a fresh one. To obtain a colloidal suspension of hexaniobate-NS, the 1 g proton exchanged solid $H_xK_{4-x}Nb_6O_{17}$ was dispersed in 250 mL of 25 mM aqueous TBAOH solution at room temperature. The schematic representation of the synthesis of exfoliated hexaniobate-NS is shown in **Fig. 3.11**.
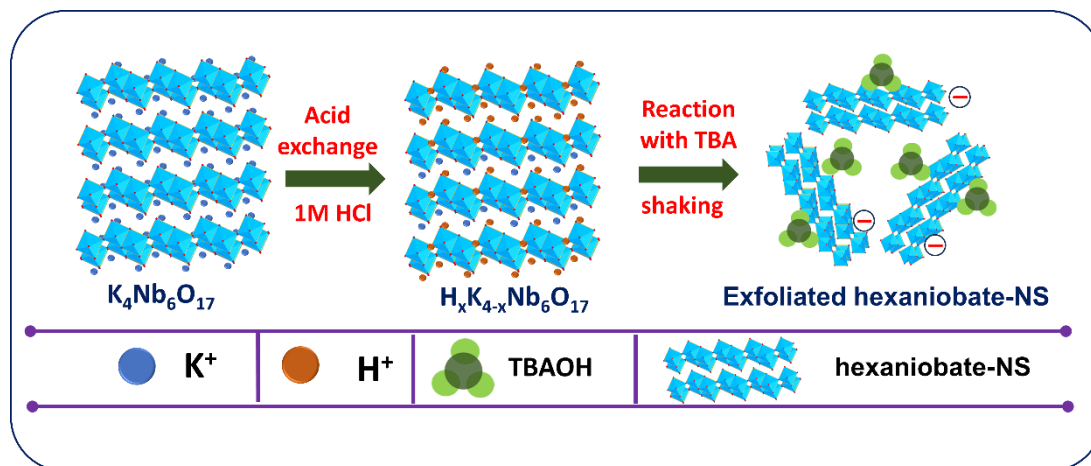
Fig. 3.11. The schematic representation of $K_4Nb_6O_{17}$ host crystals exfoliation.

3.3.1.3 Synthesis of hexaniobate-NS thin films by EPD:

The synthesis process of hexaniobate-NS thin films was similarly carried out as discussed in **Chapter 3, section 3.2.1.3,** except for its applied constant voltage and deposition time. For the deposition of hexaniobate-NS, the constant potential of 15 V DC was applied across the ITO and cathode. The deposition time of EPD was adjusted between 8 to 24 minutes. After the deposition, deposited hexaniobate-NS films were air-dried followed by annealed at 200 °C for 1 hour in the air to remove TBA and improve adherence. The annealed hexaniobate-NS thin films deposited at 8, 16, and 24 min deposition times are denoted as hexaniobate-NS-8, hexaniobate-NS-16, and hexaniobate-NS-24, respectively.

3.3.1.4 Material characterizations:

The hexaniobate-NS thin films deposited by the EPD method were characterized by various physicochemical characterization techniques, as described in **Chapter 3, section 3.2.1.4**.

3.3.2 Results and Discussion:

3.3.2.1 XRD study:

The XRD patterns of hexaniobate-NS thin films are represented in **Fig. 3.12**. All the hexaniobate-NS thin films demonstrate a broad diffraction peak centred at 11°, indicating the hexaniobate-NS are restacked layer by layer on the ITO substrate and form the oriented hexaniobate-NS. The interlayer spacing of hexaniobate-NS thin films is found to be 0.78 nm [45, 46]. Moreover, the other peaks marked by '*' originated from the ITO substrate. No other peaks are matched with other niobium oxide phases,

demonstrating the high chemical stability of hexaniobate-NS thin films. These XRD features highlight the growth of layered hexaniobate-NS on the ITO substrate.
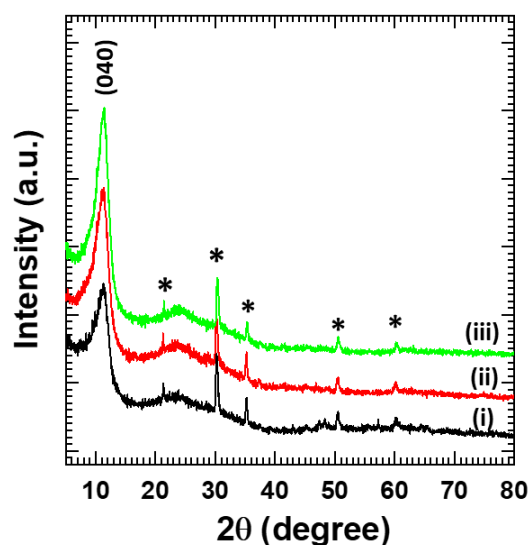
Fig. 3.12. XRD patterns of (i) hexaniobate-NS-8, (ii) hexaniobate-NS-16, and (iii) hexaniobate-NS-24 thin films.

3.3.2.2 FT-IR study:
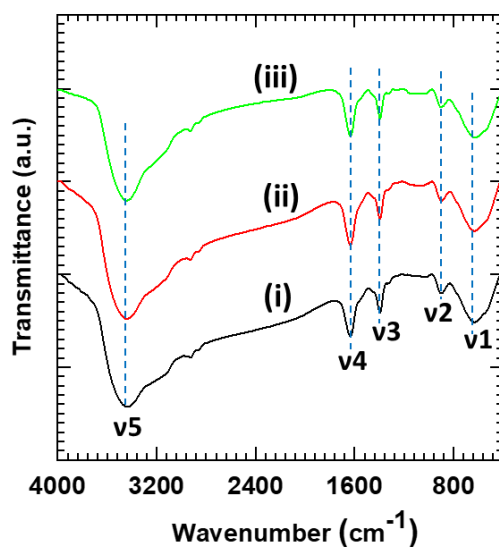
Fig. 3.13. FT-IR spectra of (i) hexaniobate-NS-8, (ii) hexaniobate-NS-16, and (iii) hexaniobate-NS-24 thin films.

The chemical bonding nature of hexaniobate-NS thin films studied with FT-IR spectroscopy is shown in **Fig. 3.13**. The FT-IR spectra of hexaniobate-NS thin films commonly show strong absorption peaks at $\nu 1$ (450-750 cm^{-1}) and $\nu 2$ (904 cm^{-1}) are associated with the O-Nb-O and Nb=O stretching vibration in the NbO$_6$ octahedron, respectively [42]. The absorption peak at $\nu 3$ (1399 cm^{-1}) is attributed to the bending

vibrations of the -CH$_2$- group in the alkyl chain of TBA [27]. The other sharp peak ν4 (1630 cm^{-1}) and broad absorption peak ν5 (3415 cm^{-1}) correspond to the bending vibrational modes of water molecules and stretching vibration of the O-H groups, respectively [28, 29]. The FT-IR measurements confirm the Nb-O bonds and structural water in the present hexaniobate-NS thin films. The presence of these IR peaks highlighted the Nb-O bonding in the EPD-deposited hexaniobate-NS thin films.

3.3.2.3 Micro-Raman study:
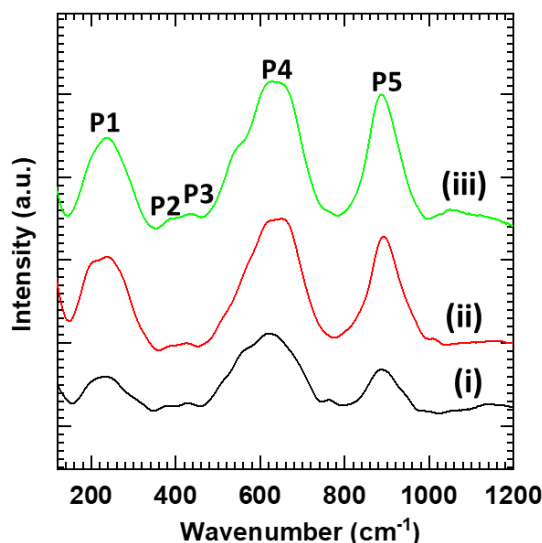
Fig. 3.14. Micro-Raman spectra of (i) hexaniobate-NS-8, (ii) hexaniobate-NS-16, and (iii) hexaniobate-NS-24 thin films.

The microscopic structural bonding characteristic of hexaniobate-NS thin films was probed with Raman spectroscopy, as shown in **Fig. 3.14**. The hexaniobate-NS thin film commonly discerns distinct Raman peaks P1 to P5 corresponding to the hexaniobate. The peaks P1-P3 (150-470 cm^{-1}) originated due to the internal bending modes of the O-Nb-O linkage. The broad peak P4 (500-700 cm^{-1}) corresponds to longer Nb-O bonds of stretching mode. In addition, the peak P5 (884 cm^{-1}) corresponds to the Nb-O terminal stretching mode of highly distorted NbO$_6$ octahedra [47-49]. The present Raman modes in hexaniobate-NS thin films underscore the formation of the layered crystal structure of hexaniobate-NS.

3.3.2.4 FE-SEM study:

The cross-sectional and top views of the hexaniobate-NS-16 thin film were probed with FE-SEM. The cross-sectional view and top-view of the hexaniobate-NS-16 thin film are displayed in **Fig. 3.15(a)** and **Fig. 3.15(b)**, respectively.
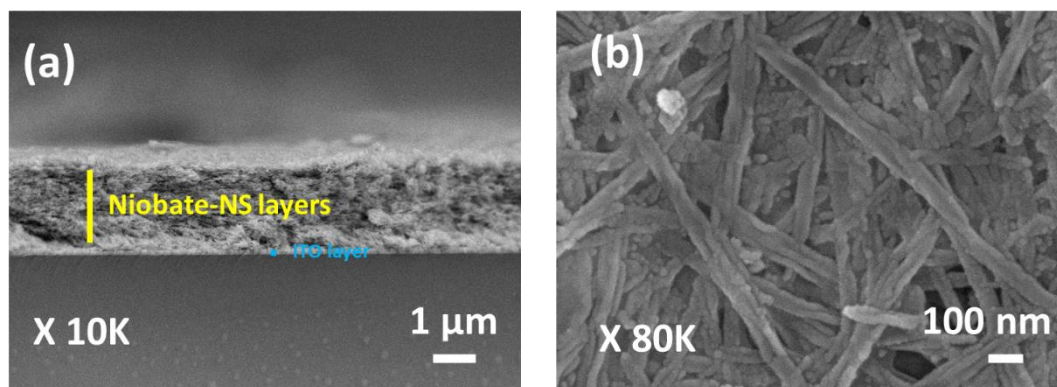
Fig. 3.15. FE-SEM micrographs of (a) cross-section view and (b) top-view of hexaniobate-NS-16 thin film.

The cross-sectional image in **Fig. 3.15(a)** shows hexaniobate nanoscrolls deposited on the ITO substrate, confirming the deposition of hexaniobate-NS. As displayed in **Fig. 3.15(b)**, the surface morphological study of hexaniobate-NS thin film shows nanoscroll-like morphology. The average nanoscrolls length and diameter are 700 nm and 30 nm, respectively. The deposited nanoscrolls are randomly aggregated on the surface of the ITO substrate, creating a porous structure of hexaniobate-NS.

3.3.2.5 XPS study:
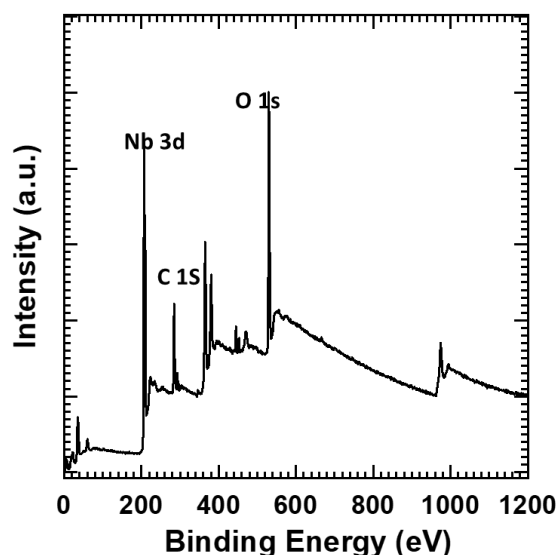
Fig. 3.16. XPS survey spectrum of hexaniobate-NS-16 thin film.

The XPS was used to determine the elements present, their chemical states, and the electronic structure of the hexaniobate-NS thin film. The survey XPS spectrum shows the characteristics signal at the binding energies of the elements Nb and O, as shown in **Fig. 3.16**. The present XPS features indicate the presence of Nb and O elements in the EPD hexaniobate-NS-16 thin film.
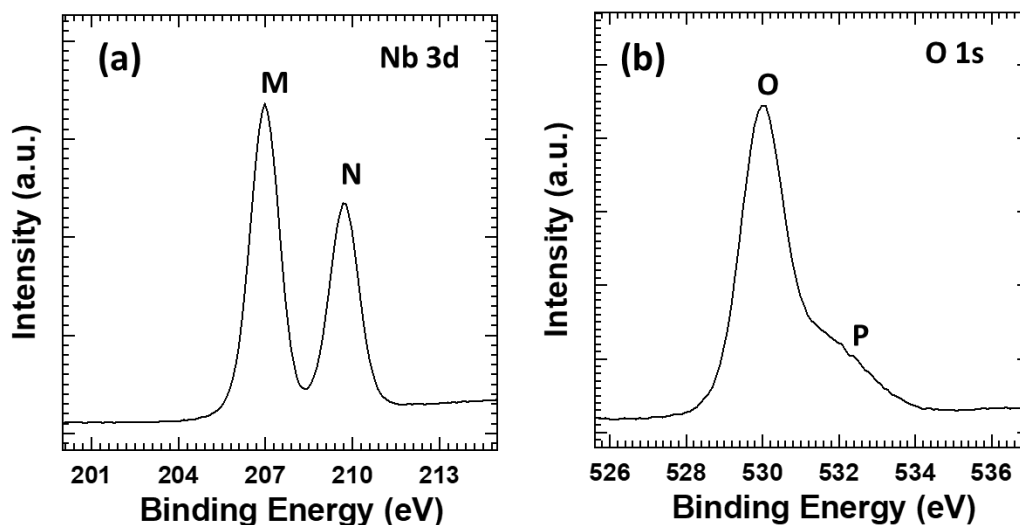
Fig. 3.17. (a) Nb 3d and (b) O 1s core-level XPS spectra of hexaniobate-NS-16 thin films.

The Nb 3d high-resolution spectrum in **Fig. 3.17(a)** exhibited two spectral features, M (207.04 eV) and N (209.7 eV), which are associated with spin-orbit splitting of Nb $3d_{5/2}$ and Nb $3d_{3/2}$, respectively. These peaks are characteristic of Nb^{5+} in hexaniobate-NS-16 thin film [50]. The core-level O 1s XPS spectrum plotted in **Fig. 3.17(b)** demonstrates major peak O (530 eV) with a shoulder at P (532.1 eV), indicating the presence of oxygen in metal oxide and a surface hydroxyl group [51]. The present XPS features clearly indicates that Nb in the Nb^{5+} oxidation state is present in the EPD-deposited hexaniobate-NS thin films.

3.3.2.6 UV-vis DRS and band structure determination study:
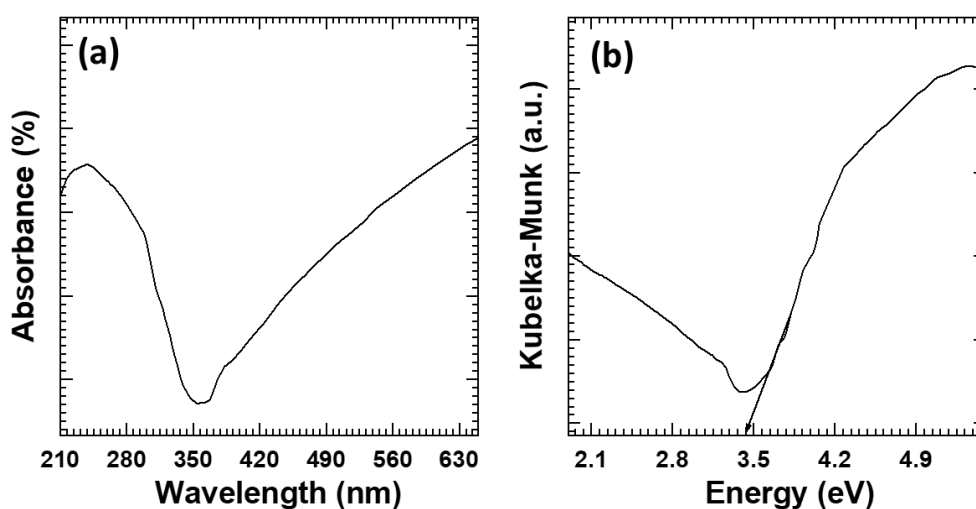
Fig. 3.18. (a) UV-vis absorbance spectrum obtained from UV-vis DRS and (b) UV-vis DRS (plotted as Kubelka-Munk function of reflectance, R) of hexaniobate-NS-16 thin film.

The optical property of hexaniobate-NS thin film was probed with UV- vis DRS. As shown in **Fig. 3.18(a)**, the absorption edge of hexaniobate-NS-16 thin film is occurred in the UV region of the solar spectrum, demonstrating the capability of hexaniobate-NS thin film to harvest UV light. The hexaniobate-NS thin film displays an indirect bandgap with a VB and CB mainly composed of O 2p and Nb 4d orbitals, respectively [52]. The hexaniobate-NS thin film absorbs UV light with a wavelength less than 360 nm. The plot of UV-vis DRS (plotted as Kubelka-Munk function of reflectance, R) of hexaniobate-NS thin film is shown in **Fig. 3.18(b)**. The energy bandgap value derived from the Kubelka-Munk function is 3.45 eV for hexaniobate-NS-16 thin film. The present study highlights the significant absorption of hexaniobate-NS thin film in the UV region of the electromagnetic spectrum. Based on the bandgap energy, the CB and VB potentials of the hexaniobate-NS thin film can be found using the formula in equations 3.2 and 3.3. Therefore, the position of VB and CB of pristine hexaniobate-NS with respect to the NHE is 2.69 eV and -0.76 eV, respectively [53]. The schematic representation of the energy band structure of hexaniobate-NS thin film is represented in **Fig. 3.19**.
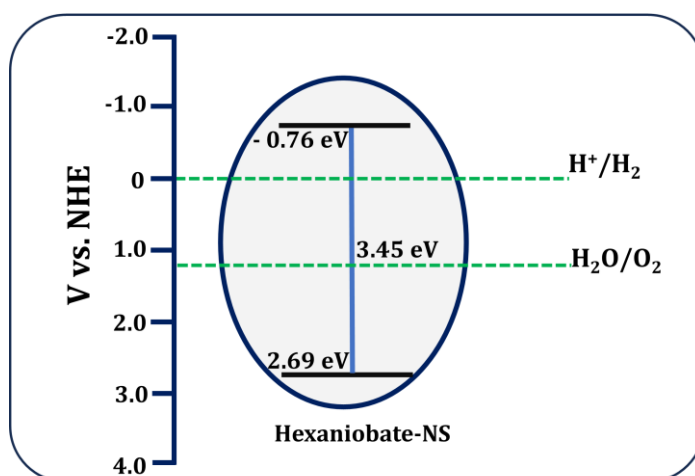
Fig. 3.19. Energy band structure of hexaniobate-NS thin film.

3.4 Conclusions:

In summary, highly crystalline layered cesium titanate ($Cs_{0.7}Ti_{1.825}\square_{0.175}O_4$, $\square$=vacancy) and potassium hexaniobate ($K_4Nb_6O_{17}$) were synthesized using a solid-state process. Exfoliated titanate-NS and hexaniobate-NS were obtained by vigorously shaking their protonated derivatives in the presence of TBAOH. Thin films of titanate-NS and hexaniobate-NS from the exfoliated suspension were deposited via EPD method at a constant potential of 10 and 15 V, respectively. The structural studies reveal that

titanate-NS and hexaniobate-NS are restacked layer by layer on the ITO-coated glass substrate. The interlayer spacing of the titanate-NS and hexaniobate-NS thin film are 0.88 and 0.78 nm, respectively. The surface morphological analysis shows that the titanate-NS thin film exhibited a nanosheet-like structure with lateral sheet sizes ranging from 500 to 600 nm. In contrast, the hexaniobate-NS thin film displays a nanoscroll-like morphology, with an average length of 700 nm and diameter of 30 nm. Optical studies indicate energy bandgaps of 3.35 eV for titanate-NS and 3.45 eV for hexaniobate-NS, making them suitable for harvesting UV light. These electrophoretically deposited thin films can serve as wide bandgap semiconducting materials for the hybridization with other narrow bandgap semiconducting materials for visible-light-driven photo-functionality.

3.5 References:

[1] U. Chakraborty, G. Bhanjana, N. Kaur, R. Sharma, G. Kaur, A. Kaushik, G. R. Chaudhary, J. Hazard. Mater., 416 (2021) 125771.

[2] M. Hasanpour and M. Hatami, J. Mol. Liq., 309 (2020) 113094.

[3] A. Rafiq, M. Ikram, S. Ali, F. Niaz, M. Khan, Q. Khan, M. Maqbool, J. Ind. Engg. Chem., 97 (2021) 111.

[4] J. Zia, F. Fatima, U. Riaz, CataL. Sci. Tech., 11 (2021) 6630.

[5] S. Jeong, D. Yoo, J. T. Jang, M. Kim, J. Cheon, J. Am. Chem. Soc., 134 (2012) 18233.

[6] S. Z. Butler, S. M. Hollen, L. Cao, Y. Cui, J. A. Gupta, H. R. Gutierrez, T. F. Heinz, S. S. Hong, J. Huang, A. F. Ismach, E. Johnston-Halperin, ACS nano, 7 (2013) 2898.

[7] M. Xu, T. Liang, M. Shi, H. Chen, Chem. Rev., 113 (2013) 3766.

[8] S. V. Sadavar, N. S. Padalkar, R. B. Shinde, S. T. Kochuveedu, U. M. Patil, A. S. Patil, R. N. Bulakhe, C. D. Lokhande, I. In, R. R. Salunkhe, J. L. Gunjakar, J. Power Sources, 524 (2022) 231065.

[9] N. S. Padalkar, S. V. Sadavar, R. B. Shinde, A. S. Patil, U. M. Patil, D. S. Dhawale, R. N. Bulakhe, H. Kim, H. Im, A. Vinu, C. D. Lokhande, J. Colloid Interface Sci., 616 (2022) 548.

[10] V. Nicolosi, M. Chhowalla, M. G. Kanatzidis, M. S. Strano, J. N. Coleman, Science, 340 (2013) 1226419.

[11] J. N. Coleman, M. Lotya, A. O'Neill, S. D. Bergin, P. J. King, U. Khan, K. Young, A. Gaucher, S. De, R. J. Smith, I. V. Shvets, S. K. Arora, G. Stanton, Hye-Y. Kim, K. Lee, G. T. Kim, G. S. Duesberg, T. Hallam, J. J. Boland, J. J. Wang, J. F. Donegan, J. C. Grunlan, G. Moriarty, A. Shmeliov, R. J. Nicholls, J. M. Perkins, E. M. Grieveson, K. Theuwissen, D. W. McComb, P. D. Nellist, V. Nicolosi, Science, 331 (2011) 568.

[12] R. B. Shinde, N. S. Padalkar, S. V. Sadavar, A. S. Patil, S. B. Kale, V. V. Magdum, Y. M. Chitare, S. P. Kulkarni, U. M. Patil, V. G. Parale, J. L. Gunjakar, Mater. Today Chem., 24 (2022) 100801.

[13] J. L. Gunjakar, I. Y. Kim, J. M. Lee, Y. K. Jo, S. J. Hwang, J. Phys. Chem. C, 118 (2014) 3847.

[14] T. Sasaki, M. Watanabe, Y. Michiue, Y. Komatsu, F. Izumi, S. Takenouchi, Chem. Mater., 7 (1995) 1001.

[15] J. L. Gunjakar, T. W. Kim, H. N. Kim, I. Y. Kim, S. J. Hwang, J. Am. Chem. Soc., 133 (2011) 14998.

[16] M. Eguchi, M. S. Angelone, H. P. Yennawar, T. E. Mallouk, J. Phys. Chem. C, 112 (2008) 11280.

[17] M. Muramatsu, K. Akatsuka, Y. Ebina, K. Wang, T. Sasaki, T. Ishida, K. Miyake, M. A. Haga, Langmuir, 21 (2005) 6590.

[18] T. Sasaki, Y. Ebina, M. Watanabe, G. Decher, Chem. Comm., 21 (2000) 2163.

[19] N. Sakai, Y. Ebina, K. Takada, T. Sasaki, J. Am. Chem. Soc., 126 (2004) 5851.

[20] M. Harada, T. Sasaki, Y. Ebina, M. Watanabe, J. Photochem. Photobio. A, 148 (2002) 273.

[21] S. H. Kweon, M. Im, W. H. Lee, S. Nahm, J. W. Choi, S. J. Hwang, J. Mater. Chem. C, 4 (2016) 178.

[22] T. Sasaki, Y. Komatsu, Y. Fujiki, J. Chem. Soc., Chem. Commun., 12 (1991) 817.

[23]   T. Sasaki and M. Watanabe, J. Am. Chem. Soc., 120 (1998) 4682.

[24]   Y. Matsumoto, A. Funatsu, D. Matsuo, U. Unal, K. Ozawa, J. Phys. Chem. B, 105 (2001) 10893.

[25]   M. Waseen, Z. Shah, R. V. Cataluna, S. L. P. Dias, É. C. Lima, G. S. D. Reis, J. C. P. Vaghetti, W. S. D. Alencar, K. Mahmood, J. Anal. Bioanal. Tech., 8 (2017) 1000348.

[26]   V. G. Erkov, S. F. Devyatova, E. L. Molodstova, T. V. Malsteva, U. A. Yanovskii, Appl. Sur. Sci., 166 (2000) 51.

[27]   R. Chroma, M. Vilkova, I. Shepa, P. Makos-Chełstowska, V. Andruch, J. Mol. Liq., 330 (2021) 115617.

[28]   R. B. Shinde, A. S. Patil, S. V. Sadavar, Y. M. Chitare, V. V. Magdum, N. S. Padalkar, U. M. Patil, S. T. Kochuveedu, V. G. Parale, H. H. Park, C. D. Lokhande, Sens. Actuators B Chem., 352 (2022) 131046.

[29]   S. V. Sadavar, N. S. Padalkar, R. B. Shinde, S. T. Kochuveedu, U. M. Patil, A. S. Patil, R. N. Bulakhe, C. D. Lokhande, I. In, R. R. Salunkhe, J. L. Gunjakar, J. Power Sources, 524 (2022) 231065.

[30]   T. Gao, H. Fjellvag, P. Norby, J. Phy. Chem. B, 112 (2008) 9400.

[31]   R. Ma, K. Fukuda, T. Sasaki, M. Osada, Y. Bando, J. Phy. Chem. B, 109 (2005) 6210.

[32]   X. Wang, R. Xia, E. Muhire, S. Jiang, X. Huo, M. Gao, Appl. Surf. Sci., 459 (2018) 9.

[33]   L. Wang, B. Cheng, L. Zhang, J. Yu, Small, 17 (2021) 2103447.

[34]   S. Bai, H. Liu, J. Sun, Y. Tian, S. Chen, J. Song, R. Luo, D. Li, A. Chen, C. C. Liu, Appl. Surf. Sci., 338 (2015) 1.

[35]   X. Sun, S. Wang, C. Shen, X. Xu, ChemCatChem, 8 (2016) 2289.

[36]   W. Zhou, N. Umezawa, R. Ma, N. Sakai, Y. Ebina, K. Sano, M. Liu, Y. Ishida, T. Aida, T. Sasaki, Chem. Mater., 30 (2018) 6449.

[37]   M. R. S. Joice, T. M. David, P. Wilson, J. Phys. Chem. C, 123 (2019) 27448.

[38]   P. Kaur, S. Kaur, D. Arora, K. Asokan, D. P. Singh, RSC Adv., 9 (2019) 20536.

[39]   E. M. Samsudin and S. B. Abd Hamid, Appl. Sur. Sci., 391 (2017) 326.

[40]   Y. Zhang and X. Xu, ACS omega, 5 (2020) 15344.

[41]   Y. Lu, J. Zhang, F. Wang, X. Chen, Z. Feng, C. Li, ACS Appl. Energy Mater., 1 (2018) 2067.

[42]   B. N. Nunes, C. Haisch, A. V. Emeline, D. W. Bahnemann, A.O.T. Patrocinio, Catal. Today, 326 (2019) 60.

[43]   R. Ma, Y. Kobayashi, W. J. Youngblood, T. E. Mallouk, J. Mater. Chem., 8 (2008) 5982.

[44]   G. B. Saupe, C. C. Waraksa, H. N. Kim, Y. J. Han, D. M. Kaschak, D. M. Skinner, T. E. Mallouk, Chem. Mater., 12 (2008) 1556.

[45]   R. Abe, M. Hara, J. N. Kondo, K. Domen, K. Shinohara, A. Tanaka, Chem. Mater., 10 (1998) 1647.

[46]   A. L. Shiguihara, M. A. Bizeto, V. R. Constantino, J. Braz. Chem. Soc., 21 (2010) 1366.

[47]   M. A. Bizeto, F. Leroux, A. L. Shiguihara, M. L. A. Temperini, O. Sala, V. R. L. Constantino, J. Phys. Chem. Solids, 71 (2010) 560.

[48]   E. C. C. Souza, J. Phys. Chem. C, 123 (2010) 24426.

[49]   B. N. Nunes, D. W. Bahnemann, A. O. T. Patrocinio, ACS Appl. Energy Mater., 4 (2021) 3681.

[50]   R. B. Shinde, N. S. Padalkar, S. V. Sadavar, S. B. Kale, V. V. Magdum, Y. M. Chitare, S. P. Kulkarni, U. M. Patil, V. G. Parale, H. H. Park, J. L. Gunjakar, J. Hazard. Mater., 432 (2022) 128734.

[51]   E. A. Skryleva, I. V. Kubasov, P. V. Kiryukhantsev-Korneev, B. R. Senatulin, R. N. Zhukov, K. V. Zakutailov, M. D. Malinkovich, Y. N. Parkhomenko, Appl. Surf. Sci., 389 (2016) 387.

[52]   Y. H. Chin, J. C. Sin, S. M. Lam, Mater. Lett., 216 (2018) 8.

[53]   Y. I. Kim, S. J. Atherton, E. S. Brigham, T. E. Mallouk, J. Phys. Chem., 97 (1993) 11802.

CHAPTER-IV

Synthesis and Characterization of WO$_3$-titanate-NS Heterostructure Thin Films by CBD: Application in Photocatalytic Dye Degradation

CHAPTER IV

Synthesis and Characterization of WO$_3$-titanate-NS Heterostructure Thin Films by CBD: Application in Photocatalytic Dye Degradation

4.1. Introduction:

Though photocatalytic oxidation of diverse organic compounds using semiconductor photocatalysts has been regarded as an environmentally friendly process, it has certain limitations. Numerous semiconductor oxides are recognized as potential photocatalysts due to their nontoxicity, photo-corrosion stability, and well-developed electronic structure [1-4]. However, their performance is limited due to the rapid recombination rate of photogenerated electron-hole pairs, unsuitable band positions, and wide bandgap (>3.2 eV) energy [5-9].

Various narrow-band gap photocatalysts are tested as visible-light active photocatalysts to utilize the maximum solar spectrum. However, such photocatalysts suffer from limited efficiency and photostability due to their inappropriate band position, low surface area, crystal morphology, and nonoptimized pore structure. Tungsten oxide (WO₃) is a representative visible light active (band gap: 2.4 to 2.8 eV) semiconductor photocatalyst with a tunable crystal structure and suitable band positions for the oxidation of water molecules [10, 11]. The photocatalytic activity of WO₃ can be further increased by coupling it with other semiconductor nanostructures.

Recently researched exfoliated 2D titanate-NS derived from the soft chemical exfoliation of layered cesium titanate ($Cs_xTi_{2-x/4}\square_{x/4}O_4$; $\square$=vacancy) have gained more attention due to their ultrathin thickness, highly anisotropic structure, negative surface charge, and high photocatalytic activity [12, 13]. 2D titanate-NS can be regarded as a highly useful candidate for coupling due to most of the constituent ions residing on its surface, that leading to a remarkably modified and intimately coupled electronic structure [14-16]. Such titanate-NS can be a useful platform for growing narrow-band gap WO₃ photocatalysts to form strongly coupled titanate-NS-WO₃ (TiW) heterostructure photocatalysts.

Various methods have been explored for the deposition of WO₃. The CBD method is highly advantageous for WO₃ deposition. Its advantages include large-area deposition, high surface area morphologies, low operating temperatures, low cost, and ambient deposition conditions. In addition, pinhole-free and uniform coating on any conducting and non-conducting substrates is obtained [17-19]. Thus, CBD-deposited WO₃ can give a nanocrystalline structure, high surface area, high-surface-area morphologies, mesoporous structure, tunable band gap, etc.

Here in this chapter, strongly coupled 2D titanate nanosheets-tungsten oxide (TiW) heterostructure thin films are synthesized and used for visible-light-driven photooxidation of MB and Rh B dyes. In the obtained TiW heterostructure thin films, the chemically grown WO_3 nanoplates are coated on the EPD-deposited titanate-NS thin films. The obtained heterostructure thin films are denoted as TiW-C thin films. The visible-light-induced photocatalytic activity of pristine WO_3, pristine titanate-NS, and TiW-C heterostructure thin films is investigated for the degradation of organic molecules such as MB and Rh B.

4.2 Synthesis and characterization of TiW-C heterostructure thin films:

4.2.1 Experimental details:

4.2.1.1 Materials:

TiO_2, Cs_2CO_3, HCl, TBAOH, C_2H_5OH, sodium tungstate dihydrate ($Na_2WO_4.H_2O$), oxalic acid ($H_2C_2O_4$), MB, and Rh B were purchased from Sigma-Aldrich and used without purification.

4.2.1.2 Synthesis of titanate-NS thin films:

The synthesis of exfoliated titanate-NS and titanate-NS thin films was similar to as discussed in **Chapter 3, sections 3.2.1.2** and **3.2.1.3**, respectively.

4.2.1.3 Synthesis of WO₃ thin film by CBD method:

The narrow band gap WO_3 thin film was deposited on a glass substrate using the CBD method. Initially, an aqueous solution of 0.1 M $Na_2WO_4.2H_2O$, 0.25 M $C_2H_2O_4$, and 2 M HCl were prepared. The 10 mL of 0.25 M of $C_2H_2O_4$ was added in 30 mL of 0.1 M $Na_2WO_4.2H_2O$ to complex it and then its pH was adjusted to 1.5 with dropwise addition of 2 M HCl. The well-cleaned glass substrates were suspended in the above solution. The deposition bath was maintained at 80 °C for 2 hours.
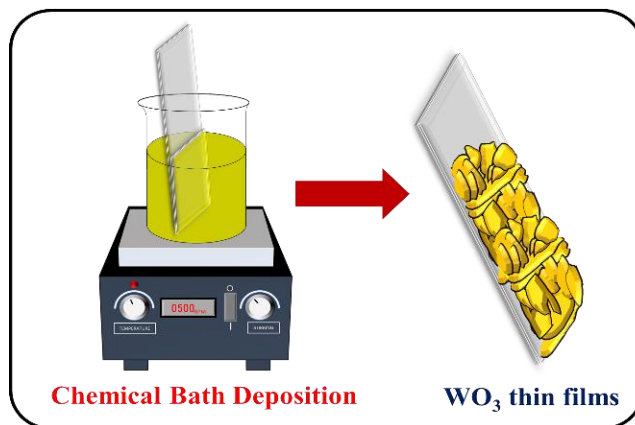
Fig. 4.1. Schematic representation of WO_3 thin film synthesis.

The schematic representation of the WO_3 thin film synthesized by the CBD process is shown in **Fig. 4.1**. The deposited WO_3 thin films were thoroughly removed from the bath, washed with DDW, and dried at room temperature. The deposited WO_3 thin film is denoted as pristine WO_3.

4.2.1.4 Synthesis of TiW-C heterostructure thin films:

The narrow band gap WO_3 was deposited over the EPD-deposited titanate-NS thin films using the CBD method. The experimental parameters for preparing the CBD bath were kept similarly, as discussed in **section 4.2.1.3**. The pre-deposited titanate-NS (titanate-NS-5, titanate-NS-10, and titanate-NS-15) thin films were placed in the above deposition bath. The deposition bath was maintained at 80 °C for 30 minutes. The deposited TiW-C heterostructure thin films were thoroughly removed from the bath, washed with DDW, and dried at room temperature. The schematic representation of the TiW-C heterostructure thin film synthesis is shown in **Fig. 4.2**. The TiW-C heterostructure thin films deposited on titanate-NS-5, titanate-NS-10, and titanate-NS-15 are denoted as TiW-5-C, TiW-10-C, and TiW-15-C, respectively.
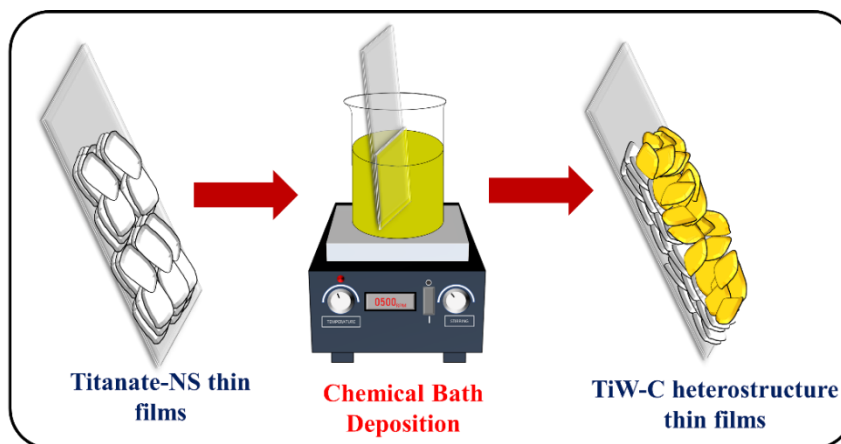
Fig. 4.2. Schematic representation of TiW-C heterostructure thin film synthesis.

4.2.1.5 Material characterizations:

The pristine WO_3, titanate-NS, and TiW-C heterostructure thin films were characterized by various physicochemical characterization techniques similar to those described in **Chapter 3, section 3.2.1.4.**

4.2.1.6 Experimental setup for dye degradation:

The photocatalytic activities of the prepared sample were studied for photooxidation of dyes (MB and Rh B) under the exposure of visible light (λ>420 nm, light intensity= 100 mW cm^{-2}). The initial concentrations of MB and Rh B were 50 and 20 µM, respectively. In a typical experiment, a prepared thin film was placed vertically

in the quartz cell filled with 3 mL of dye solution. Before irradiation by light, the dye solution was allowed to be equilibrated with target molecules in the dark for 30 min to ensure adsorption/desorption equilibrium of the dye molecules on the catalyst surface. All the photocatalytic tests were carried out at room temperature. During the photocatalytic tests, the light was calibrated by passing through the IR filter followed by AM 1.5G and cutoff (λ=420 nm) filters. The calibrated light was focused on the photocatalytic reactor. The prepared thin film was withdrawn intermittently during the illumination, and the change in the concentration of the dye solution was analyzed using a UV-vis spectrophotometer. The concentration change of MB and Rh B was monitored by measuring the absorbance at characteristic wavelengths of 665 and 554 nm, respectively. From the analysis of absorption spectra, photocatalytic degradation efficiency was determined by using the following equation [20];

$$R = \{(C_0 - C_t)/ C_0\} \times 100 \qquad (4.1)$$

where C_0 and C_t denoted absorbance of target dye molecules at times t=0 and t=t, respectively.

Also, the pseudo-first-order kinetic model is used to study degradation kinetics through the following equation [21];

$$\ln (C_0/C_t) = k*t \qquad (4.2)$$

where k, C_0 and C_t represent the rate constant (min^{-1}), absorbance at times t=0 and t=t, respectively.

4.2.2 Results and Discussion:

4.2.2.1 XRD study:

The crystal structure of pristine WO₃, titanate-NS, and TiW-C heterostructure thin films was examined using the XRD technique. The XRD patterns of pristine WO₃, titanate-NS and TiW-C heterostructure thin films are plotted in **Fig. 4.3**. As shown in **Fig. 4.3(i)**, WO₃ thin film displays a series of sharp Bragg's reflections that are well-matched with (020), (111), (040), (200), (131), (202), (222), and (113) planes of orthorhombic (Pmnb) monohydrate layered WO₃·H₂O phase (JCPDS card no. 01-084-0886). The estimated lattice parameters a=5.19 Å, b=10.76 Å, and c=5.16 Å which are in good agreement with the monohydrate layered WO₃·H₂O phase [22]. The XRD pattern of EPD-deposited titanate-NS-10 thin film from **Chapter 3, Fig 3.3,** is plotted as **Fig. 4.3(ii)** for comparison. The XRD analysis of pristine titanate-NS is discussed in **Chapter 3, section 3.2.2.1**.
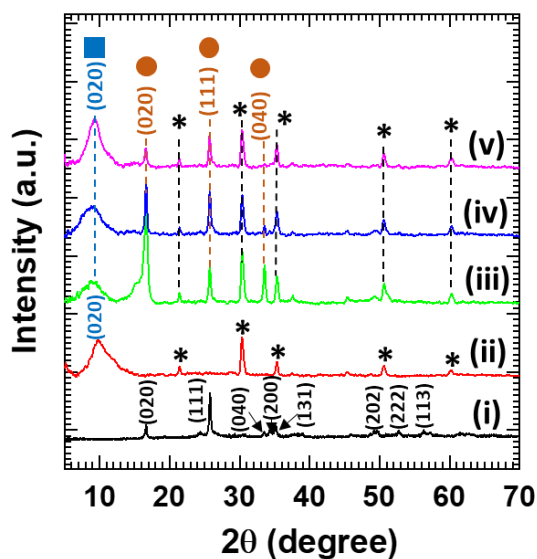
Fig. 4.3. XRD patterns of (i) WO$_3$, (ii) titanate-NS, (iii) TiW-5-C, (iv) TiW-10-C, and (v) TiW-15-C heterostructure thin films.

After the deposition of WO$_3$ over titanate-NS thin film, all TiW-C heterostructure thin films exhibit several diffraction peaks associated with lepidocrocite-type titanate-NS, orthorhombic WO$_3$, and ITO substrate. Present XRD features corresponding to the titanate-NS and WO$_3$ clearly indicate the growth of orthorhombic WO$_3$ over electrophoretically deposited titanate-NS thin films. The TiW-C heterostructure thin films exhibit a broad diffraction peak centred at 10º, suggesting the titanate nanosheets are restacked layer-by-layer on the substrate and form the oriented titanate-NS thin film. This first peak is assigned to the (020) plane of lepidocrocite-type titanate-NS with orthorhombic symmetry having a basal spacing of 0.88 nm [23]. In addition, several diffraction peaks (020), (111), and (020) are well-matched with the orthorhombic WO$_3$·H$_2$O phase [22]. The peaks marked by '*' correspond to the ITO substrate. The diffraction peaks corresponding to titanate-NS thin film indicate the intact layer-by-layer stacking with the high mechanical and chemical stability of titanate-NS thin film.

4.2.2.2 FT-IR study:

The chemical bonding nature of TiW-C heterostructures compared to the pristine WO$_3$ and titanate-NS thin films were studied using FT-IR spectroscopy, as shown in **Fig. 4.4**. The pristine WO$_3$ displays the absorption peaks ν1 (480 cm^{-1}) and ν2 (625 cm^{-1}) which are ascribed to the metal-oxygen stretching vibration (W-O-W). The absorption peaks ν3 (880 cm^{-1}) and ν4 (943 cm^{-1}) are assigned to the O-W-O and W=O vibrations, respectively [24-26]. The absorption peaks ν5 (1630 cm^{-1}) and ν6 (3415 cm^{-1}) are

attributed to the bending vibrational modes of water molecules and stretching vibrations of the O-H groups, respectively [27-28]. These characteristic absorption peaks indicate the formation of the WO_3 hydrate phase. The FT-IR spectrum of EPD-deposited titanate-NS-10 thin film from **Chapter 3, Fig 3.4,** is plotted as **Fig. 4.4(ii)** for comparison. The FT-IR analysis of pristine titanate-NS is discussed in **Chapter 3, section 3.2.2.2**.

Fig. 4.4. FT-IR spectra of (i) WO_3, (ii) titanate-NS, (iii) TiW-5-C, (iv) TiW-10-C, and (v) TiW-15-C heterostructure thin films.

Moreover, the TiW-C heterostructure thin films commonly display absorption peaks associated with WO_3 and titanate-NS. The absorption peak $\nu 11$ (483 cm^{-1}) is ascribed to the W-O-W stretching vibration. The absorption peak $\nu 12$ (625 cm^{-1}) is assigned to the stretching modes of Ti-O [29]. The absorption peaks $\nu 13$ (883 cm^{-1}) and $\nu 14$ (946 cm^{-1}) are assigned to the O-W-O and W=O vibrations, respectively. The other sharp bands $\nu 15$ (1634 cm^{-1}) and broad absorption band $\nu 16$ (3420 cm^{-1}) correspond to the bending vibrational modes of water molecules and stretching vibrations of the O-H groups, respectively [26-28]. The peaks related to metal-oxygen vibrations are broad and carry minute shoulder peaks due to superpositions of WO_3 and titanate-NS IR peaks. The broadening of these peaks can be regarded as an indicator of strong electronic coupling and hybridization between the WO_3 and titanate-NS layers. These IR characteristics indicate the successful formation of the TiW-C heterostructure.

4.2.2.3 Micro-Raman study:

The chemical bonding character of the WO_3, titanate-NS, and TiW-C heterostructures was further examined with Raman spectroscopy, as shown in **Fig. 4.5**. The pristine WO_3 shows weak intensity peaks P1 (188 cm^{-1}) and P2 (234 cm^{-1}) are

ascribed to the lattice vibrations of WO_3 and bending vibrations of W-O-W bond, respectively. The broad peak P3 (635 cm^{-1}) and sharp peak P4 (944 cm^{-1}) are ascribed to the stretching vibrations of O-W-O and terminal W=O bonds, respectively [30-32]. These typical Raman peaks displayed by WO_3 are the characteristics of the WO_3 hydrates phase. The micro-Raman spectrum of EPD-deposited titanate-NS-10 from **Chapter 3, Fig 3.5,** is plotted as **Fig. 4.5(ii)** for comparison. The micro-Raman analysis of pristine titanate-NS is discussed in **Chapter 3, section 3.2.2.3**.
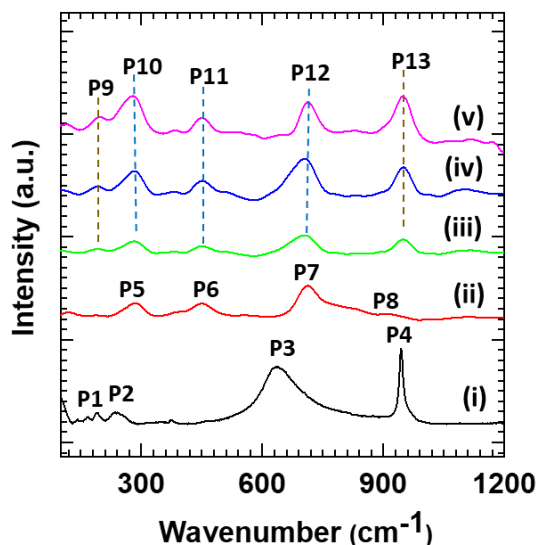
Fig. 4.5. Micro-Raman spectra of (i) WO_3, (ii) titanate-NS, (iii) TiW-5-C, (iv) TiW-10-C, and (v) TiW-15-C heterostructure thin films.

In addition, the TiW-C heterostructure thin film displays the characteristic Raman peaks corresponding to the WO_3 (P9 and P13) and titanate-NS (P10, P11 and P12) thin films. The TiW-C heterostructure thin film displays the Raman peaks P9 and P13, which correspond to the WO_3 lattice vibrations and the stretching mode of terminal W=O bonds in WO_3 thin films. In addition, the Raman peak P10 is assigned to *Ag* symmetric vibrations originating from the splitting of the degenerate mode of the TiO_6 octahedron. The Raman peaks P11 and P12 are associated with stretching vibrations of Ti-O bonds in TiW-C heterostructure thin films [33, 34]. Moreover, upon the hybridization, peaks P12 and P13 broaden due to the superposition of WO_3 and titanate-NS peaks. These characteristics Raman features related to WO_3 and titanate-NS present in TiW-C heterostructure indicate successful formation of the TiW-C heterostructure with intactness of titanate-NS lattice during heterostructure formation.

4.2.2.4 FE-SEM study:

The microstructural surface and stacking structure of TiW-C heterostructure compared to the pristine WO_3 and titanate-NS thin films were studied using FE-SEM analysis, as shown in **Fig. 4.6**. The surface microstructural analysis and cross-section of pristine titanate-NS is discussed in **Chapter 3, section 3.2.2.4**.
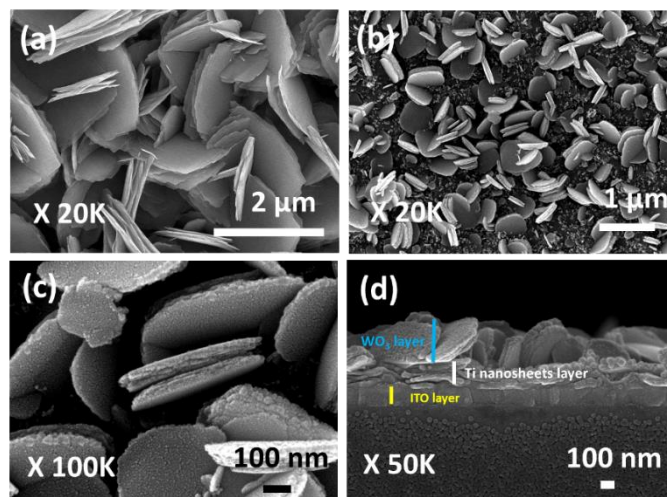
Fig. 4.6. FE-SEM images of (a) WO_3 and (b, c) TiW-10-C heterostructure thin films. The cross-sectional FE-SEM image of (d) TiW-10-C heterostructure thin film.

The chemically grown WO_3 thin film displays vertically grown interlocked WO_3 nanoplates with a dimensional length of 1500 nm, breadth of 750 nm, and thickness of 60 nm [35]. On the other hand, the TiW-10-C heterostructure thin film displays WO_3 nanodiscs vertically grown on titanate-NS. The WO_3 nanodiscs display an average nanodiscs length, width, and thickness of 650 nm, 400 nm, and 70 nm, respectively. The cross-section view of TiW-10-C heterostructure thin film clearly displays separate material layers. The bottom layers correspond to the ITO layer grown on glass. The top layers are composed of WO_3 nanodiscs grown on horizontally arranged titanate-NS. The vertical growth of WO_3 nanodiscs on titanate-NS leads to a high surface area morphology. Such a heterostructure can enable intimate electronic coupling between the titanate-NS and WO_3, which is highly beneficial in special electron-hole pair separation for solar-assisted photo-functional applications. A similar type of morphology is generally observed for 2D nanosheet-based heterostructures, which is advantageous for various applications [36, 37].

4.2.2.5 EDS study:

The distribution of constituent elements in all materials was probed with EDS and elemental mapping analysis, represented in **Fig. 4.7** and **Fig. 4.8**, respectively.
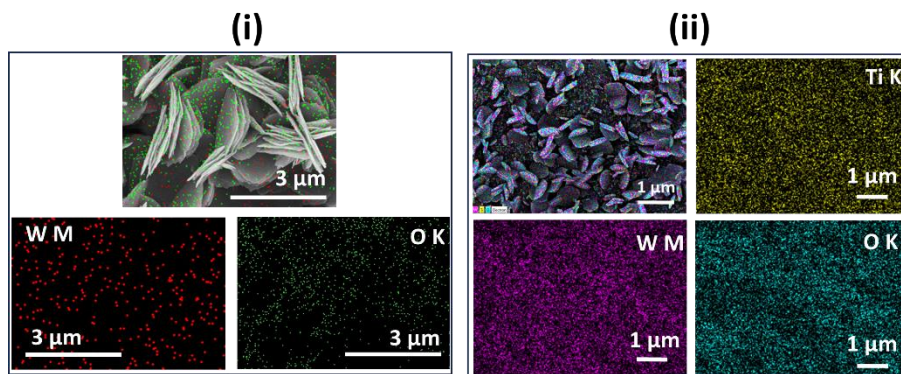
Fig. 4.7. FE-SEM images along with EDS-elemental mapping of (i) WO_3 and (ii) TiW-10-C heterostructure thin films.
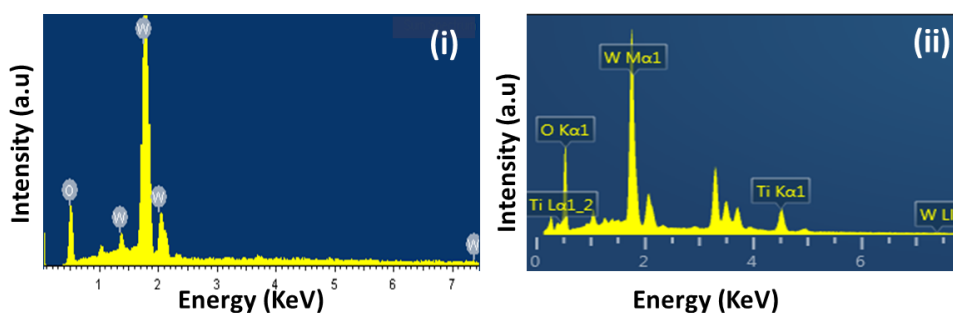
Fig. 4.8. EDS spectra of (i) WO_3 and (ii) TiW-10-C heterostructure thin films.

The atomic percentage ratio of Ti/W for TiW-10-C heterostructure thin films is 1. The TiW-C heterostructure thin film shows a uniform distribution of tungsten (W), titanium (Ti), and oxygen (O) elements across the elemental mapping area, demonstrating the homogeneous growth of WO_3 on the surface of titanate-NS thin films.
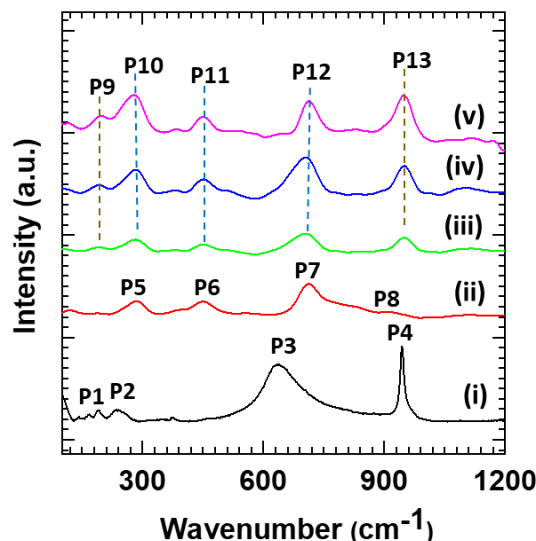
4.2.2.6 XPS study:
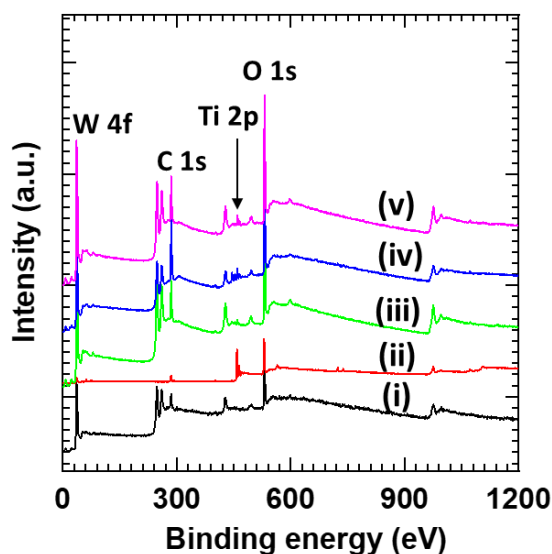
Fig. 4.9. XPS survey spectra of (i) WO_3, (ii) titanate-NS, (iii) TiW-5-C, (iv) TiW-10-C, and (v) TiW-15-C heterostructure thin films.

The oxidation states of pristine WO_3, titanate-NS, and TiW-C heterostructure thin films were probed using XPS analysis. The XPS survey spectrum of EPD-deposited titanate-NS from **Chapter 3, Fig 3.7,** is plotted as **Fig. 4.9(ii)** for comparison. The survey XPS spectrum analysis of pristine titanate-NS is discussed in **Chapter 3, section 3.2.2.5**. As shown in **Fig. 4.9**, the survey XPS spectra of pristine WO_3, titanate-NS, and TiW-C heterostructure thin films show characteristic XPS features at the W, Ti, and O binding energies. The presence of these XPS characteristics underscores the existence of W, Ti, and O in the deposited thin films.
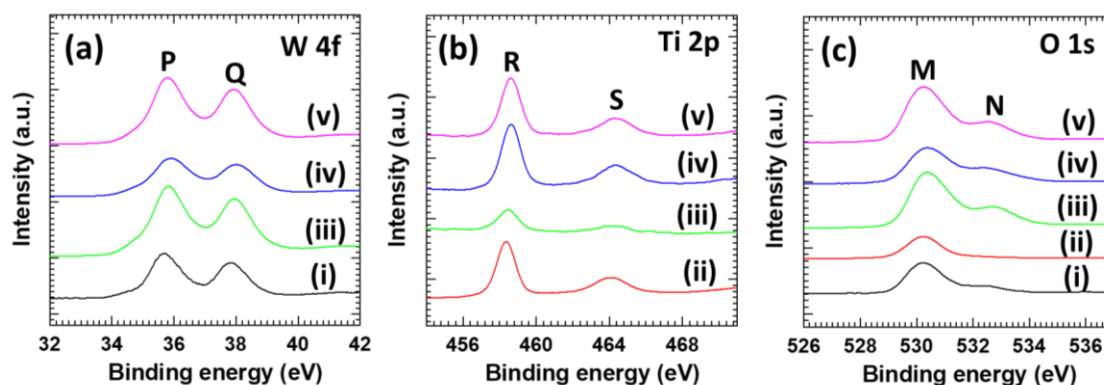
Fig. 4.10. (a) W 4f, (b) Ti 2p, and (c) O 1s core-level XPS spectra of (i) WO_3, (ii) titanate-NS, (iii) TiW-5-C, (iv) TiW-10-C, and (v) TiW-15-C heterostructure thin films.

The high-resolution core-level spectra of W 4f, Ti 2p, and O 1s are shown in **Fig. 4.10**. As shown in **Fig. 4.10(a)**, the high-resolution W 4f core-level spectra, which are only discernable for pristine WO_3 and TiW-C heterostructure thin films, show spectral features P (35.7 eV) and Q (37.8 eV) assigned to the spin-orbit splitting of W $4f_{7/2}$ and W $4f_{5/2}$, respectively. The observed spectral features are typically seen for W-O bond configuration, indicating W^{6+} in WO_3 [38]. The core-level Ti 2p and O 1s XPS spectra of titanate-NS from **Chapter 3, Fig. 3.8**, are plotted again in **Fig. 4.10** as plots **Fig. 4.10 (b(ii))** and **Fig. 4.10(c(ii))** for comparison. The XPS spectra analysis of Ti 2p and O 1s are discussed in **Chapter 3**, **section 3.2.2.5**. The high-resolution Ti 2p spectra of titanate-NS and TiW-C heterostructure thin films **(Fig. 4.10(b))** show two spectral features, R (458.3 eV) and S (464.1 eV), which are attributed to spin-orbit splitting into Ti $2p_{3/2}$ and Ti $2p_{1/2}$, respectively. These features are typical characteristics of Ti^{4+} in pristine titanate-NS and TiW-C heterostructure thin film [39]. Furthermore, the O 1s spectra of pristine WO_3, titanate-NS, and TiW-C heterostructure thin films plotted in **Fig. 4.10(c)** display a broad peak M (530.2 eV), indicating the presence of oxygen in the metal oxide. Moreover, pristine WO_3 and TiW-C heterostructure thin films show peaks

N (532.5 eV) corresponding to a hydroxyl group (-OH group) originating from water molecules [40, 41]. The observed XPS features underscore strong evidence of the presence of W^{6+} and Ti^{4+} states of W and Ti, respectively, which confirms the formation of TiW-C heterostructure. The presence of Ti and W in Ti^{4+} and W^{6+} oxidation states in the TiW-C heterostructure thin films indicates the effective hybridization between the titanate-NS and WO_3.

4.2.2.7 UV-vis DRS and energy band structure study:
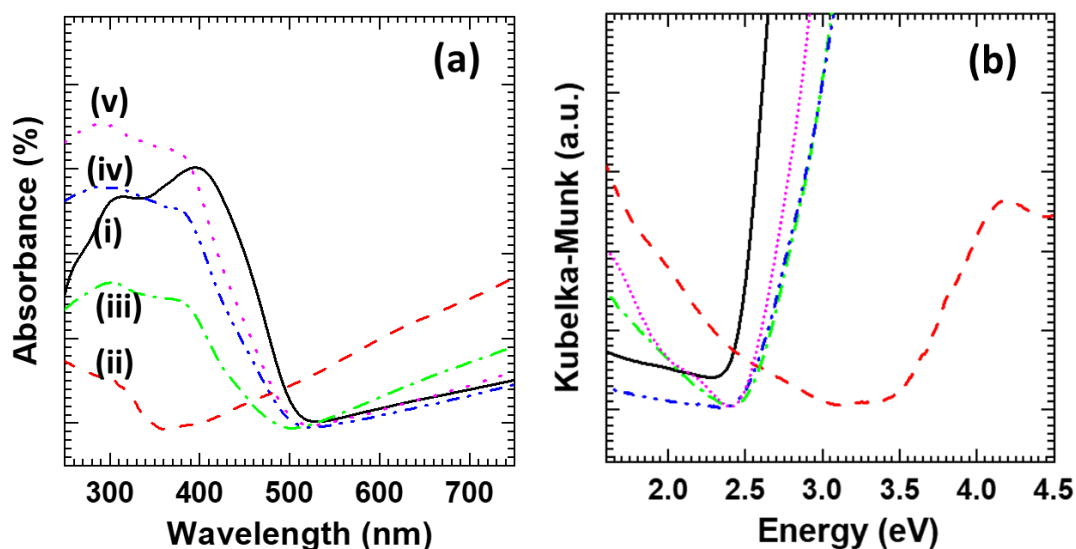
Fig. 4.11. (a) UV-vis absorbance spectra obtained from UV-vis DRS and (b) UV-vis DRS (plotted as Kubelka-Munk function of reflectance, R) of (i) WO_3 (solid lines), (ii) titanate-NS (dashed lines), (iii) TiW-5-C (dash-dotted lines), (iv) TiW-10-C (dash-dot-dotted lines), and (v) TiW-15-C (dotted lines) heterostructure thin films.

The UV-vis DRS was used to probe the optical properties of pristine WO_3, titanate-NS, and TiW-C heterostructure thin films. The UV-vis DRS absorbance spectrum of EPD-deposited titanate-NS from **Chapter 3, Fig 3.9**, is plotted as **Fig. 4.11(ii)** for comparison. The UV-vis DRS analysis of pristine titanate-NS is described in **Chapter 3, section 3.3.2.6**. As shown in **Fig. 4.11**, pristine WO_3 thin film shows prominent absorption of light in the visible region with a bandgap energy of 2.33 eV. The WO_3 is an indirect band gap material with an electronic structure comprising a VB and CB of O 2p and W 5d, respectively [42]. On the other hand, titanate-NS thin film shows remarkable absorption in the UV region with a bandgap energy of 3.34 eV. The electronic structure of titanate-NS comprises a VB and CB mainly composed of O 2p and Ti 3d orbitals, respectively [43, 44]. Interestingly, upon the heterostructure formation, the resultant TiW-C heterostructure thin films display significant absorption

in the visible region with slight shifting of absorption edge towards higher wavelength, clearly underscoring the major contribution from the top WO_3 layer and efficient electronic coupling between titanate-NS and WO_3. The TiW-C heterostructure thin films absorb visible light in the wavelength ranges from 500 to 520 nm, corresponding to the bandgap energies between 2.48 to 2.38 eV. The bandgap energies determined from the Kubelka-Munk function are summarized in **Table 4.1**. The strong visible light absorption ability of TiW-C heterostructures makes them potential candidates for visible-light-driven photocatalysis applications.

Thin film photocatalyst	Band gap energy (eV)
WO_3	2.33
titanate-NS	3.34
TiW-5-C	2.48
TiW-10-C	2.42
TiW-15-C	2.38

Table 4.1. Synthesized photocatalyst thin films and their estimated band gap energies.

Based on the bandgap energy, the CB and VB potentials of the WO_3 thin films can be estimated using equations 3.2 and 3.3. Therefore, the positions of VB and CB of pristine WO_3 with respect to the NHE are located at 3.24 eV and 0.91 eV, respectively. The estimated VB and CB positions of titanate-NS are at 2.23 eV and -1.11 eV, respectively (**Chapter 3, section 3.2.2.6**). The schematic of the electronic band edge potentials of WO_3 and titanate-NS thin films is shown in **Fig. 4.12**.
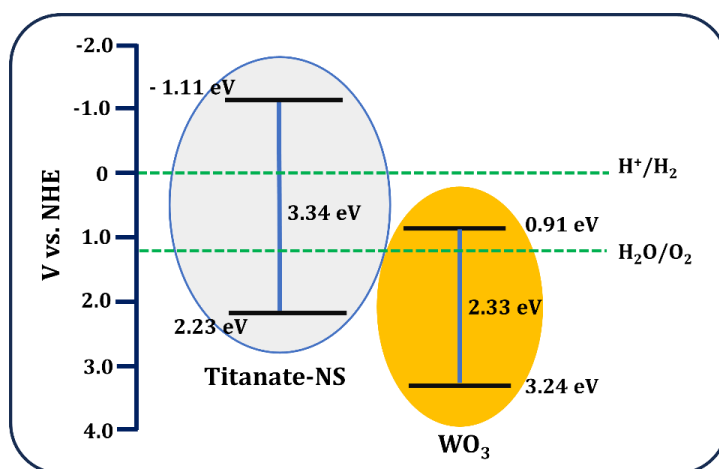
Fig. 4.12. Schematic representation for the energy band structure of titanate-NS and WO_3 thin films.

4.3 Photocatalytic Activity:

4.3.1 Dye degradation study:
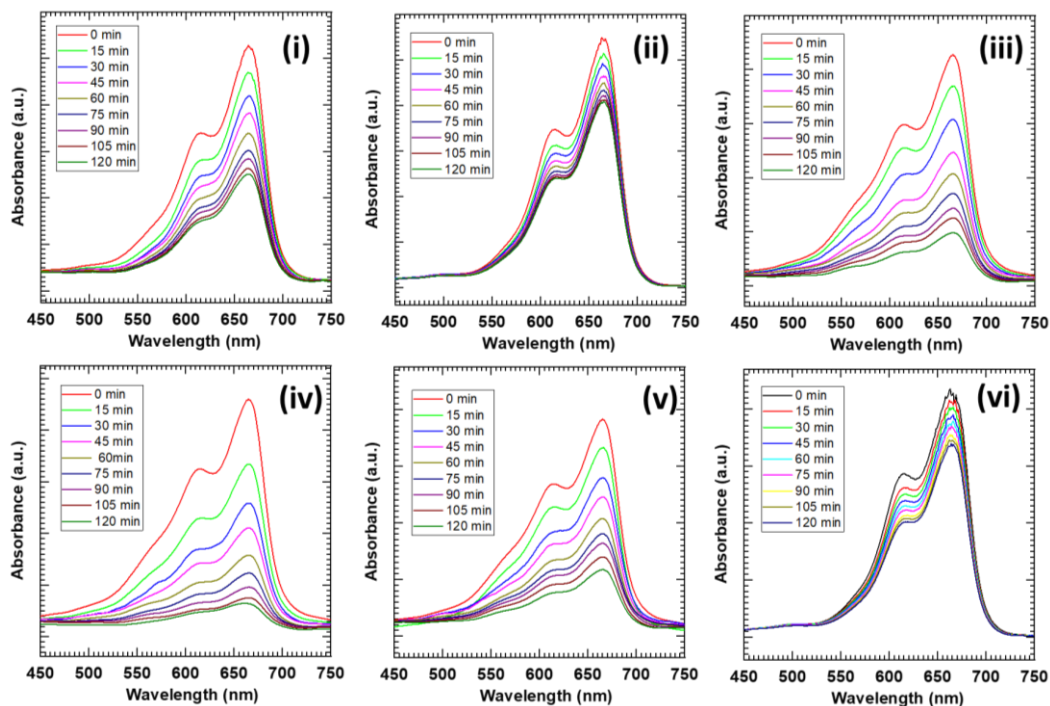
Fig. 4.13. Absorption spectra of MB for (i) WO$_3$, (ii) titanate-NS, (iii) TiW-5-C, (iv) TiW-10-C, (v) TiW-15-C heterostructure thin films, and (vi) without thin film.
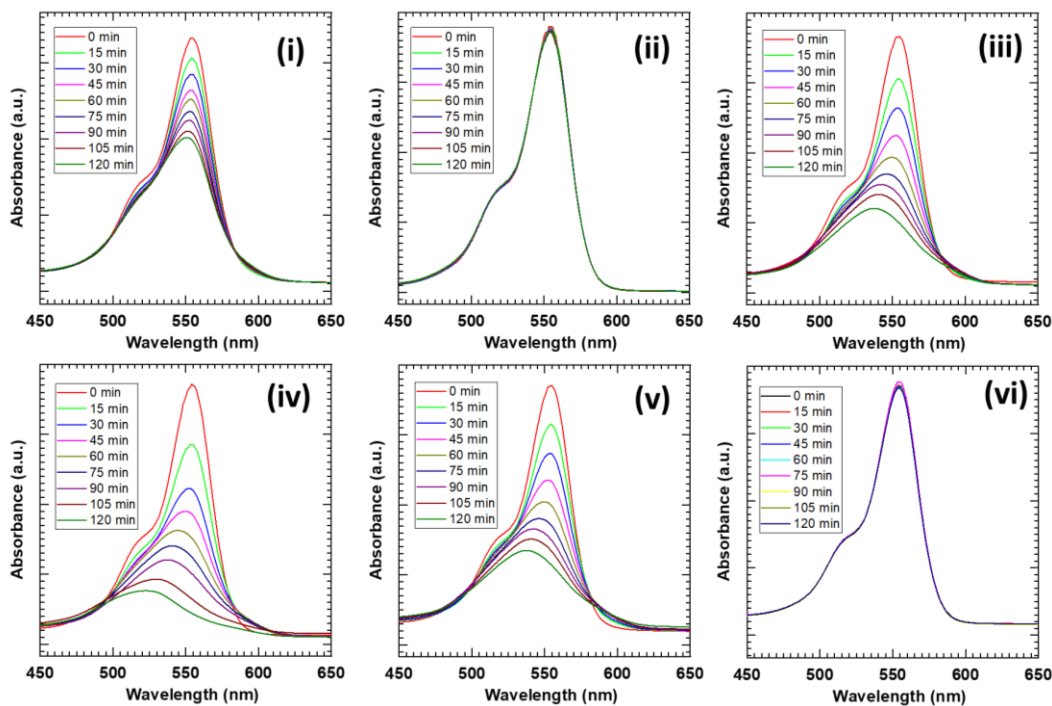
Fig. 4.14. Absorption spectra of Rh B for (i) WO$_3$, (ii) titanate-NS, (iii) TiW-5-C, (iv) TiW-10-C, (v) TiW-15-C heterostructure thin films, and (vi) without thin film.
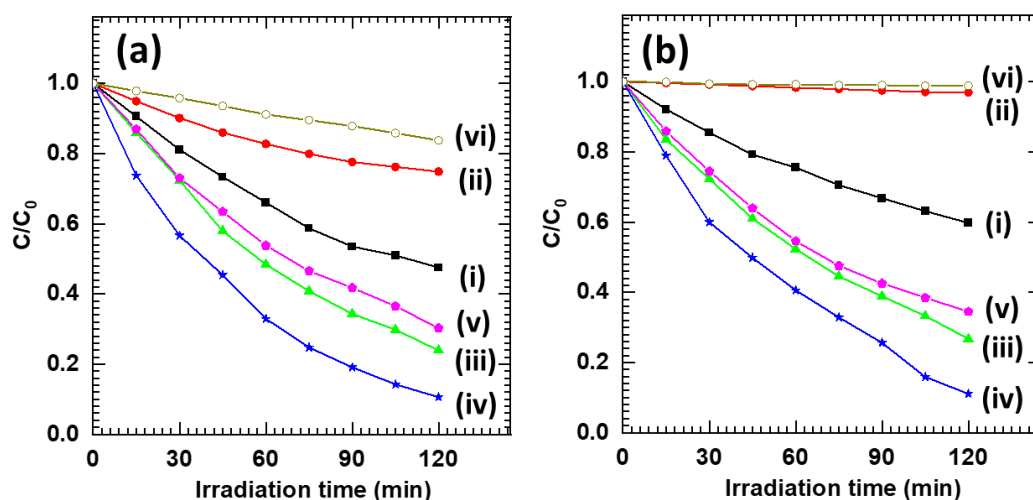
Fig. 4.15. Photocatalytic degradation performance of MB (a) and Rh B (b) for (i) WO₃, (ii) titanate-NS, (iii) TiW-5-C, (iv) TiW-10-C, (v) TiW-15-C heterostructure thin films and (vi) without thin film.

The photocatalytic activity of TiW-C heterostructure thin films was examined by monitoring the time-dependent photodegradation of MB and Rh B under visible light illumination (λ>420 nm) and compared with pristine WO₃ and titanate-NS thin films. The UV-vis absorption spectra of MB and Rh B are shown in **Fig. 4.13** and **4.14**, respectively. The absorption peak intensity of MB and Rh B at a characteristic wavelength of 665 and 554 nm decreases with visible-light-irradiation time, indicating that both the dye molecules are degraded. As shown in **Fig. 4.15 (a-b)**, pristine WO₃ and TiW-C heterostructure thin films are photocatalytically active for MB and Rh B degradation when exposed to visible light. The pristine WO₃ exhibited significant photocatalytic activity for both MB and Rh B dyes photodegradation, which is attributed to its high surface area, nanoplate morphology, and low band gap. Conversely, the titanate-NS thin film shows a negligible photodegradation performance due to its wide band gap energy, highlighting its visible-light inactivity. All the TiW-C heterostructure thin films display significantly improved photocatalytic activity due to hybridization. Among the TiW-C heterostructure thin films deposited at various deposition times, the TiW-10-C heterostructure thin film shows a maximum MB and Rh B photodegradation performance of 91 and 89% in 120 min, respectively, which is superior to the pristine WO₃ (MB: 55% and Rh B: 41%) and titanate-NS (MB: 24% and Rh B: 3%) thin films. Further, it decreases for TiW-15-C heterostructure thin film due to the peel-off of the loosely bound WO₃ layer from the film surface. Such peel-off of deposits is commonly observed for the chemically deposited thin films. The exceptional photocatalytic

degradation performance of TiW-C heterostructure thin films can be attributed to the strong visible-light harvesting ability, high surface area, porous nanoplate morphology, and reduced electron-hole pair recombination via effective electronic coupling between hybridized species.

4.3.2 Kinetic study:
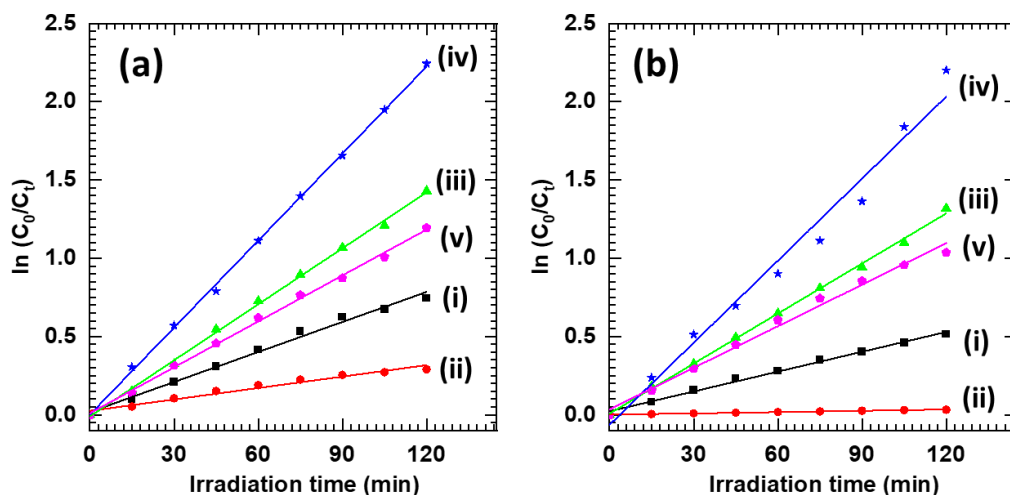
Fig. 4.16. Pseudo-first-order kinetics of MB (a) and Rh B (b) for (i) WO₃, (ii) titanate-NS, (iii) TiW-5-C, (iv) TiW-10-C, and (v) TiW-15-C heterostructure thin films.

Further, the high photocatalytic degradation activity of pristine WO₃, titanate-NS, and TiW-C heterostructure thin films is confirmed by the first-order reaction kinetics. The pseudo-first-order kinetics plot of MB and Rh B is shown in **Fig. 4.16 (a)** and **Fig. 4.16 (b)**, respectively. The rate constant (k) and linear coefficient correlation (R^2) values are given in **Table 4.2**. The TiW-10-C heterostructure thin film exhibits the highest k-value of 0.0185 min^{-1} for MB and 0.0174 min^{-1} for Rh B, confirming the highest photocatalytic activity.

Thin Film	MB		Rh B	
	k (min^{-1})	R^2	k (min^{-1})	R^2
WO₃	0.0063	0.99	0.0042	0.98
Titanate-NS	0.0024	0.98	0.00027	0.99
TiW-5-C	0.0119	0.99	0.0106	0.99
TiW-10-C	0.0185	0.99	0.0174	0.97
TiW-15-C	0.0097	0.99	0.0088	0.99

Table 4.2. The k and R^2 values of all pristine WO₃, titanate-NS, and TiW-C heterostructure thin films.

The obtained k-values for MB are 2.93 and 7.70 times higher than pristine WO_3 and titanate-NS thin film, respectively. Meanwhile, for Rh B, it is 4.14 and 64 times higher than pristine WO_3 and titanate-NS thin film, respectively. The higher k-value for TiW-C heterostructure is ascribed to the strong visible light harvesting ability, minimal electron-hole pair recombination, high photostability, and effective electronic coupling between hybridized layers. These results highlighted the usefulness of TiW-C heterostructure thin films for photocatalytic degradation of dyes.

4.3.3 Recycling study:
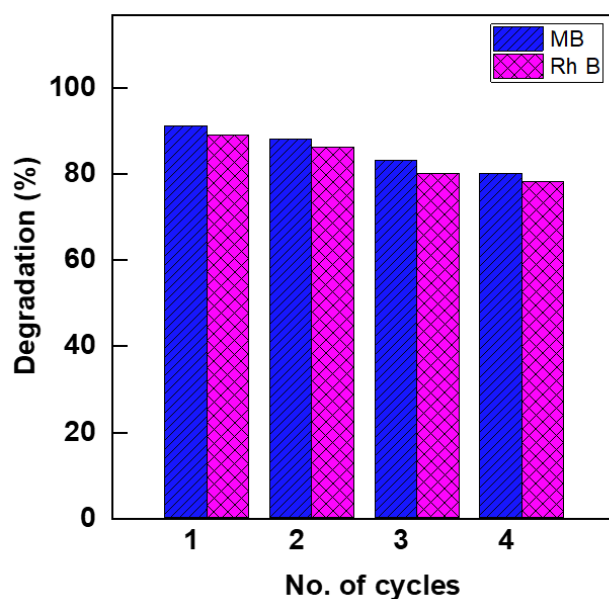
Fig. 4.17. Recyclability study of TiW-10-C heterostructure thin film.

Moreover, the recyclability of the optimized TiW-10-C heterostructure thin film for photocatalyst application is studied for four consecutive cycles of photocatalytic degradation. As represented in **Fig. 4.17**, after four consecutive cycles, TiW-10-C heterostructure thin films retain 80% and 78% of the photocatalytic performance for MB and Rh B, respectively. After the recycling study, the slight decline in performance was attributed to the loss of loosely bound photocatalyst crystals from the film and the adsorption of target organic molecules on the photocatalyst surface.

4.3.4 Photocatalytic degradation mechanism:

The photocatalytic dye degradation mechanism is based on the photogenerated charge separation and migration to the photocatalyst surface. **Fig. 4.18** illustrates the plausible photocatalytic dye degradation mechanism upon exposure to light irradiation. When photons with appropriate energy are incident on the TiW-C heterostructure, electrons from the VB of WO_3 are excited to its CB, forming electron-hole pairs

(equation 4.3). As represented in **Fig. 4.18**, the CB of titanate-NS (-1.11 eV) is more negative than that of WO_3 (0.91 eV) and the VB of WO_3 (3.24 eV) is more positive than that of titanate-NS (2.23 eV) with respect to NHE [45].
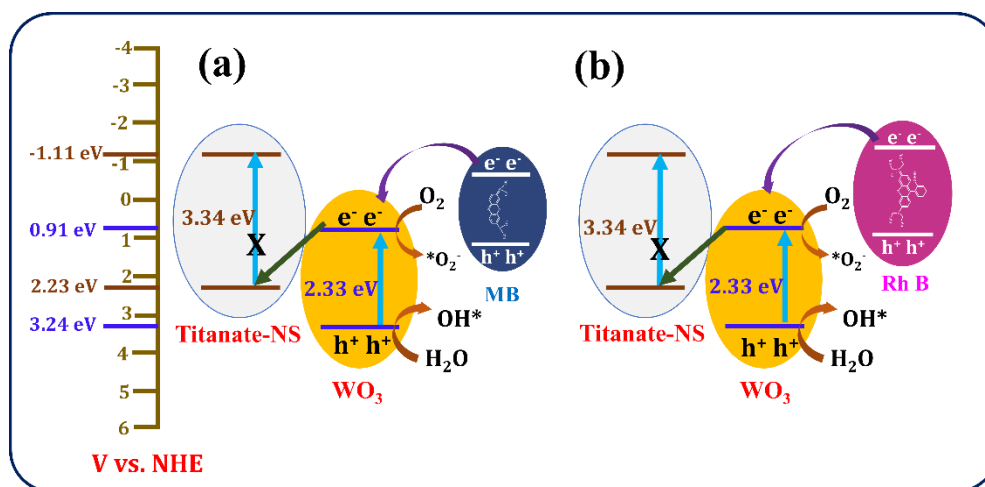
Fig. 4.18. The schematic diagram for plausible photodegradation of (a) MB and (b) Rh B.

The photogenerated electrons from the CB of WO_3 can migrate into the VB of titanate-NS, leading to the spatial separation of electrons and holes. As a result, the lifetime of holes in the VB of WO_3 increases. The holes present in VB of WO_3 react with H_2O species and generate hydroxyl radicals (OH*), whereas superoxide radicals ($^*O_2^-$) are generated when electrons in the CB of WO_3 react with O_2 (equations: 4.4-4.5). Further, the superoxide radical gets protonated, forming hydroperoxyl radicals (HOO*) and then H_2O_2. Finally, H_2O_2 dissociates into OH* radicals, which can break the chain of target organic molecules into non-toxic products (CO_2 and H_2O) (equations: 4.6-4.9) [46, 47].

The generated OH* radicals attack the MB and Rh B, forming different intermediate products and dissociating them into unharmful products. The demethylation reactions can decompose the MB in which the N-C bond between the methyl group and the N atom is broken. Further, it forms various intermediates such as azure A, azure B, and azure C [48]. The Rh B could be decomposed by N-deethylation reaction followed by decarboxylation and deamination, resulting in aromatic compounds such as o-xylene, benzoic acid, and phthalic acid via the chromophore cleavage process. The aromatic compounds finally oxidized into CO_2 and H_2O [49].

$$TiO_2 \text{ NS} - WO_3 \text{ under irradiation } \rightarrow h^+ + e^- \qquad (4.3)$$

$$h^+ + OH^- / H_2O \rightarrow {}^*OH / {}^*OH + H^+ \qquad (4.4)$$

$$O_2 + e^- \rightarrow {}^*O_2^- \tag{4.5}$$

$${}^*O_2^- + H^+ \rightarrow HOO^* \tag{4.6}$$

$$2HOO^* \rightarrow H_2O_2 + O_2 \tag{4.7}$$

$$H_2O_2 \rightarrow 2OH^* \tag{4.8}$$

$$dye + OH^* \rightarrow CO_2 + H_2O \tag{4.9}$$
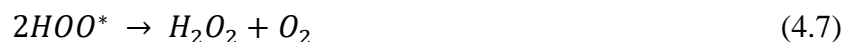
4.4 Conclusions:

In this work, TiW-C heterostructure thin films are synthesized using EPD and CBD methods for photocatalytic degradation of organic molecules under visible light. Initially, WO₃ thin films are deposited using the low-cost CBD method, which shows an orthorhombic crystal structure. The WO₃ thin film displays vertically grown interlocked WO₃ nanoplates morphology with average length, breadth, and thickness of 1500, 750, and 60 nm, respectively. The CBD-deposited WO₃ thin film shows only 55 and 41% degradation in 120 min for MB and Rh B, respectively. On the other hand, EPD-deposited titanate-NS thin film shows the formation of lepidocrocite-type titanate-NS with orthorhombic symmetry. The titanate-NS thin film shows compact morphology with significant absorption in the UV region. The pristine titanate-NS thin film exhibited a degradation performance of 24% for MB and 3% for Rh B in 120 min. The lower performance of titanate-NS is attributed to its visible light inactivity and non-porous morphology. Interestingly, controlling various preparative parameters allows us to coat the WO₃ layer on EPD-deposited titanate-NS thin film. The TiW-C heterostructure thin films show XRD peaks related to titanate-NS and WO₃, confirming the growth of WO₃ on the pre-deposited titanate-NS thin film. The TiW-C heterostructure thin films display prominent absorption in the visible region. The best-optimized TiW-10-C heterostructure thin film demonstrates enhanced visible-light-induced photodegradation performance of 91 and 89% in 120 min for MB and Rh B, respectively. The present experimental study establishes the effectiveness of heterostructure photocatalyst thin films in depressing electron-hole recombination. The present heterostructure approach can effectively employed to synthesize visible light active photocatalysts thin film based on 2D metal oxide nanosheets. This study can be effectively used to synthesize binder-free heterostructure visible-light-active thin film photocatalysts.

4.5 References:

[1]   W. S. Koe, J. W. Lee, W. C. Chong, Y. L. Pang, L. C. Sim, Environ. Sci. Pollut. Res., 27 (2020) 2522.

[2] W. A. Mohamed, H. T. Handal, I. A. Ibrahim, H. R. Galal, H. A. Mousa, A. A. Labib, J. Hazard. Mater., 404 (2021) 123962.

[3] M. Hasanpour, M. Hatami, J. Mol. Liq., 309 (2020) 113094.

[4] C. N. C. Hitam, A. A. Jalil, J. Environ. Manage., 258 (2020) 110050.

[5] M. I. Din, R. Khalid, J. Najeeb, Z. Hussain, J. Clean. Prod., 298 (2021) 126567.

[6] J. Sharma, S. Sharma, V. Soni, Reg. Stud. Mar. Sci., 45 (2021) 101802.

[7] M. R. S. Joice, T. M. David, P. Wilson, J. Phys. Chem. C., 123 (2019) 27448.

[8] K. Su, H. Liu, Z. Gao, P. Fornasiero, F. Wang, Adv. Sci., 8 (2021) 2003156.

[9] S. Tasleem, M. Tahir, Renew. Sustain. Energy Rev., 132 (2020) 110073.

[10] A. H. Jawhari, N. Hasan, I. A. Radini, M. A. Malik, K. Narasimharao, Fuel, 344 (2023) 127998.

[11] P. M. Kodam, P. A. Ghadage, D. Y. Nadargi, K. P. Shinde, I. S. Mulla, J. S. Park, S. S. Suryavanshi, Ceram. Int., 48 (2022) 17923.

[12] J. L. Gunjakar, I. Y. Kim, J. M. Lee, Y. K. Jo and S. -J. Hwang, J. Phys. Chem. C, 118 (2014) 3847.

[13] T. H. Gu, N. H. Kwon, K. G. Lee, X. Jin, S. -J. Hwang, Coord. Chem. Rev., 421 (2020) 213439.

[14] J. L. Gunjakar, T. W. Kim, H. N. Kim, I. Y. Kim, S. -J. Hwang, J. Am. Chem. Soc., 133 (2011) 14998.

[15] Y. K. Jo, J. M. Lee, S. Son, S. -J. Hwang, J. Photochem. Photobio. C Photochem. Rev., 40 (2019) 150.

[16] W. You, K. Xiang, Ceram. Int., 47 (2021) 19169.

[17] D. P. Dubal, R. Holze, P. Gomez-Romero, Sci. Rep., 4 (2014) 7349.

[18] R. S. Mane and C. D. Lokhande, Mater. Chem. Phys., 65 (2000) 1-31.

[19] S. M. Pawar, B. S. Pawar, J. H. Kim, O. S. Joo, C. D. Lokhande, Curr. Appl. Phys., 11 (2011) 117.

[20] M. Kotal, A. Sharma, S. Jakhar, V. Mishra, S. Roy, S. C. Sahoo, H. K. Sharma, S. K. Mehta, Cryst. Growth Des., 20 (2020) 4627.

[21] Y. Wang, K. Ding, R. Xu, D. Yu, W. Wang, P. Gao, B. Liu, J. Clean. Prod., 247 (2020) 119108.

[22] S. P. Gupta, M. A. More, D. J. Late, P. S. Walke, Electrochim. Acta, 366 (2021) 137389.

[23] Y. Matsumoto, A. Funatsu, D. Matsuo, U. Unal, K. Ozawa, J. Phys. Chem. B, 105 (2001) 10893.

[24] N. S. Padalkar, C. H. Cho, V. V. Magdum, Y. M. Chitare, S. P. Kulkarni, U. M. Patil, J. P. Park, J. L. Gunjakar, J. Energy Storage, 74 (2023) 109538.

[25] S. P. Gupta, H. H. Nishad, S. D. Chakane, S. W. Gosavi, D. J. Late, P. S. Walke, Nanoscale Adv., 2 (2020) 4689.

[26] H. Aliasghari, A. M. Arabi, H. Haratizadeh, Ceram. Int., 46 (2020) 403.

[27] P. P. Bagwade, V. V. Magdum, D. B. Malavekar, Y. M. Chitare, J. L. Gunjakar, U. M. Patil, C. D. Lokhande, J. Mater. Sci. Mater. Electron., 33 (2022) 24646.

[28] R. B. Shinde, A. S. Patil, S. V. Sadavar, Y. M. Chitare, V. V. Magdum, N. S. Padalkar, U. M. Patil, S. T. Kochuveedu, V. G. Parale, H. H. Park, C. D. Lokhande, J. L. Gunjakar, Sens. Actuators B: Chem., 352 (2022) 131046.

[29] V. G. Erkov, S. F. Devyatova, E. L. Molodstova, T. V. Malsteva, U. A. Yanovskii, Appl. Sur. Sci., 166 (2000) 51.

[30] Q. Hu, J. He, J. Chang, J. Gao, J. Huang, L. Feng, ACS Appl. Nano Mater., 3 (2020) 9046.

[31] Q. Yao, G. Ren, K. Xu, L. Zhu, H. Khan, M. Mohiuddin, M. W. Khan, B. Y. Zhang, A. Jannat, F. Haque, S. Z. Reza, Adv. Opt. Mater., 7 (2019) 1901383.

[32] L. Zhao, X. Chen, Y. Zhang, Z. Ye, Y. Zeng, J. Environ. Chem. Eng., 10 (2022) 107672.

[33] T. Gao, H. Fjellvag, P. Norby, J. Phy. Chem. B, 112 (2008) 9400.

[34] R. Ma, K. Fukuda, T. Sasaki, M. Osada, Y. Bando, J. Phy. Chem. B, 109 (2005) 6210.

[35] Y. M. Chitare, V. V. Magdum, S. P. Kulkarni, S. V. Talekar, S. A. Pawar, P. D. Sawant, D. B. Malavekar, U. M. Patil, C. D. Lokhande, J. L. Gunjakar, Appl. Surf. Sci. Adv., 19 (2024) 100573.

[36] J. L. Gunjakar, I. Y. Kim, J. M. Lee, N. S. Lee, S. -J. Hwang, Energy Environ. Sci., 6 (2013) 1008.

[37] J. L. Gunjakar, T. W. Kim, I. Y. Kim, J. M. Lee, S. -J. Hwang, Sci. Rep., 3 (2013) 2080.

[38] S. V. Sadavar, N. S. Padalkar, R. B. Shinde, A. S. Patil, U. M. Patil, V. V. Magdum, Y. M. Chitare, S. P. Kulkarni, S. B. Kale, R. N. Bulakhe, D. S. Bhange, S. T. Kochuveedu, J. L. Gunjakar, Energy Stor. Mater., 48 (2022) 101.

[39] L. Wang, B. Cheng, L. Zhang, J. Yu, Small, 17 (2021) 2103447.

[40]   R. B. Shinde, N. S. Padalkar, S. V. Sadavar, S. B. Kale, V. V. Magdum, Y. M. Chitare, S. P. Kulkarni, U. M. Patil, V. G. Parale, H. H. Park, J. L. Gunjakar, J. Hazard. Mater., 432 (2022) 128734.

[41]   R. B. Shinde, N. S. Padalkar, S. V. Sadavar, A. S. Patil, S. B. Kale, V. V. Magdum, Y. M. Chitare, S. P. Kulkarni, U. M. Patil, V. G. Parale, J. L. Gunjakar, Mater. Today Chem., 24 (2022) 100801.

[42]   E. Valadbeigi, A. R. Modarresi-Alam, M. Noroozifar, A. R. Rezvani, Express Poly. Lett., 16 (2022) 939.

[43]   H. Xu, R. Zheng, D. Du, L. Ren, X. Wen, X. Wang, G. Tian, C. Shu, Small, 19 (2023) 2206611.

[44]   C. G. Van de Walle and J. Neugebauer, Nature, 423 (2003) 626.

[45]   S. Meng, W. Sun, S. Zhang, X. Zheng, X. Fu, S. Chen, J. Phys. Chem. C, 122 (2018) 26326.

[46]   Z. Wang, L. Jiang, K. Wang, Y. Li, G. Zhang, J. Hazard. Mater., 410 (2021) 124948.

[47]   Y. C. Liang and C. S. Hung, CrystEngComm., 21 (2019) 5779.

[48]   X. Zhang, Y. Hui, C. Fang, Y. Wang, F. Han, X. Lou, E. K. Fodjo, Y. Cai, C. Kong, Molecules, 26 (2021) 4975.

[49]   J. Chen, X. Xiao, Y. Wang, Z. Ye, Appl. Surf. Sci. 467 (2019) 1000.

CHAPTER-V

Synthesis and Characterization of WO$_3$-titanate-NS Heterostructure Thin Films by SILAR: Application in Photocatalytic Dye Degradation

CHAPTER V

Synthesis and Characterization of WO₃-titanate-NS Heterostructure Thin Films by SILAR: Application in Photocatalytic Dye Degradation

5.1 Introduction:

Recently, heterogeneous photocatalysis has been an excellent alternative for mineralizing toxic pollutants in water. Therefore, concerning the advantages of nanohybridization to increase the photocatalytic activity of the pristine sample as described in **Chapter 1**, **section 1.8**, the 2D titanate nanosheets-tungsten oxide (TiW) heterostructure thin films for visible-light-driven photooxidation of dyes are explored in **Chapter 4**. This strategy improved the photocatalytic activity due to effective electronic coupling between hybridized species, strong visible light harvesting ability, porous morphology, and depressed electron-hole pair recombination. To deposit TiW heterostructure thin films, CBD was used to deposit the WO₃ nanoplates layer, and EPD was used to deposit the titanate-NS thin films layer (**Chapter 4**).

Chemical solution deposition methods, particularly CBD and SILAR, are often used to deposit semiconductor thin films. Each method has advantages and disadvantages, as described in **Chapter 2**, **sections 2.2** and **2.3**. SILAR typically provides better control over the thin film growth compared to CBD. In SILAR, the growth process occurs layer-by-layer; therefore, it often produces a more homogeneous thin film, whereas CBD sometimes gives non-homogeneous thin film growth [1-3]. The CBD method commonly involves the wastage of chemicals by forming bulk precipitation, which may be hazardous and environmentally unfriendly. Also, this results in a low yield of deposits in CBD. SILAR is often preferred to overcome the limitations of CBD. The EPD method for depositing titanate-NS is an indispensable tool with various advantages, as described in **Chapter 2**, **section 2.4.3**. Thus, to tune the photocatalytic activity of TiW heterostructure thin films, selecting the WO₃ deposition method is highly crucial. Considering the advantages of the SILAR method, this method can be utilized to tune the WO₃ deposition properties.

In this chapter, TiW heterostructure thin films are deposited using EPD and modified-SILAR (m-SILAR) methods. As described in **Chapter 3**, the EPD method was used to deposit titanate-NS thin films. The m-SILAR method was used to deposit WO₃ thin films over EPD-deposited titanate-NS thin films. The obtained heterostructure thin films are denoted by TiW-S heterostructure thin films. Further, the physicochemical properties and visible-light-driven photocatalytic activity of TiW-S heterostructure thin films are compared with that of pristine WO₃ and titanate-NS thin films. The MB and Rh B are selected as the target molecules for the degradation.

5.2 Synthesis and characterizations of TiW-S heterostructure thin films:

5.2.1 Experimental details:

5.2.1.1 Chemicals:

TiO_2, Cs_2CO_3, $Na_2WO_4.2H_2O$, $H_2C_2O_4$, HCl, TBAOH, C_2H_5OH, MB, and Rh B were purchased from Sigma-Aldrich and used without purification.

5.2.1.2 Synthesis of titanate-NS thin films:

The synthesis of exfoliated titanate-NS and titanate-NS thin films was similar to as discussed in **Chapter 3, sections 3.2.1.2** and **3.2.1.3**, respectively.

5.2.1.3 Synthesis of WO₃ thin film by m-SILAR method:

The visible light active WO_3 thin film was deposited using the m-SILAR method. The WO_3 thin film synthesis by the m-SILAR method comprised immersion of well-cleaned substrates into separately placed adsorption and reaction baths (two-beaker process). The adsorption bath was prepared from 30 mL of 0.1 M $Na_2WO_4.2H_2O$ complexed with 10 mL of 0.25 M of $C_2H_2O_4$. The pH of the bath was adjusted to 1.5 using 2 M HCl. The reaction bath was prepared using DDW, whose pH was maintained at 1.5 using 2 M HCl. The adsorption and reaction baths were kept at room temperature and 80 °C, respectively.

The one deposition cycle of m-SILAR comprised immersion of glass substrate into an adsorption bath for 40 seconds and then into a reaction bath for 20 seconds. The WO_3 thin film was deposited by repeating such 200 deposition cycles. The deposited WO_3 thin film was washed with DDW and dried at room temperature. The schematic representation of WO_3 thin film deposition by the m-SILAR method is represented in **Fig. 5.1**. The deposited WO_3 thin film at 200 deposition cycles is denoted as pristine WO_3.
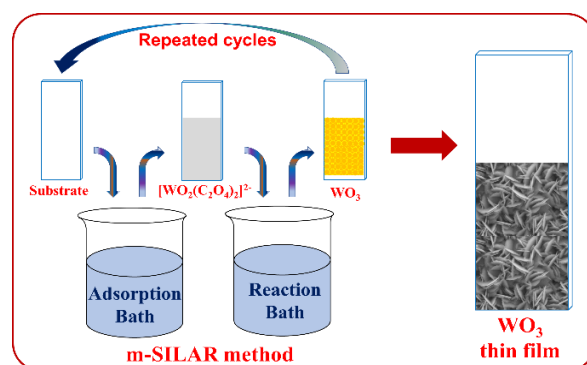
Fig. 5.1. Schematic representation of synthesis protocol for WO_3 thin film by m-SILAR method.

5.2.1.4 Synthesis of TiW-S heterostructure thin films:

The visible light active WO_3 was deposited over the EPD-deposited titanate-NS thin films by the m-SILAR method. The experimental conditions for preparing WO_3 thin film were similar to those described in **section 5.2.1.3**. The growth of WO_3 by the m-SILAR method comprising immersion of EPD-deposited titanate-NS thin film into separately placed adsorption and reaction baths (two-beaker process). The one deposition cycle of m-SILAR was completed by successive immersion of titanate-NS thin film into an adsorption bath for 40 seconds and then into a reaction bath for the next 20 seconds. The WO_3 was deposited on the titanate-NS thin film by repeating such 75 deposition cycles. The deposited TiW-S heterostructure thin films were washed with DDW and dried at room temperature. The schematic representation of TiW-S heterostructure thin film by m-SILAR method is represented in **Fig. 5.2**. The TiW-S heterostructure thin films deposited on titanate-NS-5, titanate-NS-10, and titanate-NS-15 are denoted as TiW-5-S, TiW-10-S, and TiW-15-S, respectively.
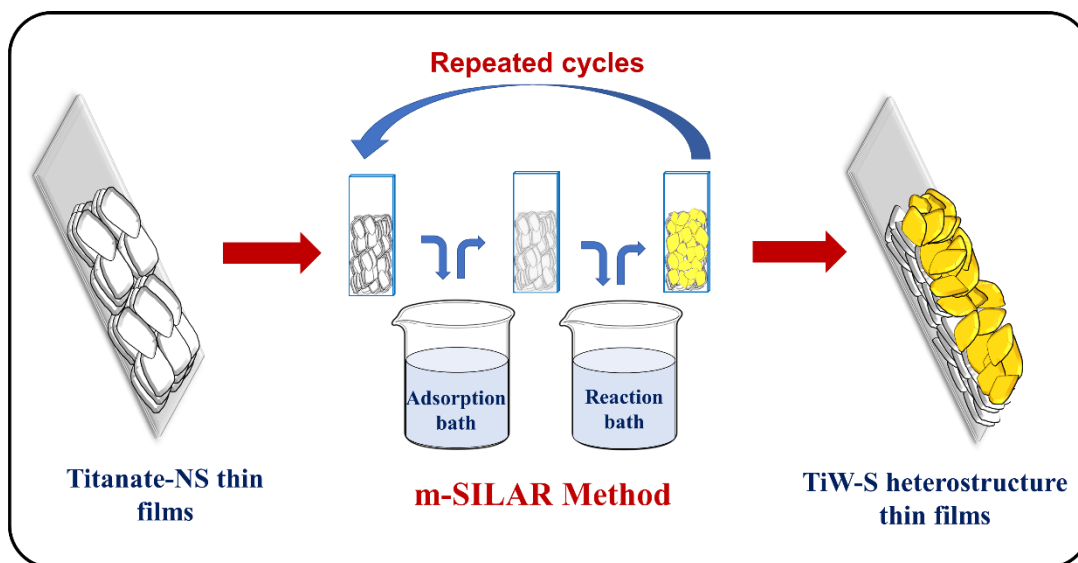
Fig. 5.2. Schematic representation of TiW-S heterostructure thin films deposition.

5.2.1.5 Material characterizations:

The pristine WO_3, titanate-NS, and TiW-S heterostructure thin films were characterized by various physicochemical characterization techniques similar to those described in **Chapter 3, section 3.2.1.4**.

5.2.1.6 Experimental setup for dye degradation:

The experimental setup for the visible-light-induced dye degradation by TiW-S heterostructures thin films is similar to that described in **Chapter 4**, **section 4.2.1.6**.

5.2.2 Results and Discussion:

5.2.2.1 XRD study:
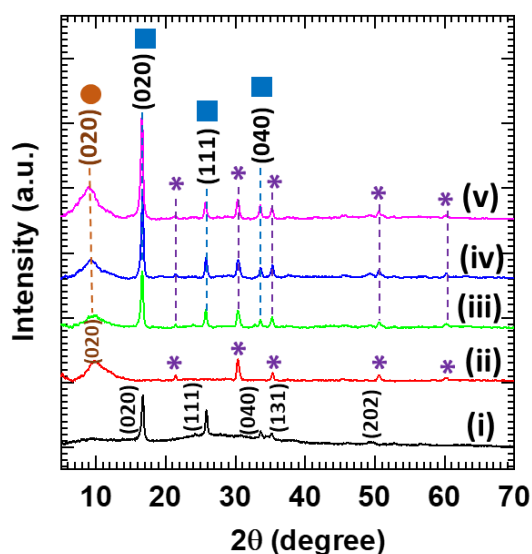
Fig. 5.3. XRD patterns of (i) WO₃, (ii) titanate-NS, (iii) TiW-5-S, (iv) TiW-10-S, and (v) TiW-15-S heterostructure thin films.

The crystal structure of TiW-S heterostructure, along with pristine WO₃ and titanate-NS thin films, was investigated by XRD analysis. The XRD patterns of pristine WO₃, titanate-NS, and TiW-S heterostructure thin films are shown in **Fig. 5.3**. The XRD pattern of pristine WO₃ thin film deposited by m-SILAR shows well-developed sharp peaks that are well matched with (020), (111), (040), (131), and (202) planes of orthorhombic $WO_3 \cdot H_2O$ phase (JCPDS card no. 01-084-0886) [4]. The estimated lattice parameters a=5.19 Å, b=10.71 Å, and c=5.12 Å, which are in good agreement with the monohydrate layered $WO_3 \cdot H_2O$ phase. The XRD pattern of EPD-deposited titanate-NS-10 from **Chapter 3, Fig 3.3,** is plotted as **Fig. 5.3(ii)** for comparison. The XRD analysis of pristine titanate-NS is discussed in **Chapter 3**, **section 3.2.2.1**. Furthermore, upon the growth of WO₃ over the electrophoretically deposited titanate-NS thin film, the TiW-S heterostructure thin films exhibit numerous diffraction peaks corresponding to lepidocrocite type titanate-NS, orthorhombic WO₃, and ITO substrate. The first broad diffraction peak is centred at 10º, suggesting the titanate nanosheets are restacked layer-by-layer on the substrate with orthorhombic symmetry having a basal spacing of 0.88 nm [5]. The other diffraction peaks (020), (111), and (040) correspond to the orthorhombic $WO_3 \cdot H_2O$ phase. The peaks marked by '*' correspond to the ITO substrate. This XRD features matching with the titanate-NS and WO₃ clearly show the deposition of WO₃ over electrophoretically deposited titanate-NS thin films, confirming

the formation of TiW-S heterostructure thin films. No other peak matches with other phases of titanium oxide exhibiting high chemical and mechanical stability of titanate-NS thin films.

5.2.2.2 FT-IR study:
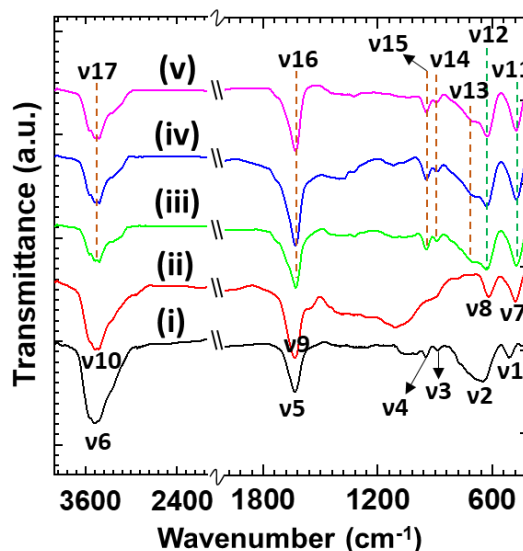
Fig. 5.4. FT-IR spectra of (i) WO₃, (ii) titanate-NS, (iii) TiW-5-S, (iv) TiW-10-S, and (v) TiW-15-S heterostructure thin films.

The chemical bonding nature of pristine WO₃, titanate-NS and TiW-S heterostructure thin films was probed with FT-IR spectroscopy. As shown in **Fig. 5.4**, the absorption peaks ν1 (484 cm⁻¹) and ν2 (665 cm⁻¹) correspond to the metal-oxygen stretching vibration (W-O-W). The absorption peaks ν3 (884 cm⁻¹) and ν4 (946 cm⁻¹) are ascribed to the O-W-O and W=O vibrations, respectively [6-8]. The absorption peaks ν5 (1634 cm⁻¹), and ν6 (3419 cm⁻¹) are related to the bending vibrational modes of water molecules and stretching vibrations of the O-H groups, respectively [9]. These characteristic absorption peaks are commonly observed in the WO₃.H₂O phase. The FT-IR spectrum of EPD-deposited titanate-NS-10 from **Chapter 3, Fig 3.4,** is plotted as **Fig. 5.4(ii)** for comparison. The FT-IR analysis of pristine titanate-NS is discussed **in Chapter 3**, **section 3.2.2.2**. However, the TiW-S heterostructure thin films commonly exhibit absorption peaks associated with WO₃ and titanate-NS. The absorption peaks ν11 (473 cm⁻¹) and ν12 (624 cm⁻¹) are ascribed to the bending and stretching modes of Ti-O, respectively [10, 11]. The absorption peaks ν13 (662 cm⁻¹), ν14 (886 cm⁻¹), and ν15 (946 cm⁻¹) are ascribed to the W-O-W, O-W-O, and W=O vibrations, respectively. The peak ν16 (1632 cm⁻¹) is related to the bending vibrational modes of water molecules, and peak ν17 (3421 cm⁻¹) corresponds to the stretching vibrations of the O-H groups [6-

9]. The broad peaks associated with metal-oxygen vibrations carry minute shoulder peaks due to the superpositions of WO_3 and titanate-NS IR peaks. The broadening of these peaks can be observed as a signature of strong coupling and hybridization between the WO_3 and titanate-NS layers. The presence of IR features related to WO_3 and titanate-NS indicates the formation of the TiW-S heterostructure.

5.2.2.3 Micro-Raman study:
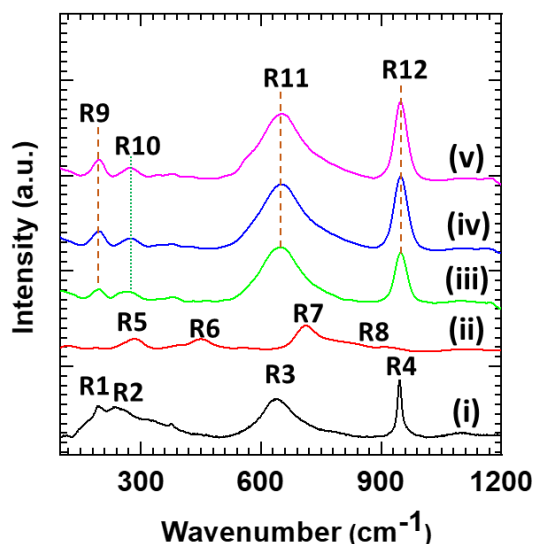
Fig. 5.5. Micro-Raman spectra of (i) WO_3, (ii) titanate-NS, (iii) TiW-5-S, (iv) TiW-10-S, and (v) TiW-15-S heterostructure thin films.

The chemical bonding character of the pristine WO_3, titanate-NS, and TiW-S heterostructure was further studied with Raman spectroscopy. As shown in **Fig. 5.5**, the WO_3 thin films commonly discern distinct Raman features R1 to R4 related to WO_3. The peaks R1 (193 cm⁻¹) and R2 (237 cm⁻¹) correspond to the lattice vibrations of WO_3 and bending vibrations of the metal-oxygen (W-O-W) bond, respectively. The broad peak R3 (636 cm⁻¹) and sharp peak R4 (946 cm⁻¹) are assigned to the stretching vibrations of O-W-O and terminal W=O bonds, respectively [12, 13]. These distinctive Raman peaks are the characteristics of the orthorhombic $WO_3.H_2O$ phase. The micro-Raman spectrum of EPD-deposited titanate-NS-10 from **Chapter 3, Fig 3.5,** is plotted as **Fig. 5.5(ii)** for comparison. The micro-Raman analysis of pristine titanate-NS (peaks R5-R8) is discussed in **Chapter 3, section 3.2.2.3**. Moreover, TiW-S heterostructure thin films exhibit the characteristic Raman peaks R9 to R12 associated with titanate-NS (R10) and WO_3 (R9, R11 and R12). The Raman peaks R9, R11, and R12 are associated with lattice vibrations of WO_3, stretching vibrations of O-W-O, and terminal W=O bonds, respectively. Meanwhile, Raman peak R10 corresponds to the *Ag* symmetric

vibrations originating from the splitting of the degenerate mode of the TiO_6 octahedron [14]. In addition, upon the growth of WO_3 over the titanate-NS, the Raman peaks R11 and R12 broaden due to the superposition of WO_3 and titanate-NS peaks. The presence of Raman peaks corresponds to the chemical bonding characteristics of WO_3 and titanate-NS, indicating the formation of TiW-S heterostructure thin films. These characteristics Raman features related to titanate-NS in TiW-S heterostructure thin films indicate the intactness of titanate nanosheets during heterostructure formation. These spectral features underscore the effective growth of WO_3 over EPD-deposited titanate-NS thin films.

5.2.2.4 FE-SEM study:
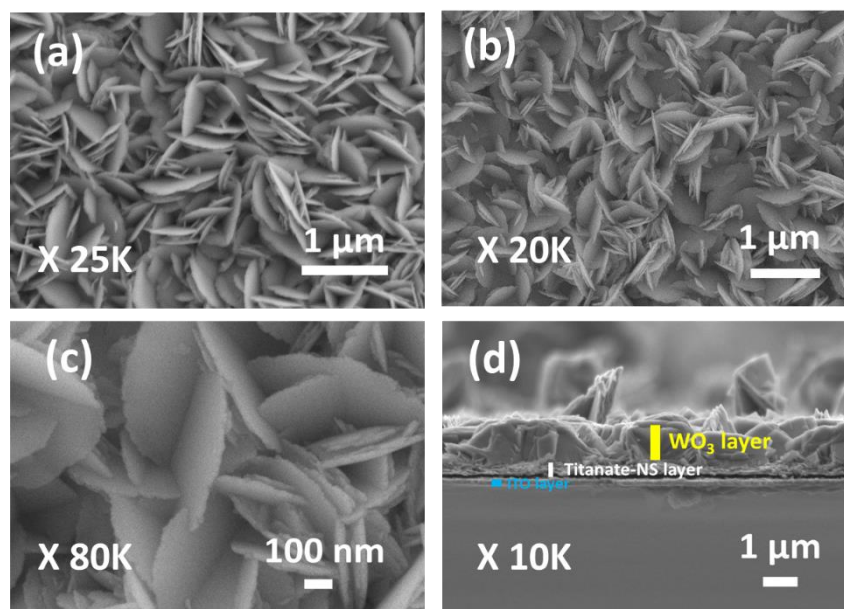
Fig. 5.6. FE-SEM images of (a) WO_3 and (b, c) TiW-10-S heterostructure thin films. The cross-sectional FE-SEM image of (d) TiW-10-S heterostructure thin film.

The surface morphology and stacking structure of pristine WO_3 and TiW-S heterostructure thin films were probed by FE-SEM. The surface microstructural analysis and cross-section of pristine titanate-NS are discussed in **Chapter 3, section 3.2.2.4**. The top-view image of the m-SILAR deposited WO_3 thin film **(Fig. 5.6(a))** shows a smooth and vertically aligned interlocked nanosheet-like structure with a nanoscale length of 670 nm, breadth of 360 nm, and thickness of 30 nm. Moreover, the FE-SEM images of the TiW-10-S heterostructure thin film **(Fig. 5.6(b-c))** show vertically grown interlocked WO_3 nanoplates grown over the titanate-NS thin film. The average length, width, and thickness of WO_3 nanoplates are 550, 390, and 22 nm, respectively. The cross-sectional image of TiW-10-S heterostructure thin film shown in **Fig. 5.6(d)** clearly

distinguishes the separate layers of deposited material on the ITO. The bottom layers are composed of the ITO layer grown on glass. The top layers are composed of WO_3 nanoplates grown on horizontally stacked titanate-NS. The vertical growth of WO_3 nanoplates on titanate-NS leads to a high surface area morphology. Such a heterostructure can enable intimate electronic coupling between the titanate-NS and WO_3, which is highly beneficial in special electron-hole pair separation for solar-assisted photo-functional applications. Such a heterostructure facilitates the intimate electronic coupling between the titanate-NS and WO_3, which is advantageous for charge separation and transport for photocatalytic application.

5.2.2.5 EDS study:
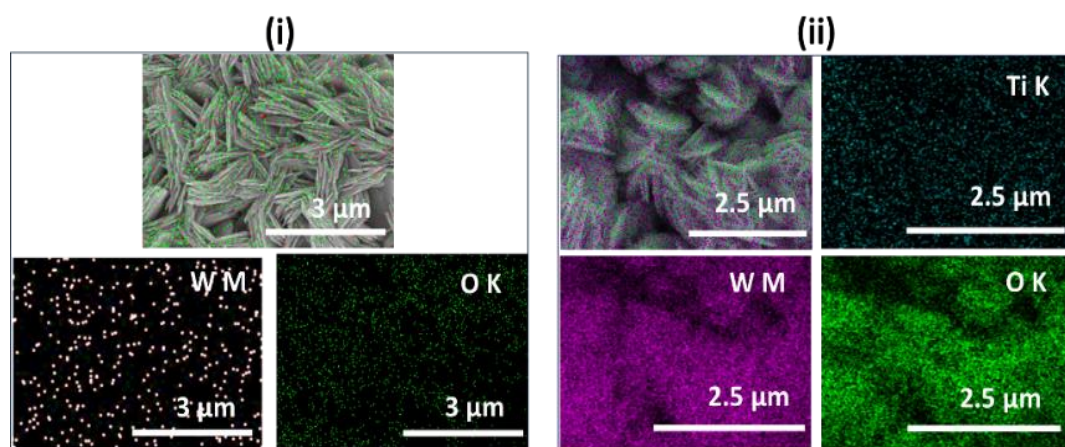
Fig. 5.7. FE-SEM images along with EDS-elemental mapping of (i) WO_3 and (ii) TiW-10-S heterostructure thin films.
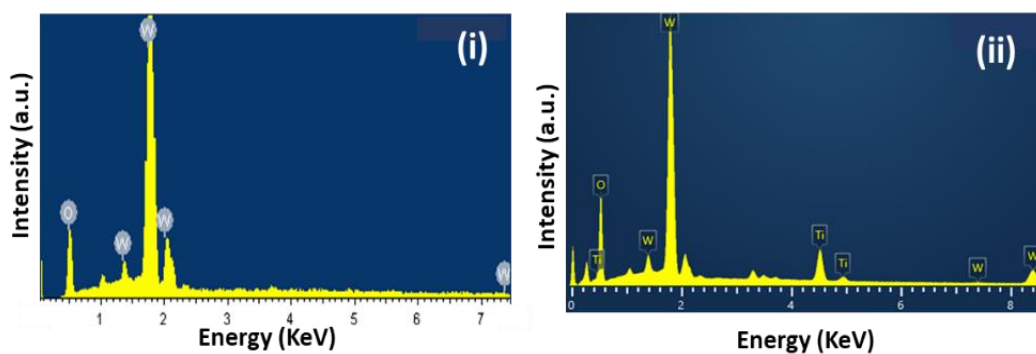
Fig. 5.8. EDS spectra of (i) WO_3 and (ii) TiW-10-S heterostructure thin films.

The distribution of constituent elements in WO_3 and TiW-10-S heterostructure thin films was probed with EDS and elemental mapping analysis and represented in **Fig. 5.7** and **Fig. 5.8**, respectively. All the constituent elements (tungsten, titanium, and oxygen) are homogeneously distributed throughout the elemental mapping area,

highlighting the uniform growth of WO_3 nanoplates on the surface of titanate-NS thin films. The atomic percentage ratio of Ti/W is 0.6 for TiW-10-S heterostructure thin film.

5.2.2.6 XPS study:
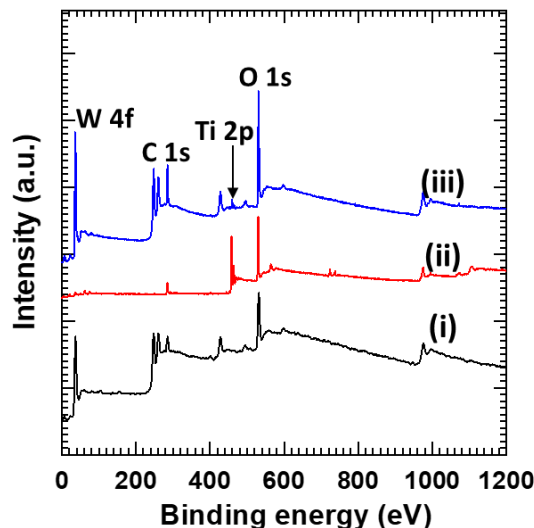
Fig. 5.9. XPS survey spectra of (i) WO_3, (ii) titanate-NS, and (iii) TiW-15-S heterostructure thin films.

The XPS analysis was used to examine the surface elemental states in the WO_3, titanate-NS, and TiW-S heterostructures. The XPS spectrum of EPD-deposited titanate-NS from **Chapter 3, Fig 3.7,** is plotted as **Fig. 5.9(ii)** for comparison. The survey XPS spectrum analysis of pristine titanate-NS is discussed in **Chapter 3, section 3.2.2.6**. The XPS survey spectra of pristine WO_3, titanate-NS, and optimized TiW-10-S heterostructures thin films (**Fig. 5.9**) commonly show characteristic XPS signatures at the binding energy of the elements W, Ti, and O indicating the presence of these elements in the deposited thin films. The presence of these XPS characteristics underscores the existence of W, Ti, and O in the deposited thin films.
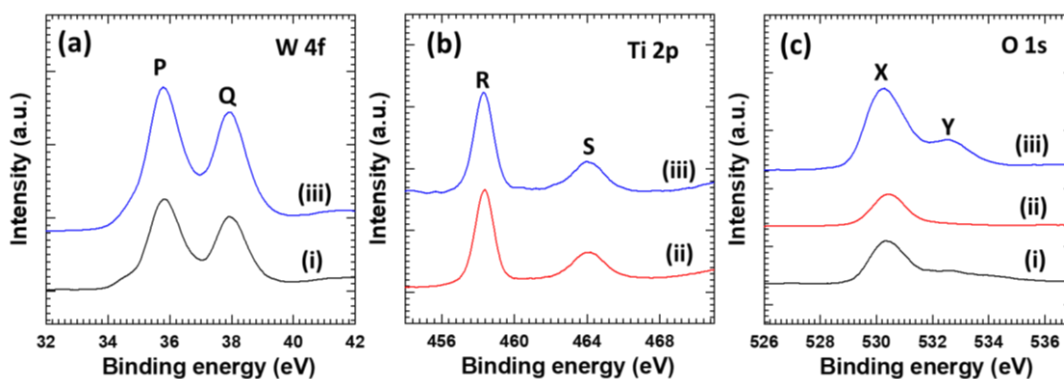
Fig. 5.10. (a) W 4f, (b) Ti 2p, and (c) O 1s core-level XPS spectra of (i) WO_3, (ii) titanate-NS, and (iii) TiW-15-S heterostructure thin films.

The high-resolution core-level spectra of W 4f, Ti 2p, and O 1s are shown in **Fig. 5.10**. As depicted in **Fig. 5.10(a)**, the high-resolution W 4f core-level spectra, which are only discernible for pristine WO₃ and TiW-10-S heterostructures thin films, display peaks P (35.7 eV) and Q (37.8 eV) because of the splitting spin-orbit components W $4f_{7/2}$ and W $4f_{5/2}$, respectively. Positions of P and Q binding energies are characteristic of the W-O bond configuration and are typically observed for W^{6+} in WO₃ [15]. The core-level Ti 2p and O 1s XPS spectra of titanate-NS from **Chapter 3, Fig. 3.8**, are plotted again in **Fig. 5.10** as plots **Fig. 5.10 (b(ii))** and **Fig. 5.10(c(ii))** for comparison. The XPS spectra analysis of Ti 2p and O 1s are discussed in **Chapter 3**, **section 3.2.2.5**. As represented in **Fig. 5.10(b)**, titanate-NS and TiW-10-S heterostructure thin films show two spectral peaks, R (458.3 eV) and S (464.1 eV), associated with the spin-orbit splitting components Ti $2p_{3/2}$ and Ti $2p_{1/2}$, respectively. These peak positions confirm Ti^{4+} in titanate-NS and TiW-10-S heterostructure thin film [16]. In addition, O 1s core-level spectra represented in **Fig. 5.10(c)** commonly show the peak X (530.5 eV) and shoulder at Y (531.7 eV), indicating the presence of oxygen in metal oxide and hydroxyl group (-OH group) originating from structural or adsorbed water molecules, respectively [17]. The observed XPS features underscore strong evidence of W^{6+} and Ti^{4+} states of W and Ti, respectively, which confirms the formation of TiW-S heterostructure.

5.2.2.7 UV-vis DRS study:
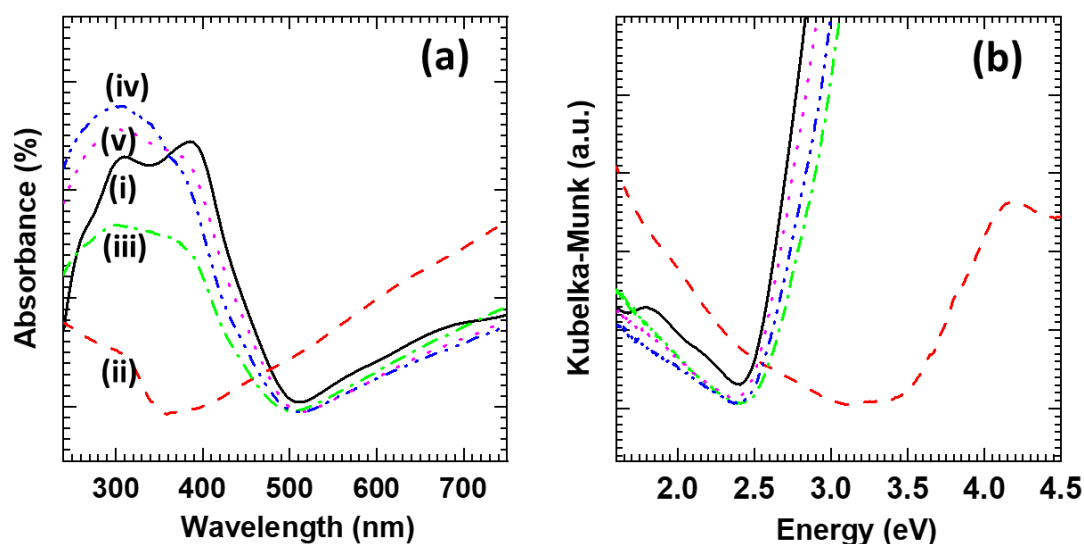
Fig. 5.11. (a) UV-vis absorbance spectra obtained from UV-vis DRS and (b) UV-vis DRS (plotted as Kubelka-Munk function of reflectance, R) of (i) WO₃ (solid lines), (ii) titanate-NS (dashed lines), (iii) TiW-5-S (dash-dotted lines), (iv) TiW-10-S (dash-dot-dotted lines), and (v) TiW-15-S (dotted lines) heterostructure thin films.

The optical properties of pristine WO_3, titanate-NS, and TiW-S heterostructure thin films were studied with UV-vis DRS. For the comparison, the UV-vis DRS absorbance spectrum of titanate-NS is plotted again in **Fig. 5.11(ii).** The UV-vis DRS absorbance spectrum of EPD-deposited titanate-NS from **Chapter 3, Fig 3.9,** is plotted in **Fig. 5.11(ii)** for comparison. The UV-vis DRS absorbance spectrum analysis of pristine titanate-NS is discussed in **Chapter 3**, **section 3.3.2.6**. As represented in **Fig. 5.11(a)**, the pristine WO_3 and titanate-NS thin film shows prominent absorption in the visible and UV region of the solar spectrum with an energy bandgap of 2.28 and 3.34 eV, respectively. The WO_3 is an indirect band gap material having an electronic structure comprising a VB and CB of O 2p and W 5d, respectively, whereas the electronic structure of titanate-NS comprises a VB and CB mainly composed of O 2p and Ti 3d orbitals, respectively [18, 19] Interestingly, after the growth of WO_3 on the titanate-NS, TiW-S heterostructure thin films show noteworthy absorption in the visible region, highlighting their visible-light harvesting capability. The TiW-S heterostructure thin films absorb visible light in the wavelength between 508- 532 nm, matching the band gap energies of 2.44- 2.33 eV. The bandgap energies determined from the Kubelka-Munk function are shown in **Fig. 5.11(b)** and **Table 5.1**. The strong visible light absorption ability of TiW-S heterostructures makes them suitable candidates for visible-light-driven photocatalytic activity.

Thin film	Energy bandgap (eV)
WO_3	2.28
titanate-NS	3.34
TiW-5-S	2.44
TiW-10-S	2.39
TiW-15-S	2.33

Table 5.1. Synthesized photocatalyst thin films and their estimated band gap energies.

Based on the bandgap energy, the CB and VB potentials of the titanate-NS and WO_3 thin films are plotted in **Chapter 3**, **section 3.2.2.6** and **Chapter 4**, **section 4.2.2.7**. The schematic of the band edge potential of WO_3 and titanate-NS thin film is shown in **Fig. 5.12**.
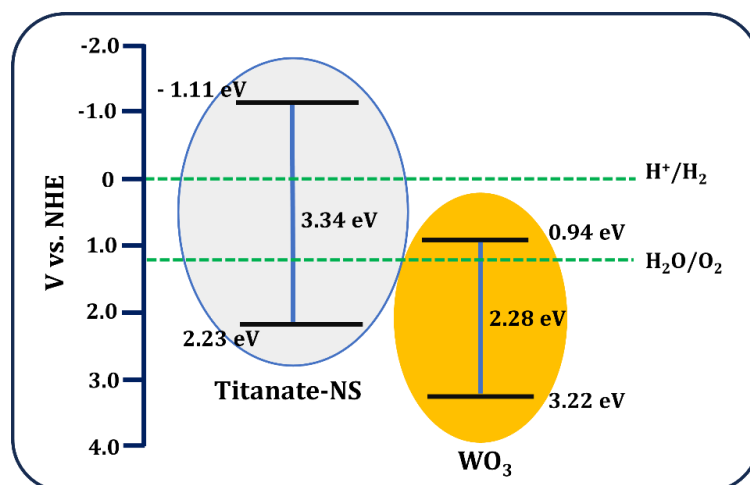
Fig. 5.12. Schematic representation for the energy band structure of titanate-NS and WO₃ thin films.

5.3 Photocatalytic activity:

5.3.1 Dye degradation study:
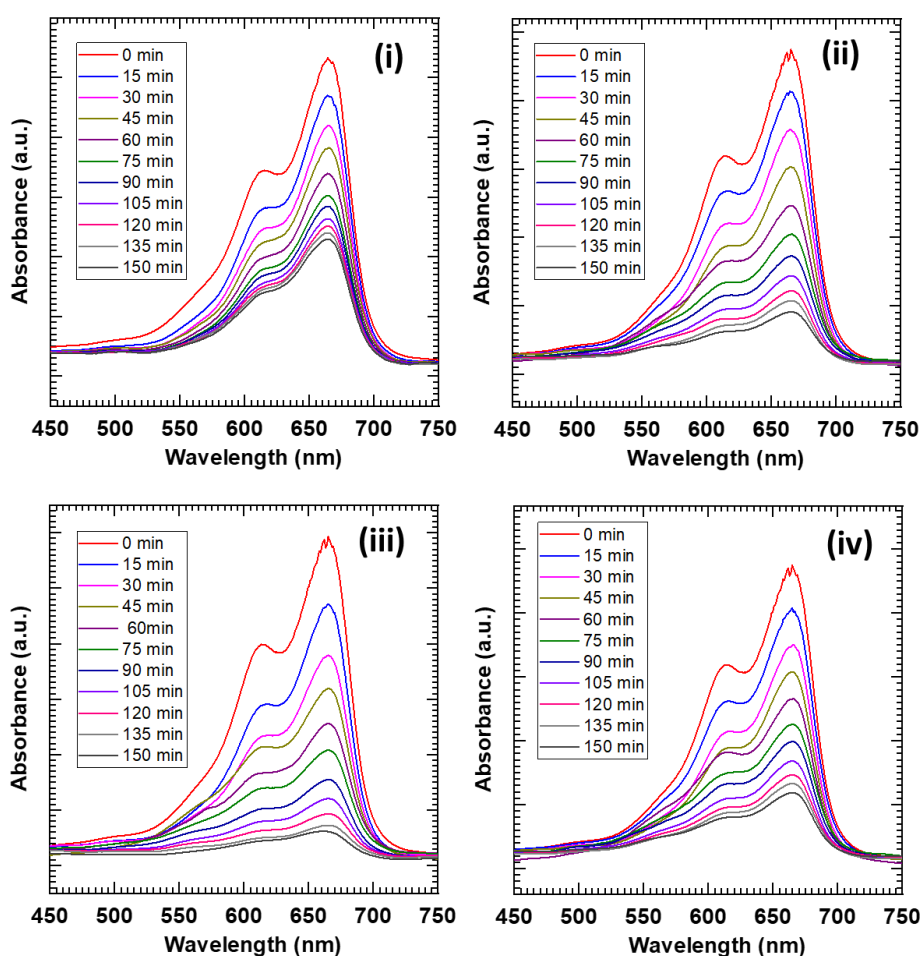
Fig. 5.13. Absorption spectra of MB for (i) WO₃, (ii) TiW-5-S, (iii) TiW-10-S, and (iv) TiW-15-S heterostructure thin films.
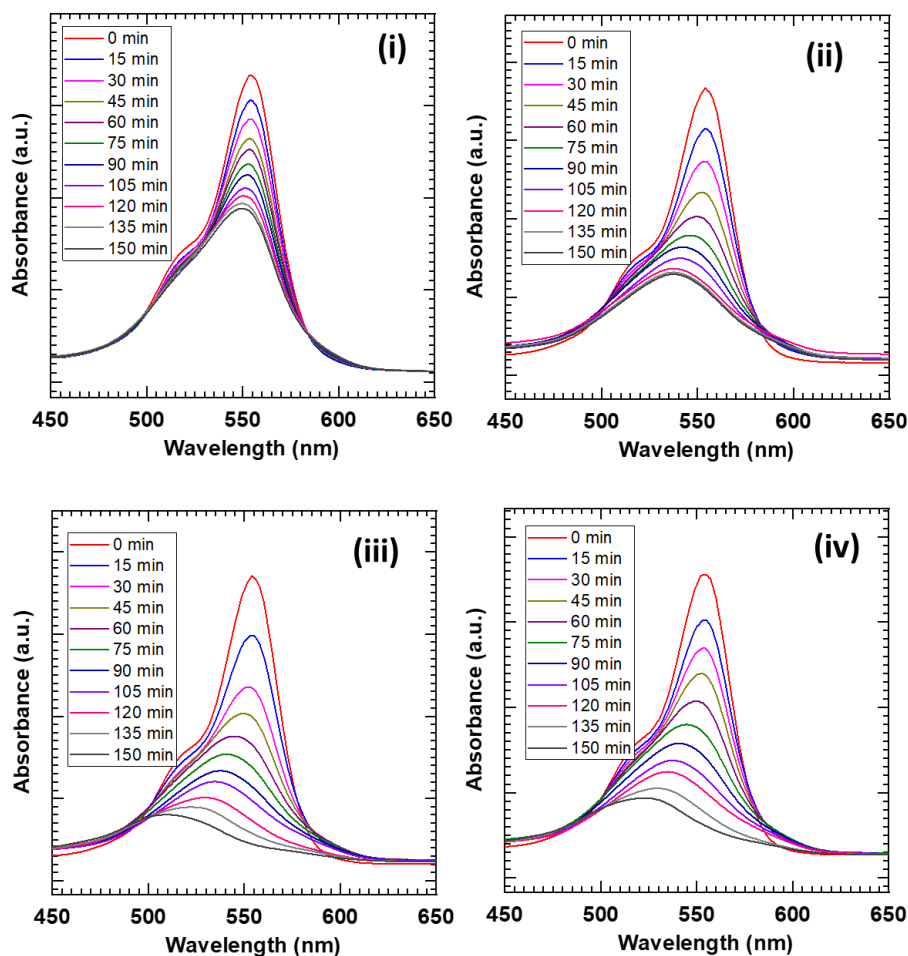
Fig. 5.14. Absorption spectra of Rh B for (i) WO$_3$, (ii) TiW-5-S, (iii) TiW-10-S, and (iv) TiW-15-S heterostructure thin films.
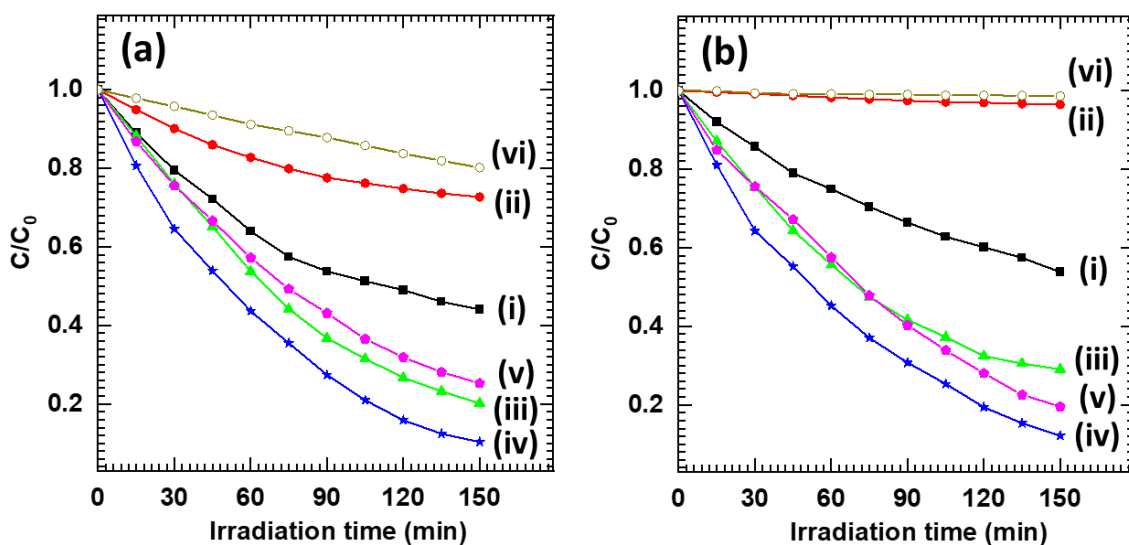
Fig. 5.15. Photocatalytic degradation performance of MB (a) and Rh B (b) for (i) WO$_3$, (ii) titanate-NS, (iii) TiW-5-S, (iv) TiW-10-S, (v) TiW-15-S heterostructure thin films and (vi) without thin film.

The visible-light-induced photocatalytic activity of TiW-S heterostructure thin films was examined by monitoring the time-dependent photodegradation of MB and Rh B and compared with pristine WO_3 and titanate-NS thin films. The time-dependent absorption spectra of MB and Rh B are represented in **Fig. 5.13** and **Fig. 5.14**, respectively. The time-dependent absorption spectra of MB and Rh B for pristine titanate-NS and without thin films are shown in **Chapter 4**, **section 4.3.1.** The pristine WO_3 and TiW-S heterostructure thin films exhibit photocatalytic activity for MB and Rh B degradation under visible light, as depicted in **Fig. 5.15(a-b)**. For the comparison, the degradation performance of MB and Rh B for titanate-NS and without thin films are plotted again in **Fig. 5.15(a)** and **Fig. 5.15(b)**, respectively. The m-SILAR deposited WO_3 demonstrates notable photocatalytic activity for MB (MB: 52% in 150 min) and Rh B (Rh B: 40% in 150 min) photodegradation, which is attributed to the low energy band gap, large number of active sites, and nanosheet morphology. In contrast, titanate-NS does not show significant activity because of the wide band gap energy, highlighting its visible-light inactivity. The photocatalytic degradation performance of WO_3 is remarkably enhanced after using TiW-S heterostructure thin films. The present finding provides strong evidence for the usefulness of heterostructure. Among the TiW-S heterostructure thin films deposited at various deposition times, the TiW-10-S heterostructure thin films exhibited enhanced performance of 89 and 88% in 150 min, which is far superior to those of pristine titanate-NS and WO_3 thin films. Furthermore, it lowers for TiW-15-S heterostructure thin film due to the peel-off of the loosely bound WO_3 layers from the film surface. This type of deposit peeling off from the surface is generally seen in chemically deposited thin films. The remarkable photocatalytic degradation activity of TiW-S heterostructure thin films can be ascribed to the strong visible-light harvesting ability, high surface area, porous nanoplate morphology, and reduced electron-hole pair recombination via effective electronic coupling between hybridized species.

5.3.2 Kinetic study:

In addition, k and R^2 values determined from the first-order reaction kinetics confirm the high photocatalytic degradation performance of deposited thin films [20]. **Fig. 5.16 (a-b)** represents the plots of pseudo-first-order kinetics for MB and Rh B. For the comparison, the first-order reaction kinetics of MB and Rh B for titanate-NS thin films are plotted again in **Fig. 5.16(a)** and **Fig. 5.16(b)**, respectively. The k and R^2 values

of pristine WO$_3$, titanate-NS, and TiW-S heterostructure thin films are given in **Table 5.2**.
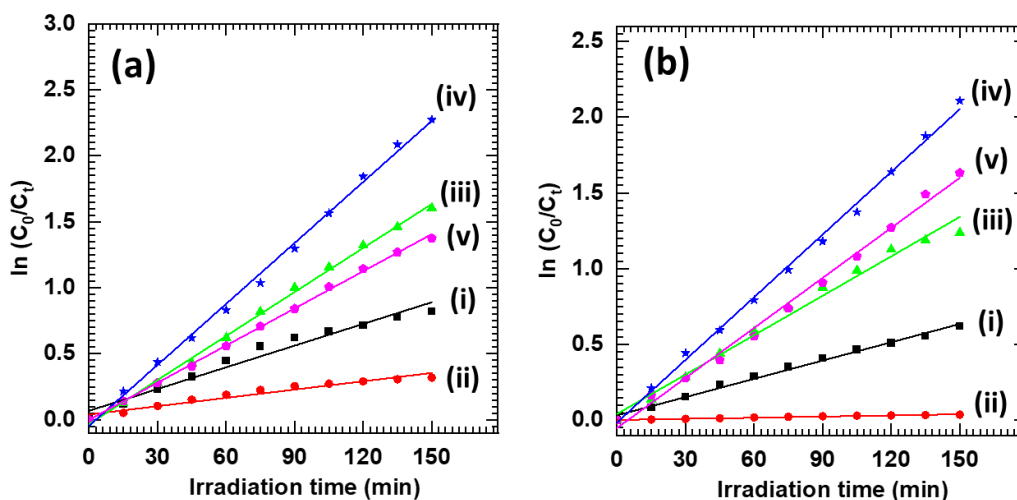
Fig. 5.16. Pseudo-first-order kinetics of MB (a) and Rh B (b) for (i) WO$_3$, (ii) titanate-NS, (iii) TiW-5-S, (iv) TiW-10-S, and (v) TiW-15-S heterostructure thin films.

The TiW-10-S heterostructure thin film exhibits the highest k values of 0.0154 and 0.0137 min^{-1} for MB and Rh B, respectively. The photocatalytic reaction rate of TiW-10-S heterostructure thin film for MB is 2.8, 7.33, 1.38, and 1.65 times higher than pristine WO$_3$, titanate-NS, TiW-5-S, and TiW-15-S heterostructure thin films, respectively. Meanwhile, for Rh B, it is 3.17, 57, 1.59, and 1.24 times higher than pristine WO$_3$, titanate-NS, TiW-5-S, and TiW-15-S heterostructure thin films, respectively. The TiW-10-S heterostructure thin film demonstrates enhanced degradation performance due to effective electronic coupling between hybridized species, strong visible light harvesting ability, porous morphology, and minimal electron-hole pair recombination.

Thin Film	MB		Rh B	
	k (min $^{-1}$)	R^2	k (min $^{-1}$)	R^2
WO$_3$	0.0055	0.97	0.0040	0.99
titanate-NS	0.0021	0.95	0.00024	0.98
TiW-10-S	0.0111	0.99	0.086	0.98
TiW-20-S	0.0154	0.99	0.0137	0.99
TiW-30-S	0.0093	0.99	0.0110	0.99

Table 5.2. The k and R^2 values of all pristine WO$_3$, titanate-NS, and TiW-S heterostructure thin films.

5.3.3 Recycling study:
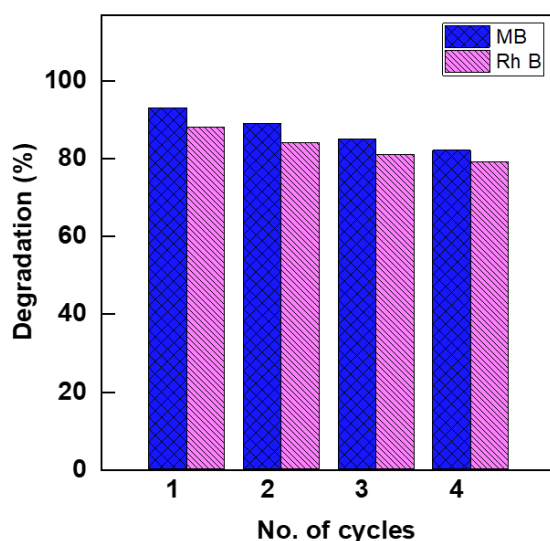
Fig. 5.17. Recyclability study of TiW-10-S heterostructure thin film.

In addition, the recyclability of the optimized TiW-10-S heterostructure thin film for photocatalyst application is studied for four consecutive cycles of photocatalytic degradation. As shown in **Fig. 5.17**, the photocatalytic performance of the TiW-10-S heterostructure thin film did not significantly deteriorate even after the four consecutive cycles, highlighting the remarkable stability of the heterostructure thin films. The minute reduction in performance following four consecutive cycles was obtained due to the adsorption of target molecules on the surface of the photocatalyst and the loss of loosely bound photocatalyst crystals from the film.

5.3.4 Photocatalytic degradation mechanism:

The photocatalytic decomposition of organic molecules involves charge separation and migration to the photocatalyst surface. Possible photocatalytic organic molecules degradation mechanism upon exposure to light irradiation, represented in **Fig. 5.18**. When visible light (λ>420 nm) is incident on the TiW-S heterostructure, electrons from the VB of WO_3 are excited to its CB, forming electron-hole pairs. As represented in **Fig. 5.18**, the CB of titanate-NS (-1.11 eV) is more negative than that of WO_3 (0.94 eV) and the VB of WO_3 (3.22 eV) is more positive than that of titanate-NS (2.23 eV) with respect to NHE [21]. The photogenerated electrons from the CB of WO_3 can migrate into the VB of titanate-NS, leading to the spatial separation of electrons and holes. As a consequence, the lifetime of holes in the VB of WO_3 increases [22, 23]. The detailed explanation of surface redox reaction is described in **Chapter 4, section 4.3.4**.
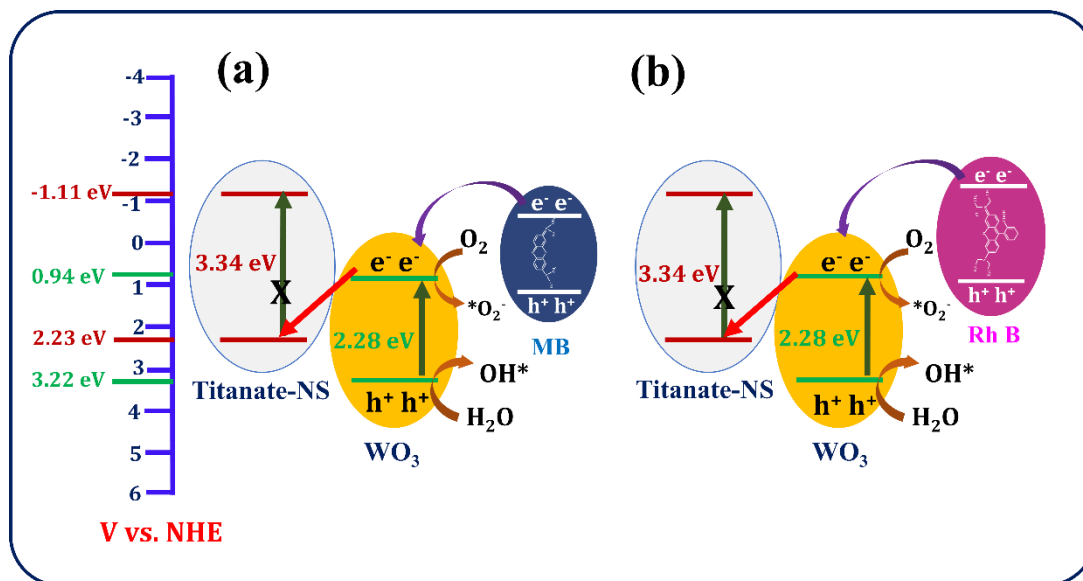
Fig. 5.18. Schematic diagram for plausible photodegradation of (a) MB and (b) Rh B.

5.4 Conclusions:

In this work, the comparative study of TiW-S heterostructure thin films with the pristine WO₃ and titanate-NS demonstrates the features of 2D titanate-NS as a platform for the synthesis of heterostructures to enhance the photocatalytic activity. The m-SILAR deposited WO₃ thin film shows an orthorhombic crystal structure with vertically grown interlocked nanosheet-like morphology. The prisitne WO₃ thin film demonstrates significant photodegradation of 52 and 40% in 150 min for MB and Rh B, respectively. The notable photodegradation is attributed to the low energy band gap, large number of active sites, and nanosheet morphology. In contrast, titanate-NS does not show significant activity because of the wide band gap energy, highlighting its visible-light inactivity. The TiW-S heterostructure thin films show the structural characteristics related to WO₃ and titanate-NS, confirming that the WO₃ is coated by the m-SILAR method on the EPD-deposited titanate-NS thin film. The TiW-S heterostructure thin film shows the WO₃ nanoplates grown vertically on the horizontally stacked titanate-NS parallel to the ITO substrate, enabling the effective electronic coupling between the titanate-NS and WO₃. The optimized TiW-10-S heterostructure thin film shows the highest degradation performance of 89 and 88% for MB and Rh B in 150 min., respectively, in visible light. The present experimental results highlight the usefulness of heterostructure thin films for prominent depression of electron-hole recombination. This study can be effectively used to synthesize binder-free layer-by-layer visible-light-active thin-film photocatalysts.

5.5. References:

[1]   R. Garza-Hernandez, S. Lugo-Loredo, F. S. Aguirre-Tostado, Thin Solid Films, 692 (2019) 137519.

[2]   S. P. Ratnayake, J. Ren, E. Colusso, M. Guglielmi, A. Martucci, E. Della Gaspera, Small, 17 (2021) 2101666.

[3]   M. Kaur, M. Shaheera, A. Pathak, S. C. Gadkari, A. K. Debnath, Sens. Actuators B Chem., 335 (2021) 129678.

[4]   S. P. Gupta, M. A. More, D. J. Late, P. S. Walke, Electrochim. Acta, 366 (2021) 137389.

[5]   Y. Matsumoto, A. Funatsu, D. Matsuo, U. Unal, K. Ozawa, J. Phys. Chem. B, 105 (2021) 10893.

[6]   M. E. Malefane, B. Ntsendwana, P. J. Mafa, N. Mabuba, U. Feleni, A. T. Kuvarega, Chem. Select, 4 (2019) 8379.

[7]   S. P. Gupta, H. H. Nishad, S. D. Chakane, S. W. Gosavi, D. J. Late, P. S. Walke, Nanoscale Adv., 2 (2020) 4689.

[8]   H. Aliasghari, A. M. Arabi, H. Haratizadeh, Ceram. Int., 46 (2020) 403.

[9]   R. B. Shinde, A. S. Patil, S. V. Sadavar, Y. M. Chitare, V. V. Magdum, N. S. Padalkar, U. M. Patil, S. T. Kochuveedu, V. G. Parale, H. H. Park, C. D. Lokhande, J. L. Gunjakar, Sens. Actuators B: Chem., 352 (2022) 131046.

[10]   M. Waseen, Z. Shah, R. V. Cataluna, S. L. P. Dias, É. C. Lima, G. S. D. Reis, J. C. P. Vaghetti, W. S. D. Alencar, K. Mahmood, J. Anal. Bioanal. Tech., 8 (2018) 1000348.

[11]   V. G. Erkov, S. F. Devyatova, E. L. Molodstova, T. V. Malsteva, U. A. Yanovskii, Appl. Sur. Sci., 166 (2000) 51.

[12]   Q. Hu, J. He, J. Chang, J. Gao, J. Huang, L. Feng, ACS Appl. Nano Mater., 3 (2020) 9046.

[13]   L. Zhao, X. Chen, Y. Zhang, Z. Ye, Y. Zeng, J. Environ. Chem. Eng., 10 (2022) 107672.

[14]   T. Gao, H. Fjellvag, P. Norby, J. Phy. Chem. B, 112 (2008) 9400.

[15]   S. V. Sadavar, N. S. Padalkar, R. B. Shinde, A. S. Patil, U. M. Patil, V. V. Magdum, Y. M. Chitare, S. P. Kulkarni, S. B. Kale, R. N. Bulakhe, D. S. Bhange, S. T. Kochuveedu, J. L. Gunjakar, Energy Storage Mater., 48 (2022) 101.

[16]   L. Wang, B. Cheng, L. Zhang, J. Yu, Small, 17 (2021) 2103447.

[17]   R. B. Shinde, N. S. Padalkar, S. V. Sadavar, S. B. Kale, V. V. Magdum, Y. M. Chitare, S. P. Kulkarni, U. M. Patil, V. G. Parale, H. H. Park, J. L. Gunjakar, J. Hazard. Mater., 432 (2022) 128734.

[18]   E. Valadbeigi, A. R. Modarresi-Alam, M. Noroozifar, A. R. Rezvani, Express Poly. Lett., 16 (2022) 939.

[19]   H. Xu, R. Zheng, D. Du, L. Ren, X. Wen, X. Wang, G. Tian, C. Shu, Small, 19 (2023) 2206611.

[20]   M. Kotal, A. Sharma, S. Jakhar, V. Mishra, S. Roy, S. C. Sahoo, H. K. Sharma, S. K. Mehta, Cryst. Growth Des., 20 (2020) 4627.

[21]   S. Meng, W. Sun, S. Zhang, X. Zheng, X. Fu, S. Chen, J. Phys. Chem. C, 122 (2018) 26326.

[22]   S. A. Patil, N. K. Shrestha, S. Hussain, J. Jung, S. W. Lee, C. Bathula, A. N. Kadam, H. Im, H. Kim, J. Hazard. Mater., 417 (2021) 126105.

[23]   S. Shi, P. Guo, M. I. Anwar, W. Zhang, W. Zhang, G. Yang, J. Hazard. Mater., 406 (2021) 124757.

CHAPTER-VI

Synthesis and Characterization of WO$_3$-hexaniobate-NS Heterostructure Thin Films by CBD: Application in Photocatalytic Dye Degradation

CHAPTER VI

Synthesis and Characterization of WO₃-hexaniobate-NS Heterostructure Thin Films by CBD: Application in Photocatalytic Dye Degradation

6.1. Introduction:

The importance of removing contaminants from wastewater using heterogeneous photocatalysts and the benefits of hybridization for improving their photocatalytic performance is described in **Chapter 1**, **section 1.8**. In that context, the visible-light active tungsten oxide thin films were grown on the common EDP-deposited titanate-NS thin film platform by CBD and m-SILAR methods. **Chapter 4** and **Chapter 5**, respectively, explored the CBD and m-SILAR methods for depositing WO_3 thin films on EPD-deposited titanate-NS thin films for visible-light-driven photooxidation of dyes. With these hybridization strategies, the photocatalytic degradation performance of pristine samples is increased due to strong visible-light harvesting ability, high surface area, porous morphology, and reduced electron-hole pair recombination via effective electronic coupling between hybridized species.

Similar to titanate-NS, the 2D nanosheets synthesized by the exfoliation of potassium hexaniobate displayed highly stable photocatalytic performance for the photooxidation of organic contaminants [1]. The potassium hexaniobate has received much attention due to ultrathin thickness, morphology, larger surface area, high photostability, well-developed electronic structure, and a distinctive lamellar structure composed of negatively charged layers with potassium ions existing between layers to maintain charge neutrality [2-4]. Also, hexaniobate-NS derived from the exfoliation of potassium hexaniobate displays ultrathin thickness, high structural flexibility, unique anisotropic structure, and high compositional flexibility. Due to these advantages, hexaniobate-NS evokes research interest as a platform to grow narrow bandgap semiconductor photocatalysts.

Due to the above advantages of hexaniobate-NS, the visible-light-active WO_3 thin films were grown on the EDP-deposited hexaniobate-NS thin film platform using the CBD method. The EPD method was used to deposit hexaniobate-NS thin films, whereas the CBD method was used to grow a WO_3 thin films on hexaniobate-NS thin films. The obtained heterostructure thin films are denoted as NbW-C heterostructure thin films. The physicochemical properties and photocatalytic activity of NbW-C heterostructure thin films were examined, and that was compared with that of pristine WO_3 and hexaniobate-NS thin films. The MB and Rh B are selected as the target molecules for the degradation.

6.2 Synthesis and characterizations of NbW-C heterostructure thin films:

6.2.1 Experimental details:

6.2.1.1 Chemicals:

Nb$_2$O$_5$, K$_2$CO$_3$, Na$_2$WO$_4$.H$_2$O, H$_2$C$_2$O$_4$, HCl, TBAOH, C$_2$H$_5$OH, MB, and Rh B were purchased from Sigma-Aldrich and used without purification.

6.2.1.2 Synthesis of hexaniobate-NS thin films:

The synthesis of exfoliated hexaniobate-NS and hexaniobate-NS thin films was similar to as discussed in **Chapter 3, sections 3.3.1.2** and **3.3.1.3**, respectively.

6.2.1.3 Synthesis of NbW-C heterostructure thin films:

The visible light active WO$_3$ was coated over the EPD-deposited hexaniobate-NS thin films using the CBD method. The schematic representation of NbW-C heterostructure thin films using the CBD method is shown in **Fig. 6.1**. The NbW-C heterostructure thin films were prepared by a similar method described in **Chapter 4, section 4.2.1.3**, wherein hexaniobate-NS thin films were used instead of titanate-NS thin films. The NbW-C heterostructure thin films deposited on hexaniobate-NS-8, hexaniobate-NS-16, and hexaniobate-NS-24 are denoted as NbW-8-C, NbW-16-C, and NbW-24-C, respectively. For comparison, the pristine WO$_3$ thin films were deposited using the same method on the glass substrate.
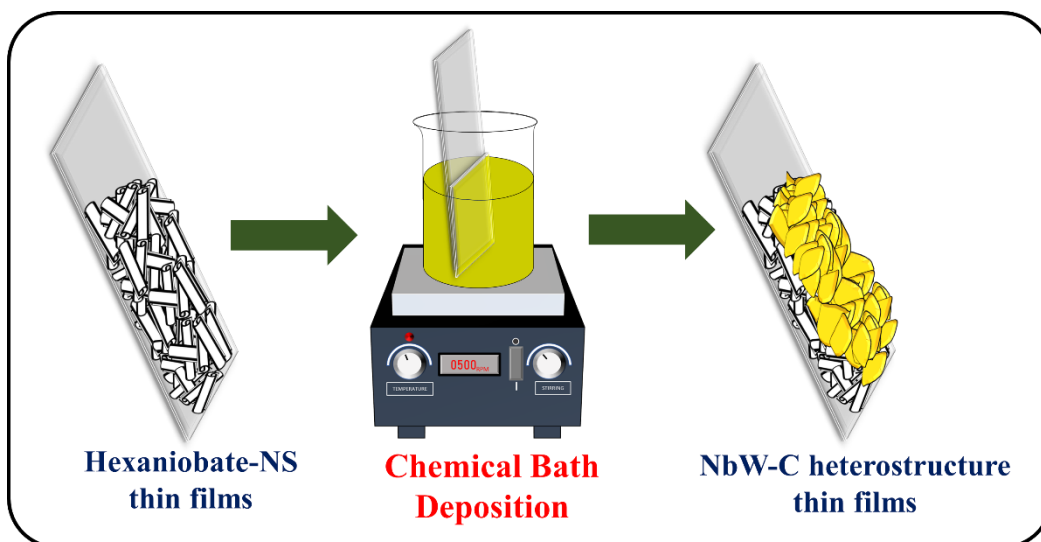
Fig. 6.1. Schematic of NbW-C heterostructure thin films deposition.

6.2.1.4 Material characterizations:

The pristine WO$_3$, hexaniobate-NS, and NbW-C heterostructure thin films were characterized by various physicochemical characterization techniques similar to those described in **Chapter 3, section 3.2.1.4.**

6.2.1.5 Experimental setup for dye degradation:

The experimental setup for the visible-light-induced dye degradation by NbW-C heterostructures thin films is similar to that described in **Chapter 4**, **section 4.2.1.6**.

6.2.2 Results and Discussion:

6.2.2.1 XRD study:
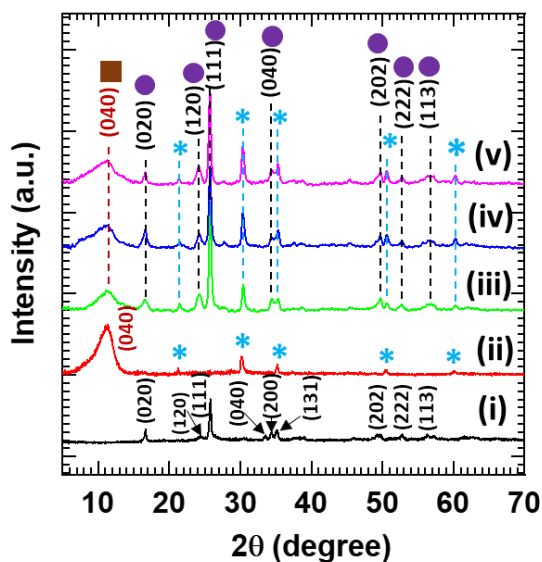
Fig. 6.2. XRD patterns of (i) WO₃, (ii) hexaniobate-NS, (iii) NbW-8-C, (iv) NbW-16-C, and (v) NbW-24-C heterostructure thin films.

The XRD patterns of pristine WO₃, hexaniobate-NS, and NbW-C heterostructure thin films are plotted in **Fig. 6.2**. For the comparison, the XRD patterns of CBD-deposited WO₃ and EPD-deposited hexaniobate-NS are plotted again in **Fig. 6.2(i)** and **Fig. 6.2(ii)**, respectively. The XRD analysis of pristine WO₃ and hexaniobate-NS thin films are discussed in **Chapter 4**, **section 4.2.2.1** and **Chapter 3**, **section 3.3.2.1**, respectively. After the coating of WO₃ over hexaniobate-NS thin film, all NbW-C heterostructure thin films show a broad diffraction peak indexed as (040) at 11.2º with a layered spacing of 0.78 nm, indicating the hexaniobate-NS are restacked layer by layer on the ITO substrate and form the oriented hexaniobate-NS thin film [5, 6]. Moreover, NbW-C heterostructure thin films also show several Braggs reflections that are well-matched with (020), (120), (111), (040), (202), (222), and (113) planes of orthorhombic (Pmnb) type monohydrate layered WO₃·H₂O phase (JCPDS card no. 01-084-0886) [7]. The peaks marked by '*' correspond to the ITO substrate. The present XRD features related to the hexaniobate-NS and WO₃ clearly indicate the growth of WO₃ over hexaniobate-NS thin films, highlighting the formation of NbW-C heterostructure thin

films. No other peak matches with other phases of hexaniobate, indicating the high mechanical and chemical stability of hexaniobate-NS thin films.

6.2.2.2 FT-IR study:
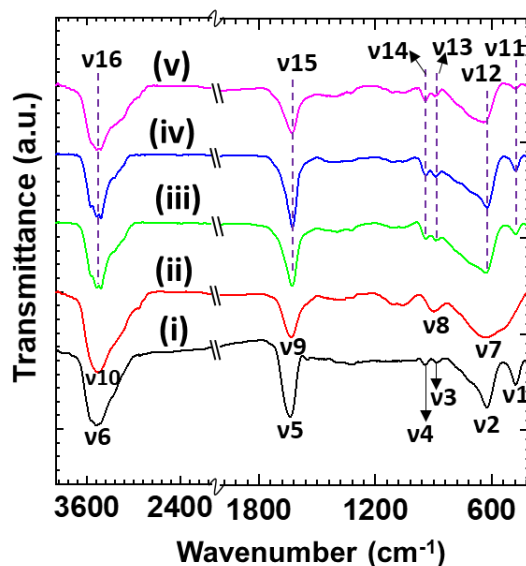
Fig. 6.3. FT-IR spectra of (i) WO₃, (ii) hexaniobate-NS, (iii) NbW-8-C, (iv) NbW-16-C, and (v) NbW-24-C heterostructure thin films.

The FT-IR spectra of pristine WO₃, hexaniobate-NS, and NbW-C heterostructure in the 400 to 4000 cm^{-1} range are shown in **Fig. 6.3**. For the comparison, the FT-IR spectra of CBD-deposited WO₃ and EPD-deposited hexaniobate-NS are plotted again in **Fig. 6.3(i)** and **Fig. 6.3(ii)**, respectively. The FT-IR analysis of pristine WO₃ and hexaniobate-NS is discussed in **Chapter 4**, **section 4.2.2.2**, and **Chapter 3**, **section 3.3.2.2**, respectively. As seen from **Fig. 6.3**, the NbW-C heterostructure thin films show absorption peaks related to the WO₃ and hexaniobate-NS. The absorption peak ν11 (482 cm^{-1}) is assigned to the W-O-W stretching vibrations. The absorption peaks ν13 (881 cm^{-1}) and ν14 (945 cm^{-1}) are assigned to the O-W-O stretching and W=O vibrations, respectively [8, 9]. These characteristic absorption peaks are related to orthorhombic WO₃. The broad absorption peak ν12 (450-750 cm^{-1}) is associated with the O-Nb-O stretching vibrations in the NbO₆ octahedron [10]. The absorption peaks ν15 (1633 cm^{-1}) and ν16 (3422 cm^{-1}) are related to the bending vibrational modes of water molecules and stretching vibration of the O-H groups, respectively [11, 12]. The peaks related to metal-oxygen vibrations are broad and carry minute shoulder peaks due to superpositions of WO₃ and hexaniobate-NS IR peaks. The broadening of these peaks can be regarded as an indicator of strong electronic coupling and hybridization between

the WO$_3$ and hexaniobate-NS layers. These IR characteristics indicate the successful formation of the NbW-C heterostructure.

6.2.2.3 Micro-Raman study:
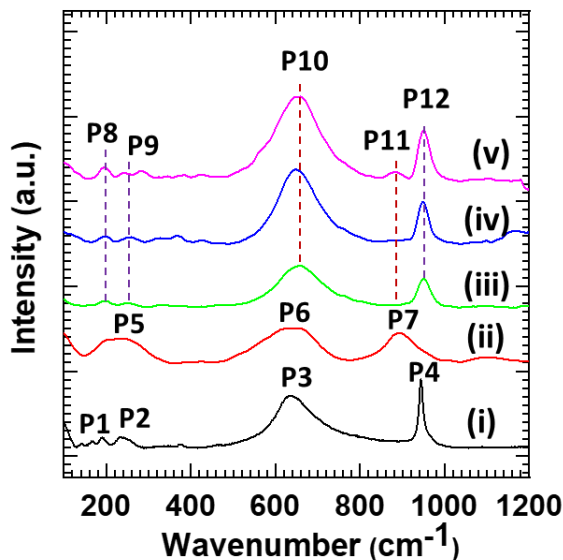
Fig. 6.4. Micro-Raman spectra of (i) WO$_3$, (ii) hexaniobate-NS, (iii) NbW-8-C, (iv) NbW-16-C, and (v) NbW-24-C heterostructure thin films.

The chemical bonding character of the WO$_3$, hexaniobate-NS, and NbW-C heterostructures is investigated with Raman spectroscopy, as shown in **Fig. 6.4**. For the comparison, the micro-Raman spectra of CBD-deposited WO$_3$ from **Chapter 4, Fig. 4.6** and EPD-deposited hexaniobate-NS from **Chapter 3, Fig. 3.14**, are plotted as **Fig. 6.4(i)** and **Fig. 6.4(ii)**, respectively. The micro-Raman analysis of pristine WO$_3$ and hexaniobate-NS are discussed in **Chapter 4**, **section 4.2.2.3** and **Chapter 3**, **section 3.3.2.3**, respectively. The NbW-C heterostructure thin film displays the low-intensity Raman peaks P8 (190 cm^{-1}) and P9 (236 cm^{-1}), which correspond to the lattice vibrations of the WO$_3$ and bending vibrations of the W-O-W bond, respectively [13, 14]. The broad peak P10 (500-700 cm^{-1}) and mild peak P11 (883 cm^{-1}) correspond to the stretching of longer Nb-O bond and Nb-O terminal group with shorter bonds, respectively [15, 16]. In addition, the Raman peak P12 (944 cm^{-1}) corresponds to the stretching vibration of W=O bonds [14]. Moreover, the Raman peaks P10 and P12 broaden due to the superposition of WO$_3$ and hexaniobate-NS peaks. These characteristics Raman features related to WO$_3$ and hexaniobate-NS in NbW-C heterostructure highlight the intactness of hexaniobate-NS during heterostructure formation. These results underscore effective hybridization between the hexaniobate-NS and WO$_3$.

6.2.2.4 FE-SEM study:
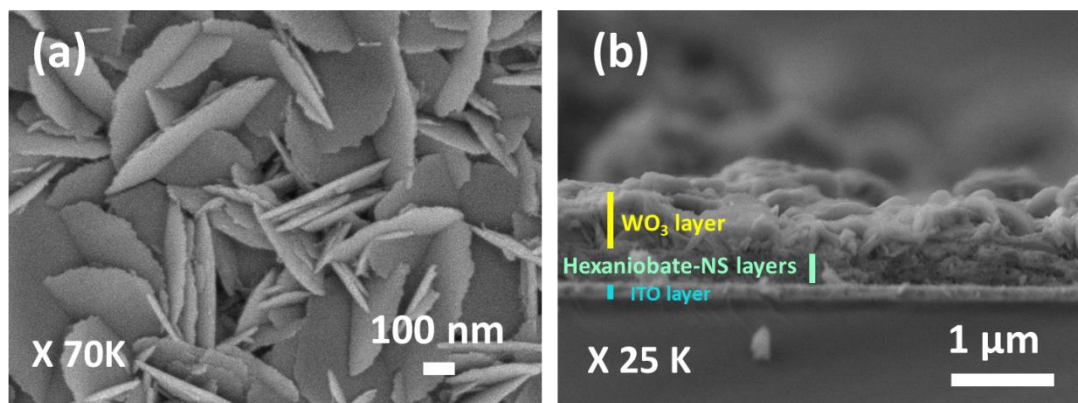
Fig. 6.5. FE-SEM images of (a) top-view and (b) cross-sectional view of NbW-16-C heterostructure thin films.

The microstructural surface and stacking structure of NbW-C heterostructures thin films were studied using FE-SEM analysis. The surface microstructural analysis of pristine WO_3 and hexaniobate-NS are discussed in **Chapter 4**, **section 4.2.2.4**, and **Chapter 3, section 3.3.2.4**, respectively. The top and cross-sectional FE-SEM images of optimized NbW-16-C heterostructure thin films are shown in **Fig. 6.5**. The top-view of NbW-16-C heterostructure thin films shows vertical growth of WO_3 nanoplates on hexaniobate-NS. The NbW-16-C heterostructure thin films display average nanoplates length, width, and thickness of 550, 350, and 26 nm, respectively. The cross-section image of the NbW-16-C heterostructure thin film clearly distinguishes separate layers of deposited materials. The bottom layers correspond to the ITO layer on a glass substrate. The top layers are composed of randomly grown WO_3 nanoplates on parallelly stacked hexaniobate-NS. The random growth of WO_3 nanoplates on hexaniobate-NS leads to a high surface area morphology. This type of heterostructure can enable intimate electronic coupling between the hexaniobate-NS and WO_3, which is highly suitable for lowering the electron-hole pair recombination in photocatalytic applications.

6.2.2.5 EDS study:

The spatial distribution of constituent elements in NbW-16-C heterostructure was studied with elemental mapping and EDS analysis, as shown in **Fig. 6.6** and **Fig 6.7**, respectively. The NbW-C heterostructure thin film shows a uniform distribution of tungsten (W), niobium (Nb), and oxygen (O) elements across the elemental mapping area, confirming the uniform growth of WO_3 nanoplates on the

surface of hexaniobate-NS thin films. The atomic percentage ratio of Nb/W is 0.8 for NbW-16-C heterostructure thin film.
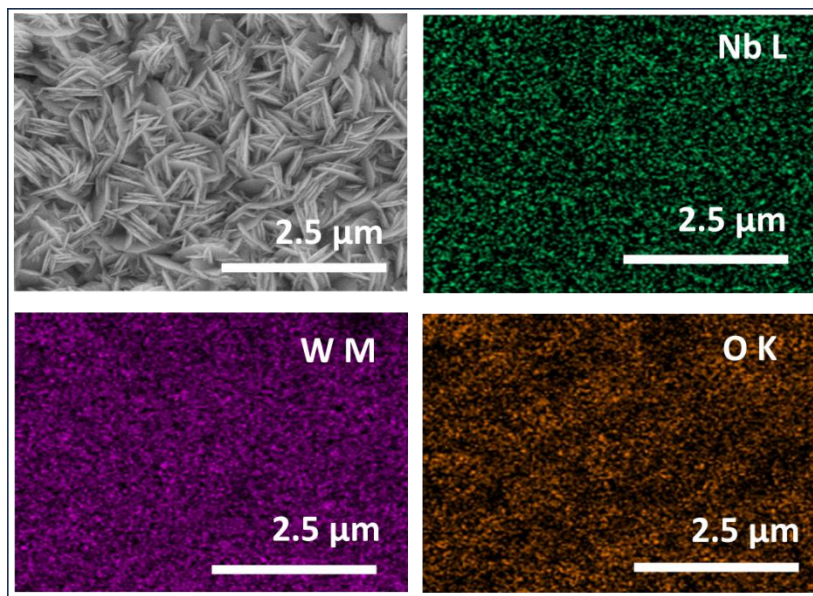
Fig. 6.6. FE-SEM image along with EDS-elemental mapping of NbW-16-C heterostructure thin film.
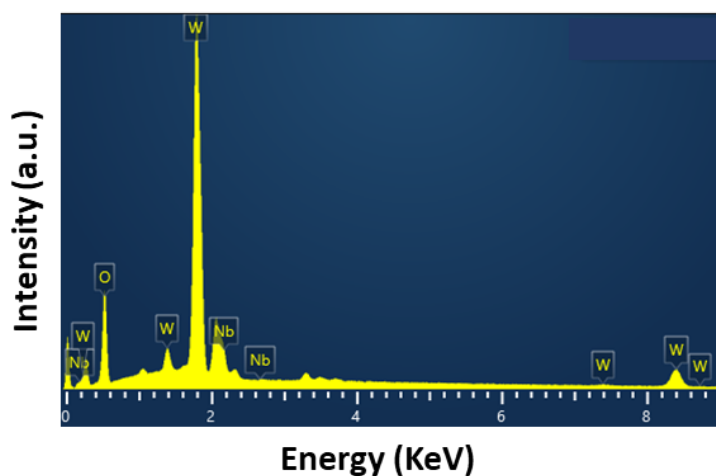
Fig. 6.7. EDS spectrum of NbW-16-C heterostructure thin film.

6.2.2.6 XPS study:

The surface elemental states present in the WO₃, hexaniobate-NS, and NbW-C heterostructures thin films were studied using XPS measurements. The survey XPS spectra of WO₃, hexaniobate-NS, and NbW-C heterostructures thin films are shown in **Fig. 6.8**. For the comparison, the XPS spectrum of CBD deposited WO₃ and EPD-deposited hexaniobate-NS are plotted again in **Fig. 6.8(i)** and **Fig. 6.8(ii)**, respectively. The XPS analysis of pristine WO₃ and hexaniobate-NS are discussed in **Chapter 4, section 4.2.2.6** and **Chapter 3, section 3.3.2.5**, respectively.
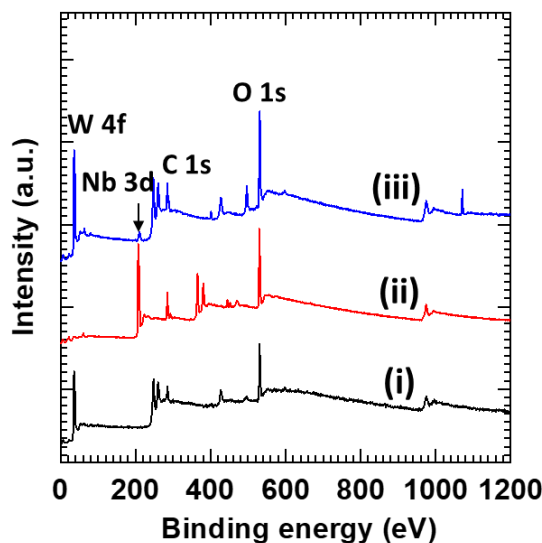
Fig. 6.8. XPS survey spectra of (i) WO₃, (ii) hexaniobate-NS, and (iii) NbW-16-C heterostructure thin films.

The survey XPS spectrum of NbW-C heterostructure thin film commonly displays spectral features at the binding energy of the elements W, Nb, and O, indicating the presence of these elements in the NbW-16-C heterostructure thin film.
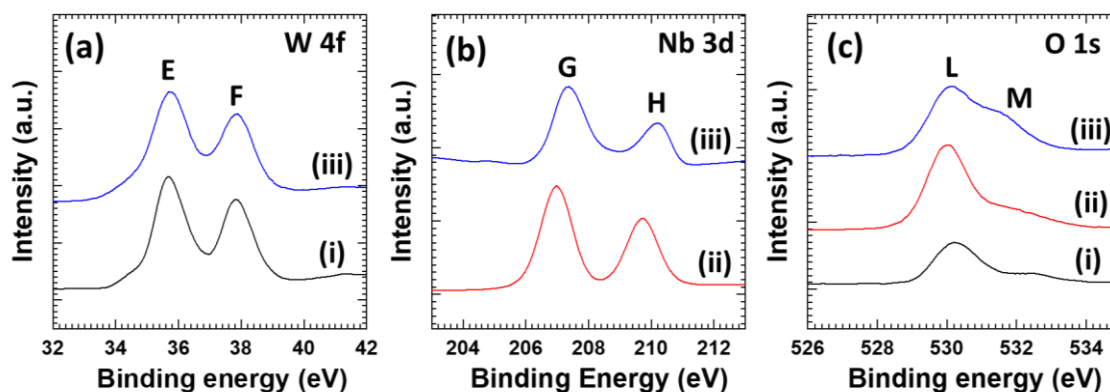
Fig. 6.9. (a) W 4f, (b) Nb 3d, and (c) O 1s core-level XPS spectra of (i) WO₃, (ii) hexaniobate-NS, and (iii) NbW-16-C heterostructure thin films.

The high-resolution core-level spectra of W 4f, Nb 3d, and O 1s are depicted in **Fig. 6.9 (a-c)**. For the comparison, the W 4f, Nb 3d, and O 1s core-level spectra of pristine WO₃ and hexaniobate-NS are plotted again as **Fig. 6.9(a)**, **Fig. 6.9(b)**, and **Fig. 6.9(c)**, respectively. The XPS analysis of core-level W 4f and Nb 3d spectra are discussed in **Chapter 4**, **section 4.2.2.6** and **Chapter 3**, **section 3.3.2.5**, respectively. As shown in **Fig. 6.9**, the high-resolution W 4f core-level spectra, which are only discernable for pristine WO₃ and NbW-16-C heterostructure thin films, show two spectral features at E (35.7 eV) and F (37.8 eV) corresponding to spin-orbit splitting of

W $4f_{7/2}$ and W $4f_{5/2}$, respectively. The observed spectral features are typically seen for W-O bond configuration, indicating W^{6+} in NbW-16-C heterostructure thin film [17]. Whereas high-resolution Nb 3d spectra of hexaniobate-NS and NbW-16-C heterostructure thin films show two spectral features, G (207 eV) and H (209.6 eV), that originated due to the spin-orbit splitting of Nb $3d_{5/2}$ and Nb $3d_{3/2}$, respectively. These spectral features indicate the presence of Nb^{5+} in the hexaniobate-NS and NbW-16-C heterostructure thin films [18]. Moreover, the O 1s core-level spectra commonly show peak L (530.3 eV) and shoulder at M (531.9 eV), indicating the presence of oxygen in metal oxide and a hydroxyl group (-OH group) originating from structural or adsorbed water molecules, respectively [19]. The observed XPS features indicate the presence of W^{6+} and Nb^{5+} states of W and Nb, respectively, confirming the formation of the NbW-C heterostructure.

6.2.2.7 UV-vis DRS study:
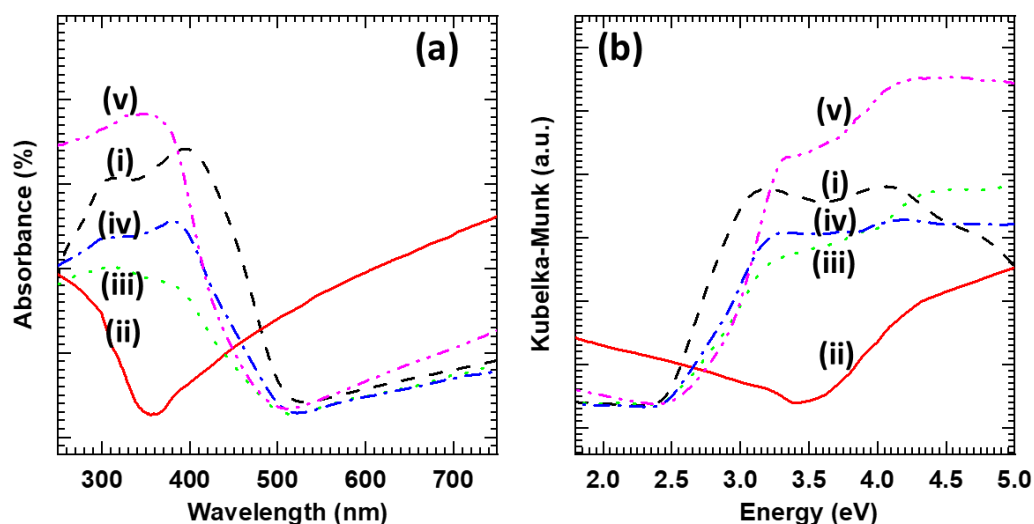
Fig. 6.10 (a) UV-vis absorbance spectra obtained from DRS and (b) UV-vis DRS (plotted as Kubelka-Munk function of reflectance, R) of (i) WO₃ (dashed lines), (ii) hexaniobate-NS (solid lines), (iii) NbW-8-C (dotted lines), (iv) NbW-16-C (dash-dotted lines), and (v) NbW-24-C (dash-dot-dotted lines) heterostructure thin films.

UV-vis DRS was used to investigate the optical properties of pristine WO₃, hexaniobate-NS, and NbW-C heterostructure thin films. As seen in **Fig. 6.10a**, pristine WO₃ and hexaniobate-NS thin films show prominent absorption in visible and UV regions of the electromagnetic spectrum, respectively. For the comparison, the UV-vis DRS spectra of CBD-deposited WO₃ and EPD-deposited hexaniobate-NS are plotted again in **Fig. 6.10(i)** and **Fig. 6.10(ii)**, respectively. The UV-vis DRS spectra analysis of

pristine WO_3 and hexaniobate-NS are discussed in **Chapter 4**, **section 4.2.2.7** and **Chapter 3**, **section 3.3.2.6**, respectively. Interestingly, upon the growth of WO_3 on the hexaniobate-NS, the resultant NbW-C heterostructure thin films show significant absorption in the visible region, clearly underscoring the efficient electronic coupling between hexaniobate-NS and WO_3. The NbW-C heterostructure thin films absorb visible light in the 510 to 527 nm wavelength range, corresponding to the bandgap energies of 2.43 to 2.35 eV. The plot of the Kubelka-Munk function vs. energy is depicted in **Fig. 10(b)**. Based on the Kubelka-Munk function, the bandgap energies are estimated and summarized in **Table 6.1**. The strong visible light absorption ability of NbW-C heterostructures makes them suitable candidates for visible-light-driven photocatalysis applications.

Thin film photocatalyst	Bandgap energy (eV)
WO_3	2.33
hexaniobate-NS	3.45
NbW-8-C	2.43
NbW-16-C	2.39
NbW-24-C	2.35

Table 6.1. Synthesized photocatalyst thin films and their estimated band gap energies.

Based on the bandgap energy, the CB and VB potentials of the hexaniobate-NS and WO_3 thin films are discussed in **Chapter 3**, **section 3.3.2.6** and **Chapter 4**, **section 4.2.2.7**. The schematic of the band edge potential of WO_3 and hexaniobate-NS thin film is shown in **Fig. 6.11**.
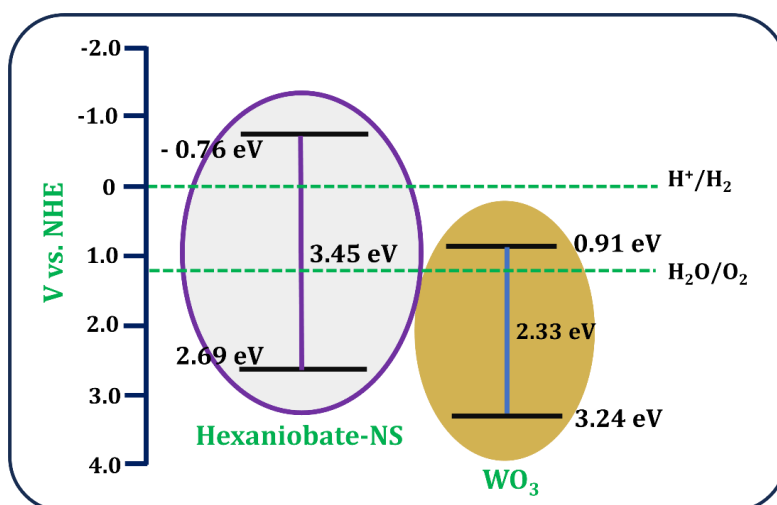
Fig. 6.11. Schematic representation for the energy band structure of hexaniobate-NS and WO_3 thin films.

6.3 Photocatalytic activity:

6.3.1 Dye degradation study:
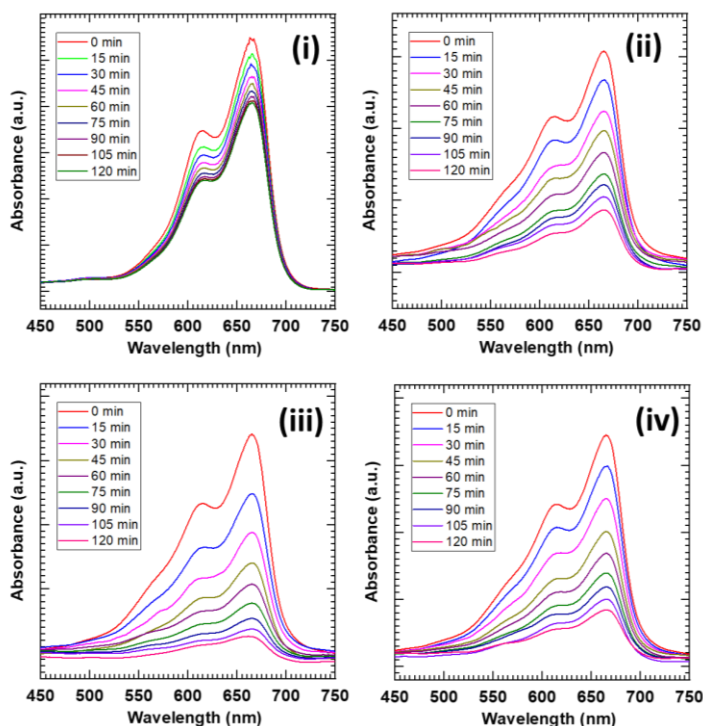
Fig. 6.12. Absorption spectra of MB for (i) hexaniobate-NS, (ii) NbW-8-C, (iii) NbW-16-C, and (iv) NbW-24-C heterostructure thin films.
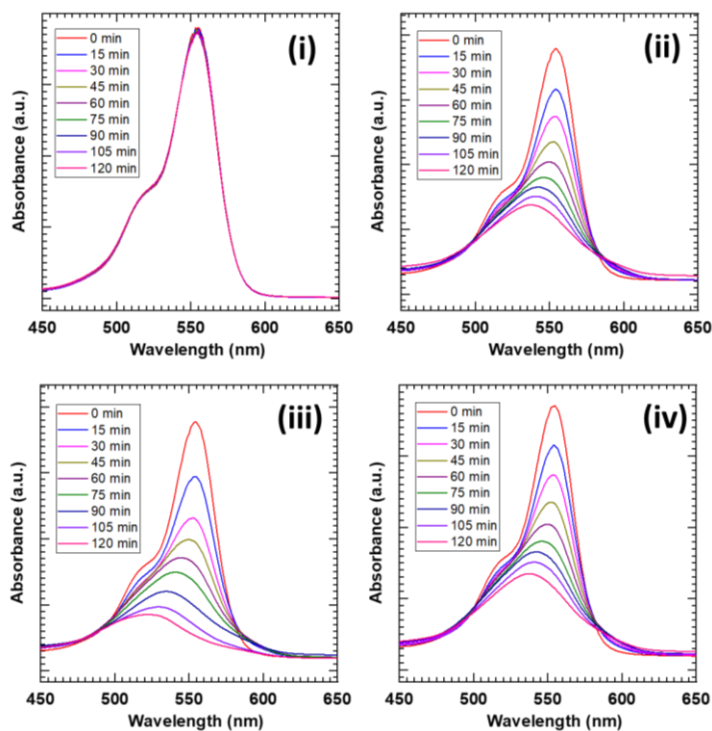
Fig. 6.13. Absorption spectra of Rh B for (i) hexaniobate-NS, (ii) NbW-8-C, (iii) NbW-16-C, and (iv) NbW-24-C heterostructure thin films.
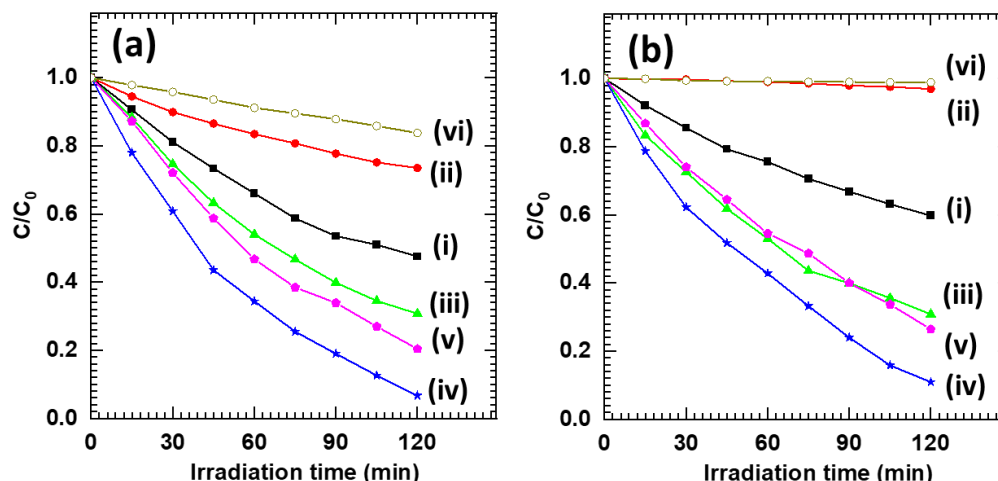
Fig. 6.14. Photocatalytic degradation performance of MB (a) and Rh B (b) for (i) WO₃, (ii) hexaniobate-NS, (iii) NbW-8-C, (iv) NbW-16-C, (v) NbW-24-C heterostructure thin films, and (vi) without thin film.

The photocatalytic activity of NbW-C heterostructure thin films was examined by monitoring the time-dependent photodegradation of MB and Rh B under visible light illumination ($\lambda > 420$ nm) and compared with pristine WO₃ and hexaniobate-NS thin films. The time-dependent absorption spectra of MB and Rh B for pristine hexaniobate-NS and NbW-C heterostructure thin films are shown in **Fig. 6.12** and **Fig. 6.13**, respectively. The time-dependent absorption spectra of MB and Rh B for pristine WO₃ and without thin films are represented in **Chapter 4, section 4.3.1**. The absorption peak intensity of MB and Rh B at a characteristic wavelength of 665 and 554 nm decreases with visible-light-irradiation time, indicating that both the dye molecules are degraded. As shown in **Fig. 6.14(a-b)**, the visible-light-driven photocatalytic degradation of MB and Rh B indicates that the pristine WO₃ and NbW-C heterostructure thin films are photocatalytically active. For the comparison, the degradation performance of MB and Rh B with and without WO₃ thin films are plotted again in **Fig. 6.14(a)** and **Fig. 6.14(b)**, respectively. The photocatalytic activity of pristine WO₃ is discussed in **Chapter 4, section 4.3.1**. However, pristine hexaniobate-NS thin film shows a negligible photodegradation performance of 26% and 4% for MB and Rh B, respectively, in 120 min. Furthermore, NbW-C heterostructure thin films show improved photocatalytic activity due to hybridization. Among the thin films of NbW-C heterostructure synthesized at different deposition times, the NbW-16-C heterostructure thin film shows a maximum photodegradation activity of 94% for MB and 90% for Rh B in the same period, which is higher than pristine WO₃ and hexaniobate-NS thin films. Further, it

decreases to nearly 78% for NbW-24-C heterostructure thin film due to the peel-off of the loosely bound WO_3 layer. Such peel-off of deposits is commonly observed for the thicker chemically deposited thin films. The enhanced photocatalytic degradation performance of NbW-C heterostructure thin films can ascribed to the porous nanoplate morphology, strong visible-light harvesting ability, and spatial separation of electron-hole pair due to the effective electronic coupling between WO_3 and hexaniobate-NS.

6.3.2 Kinetic study:
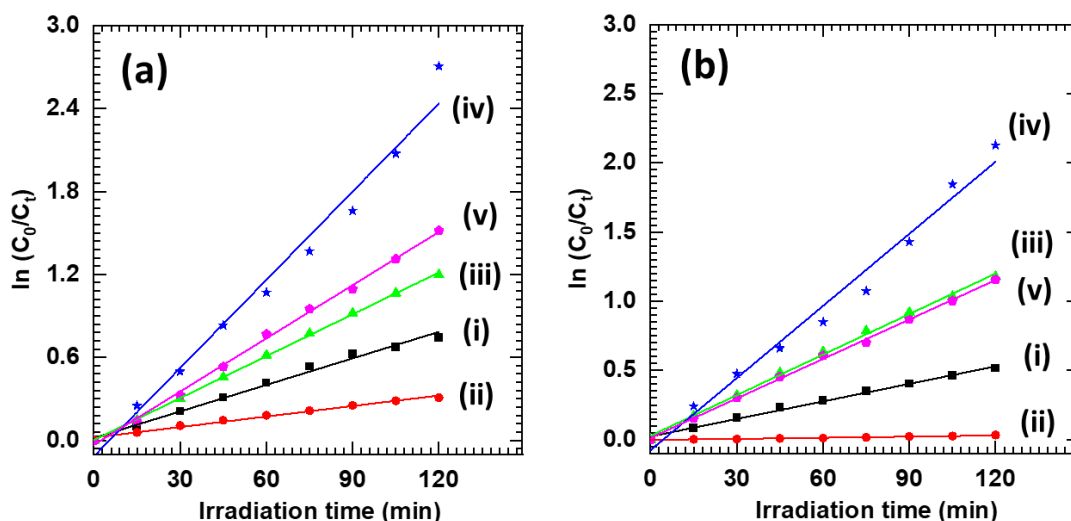
Fig. 6.15. Pseudo-first-order kinetics of MB (a) and Rh B (b) for (i) WO_3, (ii) hexaniobate-NS, (iii) NbW-8-C, (iv) NbW-16-C, and (v) NbW-24-C heterostructure thin films.

The high photocatalytic degradation performance is further confirmed by the first-order reaction kinetics [20]. **Fig. 6.15(a)** and **Fig. 6.15(b)** show the pseudo-first-order kinetics plots for MB and Rh B, respectively. For the comparison, the first-order reaction kinetics of MB and Rh B for WO_3 thin films are plotted again in **Fig. 6.15(a)** and **Fig. 6.15(b)**, respectively. The k and R^2 values are given in **Table 6.2**. The NbW-16-C heterostructure thin film exhibits the highest k-values of 0.0212 and 0.0173 min^{-1} for MB and Rh B, respectively. The photocatalytic reaction rate of NbW-16-C heterostructure thin film for MB is 3.36 and 8.48 times greater than pristine WO_3 and hexaniobate-NS, thin films, respectively. Meanwhile, for Rh B, it is 4.11 and 66.5 times higher than pristine WO_3 and hexaniobate-NS thin films, respectively. The higher k-values for NbW-C heterostructure thin film are attributed to the strong visible light harvesting ability, minimal electron-hole pair recombination, high photostability, and effective electronic coupling between hybridized layers. These results highlighted the

usefulness of NbW-C heterostructure thin films for the photocatalytic degradation of organic molecules.

Thin Film	MB		Rh B	
	k (min $^{-1}$)	R^2	k (min $^{-1}$)	R^2
WO$_3$	0.0063	0.99	0.0042	0.99
hexaniobate-NS	0.0025	0.98	0.00026	0.97
NbW-8-C	0.0101	0.99	0.097	0.99
NbW-16-C	0.0212	0.98	0.0173	0.98
NbW-24-C	0.0128	0.99	0.0095	0.99

Table 6.2. The k and R^2 values of all pristine WO$_3$, hexaniobate-NS, and NbW-C heterostructure thin films.

6.3.3 Recycling study:
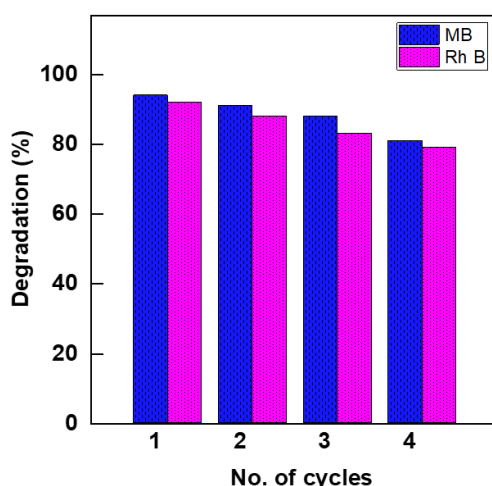
Fig. 6.16. Recyclability study of NbW-16-C heterostructure thin film.

Further, a recycling study of optimized NbW-16-C heterostructure thin film is examined over the course of four consecutive cycles. As represented in **Fig. 6.16**, after four consecutive cycles of NbW-16-C heterostructure thin films retain 81 and 76 % of the photocatalytic performance for MB and Rh B, respectively. The minute decline performance after four consecutive cycles was attributed to the adsorption of target organic molecules on the surface of the photocatalyst and the loss of loosely bound photocatalyst crystals from the film.

6.3.4 Photocatalytic degradation mechanism:

The photocatalytic decomposition of organic molecules involves charge separation and migration to the photocatalyst surface. **Fig. 6.17** illustrates the plausible photocatalytic dye degradation mechanism upon exposure to light irradiation. When

photons with appropriate energy are incident on the NbW-16-C heterostructure, electrons from the VB of WO_3 are excited to its CB, which results in the formation of electron-hole pairs. As represented in **Fig. 6.17**, the CB of hexaniobate-NS (-0.76 eV) is more negative than that of WO_3 (0.91 eV) and the VB of WO_3 (3.24 eV) is more positive than that of hexaniobate-NS (2.69 eV) with respect to NHE [21]. The photogenerated electrons from the CB of WO_3 can migrate into the VB of hexaniobate-NS, leading to the spatial separation of electrons and holes. As a result, the lifetime of holes in the VB of WO_3 increases. The detailed explanation of surface redox reaction is discussed in **Chapter 4, section 4.3.4**.
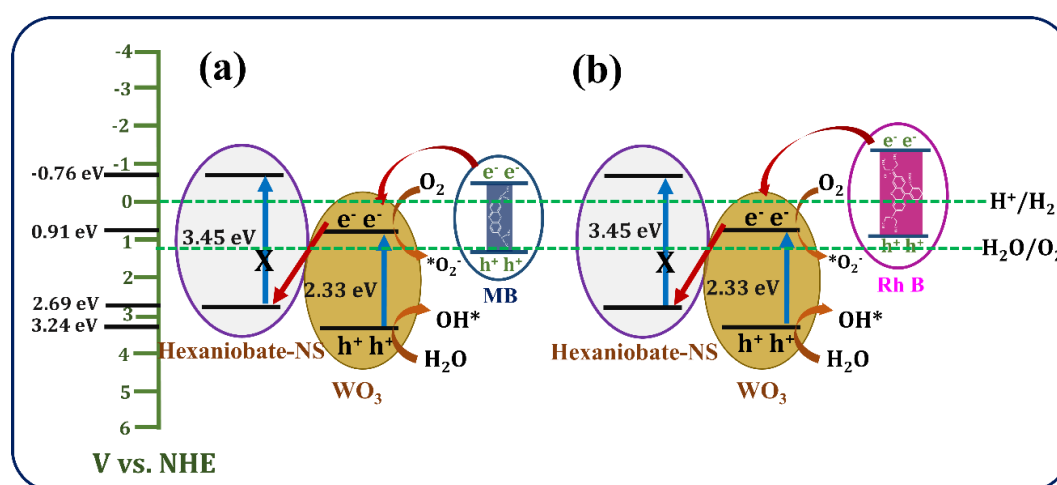
Fig. 6.17. Schematic diagram for plausible photodegradation of (a) MB and (b) Rh B.

6.4 Conclusions:

In this work, the NbW-16-C heterostructure thin films are synthesized by EPD followed by CBD methods. The deposited thin films are used to study MB and Rh B photocatalytic degradation activity under visible light. The structural analysis of NbW-16-C heterostructure thin films revealed diffraction peaks corresponding to both hexaniobate-NS and WO_3, indicating the growth of WO_3 over the EPD-deposited hexaniobate-NS thin films. Surface microstructure analysis shows that WO_3 nanoplates are vertically grown on the hexaniobate-NS surface, enabling the intimate electronic coupling between hexaniobate-NS and WO_3. An optical study demonstrated the significant absorption of visible light by the NbW-16-C heterostructure thin films. Among the different heterostructure thin films, the NbW-16-C heterostructure thin film exhibited improved visible-light active photodegradation performance of 94% with a rate constant of 0.0212 min^{-1} for MB in 120 min. Meanwhile, for Rh B, it is 90% with a rate constant of 0.0212 min^{-1}. The enhanced photocatalytic degradation performance of

heterostructure thin film photocatalysts is attributed to the strong visible-light harvesting ability, spatial separation of electron-hole pair due to the effective electronic coupling, and porous morphology. The present study highlighted the effectiveness of heterostructure thin films in depressing electron-hole recombination, which significantly enhances the photocatalytic activity of the pristine WO_3 thin films. This approach demonstrates the potential of depositing narrow-bandgap semiconductors over the wide-bandgap semiconductor to improve visible-light-driven photocatalytic performance.

6.5 References:

[1]   B. N. Nunes, D. W. Bahnemann, T. Otavi, A. Patrocinio, ChemPhotoChem, 6 (2022) 202100272.
[2]   E. C. C., ACS Appl. Nano Mater., 3 (2020) 8483.
[3]   J. Li, Z. Li, J. Dong, R. Fang, Y. Chi, C. Hu, ACS Catalysis, 13 (2023) 5272.
[4]   S. Elumalai, S. Vadivel, M. Yoshimura, Mater. Adv., 2 (2021) 1957.
[5]   R. Abe, M. Hara, J. N. Kondo, K. Domen, K. Shinohara, A. Tanaka, Chem. Mater., 10 (1998) 1647.
[6]   A. L. Shiguihara, M. A. Bizeto, V. R. Constantino, J. Braz. Chem. Soc., 21 (2018) 1366.
[7]   S. P. Gupta, M. A. More, D. J. Late, P. S. Walke, Electrochim. Acta, 366 (2021) 137389.
[8]   Y. M. Chitare, V. V. Magdum, S. P. Kulkarni, S. V. Talekar, S. A. Pawar, P. D. Sawant, D. B. Malavekar, U. M. Patil, C. D. Lokhande, J. L. Gunjakar, Appl. Surf. Sci. Adv., 19 (2024) 100573.
[9]   S. P. Gupta, H. H. Nishad, S. D. Chakane, S. W. Gosavi, D. J. Late, P. S. Walke, Nanoscale Adv., 2 (2020) 4689.
[10]   B. N. Nunes, C. Haisch, A. V. Emeline, D. W. Bahnemann, A.O.T., Patrocinio, Catal. Today, 326 (2019) 60.
[11]   P. P. Bagwade, V. V. Magdum, D. B. Malavekar, Y. M. Chitare, J. L. Gunjakar, U. M. Patil, C. D. Lokhande, J. Mater. Sci. Mater. Electron., 33 (2022) 24646.
[12]   N. S. Padalkar, C. H. Cho, V. V. Magdum, Y. M. Chitare, S. P. Kulkarni, U. M. Patil, J. P. Park, J. L. Gunjakar, J. Energy Storage, 74 (2023) 109538.
[13]   Q. Hu, J. He, J. Chang, J. Gao, J. Huang, L. Feng, ACS Appl. Nano Mater., 3 (2020) 9046.
[14]   Q. Yao, G. Ren, K. Xu, L. Zhu, H. Khan, M. Mohiuddin, M. W. Khan, B. Y. Zhang, A. Jannat, F. Haque, S. Z. Reza, Adv. Opt. Mater., 7 (2019) 1901383.
[15]   E. C. C. Souza, J. Phys. Chem. C, 123 (2019) 24426.
[16]   T. Goswami, K. M. Reddy, A. Bheemaraju, Chem. Select, 4 (2019) 6790.
[17]   S. V. Sadavar, N. S. Padalkar, R. B. Shinde, A. S. Patil, U. M. Patil, V. V. Magdum, Y. M. Chitare, S. P. Kulkarni, S. B. Kale, R. N. Bulakhe, D. S. Bhange, S. T. Kochuveedu, J. L. Gunjakar, Energy Stor. Mater., 48 (2022) 101.
[18]   R. B. Shinde, N. S. Padalkar, S. V. Sadavar, S. B. Kale, V. V. Magdum, Y. M. Chitare, S. P. Kulkarni, U. M. Patil, V. G. Parale, H. H. Park, J. L. Gunjakar, J. Hazard. Mater., 432 (2022) 128734.
[19]   N. S. Padalkar, S. V. Sadavar, R. B. Shinde, A. S. Patil, U. M. Patil, D. S. Dhawale, R. N. Bulakhe, H. Kim, H. Im, A. Vinu, C. D. Lokhande, J. L. Gunjakar, J. Colloid Interface Sci., 616 (2022) 548.
[20]   M. Kotal, A. Sharma, S. Jakhar, V. Mishra, S. Roy, S. C. Sahoo, H. K. Sharma, S. K. Mehta, Cryst. Growth Des., 20 (2020) 4627.
[21]   E. J. Hernandez-Moreno, A. M. De La Cruz, L. Hinojosa-Reyes, J. Guzman-Mar, M. A. Gracia-Pinilla, A. J. M. T. C. Hernandez-Ramirez, Mater. Today Chem., 19 (2021) 100406.

CHAPTER-VII

Synthesis and Characterization of WO$_3$-hexaniobate-NS Heterostructure Thin Films by SILAR: Application in Photocatalytic Dye Degradation

CHAPTER VII

Synthesis and Characterization of WO₃-hexaniobate-NS Heterostructure Thin Films by SILAR: Application in Photocatalytic Dye Degradation

7.1. Introduction:

Heterogeneous photocatalysis has been considered an emerging technology to remove toxic dyes from polluted water. The features of hybridization in order to enhance the photocatalytic activity of the pristine materials are described in **Chapter 1**, **section 1.8.** Moreover, **Chapter 4** and **Chapter 5** explore the utilization of CBD and m-SILAR methods for the growth of WO₃ with titanate-NS and the use of these heterostructure photocatalysts for enhancing photocatalytic efficiency. Moreover, the growth of WO₃ on hexaniobate-NS using the CBD method is explored in **Chapter 6**.

Considering the advantages of the SILAR method, as described in **Chapter 5**, **section 5.1**, this method can be utilized to synthesize NbW-S heterostructure thin films. As described in **Chapter 3**, the EPD method was used to deposit hexaniobate-NS thin films. The m-SILAR method was used to deposit WO₃ on EPD-deposited hexaniobate-NS thin films. The obtained heterostructure thin films are denoted by NbW-S thin films. Further, the physicochemical properties of NbW-S heterostructure thin films are studied and compared to those of pristine WO₃ and hexaniobate-NS thin films. The photocatalytic activity of NbW-S heterostructure thin films for MB and Rh B degradation is evaluated and compared with pristine WO₃ and hexaniobate-NS.

7.2 Synthesis and characterizations of NbW-S heterostructure thin films:

7.2.1 Experimental details:

7.2.1.1 Chemicals:

Nb₂O₅, K₂CO₃, Na₂WO₄.H₂O, H₂C₂O₄, HCl, TBAOH, C₂H₅OH, MB, and Rh B were purchased from Sigma-Aldrich and used without purification.

7.2.1.2 Synthesis of hexaniobate-NS thin films:

The synthesis of exfoliated hexaniobate-NS and hexaniobate-NS thin films was similar to as discussed in **Chapter 3, sections 3.3.1.2** and **3.3.1.3**, respectively.

7.2.1.3 Synthesis of NbW-S heterostructure thin films:

The narrow bandgap WO₃ was deposited over the EPD-deposited hexaniobate-NS thin films by the m-SILAR method. The experimental conditions for preparing WO₃ thin film were similar to those described in **Chapter 5, section 5.2.1.3**. The growth of WO₃ by the m-SILAR method comprising immersion of EPD-deposited hexaniobate-NS thin film into separately placed adsorption and reaction baths (two-beaker process). The one deposition cycle of m-SILAR was completed by successive immersion of hexaniobate-NS thin film into an adsorption bath for 40 seconds and then into a reaction

bath for the next 20 seconds. The WO$_3$ was deposited on the hexaniobate-NS thin film by repeating such 75 deposition cycles. The deposited NbW-S heterostructure thin films were washed with DDW and dried at room temperature. The schematic illustration of NbW-S heterostructure thin films using the m-SILAR method is represented in **Fig. 7.1**. The NbW-S heterostructure thin films deposited on hexaniobate-NS-8, hexaniobate-NS-16, and hexaniobate-NS-24 are denoted as NbW-8-S, NbW-16-S, and NbW-24-S, respectively.
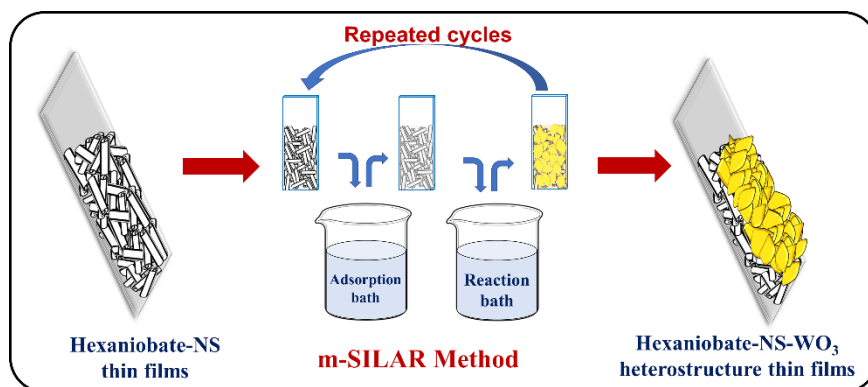
Fig. 7.1. Schematic representation of NbW-S heterostructure thin films deposition.

7.2.1.4 Material characterizations:

The pristine WO$_3$, hexaniobate-NS, and NbW-S heterostructure thin films were characterized by various physicochemical characterization techniques similar to those described in **Chapter 3, section 3.2.1.4**.

7.2.1.5 Experimental setup for dye degradation:

The experimental setup for the visible-light-induced dye degradation by NbW-S heterostructures thin films is similar to that described in **Chapter 4, section 4.2.1.6**.

7.2.2 Results and Discussion:

7.2.2.1 XRD study:

The XRD patterns of pristine WO$_3$, hexaniobate-NS, and NbW-S heterostructure thin films are plotted in **Fig. 7.2**. For the comparison, the XRD patterns of m-SILAR deposited WO$_3$ and EPD-deposited hexaniobate-NS are plotted in **Fig. 7.2(i)** and **Fig. 7.2(ii)**, respectively. The XRD analysis of pristine WO$_3$ and hexaniobate-NS is described in **Chapter 5**, **section 5.2.2.1**, and **Chapter 3**, **section 3.3.2.1**, respectively. After the deposition of WO$_3$ using the m-SILAR method, the NbW-S heterostructure thin film displays a broad diffraction peak indexed as (040) at 11.2°. According to this peak, interlayer spacing of 0.78 nm is obtained for the NbW-S heterostructure thin film, highlighting the layer-by-layer restacking of hexaniobate-NS on the ITO substrate [1].
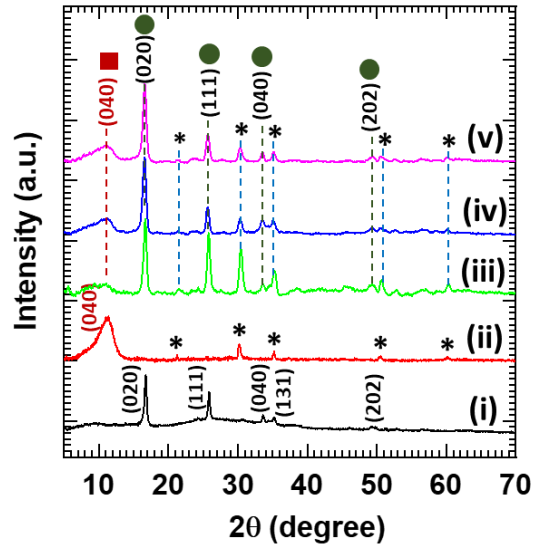
Fig. 7.2. XRD patterns of (i) WO$_3$, (ii) hexaniobate-NS, (iii) NbW-8-S, (iv) NbW-16-S, and (v) NbW-24-S heterostructure thin films.

In addition, NbW-S heterostructure thin films display the sharp diffraction peaks (020), (111), (040), and (202) are well-matched with orthorhombic WO$_3$·H$_2$O phase (JCPDS card no. 01-084-0886) [2]. However, the peaks assigned by '*' are related to the ITO substrate. This XRD features matching with the hexaniobate-NS and WO$_3$ clearly show the growth of WO$_3$ over EPD-deposited hexaniobate-NS thin films, confirming the formation of NbW-S heterostructure thin films. The diffraction peaks corresponding to hexaniobate-NS thin film indicate the layer-by-layer stacking with the high mechanical and chemical stability of hexaniobate-NS thin film.

7.2.2.2 FT-IR study:
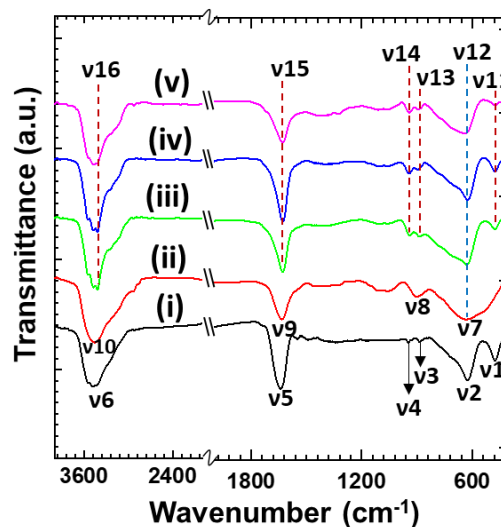
Fig. 7.3. FT-IR spectra of (i) WO$_3$, (ii) hexaniobate-NS, (iii) NbW-8-S, (iv) NbW-16-S, and (v) NbW-24-S heterostructure thin films.

The chemical bonding nature of pristine WO_3, hexaniobate-NS, and NbW-S heterostructure was probed with FT-IR spectroscopy. For the comparison, the FT-IR spectra of m-SILAR deposited WO_3 and EPD-deposited hexaniobate-NS are plotted in **Fig. 7.3(i)** and **Fig. 7.3(ii)**, respectively. The FT-IR analysis of pristine WO_3 and hexaniobate-NS is discussed in **Chapter 5**, **section 5.2.2.2**, and **Chapter 3**, **section 3.3.2.2**, respectively. The FT-IR spectra of NbW-S heterostructure thin films represented in **Fig. 7.3** show absorption peaks related to WO_3 and hexaniobate-NS. The absorption peaks ν11 (483 cm^{-1}) correspond to the metal-oxygen stretching vibration (W-O-W) [3]. The absorption peaks ν13 (882 cm^{-1}) and ν14 (945 cm^{-1}) are ascribed to the O-W-O and W=O vibrations, respectively [4]. These characteristic absorption peaks below 1000 cm^{-1} are related to the $WO_3.H_2O$ phase. In addition, O-Nb-O stretching vibration in the NbO_6 octahedron is represented by broad absorption peak ν12 (450-750 cm^{-1}) [5]. The absorption peaks ν15 (1633 cm^{-1}) and ν16 (3422 cm^{-1}) are related to the bending vibrational modes of water molecules and stretching vibration of the O-H groups, respectively [6]. The peaks related to metal-oxygen vibrations are broad and carry minute shoulder peaks due to superpositions of WO_3 and hexaniobate-NS IR peaks. These FT-IR features underscore the strong electronic coupling and hybridization between the WO_3 and hexaniobate-NS layers.

7.2.2.3 Micro-Raman study:
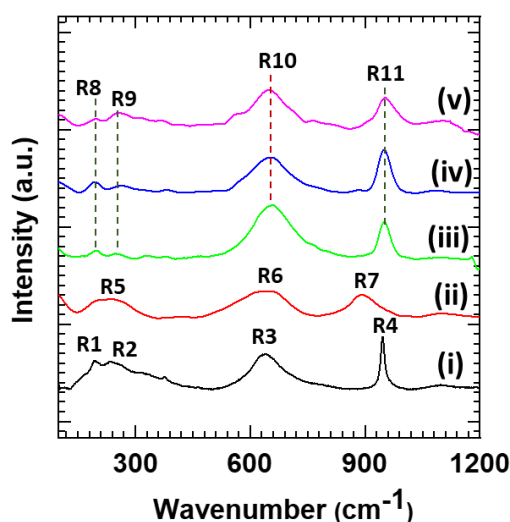
Fig. 7.4. Micro-Raman spectra of (i) WO_3, (ii) hexaniobate-NS, (iii) NbW-8-S, (iv) NbW-16-S, and (v) NbW-24-S heterostructure thin films.

Fig. 7.4 represents the micro-Raman spectra of pristine WO_3, hexaniobate-NS, and NbW-S heterostructure thin films. For the comparison, the micro-Raman spectra of

m-SILAR deposited WO_3 and EPD-deposited hexaniobate-NS are plotted in **Fig. 7.4(i)** and **Fig. 7.4(ii)**, respectively. The micro-Raman analysis of pristine WO_3 and hexaniobate-NS are described in **Chapter 5**, **section 5.2.2.3** and **Chapter 3**, **section 3.3.2.3**, respectively. After the deposition of WO_3 over EPD hexaniobate-NS thin film, NbW-S heterostructure thin films exhibit the characteristic Raman features related to WO_3 and hexaniobate-NS. The NbW-S heterostructure thin film displays the Raman peaks R8 (195 cm^{-1}) and R9 (251 cm^{-1}) related to the lattice vibrations of WO_3 and bending vibrations of the metal-oxygen (W-O-W) bond, respectively. The peak R11 (944 cm^{-1}) is assigned to the stretching vibrations of terminal W=O bonds [7, 8]. These distinctive Raman features are the characteristics of the orthorhombic $WO_3.H_2O$ phase. On the other hand, the Raman peak R10 (951 cm^{-1}) is related to the Nb-O stretching of longer Nb-O bonds [9, 10]. The peak assigned at R11 (948 cm^{-1}) is attributed to the stretching vibration of W=O bonds [8]. The peaks R10 and R11 slightly broaden due to the superposition of WO_3 and hexaniobate-NS peaks. These characteristics Raman features related to WO_3 and hexaniobate-NS in NbW-S heterostructure clearly emphasize the intactness of hexaniobate-NS during heterostructure formation. These spectral features underscore the effective growth of WO_3 over EPD-deposited hexaniobate-NS thin films.

7.2.2.4 FE-SEM study:
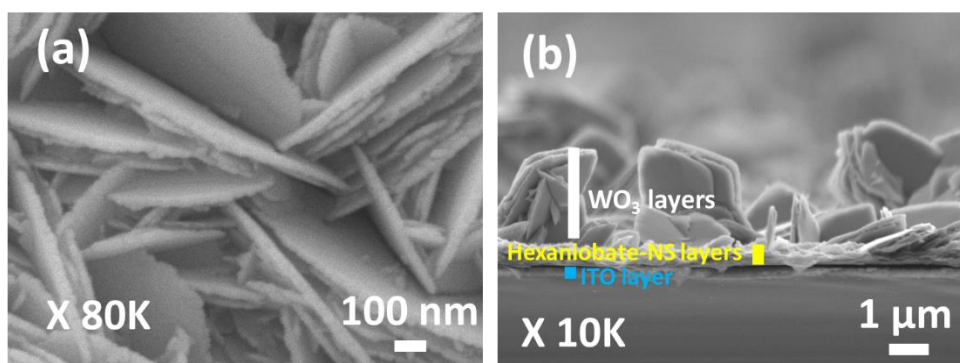
Fig. 7.5. (a) Top view and (b) cross-sectional view FE-SEM images of NbW-8-S heterostructure thin films.

The microstructural surface and stacking structure of NbW-S heterostructures thin films were studied using FE-SEM analysis. The surface microstructural analysis of pristine WO_3 and hexaniobate-NS are described in **Chapter 5**, **section 5.2.2.4**, and **Chapter 3**, **section 3.3.2.4**, respectively. The top and cross-sectional FE-SEM images of optimized NbW-8-S heterostructure thin films are shown in **Fig. 7.5**. The NbW-8-S

heterostructure thin film (**Fig. 7.5(a)**) shows growth of vertically aligned interlocked WO$_3$ nanosheets on hexaniobate-NS. The NbW-8-S heterostructure thin films display average nanosheets length, width, and thickness of 650, 380, and 23 nm, respectively. Moreover, the cross-section image of the NbW-8-S heterostructure thin film shown in **Fig. 7.5(b)** clearly distinguishes the separate layers of deposited material on the ITO-coated glass substrate. The top layers are composed of WO$_3$ nanosheets grown on horizontally stacked hexaniobate-NS. The bottom layer corresponds to a thin hexaniobate-NS layer deposited on the ITO. Such a heterostructure facilitates the intimate electronic coupling between the hexaniobate-NS and WO$_3$, which is beneficial for the depression of electron-hole pair recombination.

7.2.2.5 EDS study:
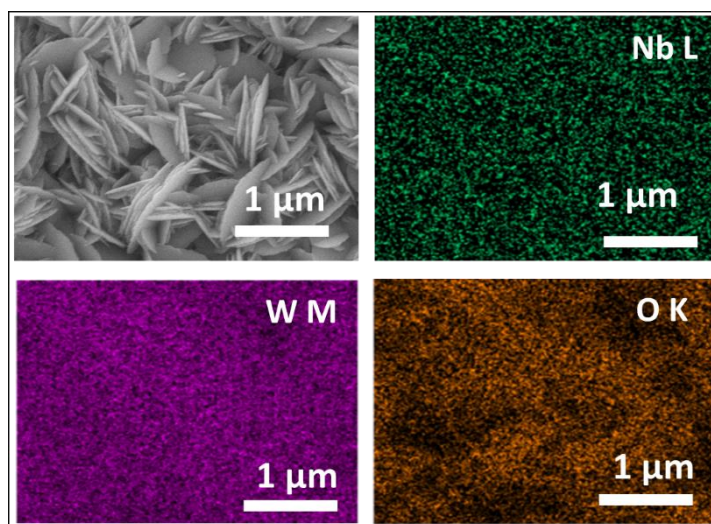
Fig. 7.6. FE-SEM image along with EDS-elemental mapping of NbW-8-S heterostructure thin film.
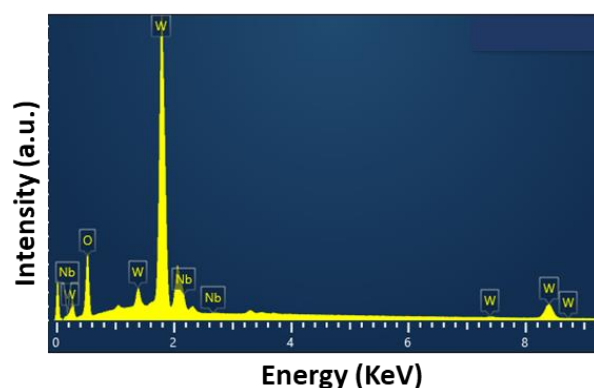
Fig. 7.7. EDS spectrum of NbW-8-S heterostructure thin film.

The spatial distribution of constituent elements in NbW-8-S heterostructure was examined with elemental mapping and EDS analysis, as shown in **Fig. 7.6** and **Fig. 7.7**,

respectively. The NbW-8-S heterostructure shows all the constituent elements (tungsten, hexaniobate, and oxygen) are uniformly distributed across the elemental mapping area, demonstrating the homogeneous growth of WO_3 on the surface of hexaniobate-NS. The atomic percentage ratio of Nb/W is 0.3 for NbW-8-S heterostructure thin film.

7.2.2.6 XPS study:
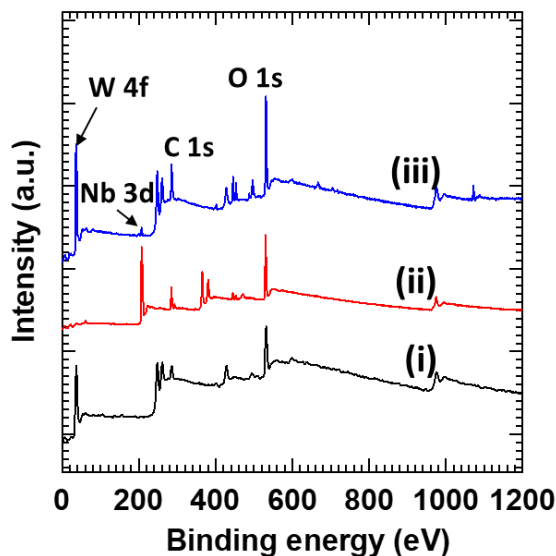
Fig. 7.8. XPS survey spectra of (i) WO_3, (ii) hexaniobate-NS, and (iii) NbW-8-S heterostructure thin films.

The XPS analysis was used to investigate the surface elemental states in the WO_3, hexaniobate-NS, and NbW-S heterostructure thin films. **Fig. 7.8** represents the survey XPS spectra of W, Nb, and O elements. For the comparison, the XPS spectrum of m-SILAR deposited WO_3 and EPD-deposited hexaniobate-NS are plotted again in **Fig. 7.8(i)** and **Fig. 7.8(ii)**, respectively. The survey XPS spectra analysis of pristine WO_3 and hexaniobate-NS are described in **Chapter 5, section 5.2.2.6** and **Chapter 3, section 3.3.2.5**, respectively. The survey XPS spectrum of NbW-8-S heterostructures thin film exhibits spectral features at the binding energy of the elements W, Nb, and O, highlighting the existence of these elements in the NbW-8-S heterostructures thin film.

The high-resolution core-level spectra of W 4f, Nb 3d, and O 1s are depicted in **Fig. 7.9**. For the comparison, the W 4f, Nb 3d, and O 1s core-level spectra of pristine WO_3 and hexaniobate-NS are plotted again in **Fig. 7.9(a)**, **Fig. 7.9(b)**, and **Fig. 7.9(c)**, respectively. The core-level spectra analysis of W 4f and Nb 3d are described in **Chapter 5, section 5.2.2.6** and **Chapter 3**, **section 3.3.2.5**, respectively. As shown in **Fig. 7.9(a)**, the high-resolution W 4f core-level spectra are only discernable for WO_3 and NbW-S heterostructure thin films.
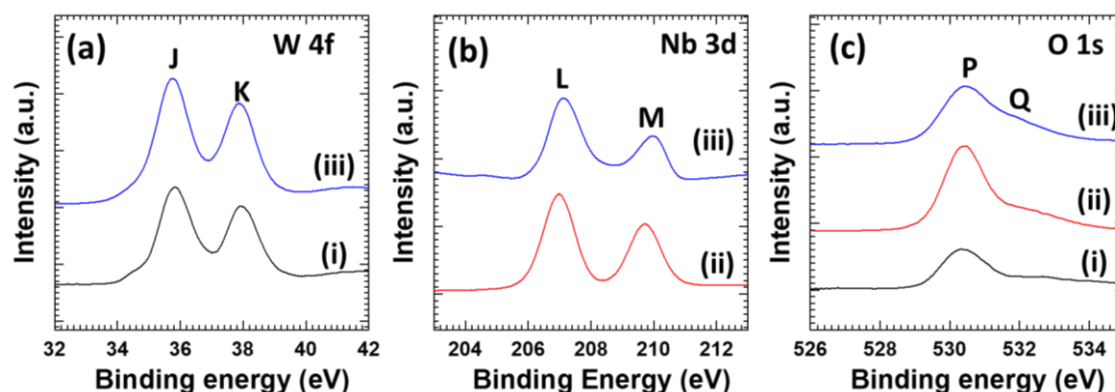
Fig. 7.9. (a) W 4f, (b) Nb 3d, and (c) O 1s core-level XPS spectra of (i) WO$_3$, (ii) hexaniobate-NS, and (iii) NbW-8-S heterostructure thin films.

The NbW-8-S heterostructure thin films show two spectral features, J (35.7 eV) and K (37.9 eV), corresponding to spin-orbit splitting W 4f$_{7/2}$ and W 4f$_{5/2}$ components, respectively. The J and K binding energies are characteristic of the W-O bond configuration, indicating W^{6+} in NbW-8-S heterostructure thin film [11]. Whereas, high-resolution Nb 3d spectra of hexaniobate-NS and NbW-8-S heterostructure thin films depicted in **Fig. 7.9(b)** show two spectral features at the binding energies L (207.1 eV) and M (209.7 eV) are ascribed to the spin-orbit splitting of Nb 3d$_{5/2}$ and Nb 3d$_{3/2}$, respectively which indicate Nb^{5+} in NbW-S heterostructure thin film [12]. In addition, the O 1s spectra represented in **Fig. 7.9(c)** commonly show peak P (530.2 eV) with a shoulder at Q (531.6 eV), indicating the presence of oxygen in metal oxide and hydroxyl group (-OH group) originating from structural or adsorbed water molecules, respectively [13]. The observed XPS features underscore the presence of W^{6+} and Nb^{5+} states of W and Nb, respectively, which confirms the formation of the NbW-S heterostructure.

7.2.2.7 UV-vis DRS study:

The optical properties of pristine WO$_3$, hexaniobate-NS, and NbW-S heterostructure thin films were studied with UV-vis DRS. As seen in **Fig. 7.10a**, pristine WO$_3$ and hexaniobate-NS thin films show prominent absorption in visible and UV regions of the electromagnetic spectrum, respectively. For the comparison, the UV-vis DRS spectra of m-SILAR deposited WO$_3$ and EPD-deposited hexaniobate-NS are plotted again in **Fig. 7.10(i)** and **Fig. 7.10(ii)**, respectively. The UV-vis DRS spectra analysis of pristine WO$_3$ and hexaniobate-NS are described in **Chapter 5**, **section 5.2.2.7** and **Chapter 3**, **section 3.3.2.6**, respectively.
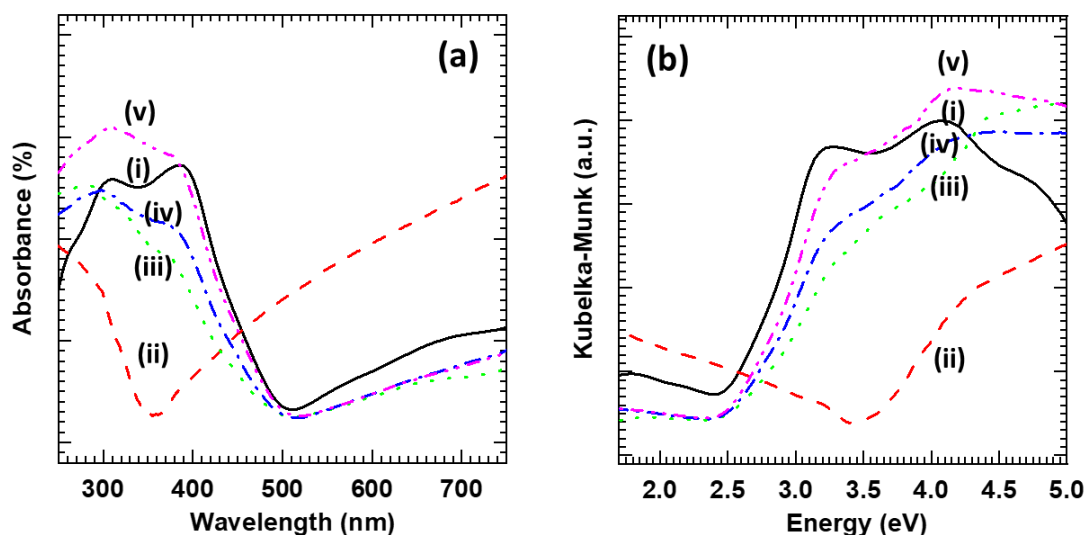
Fig. 7.10. (a) UV-vis absorbance spectra obtained from DRS and (b) UV-vis DRS (plotted as Kubelka-Munk function of reflectance, R) of (i) WO₃ (solid lines), (ii) hexaniobate-NS (dashed lines), (iii) NbW-8-S (dotted lines), (iv) NbW-16-S (dash-dotted lines), and (v) NbW-24-S (dash-dot-dotted lines) heterostructure thin films.

Moreover, the NbW-S heterostructure thin films show a prominent absorption in the visible region, highlighting the effective electronic coupling between hexaniobate-NS and WO₃. NbW-S heterostructure thin films absorb visible light in the wavelength between 527-539 nm, corresponding to the band gap energies between 2.35- 2.30 eV. The band gap energies of WO₃, pristine hexaniobate-NS, and NbW-S heterostructures thin films investigated from the Kubelka-Munk function are displayed in **Fig. 7.10(b)** and **Table 7.1**. The strong visible light absorption ability of NbW-S heterostructures makes them potential candidates for visible-light-driven photo-functional applications.

Thin film photocatalyst	Bandgap energy (eV)
WO₃	2.28
hexaniobate-NS	3.45
NbW-8-S	2.35
NbW-16-S	2.32
NbW-24-S	2.30

Table 7.1. Synthesized photocatalyst thin films and their estimated band gap energies.

Based on the energy bandgap, the CB and VB potentials of the hexaniobate-NS and WO₃ thin films are discussed in **Chapter 3, section 3.3.2.6** and **Chapter 5, section**

5.2.2.7. The schematic of the band edge potential of WO_3 and hexaniobate-NS thin film is shown in **Fig. 7.11**.
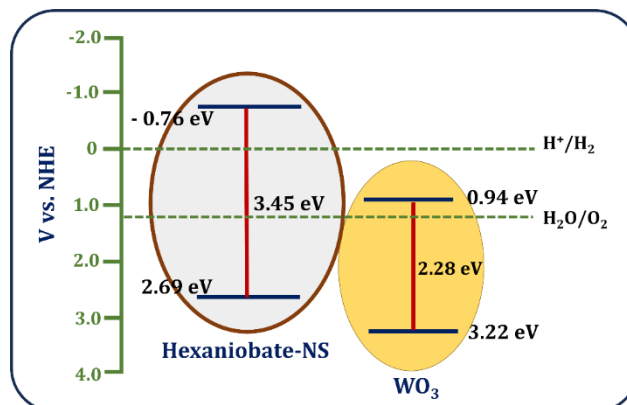
Fig. 7.11. Schematic representation for the energy band structure of hexaniobate-NS and WO_3 thin films.

7.3 Photocatalytic activity:

7.3.1 Dye degradation study:
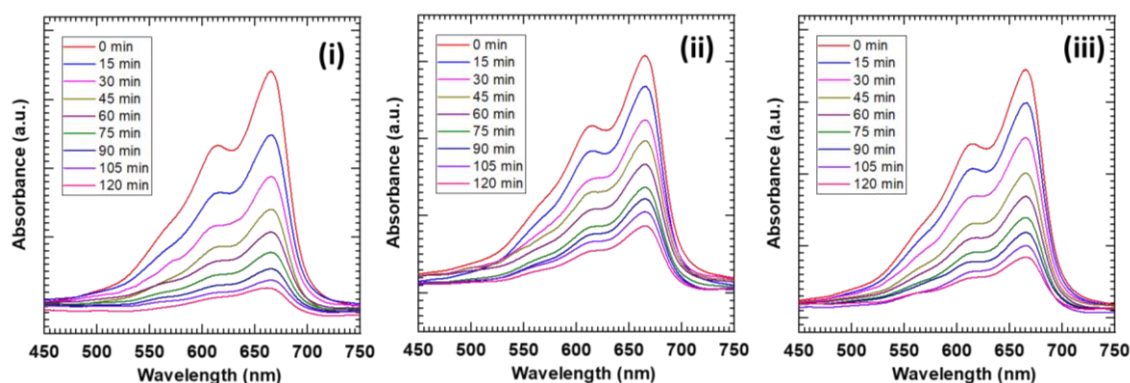
Fig. 7.12. Absorption spectra of MB for (i) NbW-8-S, (ii) NbW-16-S, and (iii) NbW-24-S heterostructure thin films.
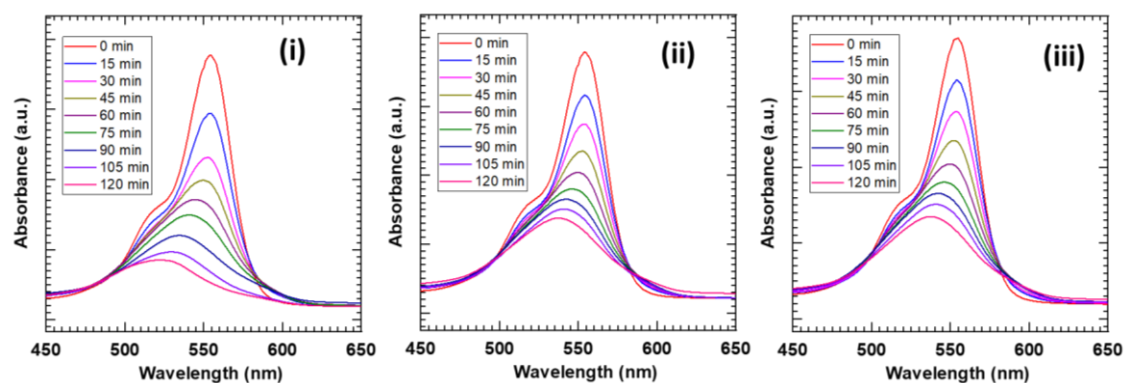
Fig. 7.13. Absorption spectra of Rh B for (i) NbW-8-S, (ii) NbW-16-S, and (iii) NbW-24-S heterostructure thin films.
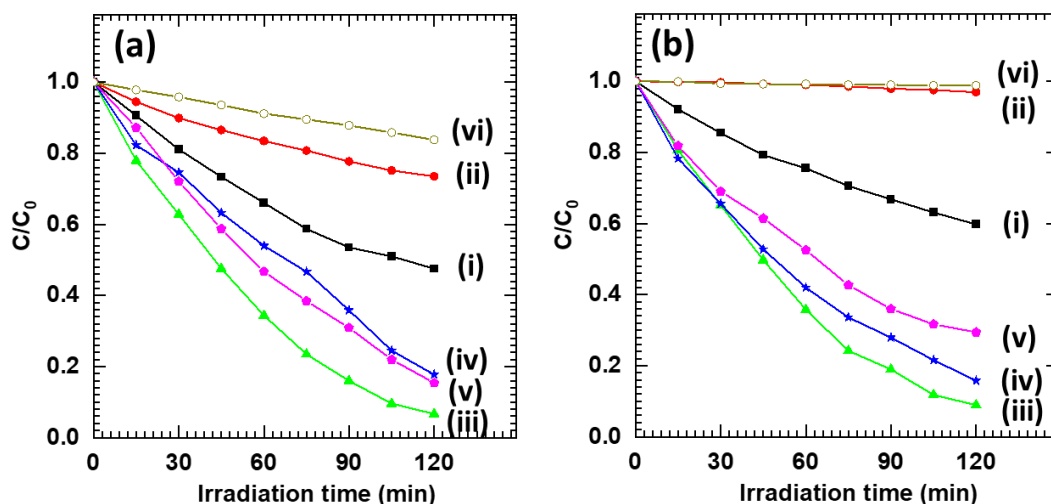
Fig. 7.14. Photocatalytic degradation performance of MB (a) and Rh B (b) for (i) WO₃, (ii) hexaniobate-NS, (iii) NbW-8-S, (iv) NbW-16-S, (v) NbW-24-S heterostructure thin films, and (vi) without thin film.

The visible-light-induced photocatalytic activity of NbW-S heterostructure thin films was examined by monitoring the time-dependent photodegradation of MB and Rh B and compared with pristine WO₃ and hexaniobate-NS thin films. The time-dependent absorption spectra of MB and Rh B for NbW-S heterostructure thin films are shown in **Fig. 7.12** and **Fig. 7.13**, respectively. The time-dependent absorption spectra of MB and Rh B for m-SILAR deposited WO₃ and EPD deposited hexaniobate-NS are shown in **Chapter 5**, **section 5.3.1** and **Chapter 6**, **section 6.3.1**, respectively. The time-dependent absorption spectra of MB and Rh B without thin film are represented in Fig. **Chapter 4**, **section 4.3.1.** As displayed in **Fig. 7.14(a-b)**, the WO₃ and NbW-S heterostructure thin films exhibit photocatalytic degradation of target molecules. For the comparison, the degradation performance of MB and Rh B for pristine WO₃, hexaniobate-NS and without thin films are plotted again in **Fig. 7.14(a)** and **Fig. 7.14(b)**, respectively. The photocatalytic activity of MB and Rh B for pristine WO₃ is discussed in **Chapter 5**, **section 5.3.1**, and for pristine hexaniobate-NS, it is discussed in **Chapter 6, section 6.3.1.** The NbW-S heterostructure thin films show improved photocatalytic activity as compared to pristine WO₃ (MB: 52% and Rh B: 40%) and hexaniobate-NS (MB: 26% and Rh B: 4%) thin films. Among the thin films of NbW-S heterostructure, NbW-8-S heterostructure thin films exhibited enhanced performance of 96 and 91% in 120 min. Furthermore, it lowers for NbW-16-S (MB: 83% and Rh B: 82%) and NbW-24-S (MB: 85% and Rh B: 72%) heterostructure thin film due to the peel-off of the

loosely bound WO_3 layers from the film surface. The NbW-S heterostructure thin films show maximum degradation performance due to the porous nanosheet morphology, visible-light harvesting ability, and depression electron-hole pair recombination via effective electronic coupling between hybridized species.

7.3.2 Kinetic study:
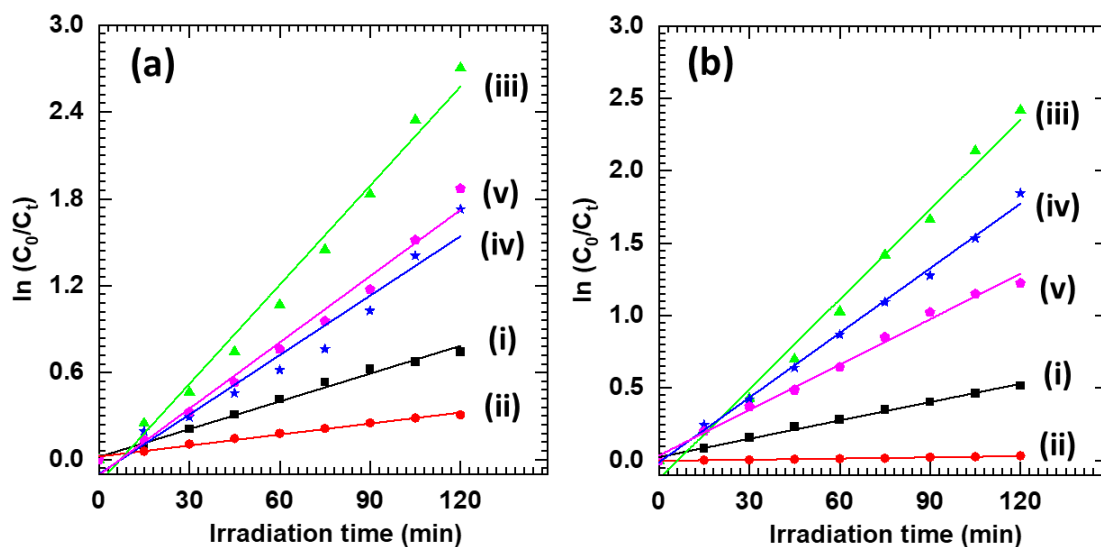
Fig. 7.15. Pseudo-first-order kinetics of MB (a) and Rh B (b) for (i) WO_3, (ii) hexaniobate-NS, (iii) NbW-8-S, (iv) NbW-16-S, and (v) NbW-24-S heterostructure thin films.

Moreover, k and R^2 values determined from the first-order reaction kinetics confirm the high photocatalytic degradation performance of the deposited thin films [14]. **Fig. 7.15 (a-b)** represents the plots of pseudo-first-order kinetics for MB and Rh B. For the comparison, the first-order reaction kinetics of MB and Rh B for WO_3 thin films are plotted again in **Fig. 7.15(a)** and **Fig. 7.15(b)**, respectively. The k and R^2 values of pristine WO_3, hexaniobate-NS, and NbW-S heterostructure thin films are given in **Table 7.2**. The NbW-8-S heterostructure thin film exhibits the highest k values of 0.0228 and 0.0206 min^{-1} for MB and Rh B, respectively. The photocatalytic reaction rate of NbW-8-S heterostructure thin film for MB is 3.61 and 9.12 times higher than pristine WO_3 and hexaniobate-NS thin films, respectively. Meanwhile, for Rh B, it is 4.9 and 79 times higher than pristine WO_3 and hexaniobate-NS thin films, respectively. The NbW-8-S heterostructure thin film demonstrates enhanced degradation performance due to effective electronic coupling between hybridized species, strong visible light harvesting ability, porous morphology, and minimal electron-hole pair recombination.

Thin Film	MB		Rh B	
	k (min $^{-1}$)	R^2	k (min $^{-1}$)	R^2
WO₃	0.0063	0.99	0.0042	0.99
hexaniobate-NS	0.0025	0.98	0.00026	0.97
NbW-8-S	0.0228	0.98	0.0206	0.99
NbW-16-S	0.0136	0.97	0.0148	0.98
NbW-24-S	0.0152	0.98	0.0104	0.97

Table 7.2. The k and R^2 values of all pristine WO₃, hexaniobate-NS, and NbW-S heterostructure thin films.

7.3.3 Recycling study:
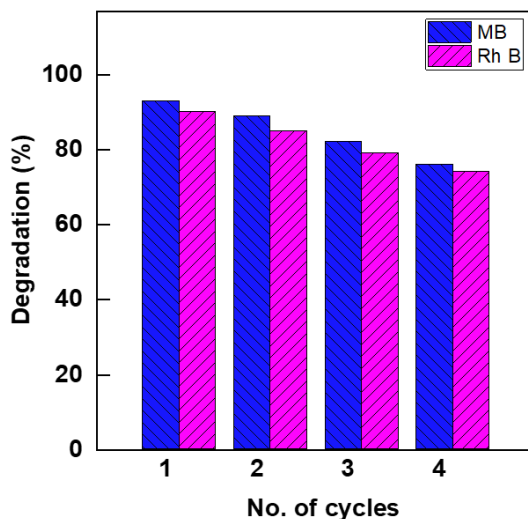
Fig. 7.16. Recyclability study of NbW-8-S heterostructure thin film.

Further, a recycling study of optimized NbW-8-S thin film is examined over the course of four consecutive cycles. As represented in **Fig. 7.16**, after four consecutive cycles of NbW-8-S heterostructure thin films retain 78% and 73% of the photocatalytic performance for MB and Rh B, respectively. The minute decline performance after four consecutive cycles was attributed to the adsorption of target organic molecules on the surface of the photocatalyst and the loss of loosely bound photocatalyst crystals from the film.

7.3.4 Photocatalytic degradation mechanism:

The plausible photocatalytic dye degradation mechanism in the presence of visible light is shown in **Fig. 7.17**. When photons with appropriate energy are incident on the NbW-S heterostructure, electrons from the VB of WO₃ are excited to its CB, forming electron-hole pairs. As shown in **Fig. 7.17**, the CB of hexaniobate-NS (-0.76

eV) is more negative than that of WO$_3$ (0.94 eV), and the VB of WO$_3$ (3.22 eV) is more positive than that of hexaniobate-NS (2.69 eV) with respect to NHE [15]. The photogenerated electrons from the CB of WO$_3$ can migrate into the VB of hexaniobate-NS, leading to the spatial separation of electrons and holes. As a result, the lifetime of holes in the VB of WO$_3$ increases. A detailed explanation of the surface redox reaction is given in **Chapter 4, section 4.3.4**.
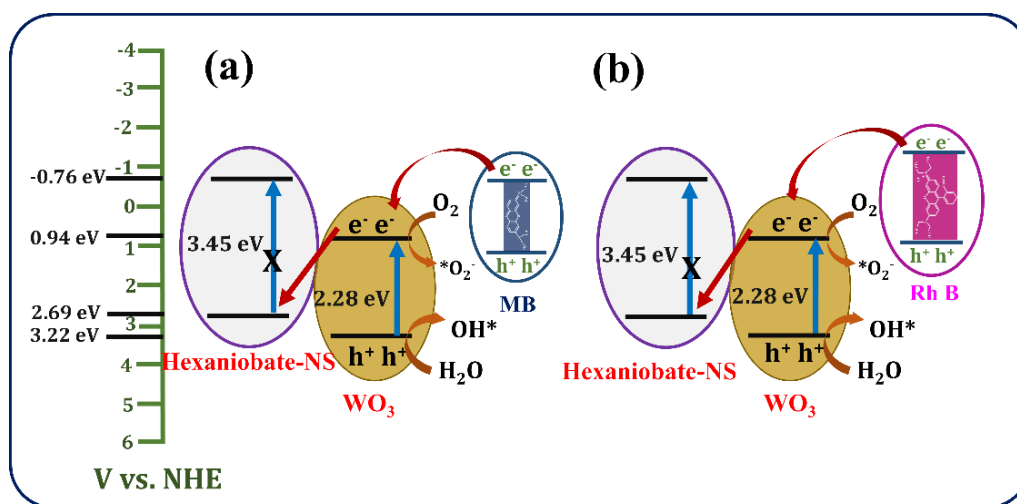
Fig. 7.17. The schematic diagram for plausible photodegradation of (a) MB and (b) Rh B.

7.4 Conclusions:

In this work, the NbW-S heterostructure thin films are deposited by a combination of EPD and m-SILAR methods for the degradation of organic molecules such as MB and Rh B under visible light illumination. The NbW-S heterostructure thin films show the XRD peaks related to WO$_3$ and hexaniobate-NS, confirming the growth of WO$_3$ over the EPD-deposited hexaniobate-NS thin film. The surface microstructure analysis of NbW-S heterostructure thin films confirms the vertically aligned WO$_3$ nanosheets are grown on the hexaniobate-NS, enabling the intimate electronic coupling between hexaniobate-NS and WO$_3$. Moreover, it shows significant absorption in the visible region, indicating its visible-light harvesting photo-functionality. The NbW-S heterostructure thin film shows an enhancement in performance compared to pristine WO$_3$ and hexaniobate-NS. The NbW-8-S heterostructure thin film exhibited maximum performance of 96 and 91 % for MB and Rh B in 120 min, respectively. The present experimental results highlight the usefulness of heterostructure thin films for lowering electron-hole recombination. This study can be effectively used to synthesize binder-free layer-by-layer visible-light-active thin-film photocatalysts.

7.5 References

[1] A. L. Shiguihara, M. A. Bizeto, V. R. Constantino, J. Braz. Chem. Soc., 21 (2018) 1366.

[2] S. P. Gupta, M. A. More, D. J. Late, P. S. Walke, Electrochim. Acta, 366 (2021) 137389.

[3] Y. M. Chitare, V. V. Magdum, S. P. Kulkarni, S. V. Talekar, S. A. Pawar, P. D. Sawant, D. B. Malavekar, U. M. Patil, C. D. Lokhande, J. L. Gunjakar, Appl. Surf. Sci. Adv., 19 (2024) 100573.

[4] S. P. Gupta, H. H. Nishad, S. D. Chakane, S. W. Gosavi, D. J. Late, P. S. Walke, Nanoscale Adv., 2 (2020) 4689.

[5] B. N. Nunes, C. Haisch, A. V. Emeline, D. W. Bahnemann, A.O.T., Patrocinio, Catal. Today, 326 (2019) 60.

[6] P. P. Bagwade, V. V. Magdum, D. B. Malavekar, Y. M. Chitare, J. L. Gunjakar, U. M. Patil, C. D. Lokhande, J. Mater. Sci. Mater. Electron., 33 (2022) 24646.

[7] N. S. Padalkar, C. H. Cho, V. V. Magdum, Y. M. Chitare, S. P. Kulkarni, U. M. Patil, J. P. Park, J. L. Gunjakar, J. Energy Storage, 74 (2023) 109538.

[8] Q. Hu, J. He, J. Chang, J. Gao, J. Huang, L. Feng, ACS Appl. Nano Mater., 3 (2020) 9046.

[9] E. C. C. Souza, J. Phys. Chem. C, 123 (2019) 24426.

[10] T. Goswami, K. M. Reddy, A. Bheemaraju, Chem. Select, 4 (2019) 6790.

[11] S. V. Sadavar, N. S. Padalkar, R. B. Shinde, A. S. Patil, U. M. Patil, V. V. Magdum, Y. M. Chitare, S. P. Kulkarni, S. B. Kale, R. N. Bulakhe, D. S. Bhange, S. T. Kochuveedu, J. L. Gunjakar, Energy Stor. Mater., 48 (2022) 101.

[12] R. B. Shinde, N. S. Padalkar, S. V. Sadavar, S. B. Kale, V. V. Magdum, Y. M. Chitare, S. P. Kulkarni, U. M. Patil, V. G. Parale, H. H. Park, J. L. Gunjakar, J. Hazard. Mater., 432 (2022) 128734.

[13] N. S. Padalkar, S. V. Sadavar, R. B. Shinde, A. S. Patil, U. M. Patil, D. S. Dhawale, R. N. Bulakhe, H. Kim, H. Im, A. Vinu, C. D. Lokhande, J. L. Gunjakar, J. Colloid Interface Sci., 616 (2022) 548.

[14] M. Kotal, A. Sharma, S. Jakhar, V. Mishra, S. Roy, S. C. Sahoo, H. K. Sharma, S. K. Mehta, Cryst. Growth Des., 20 (2020) 4627.

[15] E. J. Hernandez-Moreno, A. M. De La Cruz, L. Hinojosa-Reyes, J. Guzman-Mar, M. A. Gracia-Pinilla, A. J. M. T. C. Hernandez-Ramirez, Mater. Today Chem., 19 (2021) 100406.

CHAPTER-VIII

Summary and Conclusions

The rapid growth of industries, conventional agriculture practices, and the overuse of medicines have increased significant water pollution. In particular, hazardous dye effluents released from the textile, paper, leather, and printing sectors are toxic, mutagenic, carcinogenic, and hazardous, which adversely affects human and aquatic life. Thus, the removal of such toxic substances from the wastewater has attracted a lot of research interest. Recently, heterogeneous semiconductor photocatalysis has emerged as an excellent alternative for mineralizing toxic water pollutants. Various nanostructured semiconductors are considered potential candidates as photocatalysts due to their unique properties, such as appropriate electronic band structure, nontoxicity, high surface area, porous structure, and photostability. However, their performance is limited due to their large energy bandgap (> 3.2 eV) with only 4% solar spectrum utilization, unsuitable band positions, and rapid recombination of photogenerated electron-hole pairs.

Tungsten oxide (WO_3) is a narrow-band gap (2.4-2.8 eV) semiconductor that has been reported as a promising photocatalyst in the visible region of the solar spectrum. However, their photocatalytic performance is also limited due to the high recombination rate of photogenerated electron-hole pairs and poor chemical stability. Various reports indicate that coupling WO_3 with other semiconductors facilitates the effective separation of photogenerated charge carriers and helps to enhance photocatalytic activity. In addition, recently researched exfoliated 2D titanate-NS and hexaniobate-NS derived from the soft chemical exfoliation of layered cesium titanate and potassium hexaniobate have gained more attention due to their ultrathin thickness, highly anisotropic structure, negative surface charge, and high photocatalytic activity. 2D titanate-NS and hexaniobate-NS can be regarded as advantageous candidates for coupling due to most constituent ions residing on their surface, leading to a remarkably modified and intimately coupled electronic structure. Therefore, 2D titanate-NS and hexaniobate-NS can be useful platforms for the growth of WO_3 to form strongly coupled TiW and NbW heterostructure photocatalysts.

In this regard, the present research is focused on improving the photocatalytic activity of pristine material by chemical growth of narrow-band gap WO_3 over the titanate-NS and hexaniobate-NS. This strategy leads to depressing electron-hole pair recombination via effective electronic coupling between hybridized species, expanded surface area, and increased photostability. The present thesis work is distributed into eight chapters.

Chapter 1 comprises a general introduction describing the overview of water pollution, water pollution due to industrial dyes, classification of dyes, and various dye removal techniques. In addition, the principle of photocatalysts, the mechanism of dye degradation, and a literature survey of various photocatalysts have been included in this chapter. The purpose of a dissertation is stated at the end of this chapter.

Chapter 2 includes the theoretical background of the synthesis methods such as CBD, SILAR, solid-state reactions, and EPD. In addition, this chapter also describes the different physicochemical characterization techniques, such as XRD, FT-IR spectroscopy, Micro-Raman spectroscopy, FE-SEM with EDS, XPS, and UV-vis DRS. Finally, the experimental arrangement of photocatalytic setup coupled with UV-vis absorption spectrophotometer is explained briefly.

Chapter 3 focused on the synthesis and characterization of pristine titanate-NS and hexaniobate-NS. Layered cesium titanate ($Cs_{0.7}Ti_{1.825}\square_{0.175}O_4$, $\square$=vacancy) and potassium hexaniobate ($K_4Nb_6O_{17}$) were synthesized using a solid-state method. Their protonated derivatives were vigorously shaken with TBAOH to produce exfoliated nanosheets. The EPD method has been used to deposit titanate-NS and hexaniobate-NS thin films. The results of the various physicochemical properties probed using different characterization techniques of pristine materials are discussed in this chapter. The structural study of EPD-deposited titanate-NS and hexaniobate-NS thin films demonstrated that titanate-NS and hexaniobate-NS are restacked layer by layer on the ITO-coated glass substrate. The layered spacing of the titanate-NS and hexaniobate-NS thin film are 0.88 and 0.78 nm, respectively. The surface morphological analysis shows that the titanate-NS thin film exhibits a nanosheet-like structure with lateral sheet sizes ranging from 500 to 600 nm. In contrast, the hexaniobate-NS thin film displays a nanoscroll-like morphology, with an average length of 700 nm and diameter of 30 nm. The cross-section images confirm the deposition of titanate-NS and hexaniobate-NS on the ITO substrate. Moreover, the optical properties of the titanate-NS and hexaniobate-NS thin films show significant absorption in the UV region of the electromagnetic spectrum with bandgap energies of 3.34 and 3.45 eV, respectively.

Chapter 4 describes the synthesis and characterization of TiW-C heterostructure thin films deposited by the combination of EPD and CBD methods. This chapter describes the deposition of WO_3 by the CBD method over the EPD-deposited titanate-NS thin films. The XRD, FT-IR, Micro-Raman, FE-SEM with EDS, XPS, and UV-DRS techniques are used to investigate the physicochemical properties of the TiW-C

heterostructure thin films, and results are compared with pristine titanate-NS and WO_3 thin films. The structural study shows the XRD peaks related to titanate-NS and WO_3, confirming the growth of WO_3 on the pre-deposited titanate-NS thin film. TiW-10-C heterostructure thin film displays WO_3 nanodiscs vertically grown on titanate-NS. The WO_3 nanodiscs display an average nanodiscs length, width, and thickness of 650 nm, 400 nm, and 70 nm, respectively. The XPS features clearly indicate the presence of W^{6+} and Ti^{4+} states of W and Ti, confirming the formation of TiW-C heterostructure. The TiW-C heterostructure thin films display prominent absorption in the visible region.

In addition, this chapter deals with the photocatalytic dye degradation performance of MB and Rh B dyes for pristine CBD-deposited WO_3, EPD-deposited titanate-NS, and TiW-C heterostructure thin films. The CBD-deposited WO_3 thin film shows a degradation performance of 55 and 41% for MB and Rh B, respectively. The EPD-deposited titanate-NS thin film shows only 24 and 3% degradation performance for MB and Rh B, respectively. However, the TiW-C heterostructure thin films show improved photocatalytic performance as compared to WO_3 and titanate-NS thin films. The optimized TiW-10-C heterostructure thin films show maximum degradation performance of 91 and 89% for MB and Rh B, respectively, in 2 hours. The enhanced photocatalytic degradation performance of TiW-C heterostructure thin films can attributed to the strong visible-light harvesting ability, high surface area, porous nanoplate morphology, and reduced electron-hole pair recombination via effective electronic coupling between hybridized species.

Chapter 5 deals with the synthesis and characterization of TiW-S heterostructure thin films deposited by the combination of EPD and m-SILAR methods and used for the visible-light-driven photocatalytic degradation of MB and Rh B dyes. This chapter describes the deposition of WO_3 by the m-SILAR method over the EPD-deposited titanate-NS thin films. The XRD, FT-IR, Micro-Raman, FE-SEM with EDS, XPS, and UV-DRS techniques are used to investigate the physicochemical properties of the TiW-S heterostructure thin films. The results of the TiW-S heterostructure thin films are compared with EPD-deposited titanate-NS and m-SILAR deposited WO_3. The structural analysis of TiW-S heterostructure thin films revealed diffraction peaks corresponding to both titanate-NS and WO_3, indicating the growth of WO_3 over the EPD-deposited titanate-NS thin films. The TiW-S heterostructure thin film shows the WO_3 nanoplates grown vertically on the stacked titanate-NS parallel to the ITO substrate. This enables the effective electronic coupling between the titanate-NS and WO_3. Moreover, TiW-S

heterostructure thin films show noteworthy absorption in the visible region, highlighting the efficient electronic coupling between titanate-NS and WO_3. The strong visible light absorption ability of TiW-S heterostructures makes them suitable candidates for visible-light-driven photocatalytic activity.

The photocatalytic degradation performance of MB and Rh B for m-SILAR deposited WO_3 and TiW-S heterostructure thin films is described in this chapter. The m-SILAR deposited WO_3 thin film shows photodegradation of 52% for MB and 40% for Rh B in 150 min. Moreover, the photocatalytic dye degradation performance of m-SILAR deposited WO_3 and EPD-deposited titanate-NS thin films are compared with TiW-S heterostructure thin films. The optimized TiW-10-S heterostructure thin film enhances degradation performance of 89 and 88% for MB and Rh B, respectively. In addition, it shows a slight decrement in photocatalytic performance after four consecutive cycles, highlighting its photostability. The minute reduction in performance following four consecutive cycles was obtained due to the adsorption of target molecules on the surface of the photocatalyst and the loss of loosely bound photocatalyst crystals from the film.

Chapter 6 covers the synthesis and characterization of NbW-C heterostructure thin films deposited by the combination of EPD and CBD methods. The deposited thin films are tested for the visible-light-driven photocatalytic degradation of MB and Rh B dyes. This chapter describes the deposition of WO_3 by the CBD method over the EPD-deposited hexaniobate-NS thin films. The XRD, FT-IR, Micro-Raman, FE-SEM with EDS, XPS, and UV-DRS techniques are used to investigate the physicochemical properties of the NbW-C heterostructure, and results are compared with pristine hexaniobate-NS and WO_3. The structural analysis of NbW-C heterostructure thin films revealed diffraction peaks corresponding to both hexaniobate-NS and WO_3, indicating the growth of WO_3 over the EPD-deposited hexaniobate-NS thin films. Surface morphological analysis shows that WO_3 nanoplates are vertically grown on the EPD-deposited hexaniobate-NS surface, enabling the intimate electronic coupling between hexaniobate-NS and WO_3. The optical study demonstrated the significant absorption of visible light by the NbW-16-C heterostructure thin films.

Moreover, this chapter covers the visible-light-driven photocatalytic MB and Rh B degradation performance for pristine hexaniobate-NS and NbW-C heterostructure thin films. Visible-light-driven photocatalytic degradation performance of CBD-deposited WO_3, hexaniobate-NS, and NbW-C heterostructure thin films are compared. The

optimized NbW-16-C heterostructure thin films show improved degradation performance of 94% with a rate constant of 0.0212 min^{-1} for MB and 90% with a rate constant of 0.0173 min^{-1} for Rh B in 120 min. The enhanced photocatalytic degradation performance of NbW-C heterostructure thin films can ascribed to the porous nanoplate morphology, strong visible-light harvesting ability, and spatial separation of electron-hole pair due to the effective electronic coupling between WO_3 and hexaniobate-NS.

Chapter 7 describes the synthesis and characterization of NbW-S heterostructure thin films deposited by the combination of EPD and m-SILAR methods. This chapter describes the deposition of WO_3 by the m-SILAR method over the EPD-deposited hexaniobate-NS thin films. The XRD, FT-IR, Micro-Raman, FE-SEM with EDS, XPS, and UV-DRS techniques are used to investigate the physicochemical properties of the NbW-S heterostructure, and results are compared with pristine hexaniobate-NS and WO_3. The NbW-S heterostructure thin films show the structural characteristics related to WO_3 and hexaniobate-NS, confirming the growth of WO_3 over the EPD-deposited hexaniobate-NS thin film.

The surface morphological analysis of NbW-S heterostructure thin films confirms the vertically aligned WO_3 nanosheets are grown on the hexaniobate-NS, enabling the intimate electronic coupling between hexaniobate-NS and WO_3. The average nanosheet length, width, and thickness are 650, 380, and 23 nm, respectively. Moreover, it shows significant absorption in the visible region, indicating its visible-light harvesting photo-functionality. Moreover, this chapter describes the photocatalytic dye degradation performance of NbW-S heterostructure thin films. The optimized NbW-8-S heterostructure thin films show a degradation performance of 96% with a rate constant of 0.0228 min^{-1} for MB in 120 min. Meanwhile, for Rh B, it is 91% with a rate constant of 0.0206 min^{-1}. The NbW-S heterostructure thin films show maximum degradation performance due to the porous nanosheet morphology, visible-light harvesting ability, and depression electron-hole pair recombination via effective electronic coupling between hybridized species.

Table 8.1 clearly highlights that all the heterostructures are useful for enhancing photocatalytic dye degradation of MB and Rh B dyes. The visible-light-driven photocatalytic degradation performance of all heterostructure thin films is given in **Table 8.1**. From **Table 8.1**, it is also reflected that NbW-S heterostructure thin films deposited by the combination of EPD and m-SILAR methods demonstrated a maximum degradation performance of 96% with a rate constant of 0.0228min^{-1} for MB and 91%

with a rate constant of 0.0206 min^{-1} for Rh B. The highest degradation performance is obtained for NbW-S heterostructure thin films as compared to other heterostructure (TiW-C, TiW-S, and NbW-C) thin films, which may be due to the strong visible-light harvesting ability, porous morphology, reduced electron-hole pair recombination via effective electronic coupling between WO$_3$ and hexaniobate-NS.

Therefore, it is concluded that the EPD method has the potential to deposit homogeneous hexaniobate-NS thin films from their colloidal suspensions. Also, the m-SILAR method is highly suitable for the growth of WO$_3$ over hexaniobate-NS thin films. The SILAR method typically provides better control over the thin film growth than CBD. In SILAR, the growth process occurs layer-by-layer; therefore, it often produces a more homogeneous thin film, whereas CBD sometimes gives non-homogeneous thin film growth. Also, it is inexpensive, avoids hazardous chemical waste by forming bulk precipitation, and is suitable for large-area deposition.

Table 8.1. Photocatalytic degradation performance of all heterostructure thin films.

Sr. No.	Heterostructure thin film photocatalyst	Dye	Dye degradation performance (%)	K (min^{-1})	Time (min)
1	TiW-10-C	MB	91	0.0185	120
		Rh B	89	0.0174	
2	TiW-10-S	MB	89	0.0154	150
		Rh B	88	0.0137	
3	NbW-16-C	MB	94	0.0212	120
		Rh B	90	0.0173	
4	**NbW-8-S**	**MB**	**96**	**0.0228**	**120**
		Rh B	**91**	**0.0206**	

CHAPTER-IX

80-Recommendations

9.1 Recommendations:

2D titanate-NS and hexaniobate-NS, a typical material from the layered structure class, is a potential photocatalyst material. However, its photoactivity is restricted due to its large energy bandgap (>3.2 eV), only 4% solar spectrum utilization, the rapid recombination rate of photogenerated electron-hole pairs, and unsuitable band position. On the other hand, narrow-band gap WO_3 is tested as a visible-light active photocatalyst that utilizes the maximum solar spectrum. However, it suffers from a high recombination rate of photogenerated charge carriers and limited photostability. Therefore, the photocatalytic activity of WO_3 can be further increased by coupling it with 2D titanate-NS and hexaniobate-NS.

Several recommendations are provided in accordance with the research findings of synthesis, characterizations, and visible-light-driven photocatalytic dye degradation activity of TiW and NbW heterostructure thin films. Upon the growth of narrow-bandgap WO_3 over the wide-bandgap titanate-NS and hexaniobate-NS thin films, the resultant TiW and NbW heterostructure thin films exhibited significant absorption in the visible region of the electromagnetic spectrum, underscoring the effective electronic coupling between the hybridized species. In addition, all the present heterostructure thin films display porous structure, which is highly beneficial for photocatalytic activity. The photocatalytic degradation performance of CBD and m-SILAR deposited WO_3 thin film is significantly enhanced after coupling with titanate-NS and hexaniobate-NS due to the lowering of electron-hole pairs recombination. The obtained TiW-C, TiW-S, NbW-C, and NbW-S heterostructure thin films enhance MB and Rh B degradation performance.

Among the heterostructure thin films, the comparative analysis of the visible-light-driven photodegradation performance of MB and Rh B indicates that the NbW-S heterostructure thin films exhibit the highest photocatalytic activity of 96% with a maximum rate constant of 0.0228 min^{-1} for MB in 120 min. Meanwhile, it is 91% with a rate constant of 0.0206 min^{-1} for Rh B. Also, the optimized NbW-S thin film shows a slightly decreased photocatalytic performance after four cycles, highlighting its high photostability. From these results, it is recommended that, among the tested heterostructured thin films, the hexaniobate-NS thin film is the best choice for the growth of narrow-band gap WO_3 by the m-SILAR method. The SILAR method typically provides better control over the thin film growth than CBD. In SILAR, the growth process occurs layer-by-layer; therefore, it often produces a more homogeneous thin film, whereas CBD sometimes gives non-homogeneous thin film growth.

9.2 Future finding:

Present research work effectively improved the photocatalytic dye degradation performance of CBD and m-SILAR deposited WO_3 by making TiW-C, TiW-S, NbW-C, and NbW-S heterostructure thin films and applied them as photocatalysts. Present research work opens up new prospects for exploring 2D titanate-NS and hexaniobate-NS-based photocatalyst thin films for the degradation of organic molecules. The highest photodegradation performance and stability of titanate-NS and hexaniobate-NS-based photocatalyst thin films need to be further increased for their practical applications.

Nevertheless, present research work validated state-of-the-art achievements for 2D titanate-NS and hexaniobate-NS-based photocatalysts; few challenges endured to increase their photocatalytic performance further. Thus, the present research work also opens up possibilities to further enhance the photocatalytic dye degradation performance of 2D metal oxide-based materials.

- The water exfoliation of metal oxide nanosheets could bring a breakthrough in the field of metal oxide nanosheets.
- Novel compounds based on titanate-NS and hexaniobate-NS need to be explored to enable the library of hybrid materials.
- Considering the fascinating physicochemical properties of titanate-NS and hexaniobate-NS, they can be employed for various applications such as photocatalytic antibiotics and pesticide degradation.
- Other metal oxides and their hybrids need to be explored for photocatalytic applications.
- The layers of titanate-NS and hexaniobate-NS can be deposited using other deposition methods such as dip-coating, spin coating, spray coating, etc.
- A group of layered metal oxide-based heterostructures can be helpful in enhancing the catalytic activity.
- The layer-by-layer deposition of 2D metal oxide-NS and different guest species can be advantageous in synthesizing 2D metal oxide-based hybrid thin film photocatalysts.
- Advanced technologies must be developed and apply to determine intermediate products of photocatalysis.

Preferentially oriented m-tuned WO₃ thin-films photocatalysts for the multitargeted degradation of organic molecules

Yogesh M. Chitare [a], Vikas V. Magdum [a], Shirin P. Kulkarni [a], Shweta V. Talekar [a], Shraddha A. Pawar [a], Prashant D. Sawant [a], Dhanaji B. Malavekar [b], Umakant M. Patil [a], Chandrakant D. Lokhande [a], Jayavant L. Gunjakar [a,*]

[a] *Centre for Interdisciplinary Research, D. Y. Patil Education Society (Deemed to be University), Kolhapur, Maharashtra 416006, India*
[b] *Optoelectronic Convergence Research Centre, Department of Materials Science and Engineering, Chonnam National University, Gwangju 61186, South Korea*

ARTICLE INFO

ABSTRACT

In this work, morphology-tuned tungsten oxide (m-tuned WO₃) thin films are deposited on a glass substrate by a simple and cost-effective chemical bath deposition (CBD) method. The deposition pH is varied to tune the physicochemical properties of m-tuned WO₃ thin films. The m-tuned WO₃ thin films show an orthorhombic crystal structure with a preferred orientation along the (020) plane. The morphological study demonstrated the conversion of 'rice hull' to 'interlocked nanosheets' to 'reticulated nanosheets composed of nanorods' upon changing pH, highlighting the significant role of pH in m-tuned WO₃ thin film synthesis. The m-tuned WO₃ thin films show good absorption in the visible-light region (390–780 nm) of the solar spectrum. The m-tuned WO₃ thin films are used for the visible light active photocatalytic degradation of organic molecules such as methylene blue (MB), rhodamine B (Rh B), and tetracycline hydrochloride (TC). The optimized m-tuned WO₃ thin film shows maximum photocatalytic performance of 95, 94, and 86 % in 180 min for MB, Rh B, and TC, respectively. The present study demonstrates the usefulness of the CBD method for the deposition of m-tuned WO₃ and improved photocatalytic performance.

1. Introduction

Globally accelerated industrial development, traditional agricultural practices, industrial emissions and excessive antibiotics usage have increased water pollution. Humans and aquatic life are now seriously threatened due to water pollution by numerous industrial dyes, antibiotics, and pesticides. Many modern sectors such as plastic, leather, textile, cosmetics, rubber, pharmaceutical, printing, food processing, etc. widely utilize synthetic dyes [1]. Currently, around 10,000 commercial dyes are available globally, and above 700,000 tonnes of dyes are manufactured and utilized in the above sectors annually [2]. In textile industries, a significant portion of these dyes (~20 %) are wasted in the manufacturing process and end up in industrial wastewater, significantly contributing to water pollution. Most industrial dyes are toxic, mutagenic, carcinogenic, and hazardous, adversely affecting human and aquatic life. Moreover, excessive usage and slow metabolism of antibiotics cause their foreseeable expulsion to aquatic environments, leading to untraceable water pollution. Such discharge of antibiotics

leads to the spread of bacteria with antibiotic and multiple drug resistance, which may cause fetal diseases [3]. Thus, removing such contaminants from wastewater has garnered much research interest. In recent years, heterogeneous photocatalysis has emerged as an effective approach for degrading various organic molecules from polluted water [4]. It is considered a green process since it utilizes natural light in the presence of a semiconductor photocatalyst to decompose a range of toxic and hazardous organic water pollutants. Consequently, nanostructured semiconducting materials (TiO₂, ZnO, CuO, CoO, BiVO₄, and WO₃, etc.) with suitable composition, structure, and optical properties have been investigated as photocatalytic materials [5–12]. TiO₂ and ZnO are the most studied photocatalysts due to their good stability; however, their performance is highly limited due to their wide band gap (>3.2 eV) with only 4% solar spectrum utilization [13]. Thus, efforts are escalated to find visible light active photocatalysts such as CuO, CoO, BiVO₄, Ag₃PO₄, WO₃, etc.

However, most visible light active photocatalysts do not possess sufficiently high efficiency and stability due to their nonoptimized

Vertically aligned interlocked tungsten oxide nanosheet thin film for photocatalytic application: effect of deposition cycles

Yogesh M. Chitare[1], Vikas V. Magdum[1], Shirin P. Kulkarni[1], Shweta V. Talekar[1], Shraddha A. Pawar[1], Prashant D. Sawant[1], Dhanaji B. Malavekar[2], Umakant M. Patil[1], Jin H. Kim[2], Sabah Ansar[3], and Jayavant L. Gunjakar[1,*] ⓘ

[1] *Centre for Interdisciplinary Research, D. Y. Patil Education Society (Deemed to Be University), Kolhapur, Maharashtra 416 006, India*

[2] *Department of Materials Science and Engineering, Optoelectronic Convergence Research Centre, Chonnam National University, Gwangju 61186, South Korea*

[3] *Department of Clinical Laboratory Sciences, College of Applied Medical Sciences, King Saud University, P.O. Box 10219, Riyadh 11433, Saudi Arabia*

ABSTRACT

In this work, vertically aligned interlocked tungsten oxide (WO_3) nanosheets are deposited on non-conducting substrates using the modified chemical solution deposition (MCSD) method. The number of deposition cycles is varied to tune the physicochemical properties of WO_3 thin films. The WO_3 thin films exhibit an orthorhombic crystal structure with a preferred orientation along the (111) plane. The WO_3 thin film shows the vertically aligned interlocked nanosheet morphology with a change in the lateral dimensions upon varying the number of deposition cycles. All the WO_3 thin films exhibited strong visible light harvesting characteristics in the 510–530 nm wavelength range. The WO_3 thin films are used for the visible-light-active photocatalytic degradation of organic molecules such as methylene blue (MB), rhodamine B (Rh B) and tetracycline hydrochloride (TC). The optimized WO_3 thin film shows maximum photocatalytic degradation performance of 92, 89 and 87% in 210 min for MB, Rh B and TC, respectively. The present study illustrates the usefulness of the MCSD approach for depositing vertically aligned interlocked WO_3 nanosheet thin films and enhancing photocatalytic performance.

1 Introduction

Rapid industrial development leads to serious environmental pollution problems. In particular, organic pollutants such as synthetic dyes, antibiotics, and pesticides have emerged as one of the most challenging problems because of their high toxicity, massive accumulation, and difficulty in degradation [1, 2]. Their excessive use and uncontrolled release into the aqueous reservoirs are highly hazardous to the

Metal Oxide-Based Composites in Nonenzymatic Electrochemical Glucose Sensors

Yogesh M. Chitare,[†] Satish B. Jadhav,[†] Padamaja N. Pawaskar,[*] Vikas V. Magdum, Jayavant L. Gunjakar, and Chandrakant D. Lokhande

Cite This: https://doi.org/10.1021/acs.iecr.1c03662

Read Online

ACCESS | Metrics & More | Article Recommendations | Supporting Information

ABSTRACT: The new generation of glucose biosensors has gained immense research interest owing to its cost effectiveness, quick response, good stability, reproducibility, and low detection limit. The enzymatic glucose sensor suffers from numerous intrinsic disadvantages; therefore, there is a need to develop a new biosensor which can overcome the disadvantages of enzymatic glucose biosensors. In that context, metal oxide-based nanostructures and their compostites exhibit properties that can overcome the drawbacks of enzymatic glucose sensors. This review discusses recent developments in some of the metal oxides (CoO, NiO, CuO, and ZnO) along with their composites as well as their applications toward nonenzymatic glucose sensors. The metal oxide composites possess excellent features which signify the potential commercial applications of metal oxide-based composites for nonenzymatic electrochemical glucose sensing.
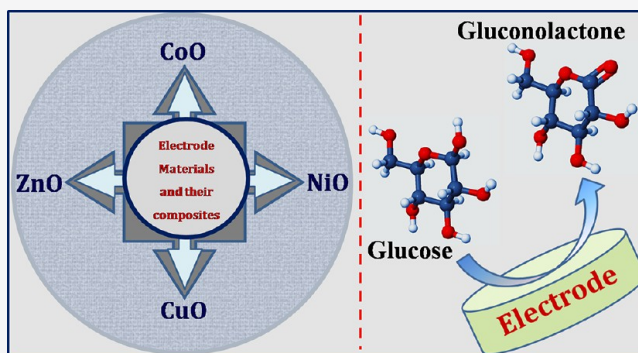
1. INTRODUCTION

Diabetes has emerged as a severe threat to public health problems worldwide. Today about 9.5% of the world population is suffering from diabetes. It can lead to various health problems such as heart disease, kidney failure, strokes, eye diseases, gum and other dental diseases, and so on.[1] The International Diabetes Federation (IDF) reported that due to diabetes 5 million deaths occurred in 2015, equivalent to a death every six seconds.[2] A decade ago, in 2010, around 438 million people were thought to be diagnosed with diabetes. According to IDF, by 2030, diabetes will affect 578 million adults and 700 million by 2045. Figure 1 shows projected and estimate number of adults with diabetes.

As per the World Health Organization, diabetes will become the seventh leading cause of death by 2030. Insufficient production of insulin in the body (called as type 1 diabetes) or incapability to use produce insulin (called as type 2 diabetes) can be treated effectively by supplying requisite insulin to the body. Otherwise, the glucose level in the blood reaches a point where it affects human health and causes several problems.[3] Regular measurement of glucose concentrations level in blood samples is required to check whether treatment works effectively or not.[4] Due to the large number of applications in the field of medicine, food, pharmaceuticals, biotechnology, environmental industry, and more, quantitative and qualitative analyses of glucose has gained great attention. Specifically, to avoid challenges initiated by diabetes diseases, very fast and trustworthy diagnoses of glucose levels in the blood samples are required to give determine the right treatment and strict control. Therefore, for clinical diagnostics, development of highly sensitive, precise, fast, and quick sensing devices to check glucose concentrations in human blood samples possess intense challenges in the present scenario.[1,5]

Various methods including colorimetry, conductometry, electrochemical, optical, and fluorescent spectroscopy have been employed for glucose sensing. Out of theses, for the last four decades, the glucose sensing domain was dominated by electrochemical glucose sensors due to their fast response, simple instrumentation, sensitivity, excellent stability, low cost, high specificity, and low detection limit (LOD). Within the electrochemical method, two specific methods, viz., potentiometric and amperometric methods, are used mostly in monitoring glucose concentration. In the potentiometric method, the potential difference between the working electrode and reference electrode is measured at zero applied current. It is commonly used to measure glucose concentration on the order of few μM. As the concentration of glucose changes, the potential of the working electrode also changes.[6,7] In the amperometric method, constant bias potential is

Rare Earth Element-Based Nonenzymatic Glucose Sensor

Yogesh M. Chitare, Vikas V. Magdum, Satish B. Jadhav, Shirin P. Kulkarni, Chandrakant D. Lokhande, and Jayavant L. Gunjakar

Abbreviations

AA	Ascorbic acid
ACM	Activated chemisorption model
CV	Cyclic voltammetry
DA	Dopamine
FE-SEM	Field emission scanning electron microscope
Fru	Fructose
GCE	Glassy carbon electrode
IHOAM	Incipient hydrous oxide adatom mediator model
Lac	Lactose
LOD	Limit of detection
MOH	Metal hydroxide
PBS	Phosphate buffer solution
PVP	Polyvinyl pyrrolidone
REEs	Rare earth elements
RGO	Reduced graphene oxide
RSD	Relative standard deviation
SWV	Square wave voltammetry
UA	Uric acid

Y. M. Chitare · V. V. Magdum · S. B. Jadhav · S. P. Kulkarni · C. D. Lokhande (✉) ·
J. L. Gunjakar (✉)
Centre for Interdisciplinary Research, D. Y. Patil Education Society (Institution Deemed to be University), Kolhapur, India

Tailoring the physicochemical properties of chemically deposited MoS$_2$ thin films for photocatalytic dye and TC degradation: effect of different cationic precursors

Vikas V. Magdum[1], Yogesh M. Chitare[1], Shirin P. Kulkarni[1], Dhanaji B. Malavekar[2], Amol U. Pawar[3], Ravindra N. Bulakhe[4], Chandrakant D. Lokhande[1], Umakant M. Patil[1], Sharad B. Patil[1,*], and Jayavant L. Gunjakar[1,*] 📵

[1] *Centre for Interdisciplinary Research, D. Y. Patil Education Society (Deemed to Be University), Kolhapur, MS 416 006, India*

[2] *Department of Materials Science and Engineering, Optoelectronic Convergence Research Centre, Chonnam National University, Gwangju 61186, South Korea*

[3] *Environmental and Climate Technology, Korea Institute of Energy Technology, Naju-Si, Jeollanamdo 58219, Republic of Korea*

[4] *Department of Chemistry, Sungkyunkwan University, Suwon 16419, Republic of Korea*

ABSTRACT

Precursor chemicals significantly impact the physicochemical properties of chemically deposited thin films. Herein, different cationic precursors such as ammonium molybdate (AM), molybdenum trioxide (MO) and sodium molybdate (NM) are used to deposit MoS$_2$ thin films using chemical bath deposition (CBD). Their effect on film formation, physicochemical properties and photocatalytic performance is investigated. The MoS$_2$ thin films display a hexagonal phase of MoS$_2$ with nanocrystalline characteristics. All MoS$_2$ thin films display nanospherical morphology with an optical bandgap of 1.6 eV. The MoS$_2$ thin film deposited using NM precursor shows a higher surface area of 31 m^{2}g^{-1} than that of the MoS$_2$ thin films deposited using AM (28 m^{2}g^{-1}) and MO (22 m^{2}g^{-1}) precursors. All MoS$_2$ thin films are highly active for the photocatalytic degradation of target organic molecules like methylene blue (MB), rhodamine B (RhB) and tetracycline hydrochloride (TC) antibiotic. Among all, the MoS$_2$ thin film deposited using NM demonstrated excellent photocatalytic performance by degrading 84, 71 and 74% of RhB, MB and TC in 2 h of visible light irradiation with a pseudo-first-order rate constant of 0.038, 0.033 and 0.026 min^{-1}, respectively. This work shows that MoS$_2$ thin films deposited using NM exhibit better photocatalytic performance than those deposited using AM and MO precursors.

Address correspondence to E-mail: sbpphy@gmail.com; jlgunjakar@gmail.com

🙂 Springer

Article

Nanohybrids of Layered Titanate and Bismuth Vanadate as Visible-Light-Driven Photocatalysts for the Degradation of Dyes and Antibiotic

Shirin P. Kulkarni, Yogesh M. Chitare, Vikas V. Magdum, Prashant D. Sawant, Shweta V. Talekar, Shraddha A. Pawar, Dhanaji B. Malavekar, Sabah Ansar, Jin H. Kim, and Jayavant L. Gunjakar*

Read Online

ACCESS | Metrics & More | Article Recommendations | Supporting Information

ABSTRACT: The present article reports a novel approach for synthesizing two-dimensional (2D) lattice-engineered layered titanate–bismuth vanadate (NS-titanate–BiVO$_4$) nanohybrid thin films by a combination of electrophoretic deposition (EPD) and chemical solution growth (CSG) methods. The synthesized nanohybrid thin films display significant absorption of visible light and depressed electron–hole recombination, demonstrating the strong electronic coupling between the hybridized species. Upon hybridization, the chemical stability of pristine BiVO$_4$ is significantly enhanced due to the highly stable NS-titanate. The hybridization of NS-titanate with BiVO$_4$ leads to the formation of highly mesoporous house-of-cards-type morphology beneficial for improved photocatalytic activity. The resultant nanohybrids are very effective for visible-light-driven photocatalytic degradation of dyes (methylene blue (MB), rhodamine-B (Rh-B)) and tetracycline hydrochloride (TC) antibiotic with photodegradation rates of 85.1, 97, and 73%, respectively, higher than that of pristine BiVO$_4$ which is one of the most prominent visible-light-active photocatalysts. Present results underscore the superior photofunctionality of the NS-titanate–BiVO$_4$ nanohybrids as an effective visible-light-driven photocatalyst. Moreover, these findings vividly demonstrate that NS-titanate-based nanohybrids are quite effective in enhancing photocatalytic activity and developing various types of 2D nanosheet-based hybrid materials.

KEYWORDS: *BiVO$_4$, nanohybrid, nanosheet, photocatalyst, thin film, titanate*
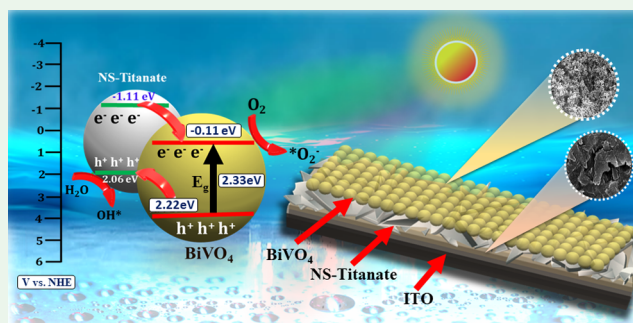
1. INTRODUCTION

The contamination of water resources due to toxic dye effluents is a significant issue in modern society.[1] Among the various techniques developed for toxic dye removal, photocatalysis has attracted considerable research attention as it is a cost-effective and environmentally friendly process.[2,3] Many low-dimensional nanostructured semiconducting materials have been designed and explored as photocatalysts. Considering the efficient use of the solar spectrum (3−5% UV light, 42−43% visible light, and 52−55% near-infrared (NIR) light), developing visible-light-active photocatalysts is highly crucial.

During the past few decades, researchers have explored a variety of inorganic materials for visible-light-driven active photocatalysis. Most visible-light photocatalysts suffer from low efficiency, high exciton recombination, poor photostability, and inappropriate band positions to reduce protons and oxidize oxide ions.[4,5] Consequently, attempts were made to enhance the photocatalytic activity by doping, nanostructuring photocatalysts, and hybridization with wide-band gap semiconductors. Nanostructure hybridization with intimate electronic coupling can enable effective electron–hole pair separation, thus improving the photocatalytic activity of semiconducting materials.[6] Many low-dimensional wide-band gap semiconductor materials are coupled with narrow-band gap semiconductors and explored in thin film form for efficient visible-light-active photocatalysts. Such coupled thin film photocatalyst systems mainly comprise TiO$_2$, Nb$_2$O$_5$, ZnO, etc., as wide-band gap semiconductors and CdS, PbI, CdSe, Ag$_3$PO$_4$, etc., as narrow-band gap semiconductors.[7−10] The coupled semiconductor photocatalyst systems still suffer from limited efficiency and stability.[8] Recently, advanced two-dimensional (2D) metal oxide nanosheets (MONs) have been widely explored as basic building blocks for the development of various lattice-engineered nanohybrids owing to their fascinating characteristics.[11] These wide-band gap 2D
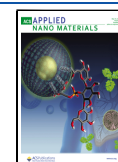
Chemically synthesized facet-controlled visible light active BiVO$_4$ thin films for photoelectrochemical water splitting

Shirin P. Kulkarni[1] · Yogesh M. Chitare[1] · Vikas V. Magdum[1] · Prashant D. Sawant[1] · Shweta V. Talekar[1] ·
Shraddha A. Pawar[1] · Umakant M. Patil[1] · Kishor V. Gurav[2] · Dhanaji B. Malavekar[3] · Amol U. Pawar[4] ·
Jayavant L. Gunjakar[1]

Abstract

The facile and cost-effective chemical bath deposition (CBD) method is used to synthesize highly photoactive facet-controlled bismuth vanadate (BiVO$_4$) thin films on glass and stainless steel (SS) substrates. The facet-controlled BiVO$_4$ thin films are synthesized by variation in anionic precursor with fine tuning of chemical bath pH from alkaline to acidic media. The variation of anionic precursor evolves the morphology of BiVO$_4$ from dispersed nanoparticles to faceted microcrystals. Furthermore, the fine-tuning of chemical bath pH leads to the well-defined octahedral BiVO$_4$ microcrystals. Compared to dispersed nanoparticulate BiVO$_4$ photoanodes, the octahedral BiVO$_4$ photoanodes demonstrated superior photocurrent density of 2.75 mA cm^{-2} (at 1.23 V vs. RHE), good photostability and charge separation efficiency (45.5%) owing to their excellent PEC reaction kinetics. The present study underscores the usefulness of the CBD method for facet-controlled synthesis of semiconducting thin films for different photo-functional applications.

1 Introduction

In recent years, energy crises and environmental pollution have increased market demands for clean energy storage sources that can replace fossil fuels and provide energy when needed. Sustainable hydrogen (H$_2$) production is a key challenge for developing alternative energy systems that provide an environmentally friendly and inexpensive energy supply [1, 2]. Among the numerous renewable energy sources, solar energy has tremendous potential for energy conversion as it is one of the most abundant, cost-free and clean sources [3]. The conversion of solar energy into H$_2$ via the solar-assisted water-splitting process is one of the most promising technologies because of its potential for green and sustainable H$_2$ production [4]. Photoelectrochemical (PEC) water-splitting technology has emerged as an effective approach for producing H$_2$ using semiconducting photoelectrodes [5]. The PEC water-splitting is an environmentally friendly process, because it uses natural sunlight for water-splitting reactions in the presence of semiconductor photoelectrode.

During the past few decades, ZnO and TiO$_2$ have been extensively studied as photoelectrodes in PEC water splitting due to their high chemical stability and non-toxicity [6, 7]. However, their performance is limited owing to the wide bandgap energy (absorb only ultraviolet radiations; < 4% of solar spectrum). Hence, lots of efforts were put forward on narrow bandgap materials, such as doped-metal oxides, metal sulfides and nitrides for improved PEC water splitting [8–12]. Compared with other photocatalysts, BiVO$_4$ with suitable bandgap energy (~ 2.4 eV), highest photostability, high optical absorption coefficient, least photo-corrosion,

✉ Jayavant L. Gunjakar
jlgunjakar@gmail.com

1 Centre for Interdisciplinary Research, D. Y. Patil Education Society (Deemed to Be University), Kolhapur, MS 416 006, India

2 Energy Conversion and Storage Research Laboratory, Department of Physics, Devchand College, Arjunnagar, MS 591 237, India

3 Department of Materials Science and Engineering, Optoelectronic Convergence Research Centre, Chonnam National University, Gwangju 61186, South Korea

4 Environmental and Climate Technology, Korea Institute of Energy Technology, Naju-Si, Jeollanamdo 58219, Republic of Korea

Invited paper

Modified successive ionic layer adsorption and reaction for interconnected bismuth vanadate nanograins: Highly active visible light harvesting photoanodes

Shirin P. Kulkarni [a], Vikas V. Magdum [a], Yogesh M. Chitare [a], Prashant D. Sawant [a], Shweta V. Talekar [a], Shraddha A. Pawar [a], Amol U. Pawar [b], Dhanaji B. Malavekar [c], Shrikrishna D. Sartale [d], Ayman A. Ghfar [e], Jayavant L. Gunjakar [a,*]
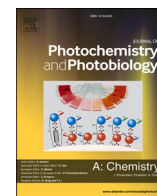
[a] *Centre for Interdisciplinary Research, D. Y. Patil Education Society (Deemed to be University), Kolhapur 416 006, MS, India*
[b] *Environmental and Climate Technology, Korea Institute of Energy Technology, Naju-Si, Jeollanamdo 58219, Republic of Korea*
[c] *Optoelectronic Convergence Research Centre, Department of Materials Science and Engineering, Chonnam National University, Gwangju 61186, Republic of Korea*
[d] *Department of Physics, Savitribai Phule Pune University, Pune 411 007, MS, India*
[e] *Department of Chemistry, College of Science, King Saud University, P.O. Box 2455, Riyadh 11451, Saudi Arabia*

ABSTRACT

A modified successive ionic layer adsorption and reaction (SILAR) method is developed for depositing interconnected bismuth vanadate (BiVO₄) nanoparticles with improved visible light harvesting activity. Facile control of preparative parameters like deposition cycles, anionic precursor, pH and deposition temperature significantly altered BiVO₄ surface morphology. BiVO₄ thin films prepared with Na_3VO_4 anionic precursor show dispersed nanoparticles type morphology and that deposited with $NaVO_3$ precursor displays 3D interconnected nanoparticles morphology. The BiVO₄ photoanodes with 3D interconnected nanoparticles morphology exhibits an excellent photocurrent density of 5.19 mA cm⁻² at 1.23 V vs. RHE with superior photostability and improved applied bias photon to current efficiency (ABPE) (1.50 %) compared to dispersed nanostructured BiVO₄ photoanodes. The excellent photoelectrochemical (PEC) characteristics of BiVO₄ photoanodes with 3D interconnected nanoparticle morphology can be ascribed to porous morphology, optimum thickness, narrow band gap energy and favorable electronic band structure for water splitting. The current study illustrates the usefulness of the modified SILAR approach for depositing 3D interconnected BiVO₄ nanoparticle morphology in a single step that is superior and efficient to previously reported multistep processes.

1. Introduction

In recent years, photoelectrochemical (PEC) water splitting has attracted intense research interest for photoinduced production of H_2 and O_2 molecules using semiconductor photoelectrodes as it is one of the most environmentally friendly processes ever developed [1,2]. Overall, the PEC water-splitting process comprises electron-hole pairs generation upon light exposure; these charge carriers get separated and migrate toward the respective electrodes to perform redox reactions [3,4]. The suitable band positions and band gap energy of photocatalyst electrodes are the most crucial points for visible-light-driven PEC water-splitting applications [5]. Researchers have investigated several inorganic compounds such as transition metal oxides, carbides, nitrides, carbonitrides

and chalcogenides as photocatalysts to attain greater efficiency for PEC water-splitting [6]. Compared with others, transition metal oxides are regarded as the most potential photocatalysts because of their high chemical stability and non-toxicity.

BiVO₄ is an n-type direct band gap semiconducting oxide, exhibited excellent properties such as suitable band positions for water splitting reactions, a narrow band gap energy (2.4 eV) with improved photostability, low photo-corrosion, low toxicity, a high optical absorption coefficient and excellent theoretical solar to hydrogen conversion efficiency [7]. Therefore, it is widely employed as a photocatalyst or photoelectrode in a wide range of photo-functional applications such as photocatalytic/photoelectrocatalytic-PEC water splitting, PEC CO_2 reduction, PEC glucose sensing and photocatalytic dye/antibiotic

---

Research article

2D porous hexaniobate-bismuth vanadate hybrid photocatalyst for photodegradation of aquatic refractory pollutants

Shirin P. Kulkarni [a], Vikas V. Magdum [a], Yogesh M. Chitare [a], Dhanaji B. Malavekar [b], Jin H. Kim [b], Sultan Alshehri [c], Jayavant L. Gunjakar [a,*], Shashikant P. Patole [d,**]

[a] Centre for Interdisciplinary Research, D. Y. Patil Education Society (Deemed to Be University), Kolhapur, 416 006, MS, India
[b] Optoelectronic Convergence Research Centre, Department of Materials Science and Engineering, Chonnam National University, Gwangju, 61186, South Korea
[c] Department of Pharmaceutics, College of Pharmacy, King Saud University, Riyadh, 11451, Saudi Arabia
[d] Department of Physics, Khalifa University of Science and Technology, AbuDhabi, 127788, United Arab Emirates

ABSTRACT

Metal oxide semiconductors are highly promising due to their excellent photocatalytic performance in the photodegradation of industrial waste containing refractory chemical compounds. A hybrid structure with other semiconductors provides improved photocatalytic performance. In this work, porous and two-dimensional (2D) hexaniobate-bismuth vanadate (Nb_6-$BiVO_4$) Z-scheme hybrid photocatalysts are synthesized by chemical solution growth (CSG) of $BiVO_4$ over electrophoretically deposited Nb_6 thin films. The structural and morphological analysis of Nb_6-$BiVO_4$ hybrid thin films evidenced the well-crystalline uniform growth of monoclinic scheelite $BiVO_4$ over lamellar Nb_6 nanosheets. The Nb_6-$BiVO_4$ hybrid thin films exhibit a highly porous randomly aggregated nanosheet network, creating the house-of-cards type morphology. The Nb_6-$BiVO_4$ hybrid thin films display a strong visible light absorption with band gap energy of 2.29 eV and highly quenched photoluminescence signal, indicating their visible light harvesting nature and intimate electronic coupling between hybridized species beneficial for photocatalytic applications. The visible-light-driven photodegradation performance of methylene blue (MB), rhodamine-B (Rh-B) dyes, and tetracycline hydrochloride (TC) antibiotic over Nb_6-$BiVO_4$ hybrid are studied. The best optimized Nb_6-$BiVO_4$ thin film shows superior photocatalytic activity for photodegradation of MB, Rh-B dyes, and TC antibiotic with photodegradation rates of 87.3, 92.8, and 64.7 %, respectively, exceptionally higher than that of pristine $BiVO_4$. Furthermore, the mineralization study of Nb_6-$BiVO_4$ thin film is conducted using chemical oxygen demand (COD) analysis. The optimized Nb_6-$BiVO_4$ thin film shows superior percentage COD removal of 83.33, 85.42, and 61.36 % for MB, Rh-B dyes and TC antibiotic, respectively. The present results highlight the expediency of hybridization in enhancing the photocatalytic activity of pristine $BiVO_4$ by minimizing its charge recombination rate and improving chemical stability.

* Corresponding author.
** Corresponding author.
E-mail addresses: jlgunjakar@gmail.com (J.L. Gunjakar), shashikant.patole@ku.ac.ae (S.P. Patole).
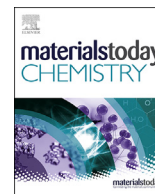
Lattice engineering route for self-assembled nanohybrids of 2D layered double hydroxide with 0D isopolyoxovanadate: chemiresistive SO₂ sensor

R.B. Shinde [a], N.S. Padalkar [a], S.V. Sadavar [a], A.S. Patil [a], S.B. Kale [a], V.V. Magdum [a], Y.M. Chitare [a], S.P. Kulkarni [a], U.M. Patil [a], V.G. Parale [b], J.L. Gunjakar [a, *]

[a] Centre for Interdisciplinary Research, D. Y. Patil Education Society (Institution Deemed to Be University), Kolhapur, 416 006, MS, India
[b] Department of Materials Science and Engineering, Yonsei University, 50 Yonsei-ro, Seodaemun-gu, Seoul, 03722, South Korea

A B S T R A C T

Tuning the interior chemical composition of layered double hydroxides (LDHs) via lattice engineering route is a unique approach to enable multifunctional applications of LDHs. In this regard, the exfoliated 2D LDH nanosheets coupled with various guest species lead to the lattice-engineered LDH-based multifunctional self-assembly with precisely tuned chemical composition. This article reports the synthesis and characterization of mesoporous zinc—chromium-LDH (ZC-LDH) hybridized with iso-polyoxovanadate nanohybrids (ZCiV) via lattice-engineered self-assembly between delaminated ZC-LDH nanosheets and isopolyoxovanadate (iPOV) anions. Electrostatic self-assembly between 2D ZC-LDH monolayers and 0D iPOV significantly altered structural, morphological, and surface properties of ZC-LDH. The structural and morphological study demonstrated the formation of mesoporous inter-connected sheet-like architectures composed of restacked ZCiV nanosheets with expanded surface area and interlayer spacing. In addition, the ZCiV nanohybrid resistive elements were used as a room-temperature gas sensor. The selectivity of ZCiV nanohybrid was tested for various oxidizing (SO₂, Cl₂, and NO₂) gases and reducing (LPG, CO, H₂, H₂S, and NH₃) gases. The optimized ZCiV nanohybrid demonstrated highly selective SO₂ detection with the maximum SO₂ response (72%), the fast response time (20 s), low detection limit (0.1 ppm), and long-term stability at room temperature (27 ± 2 °C). Of prime importance, ZCiV nanohybrids exhibited moderately affected SO₂ sensing responses with high relative humidity conditions (80%—95%). The outstanding SO₂ sensing performance of ZCiV is attributed to the active surface gas adsorptive sites via plenty of mesopores induced by a unique lattice-engineered interconnected sheet-like microstructure and expanded interlayer spacing.

© 2022 Elsevier Ltd. All rights reserved.

1. Introduction

In the modern era of worldwide industrialization and urbanization, the air quality inhaled is a foremost important concern due to the continuously increasing concentration of numerous toxic and harmful gases [1]. The quality of the air we inhale, which is a prime health concern in this era, is degrading day by day due to increased emissions of these gases. The prime contribution to this degradation is different pollutant emitting centers such as modern industries, automobiles, houses, etc. Numerous hazardous pollutants such as oxides of carbon, sulfur and nitrogen, numerous miscible vapors such as NH₃ and HCl above their threshold values are hazardous to the ecosystem [2—4]. Along with human health hazards, these pollutants are also responsible for ecological imbalances like global warming, ozone depletion, acid rain, and greenhouse effects. Thus, reliable sensing of these polluting gases is of utmost necessity in various applications. Out of various pollutants, oxides of sulfur (SOₓ) are a highly poisonous and devastating family of pollutants that adversely affects human health (skin and eye irritation, human respiratory, nervous system malfunction, lung failure, and death in acute conditions) [5]. It is also a significant contributor to acid rain, soil acidification, and climate change. Among the SOₓ family (SO, SO₂, and SO₃), sulfur dioxide (SO₂) is a significant automobile and industrial emission component and is considered a highly

Research Paper

2D–2D lattice engineering route for intimately coupled nanohybrids of layered double hydroxide and potassium hexaniobate: Chemiresistive SO$_2$ sensor

Rohini B. Shinde [a], Navnath S. Padalkar [a], Shrikant V. Sadavar [a], Shital B. Kale [a], Vikas V. Magdum [a], Yogesh M. Chitare [a], Shirin P. Kulkarni [a], Umakant M. Patil [a], Vinayak G. Parale [b], Hyung-Ho Park [b], Jayavant L. Gunjakar [a,*]

[a] Centre for Interdisciplinary Research, D. Y. Patil Education Society (Institution Deemed to be University), Kolhapur 416 006, Maharastra, India
[b] Department of Materials Science and Engineering, Yonsei University, 50 Yonsei-ro, Seodaemun-gu, Seoul 03722, South Korea

HIGHLIGHTS

- Nanohybrids of ZC-LDH and HNb (ZCNb) nanosheets are prepared via lattice-engineered self-assembly method.
- ZCNb nanohybrids shows high surface area mesoporous structure.
- The ZCNb nanohybrids shows excellent sensitivity for the detection of SO$_2$ at 150 °C.
- The enhanced SO$_2$ sensing performance of ZCNb nanohybrids is attributed to porous microstructure and expanded surface area.

GRAPHICAL ABSTRACT
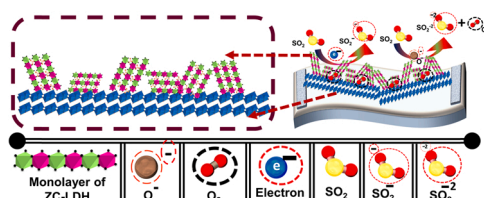
ARTICLE INFO

Editor: Dr. H. Zaher

ABSTRACT

2D–2D lattice engineering route is used to synthesize intimately coupled nanohybrids of layered double hydroxide (LDH) and potassium hexaniobate. The 2D–2D lattice engineering route is based on the electrostatically derived self-assembly of delaminated zinc-chromium-layered double hydroxide (ZC-LDH) nanosheets and potassium hexaniobate (HNb) nanosheets (ZCNb nanohybrids). The 2D–2D lattice-engineered ZCNb nanohybrids display expanded surface area, mesoporous anchored nanosheets network morphology, and intimate coupling between nanosheets. The 2D–2D lattice engineered ZCNb nanohybrids are used for the low temperature operated gas sensor. The ZCNb nanohybrids display outstanding selectivity for the SO$_2$, with the high response of 61.5% compared to pristine ZC-LDH (28.08%) and potassium niobate (8%) at 150 °C. Moreover, ZCNb sensors demonstrate superior response and recovery periods of 6 and 167 s at 150 °C, respectively. This result underscores the exceptional functionality of the ZCNb nanohybrids as efficient SO$_2$ sensors. Moreover, these findings vividly demonstrate that the 2D–2D lattice-engineered ZCNb nanohybrids are quite effective not only in improving the gas sensor activity but also in developing of new type of intimately coupled mesoporous LDH-metal-oxide based hybrid materials.

Polyoxotungstate intercalated self-assembled nanohybrids of Zn-Cr-LDH for room temperature Cl₂ sensing

Rohini B. Shinde [a], Akash S. Patil [a], Shrikant V. Sadavar [a], Yogesh M. Chitare [a], Vikas V. Magdum [a], Navnath S. Padalkar [a], Umakant M. Patil [a], Saji T. Kochuveedu [a], Vinayak G. Parale [b], Hyung-Ho Park [b], Chandrakant D. Lokhande [a], Jayavant L. Gunjakar [a,*]

[a] Centre for Interdisciplinary Research, D. Y. Patil Education Society (Institution Deemed to be University), Kolhapur 416006, MS, India
[b] Department of Materials Science and Engineering, Yonsei University, 50 Yonsei-ro, Seodaemun-gu, Seoul 03722, South Korea

ABSTRACT

This article reports the preparation of mesoporous layered nanohybrids of zinc chromium layered double hydroxide (Zn-Cr-LDH) and polyoxotungstate (POW) anions via an exfoliation-reassembling process. The hybridization of Zn-Cr-LDH and POW anions leads to forming a layer-by-layer intercalated structure with a randomly interconnected mesoporous nanoplate network composed of 'restacked POW intercalated Zn-Cr-LDH nanosheets' (Zn-Cr-WO). The gas-sensing performance of the pristine Zn-Cr-LDH and Zn-Cr-WO was investigated for oxidizing (NO_2 and Cl_2), and reducing (LPG, H_2, H_2S, CO and NH_3) gases at room temperature. The Zn-Cr-WO nanohybrids displayed the highest selectivity towards Cl_2. The Cl_2 gas response for the pristine Zn-Cr-LDH is 25.2% which further increased to 66.8% after hybridization with POW anions. The Zn-Cr-WO nanohybrids showed fastest response and recovery times of 5 and 133 s, respectively, at room temperature.

1. Introduction

Technology development, ongoing industrialization, and rapid urbanization resulted in substantial consumption of fossil fuels and organic chemical compounds that lead to ambient air pollution worldwide. Air pollution, produced by toxic and combustible gases, such as Cl_2, SO_2, NH_3, NO_2, and H_2 is responsible for global warming, climate change and is harmful to human health [1–5]. Nowadays, due to cognizance about environmental pollution, climate mitigation, ever-changing sociology, hygiene, human health, etc., and adverse outcomes due to excessive consumption of potentially harmful gases, gas sensors received considerable attention for their development. Until now, various techniques have been explored for effective sensing of these gases. The quantitative evaluation of harmful gases can be done by optochemical sensors, gas chromatography, resistive gas sensors, impedance sensors, conductometric gas sensors, etc. [6]. In addition, the chemiresistive gas sensors based on semiconducting materials are widely used for gas sensing applications due to their inherent characteristics, such as excellent sensitivity, superior selectivity, ease of fabrication, compactness and mobility, and low power consumption during real-time applications [7]. Considerable efforts have been taken

to develop chemiresistive gas sensors based on metal oxides such as SnO_2, ZnO, TiO_2, WO_3, etc. However, lack of stability and sensitivity, the influence of changing ambient atmosphere, and higher operating temperatures are some of the concerned challenges with such gas sensors [8, 9]. Thus, significant and imperative efforts must be taken for developing a room temperature operated gas sensor with high sensitivity, superior selectivity, long-time stability and low detection limit (DL).

Layered double hydroxides (LDHs) are being explored nowadays to design and fabricate gas sensors that exhibit a larger surface area and produce excellent sensing performance [10]. LDHs are the class of two-dimensional (2D) layered inorganic matrices having hydrotalcite-like structure belonging to the group of layered anionic clays. It can be generalize by formula, $[M^{2+}_{1-x}M^{3+}_x(OH)_2]^{x+}(A^{n-})_{x/n} \cdot mH_2O$, in which M^{2+} (Ni^{2+}, Mg^{2+}, Co^{2+}, Zn^{2+} etc.), M^{3+} (Fe^{3+}, Al^{3+}, Cr^{3+}, Ga^{3+} etc.), and A^{n-} (Cl^-, OH^-, NO_3^-, SO_4^{2-} etc.) denote divalent metal cations, trivalent metal cations, and intercalated charge balancing anions, respectively [11,12]. This class of materials attracted attention in the field of gas sensors due to their inherent characteristics such as hierarchical structure, significantly higher stability over a prolonged period, larger specific surface area, compositional flexibility, anion exchangeability, etc. [13]. Of prime

---

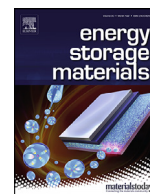# Lattice engineering exfoliation-restacking route for 2D layered double hydroxide hybridized with 0D polyoxotungstate anions: Cathode for hybrid asymmetric supercapacitors

Shrikant V. Sadavar[a], Navnath S. Padalkar[a], Rohini B. Shinde[a], Akash S. Patil[a], Umakant M. Patil[a], Vikas V. Magdum[a], Yogesh M. Chitare[a], Shirin P. Kulkarni[a], Shital B. Kale[b], Ravindra N. Bulakhe[c], Deu S. Bhange[d], Saji T. Kochuveedu[a], Jayavant L. Gunjakar[a],*

[a] Centre for Interdisciplinary Research, D. Y. Patil Education Society, Deemed to be University, Kasaba Bawada, Kolhapur, 416 006 (India)
[b] Department of materials science and engineering, Chonnam National University, Gwangju, 500-757, South Korea
[c] School of Mechanical Engineering, Chung-Ang University, Seoul, (South Korea)
[d] Department of Chemistry, Shivaji University, Kolhapur, 416004, MS, India

ARTICLE INFO

ABSTRACT

A lattice engineering exfoliation-reassembling route is used to prepare porous layer-by-layer self-assembled nanohybrids of cobalt-chromium-layered double hydroxide (Co-Cr-LDH) intercalated with 0D polyoxotungstate anions (CCW). The CCW nanohybrids provide interconnected nanosheets morphology, highly porous stacking structure, flexible chemical composition, and exceptional electrochemical activity. The self-assembled CCW nanohybrids display a high specific capacity of 1303 C g^{-1} with a capacity retention of 85.43 % over 5000 cycles. An aqueous hybrid asymmetric supercapacitor (AHAS) and all-solid-state hybrid asymmetric supercapacitor (ASHAS) devices are fabricated using CCW nanohybrids and reduced graphene oxide (rGO) as cathode and anode, respectively. The AHAS device demonstrates a high specific capacitance of 167 F g^{-1} at 0.8 A g^{-1} and specific energy (SE) of 59.37 Wh kg^{-1} at specific power (SP) of 640 W kg^{-1} with capacitance retention of 91 % after 10,000 cycles. Moreover, the ASHAS device delivers high specific capacitance of 126 F g^{-1} at 1.92 A g^{-1} and SE of 44.58 Wh kg^{-1} at SP of 1536 W kg^{-1} with capacitance retention of 87 % over 10,000 cycles. The POW intercalative hybridization significantly improves the electrode activity of the CCW nanohybrids, representing an effective method for developing LDH-based nanohybrid materials.

1. Introduction

Various energy storage technologies are emerged to address the balance between intermittent energy transformation and its utilization. Electrochemical capacitor or supercapacitor (SC) attracts enormous research attention as a pulse power source due to their high energy density, fast delivery, and extended durability. Among the various SC types, burgeoning research efforts are put forward on hybrid supercapacitors (HSCs) with one battery-type electrode (source of energy) and another electrical-double-layer-capacitors (EDLCs)-type electrode (power source). Due to their high energy and power delivery, HSCs can fulfill the gap between battery and SC. Carbon-based materials with high surface area, including activated carbon, carbon aerogels, carbon nanotubes, carbon fabrics and reduced graphene oxide (rGO), have been tested as EDLC electrodes in HSC. rGO with high conductivity and expanded surface area is one of the promising EDLC-type electrode materials that

exhibited a maximum capacity value of 127 mAh g^{-1} [1]. On the other hand, various transition metal oxides/hydroxides (RuO_2, MnO_2, Co_3O_4, NiO, $Ni(OH)_2$), conducting polymers (polyaniline, polypyrrole, and polythiophene) and metal chalcogenides (MnS, NiS, CoS, CuS, $NiCo_2S_4$) have been developed as a potential pseudocapacitive- or redox-type electrode material [2–5].

Among the various metal hydroxides, layer-double-hydroxide (LDHs) has emerged as a promising redox-type SC electrode material due to their special anion intercalated layered structure with tunable interlayer chemical composition and space. However, most of LDH-based supercapacitor state of the art is devoted to tuning the high surface area, chemical composition, electrical conductivity and making composites with various conducting carbonaceous nanostructures [6]. Electrode functionality of LDHs is significantly influenced by the chemical composition as well as interlayer space [7]. Consequently, the research efforts were put forward to tune the LDH chemical composition

Article

Graphene Oxide as an Efficient Hybridization Matrix for Exploring Electrochemical Activity of Two-Dimensional Cobalt-Chromium-Layered Double Hydroxide-Based Nanohybrids

Shrikant V. Sadavar, Navnath S. Padalkar, Rohini B. Shinde, Akash S. Patil, Umakant M. Patil, Vikas V. Magdum, Yogesh M. Chitare, Shirin P. Kulkarni, Ravindra N. Bulakhe, Vinayak G. Parale, and Jayavant L. Gunjakar*

Cite This: https://doi.org/10.1021/acsaem.1c03619

Read Online

| ACCESS | Metrics & More | Article Recommendations | Supporting Information |
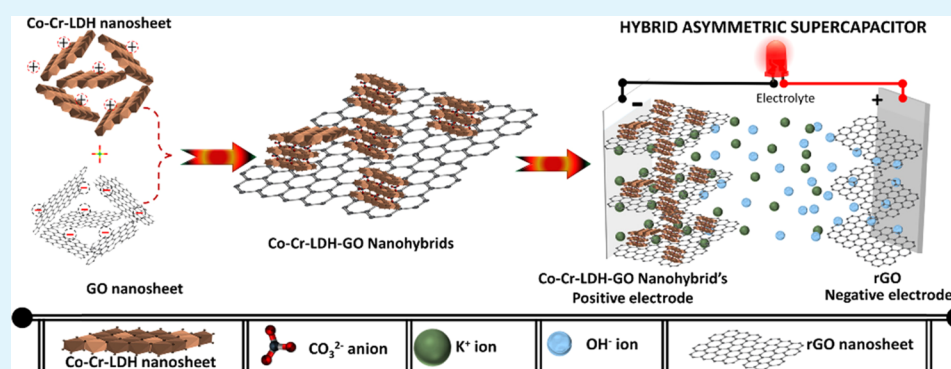
ABSTRACT: Two-dimensional graphene oxide (GO) nanosheets with high electrical conductivity and electrochemical stability are employed as a hybridization matrix to improve the electrode performance of layered double hydroxides (LDHs). A cobalt-chromium-LDH hybridized with a GO matrix leads to anchored Co-Cr-LDH-GO (CCG) self-assembly with a high surface area, mesoporous morphology, high electrical conductivity, and high charge transfer kinetics. The CCG nanohybrids display enhanced specific capacity (1502 C g^{-1}) with high-rate characteristics compared to pristine Co-Cr-LDH (591 C g^{-1}), signifying the crucial role of GO as a hybridization matrix for improving the electrode performance of LDH materials. Aqueous and all-solid-state hybrid supercapacitors are fabricated using the best-optimized CCG nanohybrid and reduced graphene oxide as an anode and a cathode, respectively. The aqueous device delivers a specific capacitance of 181 F g^{-1}, a specific energy (SE) of 56.66 Wh kg^{-1}, and a specific power (SP) of 600 W kg^{-1} at 0.8 A g^{-1}. Moreover, the solid-state device delivers a specific capacitance of 130.8 F g^{-1}, a SE of 46.50 Wh kg^{-1}, and a SP of 1536 W kg^{-1} at 1.92 A g^{-1}. The present study clearly demonstrates the usefulness of conducting GO as an efficient hybridization matrix to improve the electrode performance of LDHs.

KEYWORDS: anchor assembly, graphene oxide, layered double hydroxide, nanosheets, hybrid asymmetric supercapacitor

1. INTRODUCTION

At present, considerable research has been focused on portable energy storage devices that can deliver a high energy and power density. Hybrid supercapacitors (HSCs) with one battery- or pseudocapacitive (PC)-type anode and other electrical double-layered capacitor (EDLC)-type cathodes are the most promising devices to fulfill this demand.[1] Carbon-based electrode materials like reduced graphene oxide (rGO) and activated carbon are the most suitable EDLC-type electrode materials for HSCs because of their high surface area, high conductivity, and excellent chemical stability. On the other hand, several layered inorganic materials (transition metal oxides/hydroxides/carbides/nitrides/carbonitrides/chalcogenides) have been tested as PC- or battery-type electrodes

because of their distinctive electrochemical properties.[1,2] In this regard, layered double hydroxides (LDHs) have garnered special attention because of their unique anion-intercalated layered crystal structure, tunable interlayer space, and chemical composition, thus enabling highly flexible electrochemical properties. However, the electrochemical activity of LDH-based electrodes is primarily limited by the highly compact
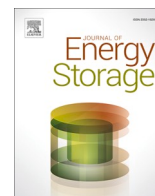
Research Papers

Self-assembled architecture of 2D layered double hydroxide pillared with 0D polyoxomolybdate anions: High-performance redox-type cathode for solid-state hybrid supercapacitor

Navnath S. Padalkar [a,b], Chae Hwan Cho [b], Vikas V. Magdum [a], Yogesh M. Chitare [a], Shirin P. Kulkarni [a], Umakant M. Patil [a], Jong Pil Park [b,*], Jayavant L. Gunjakar [a,*]

[a] *Centre for Interdisciplinary Research, D. Y. Patil Education Society, Deemed to be University, Kasaba Bawada, Kolhapur 416 006, India*
[b] *Basic Research Laboratory, Department of Food Science and Technology, Chung-Ang University, Anseong 17546, Republic of Korea*

ARTICLE INFO

ABSTRACT

Herein, mesoporous self-assembled architecture of two-dimensional (2D) nickel chromium-layered double hydroxide (NiCr–LDH) monolayers pillared with 0D polyoxomolybdate anions (NCMo) was prepared via a lattice engineering rapid exfoliation–restacking synthesis route. The self-assembled 2D-0D NCMo architecture exhibited expanded surface area, porous interconnected nanosheet morphology, flexible chemical composition, layer-by-layer stacking structure, and excellent electrochemical activity. The NCMo architecture exhibited promising electrochemical performance with a large specific capacity of 567 C g^{-1} at a current density of 1 A g^{-1}, and an excellent cyclic retention of 89 % after 5000 charge–discharge cycles. Additionally, an all-solid-state hybrid supercapacitor (HSC) device was assembled using NCMo architecture as the redox-type cathode, reduced graphene oxide (rGO) as the EDLC-type anode, and PVA-KOH gel as the electrolyte. The NCMo-2//PVA-KOH/rGO HSC device exhibited a high specific capacitance (171.8 F g^{-1} at 10 A g^{-1}), decent cycling stability (91 % after 10,000 cycles), and a high energy/power density (61.1 Wh kg^{-1}/6.7 W kg^{-1}). The findings of this study demonstrate that the intercalation of polyoxomolybdate is an effective lattice-engineered method for improving the electrode functionality of self-assembled LDH-based architectures.

1. Introduction

Recent years have experienced a rapid increase usage of fossil fuels and, which has triggered the need for sustainable and renewable energy resources [1,2]. Electrochemical devices such as solar cells, fuel cells, lead-acid batteries, zinc-ion batteries, lithium-ion batteries, and supercapacitors (SCs) have been used for electrochemical energy storage and conversion [3,4]. Among existing electrochemical devices, batteries exhibit the highest energy density (ED) but a low power density (PD) and long charge-discharge time [5–7]. In contrast, SCs possess high PD due to fast charge-discharge processes, but their relatively lower ED limits their practical applications [8–10]. To address these problems, among various types of SCs, hybrid supercapacitors (HSCs) have attracted increasing attention. The HSC devices, in which one electrode is a redox-type (energy source) and the other is an electric double-layer capacitor-type (EDLC) (power source), can fill the gap between the batteries and SCs [11–13]. Typically, HSCs are constructed using various

transition metal-based oxide/hydroxide (e.g., MnO$_2$, RuO$_2$, NiO, NiCo$_2$O$_4$, NiCoP, Co(OH)$_2$)-based electrodes with a high specific capacity, and carbon-based electrodes (e.g., activated carbon, carbon nanotube, reduced graphene oxide, carbon fabrics, and carbon aerogel) with high PD [13–20].

Among the various layered metal hydroxide, 2D layered double hydroxides (LDHs) can be applied as redox-type electrode materials for HSCs owing to their tunable interlayer chemical composition and space with unique anion-intercalated layered structure [21]. Most current research on LDH-based SCs focuses on tuning the surface area, electrical conductivity, and chemical composition and constructing composites with various conductive materials [22]. For example, a previous study demonstrated the effectiveness of LDHs-graphene composite in improving electrochemical conductivity [23]. However, the interlayer space and chemical composition of LDHs significantly affects their electrode performance. Consequently, efforts have been devoted to tuning the chemical composition and enlarging the interlayer distance of

---

2D-2D nanohybrids of Ni–Cr-layered double hydroxide and graphene oxide nanosheets: Electrode for hybrid asymmetric supercapacitors

Navnath S. Padalkar [a], Shrikant V. Sadavar [a], Rohini B. Shinde [a], Akash S. Patil [a], Umakant M. Patil [a], Vikas V. Magdum [a], Yogesh M. Chitare [a], Shirin P. Kulkarni [a], Ravindra N. Bulakhe [b], Vinayak G. Parale [c], Jayavant L. Gunjakar [a,*]

[a] Centre for Interdisciplinary Research, D. Y. Patil Education Society, Deemed to be University, Kasaba Bawada, Kolhapur 416006, India
[b] School of Mechanical Engineering, Chung-Ang University, Seoul, South Korea
[c] Department of Materials Science and Engineering, Yonsei University, 50 Yonsei-ro, Seodaemun-gu, Seoul 03722, South Korea

ARTICLE INFO

ABSTRACT

Nanohybrids of 2D Ni–Cr-layered double hydroxide (Ni–Cr-LDH) and graphene oxide (GO) nanosheets (Ni–Cr-LDH–GO) are prepared by electrostatic self-assembly between cationic Ni–Cr-LDH nanosheets and anionic GO nanosheets. Anionic GO nanosheets provide charge-transporting conducting channels leading to remarkably improved electrochemical activity of Ni–Cr-LDH–GO nanohybrid. The unique Ni–Cr-LDH–GO nanohybrid electrodes enable stable electrochemical structure, abundant active electrochemical sites, and fast electron-transporting channels, which play a crucial role in improving the specific capacities, cycle stability, and rate capacity. As a result, Ni–Cr-LDH–GO nanohybrid electrodes demonstrate excellent electrochemical performance with a specific capacity of 815 C g^{-1} at 1 A g^{-1}, superior to pristine Ni–Cr-LDH (354 C g^{-1}). An aqueous hybrid supercapacitor (AHS) device displays outstanding electrochemical performance with improved energy density (ED) of 51.85 Wh kg^{-1} and power density (PD) of 1.34 kW kg^{-1}. An all-solid-state hybrid supercapacitor (ASSHS) displays ED of 38.51 Wh kg^{-1} and PD of 1.33 kW kg^{-1}. Furthermore, AHS and ASSHS show excellent cycling stability of 89% and 86% capacitance retention after 10,000 galvanostatic charge/discharge (GCD) cycles, respectively. The present exfoliation-restacking strategy provides a useful method for developing a 2D-2D Ni–Cr-LDH–GO structure for a highly active hybrid-type supercapacitor structure.

1. Introduction

Energy storage via batteries and supercapacitors (SCs) focuses on an enormous amount of research activity due to their usefulness in new-generation electric automobiles, portable electronics, healthcare, and defense equipment [1–3]. SCs or electrochemical capacitors garnered colossal attention because of their advantages like high power delivery, extended cycle life, good operational safety and high rate characteristic [4]. However, the lower energy density (ED) associated with commercially available carbon-based SCs cannot meet the requirement of advanced applications, especially hybrid electric vehicles [5]. Thus, numerous efforts are put forward on the hybrid SCs (HSCs) with one pseudocapacitor or battery-type and other electrochemical double-layer capacitance (EDLC)-type electrode [6–11]. As SCs electrode materials design significantly impacts its performance, exploration of the novel

electrode materials with characteristics of high ED, power density (PD) and electrochemical stability is the key to achieving desired electrochemical performance. The expanded surface area carbon-based materials perform exceptionally well as an EDLC-type electrode in HSC [12]. However, materials like transition metal oxide, hydroxides, and conducting polymers are potential pseudocapacitive or battery-type electrode materials in HSC [13–16].

Nickel–chromium-layered double hydroxide (Ni–Cr-LDH) is a lamellar compound, which comprises stacking of positively charged brucite-like Ni–Cr-$(OH)_2$ monolayers and charge-balancing anions sandwiched between the monolayers. Ni–Cr-LDH is regarded as a high-performance battery-type SC electrode material due to its unique properties like anisotropic crystal structure, flexible chemical composition, anion intercalated layered structure, ion exchange capacity and tunable interlayer space [17,18]. Numerous research efforts have been

---

Synthesis, characterization and visible light driven dye degradation performance of one-pot synthesized amorphous CoWO$_4$ powder

P. P. Bagwade[1] (iD), V. V. Magdum[1], D. B. Malavekar[1], Y. M. Chitare[1], J. L. Gunjakar[1], U. M. Patil[1], and C. D. Lokhande[1,*]

[1] *Centre for Interdisciplinary Research, D. Y. Patil Education Society, Kolhapur 416 006, India*

ABSTRACT

This study illustrates the first ever report on degradation of methylene blue (MB) and rhodamine B (RhB) within visible light using facile one-pot synthesized amorphous cobalt tungstate (a-CoWO$_4$) powder via wet chemical method. Various physico-chemical techniques including X-ray diffraction, field emission scanning electron microscope, X-ray photoelectron spectroscopy, and ultra-violet diffuse reflectance spectroscopy confirmed the successful formation of CoWO$_4$. The a-CoWO$_4$ exhibited spherical morphology with direct band gap of 2.51 eV, as estimated using the Kubelka Munk method. Furthermore, CoWO$_4$ powder used for the photocatalytic degradation of rhodamine B (RhB) and methylene blue (MB) dyes demonstrated excellent performance by degrading 94% RhB and 89% MB dye in 2 hour (h). The a-CoWO$_4$ demonstrates excellent recyclability as well as stability. The superior performance was ascribed to a larger surface area as well as reduced band gap due to the amorphous nature which enabled the response to the visible light. This work highlights the potential of a-CoWO$_4$ powder for visible light active photocatalysis.

1 Introduction

Metal tungstates exhibit a wide range of materials (AWO$_4$) which are disunited in two arrays; Wolframite (A = Cd, Co, Mn, Zn, and Cu) and Scheelite (A = Ca, Sr, Ba, and Pb) [1–3]. Metal tungstates are fascinating between specific transition metal oxides due to less harmfulness, rich divergence, natural kindness, and secure versatile resources. However, few reports are associated with photocatalytic studies [4–6]. CoWO$_4$, on the other hand, is an ultimate relevant compound, with outstanding catalytic and electrochemical properties. Various methods have been developed to synthesize CoWO$_4$ nanomaterials, including conventional solid-state reaction at high temperature, co-precipitation, spray pyrolysis, low temperature molten salt route and hydro/solvothermal approaches [7–13]. It is a p-type material possessing appropriate valence and conduction band

🎗 Springer

REVIEW

Check for updates

Versatility of group VI layered metal chalcogenide thin films synthesized by solution-based deposition methods

Vikas V. Magdum, (iD) Yogesh M. Chitare, (iD) Shirin P. Kulkarni, (iD) Prashant D. Sawant, (iD) Shraddha A. Pawar, (iD) Shweta V. Talekar, (iD) Chandrakant D. Lokhande, Umakant M. Patil, (iD) Sharad B. Patil (iD) and Jayavant L. Gunjakar (iD) *
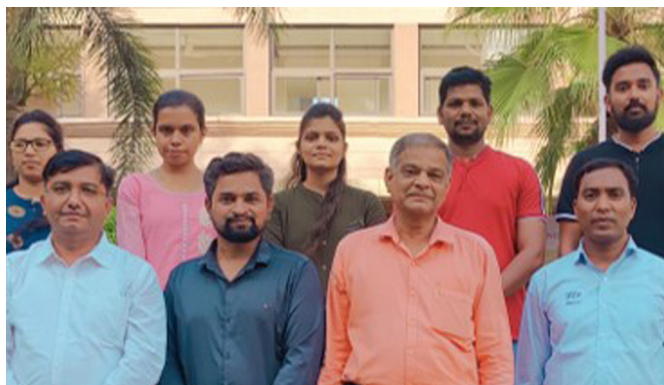
Among transition metal dichalcogenides (TMDs), group VI layered metal (Mo and W) dichalcogenides (LMD) have received increased research interest for numerous applications due to their layered structure as well as interesting physicochemical properties that facilitate tunable physical, chemical, electrical and optical properties. These features extend LMDs' use in energy storage, catalysis, optoelectronics *etc.* The use of solution-based methods such as the successive ionic layer adsorption and reaction (SILAR), chemical bath deposition (CBD), electrodeposition, and hydrothermal method for the deposition of group VI LMDs over vapor-based methods such as chemical vapor deposition (CVD) and various sputtering techniques allows one to tune the physicochemical properties. With such promising features, solution-based deposited group VI LMDs possess a vast scope for their application in diverse fields. Hence, it is important to underscore the research progress in group VI LMDs and their future scope. The present study focuses on the versatility of solution-based deposited group VI LMDs in diverse fields. In addition, various solution-based deposition methods, different fascinating properties, and a thorough literature review of solution-based deposited group VI LMDs, along with the future scope, are discussed.

Centre for Interdisciplinary Research, D. Y. Patil Education Society (Deemed to be University), Kolhapur, 416 006, MS, India. E-mail: jlgunjakar@gmail.com

Vikas V. Magdum

From left- top row-S. A. Pawar, S. P. Kulkarni, S. V. Talekar, Y. M. Chitare, and P. D. Sawant. From left- bottom row- Dr. J. L. Gunjakar, V. V. Magdum, Prof. C. D. Lokhande, and Dr. S. B. Patil. Vikas V. Magdum, Yogesh M. Chitare, Shirin P. Kulkarni, Prashant D. Sawant, Shraddha A. Pawar, and Shweta V. Talekar are pursuing PhD degree at D. Y. Patil Education Society, Kolhapur (DYPES). Their research area includes the synthesis of 2D hybrids for energy storage, photocatalysis, electrocatalysis and gas sensor application. Dr. Umakant. M. Patil is currently working as an associate professor at DYPES. His research work includes the synthesis of metal phosphates for energy storage and catalysis applications. Dr. Sharad. B. Patil is currently working as an assistant professor at DYPES. His research interest lies in the synthesis of 2D hybrids for battery application. Dr. Jayavant L. Gunjakar is working as a Ramanujan Fellow at D. Y. Patil Education Society, Kolhapur. His
research interest includes the synthesis of 2D hybrids for energy storage, catalysis, and sensing applications. Prof. C. D. Lokhande is currently a Professor at D. Y. Patil Education Society, Kolhapur, India. His current research is focused on the synthesis of thin films by chemical methods for energy storage and catalysis.

पेटेंट कार्यालय,भारत सरकार

The Patent Office, Government Of India

पेटेंट प्रमाण पत्र | **Patent Certificate**

(पेटेंट नियमावली का नियम 74) | (Rule 74 of The Patents Rules)

पेटेंट सं. / Patent No.	:	501334
आवेदन सं. / Application No.	:	202121000897
फाइल करने की तारीख / Date of Filing	:	08/01/2021
पेटेंटी / Patentee	:	Dr. Jayavant Laxman Gunjakar.
आविष्कारक (जहां लागू हो)/ Inventor(s)	:	1.Dr. Jayavant Laxman Gunjakar 2.Mr. Akash Shashikant Patil 3.Mr. Vikas Vijay Magdum 4.Mr. Yogesh Murlidhar Chitare 5.Miss. Abhaya Shashikant Patil

प्रमाणित किया जाता है कि पेटेंटी को, उपरोक्त आवेदन में यथाप्रकटित *LIQUID COLUMN BASED OPTICAL INFRARED FILTER* नामक आविष्कार के लिए, पेटेंट अधिनियम, 1970 के उपबंधों के अनुसार आज तारीख जनवरी 2023 के आठवें दिन से बीस वर्ष की अवधि के लिए पेटेंट अनुदत्त किया गया है।

It is hereby certified that a patent has been granted to the patentee for an invention entitled *LIQUID COLUMN BASED OPTICAL INFRARED FILTER* as disclosed in the above mentioned application for the term of 20 years from the 8th day of January 2023 in accordance with the provisions of the Patents Act,1970.

अनुदान की तारीख :
Date of Grant : 19/01/2024

पेटेंट नियंत्रक
Controller of Patent

तिप्पणी – इस पेटेंट के नवीकरण के लिए फीस, यदि इसे बनाए रखा जाना है, जनवरी 2023 के आठवें दिन को और उसके पश्चात प्रत्येक वर्ष मे उसी दिन देय होगी।

Note. - The fees for renewal of this patent, if it is to be maintained will fall / has fallen due on 8th day of January 2023 and on the same day in every year thereafter.

पेटेंट कार्यालय, भारत सरकार **The Patent Office, Government Of India**

डिजाइन के पंजीकरण का प्रमाण पत्र | Certificate of Registration of Design

डिजाइन सं. / Design No. : 407337-001

तारीख / Date : 12/02/2024

पारस्परिकता तारीख / Reciprocity Date* :

देश / Country :

प्रमाणित किया जाता है कि संलग्न प्रति में वर्णित डिजाइन जो *INFRARED (IR) CUT-OFF WATER FILTER ASSEMBLY* से संबंधित है, का पंजीकरण, श्रेणी 23-01 में 1.D. Y. Patil Education Society Kolhapur 2. Dr. Jayavant L. Gunjakar 3.Mr. Yogesh M. Chitare 4.Mr. Vikas V. Magdum 5.Miss. Shirin P. Kulkarni 6.Mr. Akash S. Patil 7.Miss Abhaya S. Patil के नाम में उपर्युक्त संख्या और तारीख में कर लिया गया है।

Certified that the design of which a copy is annexed hereto has been registered as of the number and date given above in class 23-01 in respect of the application of such design to *INFRARED (IR) CUT-OFF WATER FILTER ASSEMBLY* in the name of 1.D. Y. Patil Education Society Kolhapur 2. Dr. Jayavant L. Gunjakar 3.Mr. Yogesh M. Chitare 4.Mr. Vikas V. Magdum 5.Miss. Shirin P. Kulkarni 6.Mr. Akash S. Patil 7.Miss Abhaya S. Patil.

डिजाइन अधिनियम, 2000 तथा डिजाइन नियम, 2001 के अध्यधीन प्रावधानों के अनुसरण में।

In pursuance of and subject to the provisions of the Designs Act, 2000 and the Designs Rules, 2001.

जारी करने की तिथि :
Date of Issue : 10/04/2024

महानियंत्रक पेटेंट, डिजाइन और व्यापार चिह्न
Controller General of Patents, Designs and Trade Marks

प्रतिलिप्यधिकार कार्यालय, भारत सरकार | Copyright Office, Government Of India

दिनांक/Dated:27/02/2024

L-144382/2024

1.	पंजीकरण संख्या/Registration Number	:	
2.	आवेदक का नाम, पता तथा राष्ट्रीयता Name, address and nationality of the applicant	:	THE REGISTRAR , D. Y. PATIL EDUCATION SOCIETY, DEEMED TO BE UNIVERSITY, KASABA BAWADA, KOLHAPUR-416006 INDIAN
3.	कृति के प्रतिलिप्यधिकार में आवेदक के हित की प्रकृति Nature of the applicant's interest in the copyright of the work	:	PUBLISHER
4.	कृति का वर्ग और वर्णन Class and description of the work	:	LITERARY/ DRAMATIC WORK
5.	कृति का शीर्षक Title of the work	:	THIN FILM PHOTOCATALYST SETUP FOR DYE DEGRADATION
6.	कृति की भाषा Language of the work	:	ENGLISH
7.	रचयिता का नाम, पता और राष्ट्रीयता तथा यदि रचयिता की मृत्यु हो गई है, तो मृत्यु की तिथि Name, address and nationality of the author and if the author is deceased, date of his decease	:	DR. JAYAVANT L. GUNJAKAR , ASSOCIATE PROFESSOR , CENTRE FOR INTERDISCIPLINARY RESEARCH, D. Y. PATIL EDUCATION SOCIETY, DEEMED TO BE UNIVERSITY, KASABA BAWADA, KOLHAPUR-416006 INDIAN MR. YOGESH M. CHITARE, PH.D. SCHOLAR , CENTRE FOR INTERDISCIPLINARY RESEARCH, D. Y. PATIL EDUCATION SOCIETY, DEEMED TO BE UNIVERSITY, KASABA BAWADA, KOLHAPUR-416006 INDIAN MR. VIKAS V. MAGDUM, PH.D. SCHOLAR, , CENTRE FOR INTERDISCIPLINARY RESEARCH, D. Y. PATIL EDUCATION SOCIETY, DEEMED TO BE UNIVERSITY, KASABA BAWADA, KOLHAPUR-416006 INDIAN
8.	कृति प्रकाशित है या अप्रकाशित Whether the work is published or unpublished	:	PUBLISHED
9.	प्रथम प्रकाशन का वर्ष और देश तथा प्रकाशक का नाम, पता और राष्ट्रीयता Year and country of first publication and name, address and nationality of the publisher	:	2024 INDIA THE REGISTRAR , D. Y. PATIL EDUCATION SOCIETY, DEEMED TO BE UNIVERSITY, KASABA BAWADA, KOLHAPUR-416006 INDIAN
10.	बाद के प्रकाशनों के वर्ष और देश, यदि कोई हों, और प्रकाशकों के नाम, पते और राष्ट्रीयताएँ Years and countries of subsequent publications, if any, and names, addresses and nationalities of the publishers	:	N.A.
11.	कृति में प्रतिलिप्यधिकार सहित विभिन्न अधिकारों के स्वामियों के नाम, पते और राष्ट्रीयताएं और समनुदेशन और अनुज्ञप्तियों के विवरण के साथ प्रत्येक के अधिकार का विस्तार, यदि कोई हो। Names, addresses and nationalities of the owners of various rights comprising the copyright in the work and the extent of rights held by each, together with particulars of assignments and licences, if any	:	THE REGISTRAR , D. Y. PATIL EDUCATION SOCIETY, DEEMED TO BE UNIVERSITY, KASABA BAWADA, KOLHAPUR-416006 INDIAN
12.	अन्य व्यक्तियों के नाम, पते और राष्ट्रीयताएं, यदि कोई हों, जो प्रतिलिप्यधिकार वाले अधिकारों को समनुदेशित करने या अनुज्ञप्ति देने के लिए अधिकृत हों Names, addresses and nationalities of other persons, if any, authorised to assign or licence of rights comprising the copyright	:	N.A.
13.	यदि कृति एक 'कलात्मक कृति है, तो कृति पर अधिकार रखने वाले व्यक्ति का नाम, पता और राष्ट्रीयता सहित मूल कृति का स्थान। (एक वास्तुशिल्प कृति के मामले में कृति पूरी होने का वर्ष भी दिखाया जाना चाहिए) If the work is an 'Artistic work', the location of the original work, including name, address and nationality of the person in possession of the work. (In the case of an architectural work, the year of completion of the work should also be shown).	:	N.A.
14.	यदि कृति एक 'कलात्मक कृति है जो किसी भी माल या सेवाओं के संबंध में उपयोग की जाती है या उपयोग किए जाने में सक्षम है, तो आवेदन में प्रतिलिप्यधिकार अधिनियम, 1957 की धारा 45 की उप–धारा (i) के प्रावधान के अनुसार व्यापार चिह्न रजिस्ट्रार से प्रमाणन शामिल होना चाहिए If the work is an 'Artistic work' which is used or capable of being used in relation to any goods or services, the application should include a certification from the Registrar of Trade Marks in terms of the provision to Sub-Section (i) of Section 45 of the Copyright Act, 1957.	:	N.A.
15.	यदि कृति एक 'कलात्मक कृति' है, तो क्या यह डिजाइन अधिनियम 2000 के अंतर्गत पंजीकृत है? यदि हां, तो विवरण दें। If the work is an 'Artistic work', whether it is registered under the Designs Act 2000, if yes give details.	:	N.A.
16.	यदि कृति एक 'कलात्मक कृति' है, जो डिजाइन अधिनियम 2000 के एक डिजाइन के रूप में पंजीकृत होने में सक्षम है, तो क्या यह औद्योगिक प्रक्रिया के माध्यम से किसी वस्तु पर प्रयुक्त की गई है और यदि हां, तो कितनी बार पुनरुत्पादित किया गया है? If the work is an 'Artistic work', capable of being registered as a design under the Designs Act 2000.whether it has been applied to an article though an industrial process and ,if yes ,the number of times it is reproduced.	:	N.A.

Registrar of Copyrights

प्रतिलिप्यधिकार कार्यालय, भारत सरकार | **Copyright Office, Government Of India**

दिनांक/Dated:23/04/2024

1.	पंजीकरण संख्या/Registration Number	:	**L-147009/2024**
2.	आवेदक का नाम, पता तथा राष्ट्रीयता Name, address and nationality of the applicant	:	THE REGISTRAR , D. Y. PATIL EDUCATION SOCIETY, DEEMED TO BE UNIVERSITY, KASABA BAWADA, KOLHAPUR-416006 INDIAN
3.	कृति के प्रतिलिप्यधिकार में आवेदक के हित की प्रकृति Nature of the applicant's interest in the copyright of the work	:	PUBLISHER
4.	कृति का वर्ग और वर्णन Class and description of the work	:	LITERARY/ DRAMATIC WORK
5.	कृति का शीर्षक Title of the work	:	FIGURE REPRESENTING SCHEMATIC OF MICROPROCESSOR-CONTROLLED DIP-COATING INSTRUMENT
6.	कृति की भाषा Language of the work	:	ENGLISH
7.	रचयिता का नाम, पता और राष्ट्रीयता तथा यदि रचयिता की मृत्यु हो गई है, तो मृत्यु की तिथि Name, address and nationality of the author and if the author is deceased, date of his decease	:	DR. JAYAVANT L. GUNJAKAR, ASSOCIATE PROFESSOR , CENTRE FOR INTERDISCIPLINARY RESEARCH, D. Y. PATIL EDUCATION SOCIETY, DEEMED TO BE UNIVERSITY, KOLHAPUR-416006 INDIAN MR. VIKAS V. MAGDUM, PH.D. SCHOLAR , CENTRE FOR INTERDISCIPLINARY RESEARCH, D. Y. PATIL EDUCATION SOCIETY, DEEMED TO BE UNIVERSITY, KOLHAPUR-416006 INDIAN MR. YOGESH M. CHITARE, PH.D. SCHOLAR , CENTRE FOR INTERDISCIPLINARY RESEARCH, D. Y. PATIL EDUCATION SOCIETY, DEEMED TO BE UNIVERSITY, KOLHAPUR-416006 INDIAN
8.	कृति प्रकाशित है या अप्रकाशित Whether the work is published or unpublished	:	PUBLISHED
9.	प्रथम प्रकाशन का वर्ष और देश तथा प्रकाशक का नाम, पता और राष्ट्रीयता Year and country of first publication and name, address and nationality of the publisher	:	2024 INDIA THE REGISTRAR , D. Y. PATIL EDUCATION SOCIETY, DEEMED TO BE UNIVERSITY, KASABA BAWADA, KOLHAPUR-416006 INDIAN
10.	बाद के प्रकाशनों के वर्ष और देश, यदि कोई हों, और प्रकाशकों के नाम, पते और राष्ट्रीयताएँ Years and countries of subsequent publications, if any, and names, addresses and nationalities of the publishers	:	N.A.
11.	कृति में प्रतिलिप्यधिकार सहित विभिन्न अधिकारों के स्वामियों के नाम, पते और राष्ट्रीयताएं और समनुदेशन और अनुज्ञप्तियों के विवरण के साथ प्रत्येक के अधिकार का विस्तार, यदि कोई हो। Names, addresses and nationalities of the owners of various rights comprising the copyright in the work and the extent of rights held by each, together with particulars of assignments and licences, if any	:	THE REGISTRAR , D. Y. PATIL EDUCATION SOCIETY, DEEMED TO BE UNIVERSITY, KASABA BAWADA, KOLHAPUR-416006 INDIAN
12.	अन्य व्यक्तियों के नाम, पते और राष्ट्रीयताएं, यदि कोई हों, जो प्रतिलिप्यधिकार वाले अधिकारों को समनुदेशित करने या अनुज्ञप्ति देने के लिए अधिकृत हों Names, addresses and nationalities of other persons, if any, authorised to assign or licence of rights comprising the copyright	:	N.A.
13.	यदि कृति एक 'कलात्मक कृति' है, तो कृति पर अधिकार रखने वाले व्यक्ति का नाम, पता और राष्ट्रीयता सहित मूल कृति का स्थान। (एक वास्तुशिल्प कृति के मामले में कृति पूरी होने का वर्ष भी दिखाया जाना चाहिए) If the work is an 'Artistic work', the location of the original work, including name, address and nationality of the person in possession of the work. (In the case of an architectural work, the year of completion of the work should also be shown).	:	N.A.
14.	यदि कृति एक 'कलात्मक कृति' है जो किसी भी माल या सेवाओं के संबंध में उपयोग की जाती है या उपयोग किए जाने में सक्षम है, तो आवेदन में प्रतिलिप्यधिकार अधिनियम, 1957 की धारा 45 की उप–धारा (i) के प्रावधान के अनुसार व्यापार चिह्न रजिस्ट्रार से कृति मूल कृति का स्थान शामिल होना चाहिए। If the work is an 'Artistic work' which is used or capable of being used in relation to any goods or services, the application should include a certification from the Registrar of Trade Marks in terms of the provision to Sub-Section (i) of Section 45 of the Copyright Act, 1957.	:	N.A.
15.	यदि कृति एक 'कलात्मक कृति' है, तो क्या यह डिजाइन अधिनियम 2000 के अंतर्गत पंजीकृत है? यदि हां, तो विवरण दें। If the work is an 'Artistic work', whether it is registered under the Designs Act 2000, if yes give details.	:	N.A.
16.	यदि कृति एक 'कलात्मक कृति' है, जो डिजाइन अधिनियम 2000 के अंतर्गत एक डिजाइन के रूप में पंजीकृत होने में सक्षम है, तो क्या यह औद्योगिक प्रक्रिया के माध्यम से किसी वस्तु पर प्रयुक्त की गई है और यदि हां, तो कितनी बार पुनरुत्पादित किया गया है? If the work is an 'Artistic work', capable of being registered as a design under the Designs Act 2000.whether it has been applied to an article though an industrial process and ,if yes ,the number of times it is reproduced.	:	N.A.

Registrar of Copyrights

Shardabai Pawar Mahila Arts, Commerce & Science College,
Shardanagar, Malegaon Bk., Tal- Baramati , Dist. - Pune , 413115

Recent Trends in Functional Materials and Their Applications

SERB Sponsored

National Conference

on

(RTFMA - 2024)

Award Certificate

Presented to Dr./Mr./Mrs./Miss. ___chitare yogesh___ from _____

___D.Y.Patil , kolhapur_____, has received *Best Oral /*

Poster presentation award in SERB sponsored National conference organized by Department of

Physics on 13th - 14th March 2024.

Dr. V.R.Shinde & Ms.S.J.Shinde
Organising Secretary

Dr. T.P.Gujar
Coordinator & Head

Prof. Dr. S.V.Mahamuni
Convener & Principal

D. Y. PATIL EDUCATION SOCIETY

(Deemed to be University), KOLHAPUR

NAAC 'A'' Grade in 3rd Cycle

Certificate

This is to certify that **Mr. /Ms. Chitare Yogesh Murlidhar** of Centre for Interdisciplinary Research, DYPES, Kolhapur has delivered invited talk / chaired the session / presented oral / presented poster / participated in the **International Conference on Nanotechnology Addressing the Convergence of Materials Science, Biotechnology and Medical Science (IC-NACMBM-2024)** held at the Centre for Interdisciplinary Research, D. Y. Patil Education Society (Deemed to be University), Kolhapur, Maharashtra, India during 12th to 14th February 2024. His / Her contribution to the conference is highly appreciated.

Dr. Jayavant L. Gunjakar

Convener

Prof. Meghnad G. Joshi

Convener

Prof. Chandrakant D. Lokhande

Chairman

60th

ACC 2023
Annual Convention of Chemists

20th-21st Dec 2023 | IIT Delhi Campus, Hauz Khas, New Delhi

— THEME —

NET ZERO GOAL & SUSTAINABILITY: ROLE OF CHEMICAL SCIENCES IN GREEN ENERGY, CIRCULAR ECONOMY AND PROSPERITY OF INDIA

CERTIFICATE OF PARTICIPATION

THIS CERTIFICATE IS PROUDLY PRESENTED TO

MR.YOGESH CHITARE

FOR PARTICIPATING

POSTER SESSION

AT 60TH ANNUAL CONVENTION OF CHEMISTS

Organiser

Co-Host

CENTENNIAL JUBILEE CELEBRATION
★ ★ ★

Prof. Akhilesh K. Verma
Convenor, 60th ACC 2023
Department of Chemistry, University of Delhi

Prof. G. D. Yadav
Chairman, 60th ACC
President, Indian Chemical Society

SHIVAJI UNIVERSITY, KOLHAPUR

SOPHISTICATED ANALYTICAL INSTRUMENT FACILITY (SAIF) – COMMON FACILITY CENTRE (CFC)

WORKSHOP & HANDS-ON TRAINING ON XRD ORGANISED

BY SAIF-CFC UNDER STRIDE PROGRAMME

Certificate of Participation

This is certify that Mr. _Chitare Yogesh Murlidhar_ has successfully participated in the workshop & hands-on training on XRD organised by SAIF (CFC), Shivaji University, Kolhapur held during 11-12 Nov, 2021 under the STRIDE (Scheme for Trans-disciplinary Research for India's Developing Economy) programme.

Prof. R. G. Sonkawade
Co-ordinator : SAIF, Head (i/c) : CFC
Shivaji University, Kolhapur.
Chairman